Atomistic Modeling of Pulsed Laser Interactions with Metals in a Liquid Environment

A Dissertation

Presented to
the faculty of the School of Engineering and Applied Science
University of Virginia

in partial fulfillment
of the requirements for the degree

Doctor of Philosophy

by

Cheng-Yu Shih

August

2017

APPROVAL SHEET

The dissertation
is submitted in partial fulfillment of the requirements
for the degree of
Doctor of Philosophy

Cheng-Ta Shih
AUTHOR

The dissertation has been read and approved by the examining committee:

Leonid Zhigilei
Advisor

Petra Reinke

Mool Gupta

James Fitz-Gerald

Bilal Gökce

Sean Agnew

Accepted for the School of Engineering and Applied Science:

Craig H. Benson, Dean, School of Engineering and Applied Science

August
2017

Contents

Acknowledgements

It has been a magical journey during my stay in UVa, and the person who has always been there for me is my advisor, Professor. Leonid V. Zhigilei. I cannot express enough how lucky I am to work with Leo. Leo is not only a knowledgeable mentor but also a humble role model that I should strive on with diligence. Starting as a clueless undergraduate sitting in Introduction to Materials Science and Engineering taught by Leo in my first semester, I was inspired by Leo's ardent passion for teaching and research, and decided to join his group. While the progress of my research had gone extremely slow during the first few semesters, Leo has always been wholeheartedly supportive and even actively looking out more learning opportunities for me. Scientific discussion with Leo has always been intriguing and encouraging, he has always shown me a clear vision from my messy research problems. Not only a sophisticated scholar, Leo is also a great leader who always puts others at first and never stops to think for himself. While exploring a broad range of research topics and mentoring a large research group, he never lefts any student behind. His unflagging commitment to scientific research is admirable.

I am really grateful for Professor. Petra Reinke, Professor. James Fitz-Gerald, Professor. Patrick Hopkins, Dr. Bilal Gökce, Professor. Mool Gupta, and Professor. Sean Agnew to allot their precious time to kindly serve in my dissertation committee. Their advices have been greatly valuable to my research.

I want to give special thanks to Dr. Katherine Holcomb, Dr. Chengping Wu and Maxim V. Shugaev, who have helped me generously throughout my research. Starting as a total beginner (just learnt "Hello-world"), Dr. Katherine Holcomb had painstakingly taught me the fundamentals of scientific programming, and always available for my naïve programming questions. Dr. Chengping Wu had guided me through countless hours of learning of our legacy code. He has not only taught me the technical perspectives of atomistic modeling, but also always willingly helped me on my pesty debugging questions. Maxim V. Shugaev has selflessly shared his knowledge, and taught me many advanced computational techniques to be a better computational scientist. The scientific discussion with Dr. Chengping Wu and Maxim V. Shuagev has always been stimulating and insightful; I truly appreciate working with them.

I would like to express my gratitude to Dr. Bilal Gökce and Professor. Stephan Barcikowski that generously invited me to stay a month with their mega group in University of Essen-Duisburg, Germany. As the world-class leading research group in the field of pulsed laser ablation in liquids, they had shown me the advancement of the field that truly broadens my horizons. The invited stay helped me think more pragmatically about my research on how to connect the experimental observation with computational modeling.

I want to thank all my former and current colleagues in the Computational Materials Group, Professor. Alexey Volkov, Dr. Chengping Wu, Dr. Marshall Tabetah, Dr. Richard Salaway, Dr. Eaman Tahir Abdul, Bernard Wittmaack, Miao He, Hao Huang, Han Wu, Jing Zou, and Maxim Shugaev. With everyone's effort, we have created a positive and joyful research environment.

Being away from home for more than a decade to pursue education, I deeply miss my parents and brother; their unconditional support gives me the emotional strength to face all the challenges. Every week the most urgent thing I can possibly do is to have a good chatting with them, no matter how trivial the gossip is, their voice always fuels me with energy to go further. They mean the world to me, but I probably don't tell them enough. Anyway, words are insufficient to express my infinite gratitude to them. I cant wait to embark on the next chapter of my life with them side by side.

Abstract

The synthesis of chemically clean and environmentally friendly nanoparticles through pulsed laser ablation in liquids has shown a number of advantages over conventional chemical synthesis methods and has evolved into a thriving research field attracting various applications. While eclipsed by the rapid progress of nanoparticle generation, controlled modification of surface morphology and microstructure through laser processing in liquids has also been demonstrated to be a viable technique. The fundamental understanding of processes leading to the nanoparticle generation and surface structuring, however, still remains elusive. A hybrid computational model combining coarse-grained representation of liquid and a fully atomistic description of laser interactions with metal targets is developed to investigate the microscopic mechanisms of nanoparticle generation and surface structuring in pulsed laser ablation in liquids.

The simulations reveal the critical role of dynamic interactions between ablation plume and liquid environment resulting in multiple nanoparticle generation mechanisms corresponding to distinctively different sizes of nanoparticles. The presence of liquid can effectively decelerate the ejected ablation plume, and the liquid in contact with the plume is heated up to supercritical state leading to a formation of a low-density vapor region (precursor of a cavitation bubble observed in experiments). One of nanoparticle generation mechanisms is nucleation and growth of small nanoparticles (mostly < 10 nanometers) from vapor-phase metal atoms in the low-density vapor region. This nanoparticle generation mechanism is observed consistently regardless target geometry, material type and pulse duration. For short laser pulses (< 10 picoseconds), simulations reveal the formation of a dense molten metal layer at plume-liquid interface due to the conditions of strong stress confinement. The surface of the molten metal layer rapidly develops complex morphological features attributed to the Rayleigh-Taylor instability. A subsequent evolution of hydrodynamic instabilities at the plume-liquid interface can result in the layer disintegration and/or ejection of large (10s of nanometers) nanoparticles into the liquid environment. The computational predictions are supported by a series of stroboscopic videography and double pulse experiments performed by collaborators from the University of Duisburg-Essen, Germany. Two distinctive nanoparticle generations mechanisms responsible for two characteristic nanoparticle sizes can be related to the bimodal nanoparticle size distributions commonly observed in short pulse laser ablation in liquids. The simulations also predict that fast quenching induced by the interaction with liquid environment results in crystallization of nanoparticles on nanosecond timescale. Extending the simulations to longer, sub-nanosecond and nanosecond, laser pulses reveals that “gentler” ablation conditions do not produce the accumulation of a thick molten metal layer at the plume-liquid interface, and the ablation plume remains as a mixture of metal vapor and small droplets confined by liquid. In addition to the aforementioned generation of nanoparticles through the nucleation and growth from metal vapor in the expanding low-density region, the interaction of the ablation plume with liquid environment results in a condensation of a thin transient metal layer at the plume-liquid interface, which ruptures into large nanoparticles (10s of nanometers). The supercritical liquid streaming through ruptured layer deeper into the ablation plume induces rapid cooling and massive nucleation of nanoparticles with sizes mostly less than 10 nm throughout the ablation plume.

Series of simulations are also performed to investigate the potential role of liquid environment in laser-assisted surface engineering. The presence of liquid is found to suppress nucleation of sub-surface voids characteristic for laser processing in vacuum and provide an additional pathway for surface cooling, thus facilitating the formation of nanocrystalline surface layer. In the irradiation regime of photomechanical spallation, the liquid environment is shown to prevent the complete separation of the spalled layer from the target, leading to the formation of large subsurface voids stabilized by rapid cooling and solidification. The subsequent irradiation of the laser-modified surface is found to result in a more efficient ablation and nanoparticle generation, thus suggesting the possibility of the incubation effect in multipulse laser ablation in liquids. Finally, the effect of liquid environment on the recently invented surface nanostructuring technique, single-pulse ablative generation of laser induced periodic surface structures, is also investigated. The presence of liquid induces complex hydrodynamic flow that not only affects the characteristics of the periodic surface structures, but also suggests the possibility of surface hyperdoping through liquid-assisted laser processing.

The initial applications of the hybrid computational model demonstrate its unique capability to reveal microscopic mechanisms responsible for nanoparticle generation and surface structuring. The model can be further applied to facilitate the design of innovative experimental techniques aimed fine-tuning nanoparticle distributions, engineering desirable alloy nanoparticles, and producing surface layers with unusual non-equilibrium structures and phase compositions.

List of Figures

List of Tables

1. Introduction

1.1. Background of pulsed laser ablation in liquids

Pulsed laser ablation in liquid (PLAL) has recently emerged as a particularly promising approach to the generation of colloidal solutions of contamination-free nanoparticles[1-11] suitable for applications in various fields, including biomedicine,[12-14] chemical catalysis,[15-18] and plasmonics[19-20]. The characteristics of nanoparticles in this case are affected by various external variables including the choice of the liquid medium,[21-24] its temperature and pressure,[25-27] and introduction of solutes.[28-30] While the setup for experiments is simple, the highly non-equilibrium conditions created by the interaction of the ablation plume with liquid environment can result in the formation of nanoparticles with unusual structure, shape and composition, such as nanocubes,[31] hollow spheroids,[32-34] patch-joint football-like AgGe microspheres,[35] and diamond nanocrystallites produced by laser ablation of graphite.[36] Moreover, post irradiation processes including pulsed laser fragmentation in liquids (PLFL)[14, 37-38] and pulsed laser melting in liquids (PLML)[12, 39] can expand the range of size control from 4 to 400 nm.[2] Further optimization of experimental parameters in PLAL for the efficient generation of nanoparticles with structures, compositions and size distributions fine-tuned to the needs of practical applications can be facilitated by improved physical understanding of the involved processes. Despite the continuous advancements in the application of PLAL for improved production and process-stability[40-41] of nanoparticles for an increasingly wide range of material systems[2, 10-11] and targeted experimental studies aimed at reveling the key processes responsible for the nanoparticle generation,[42-52] the fundamental mechanisms of the nanoparticle formation by laser ablation in liquids are still not fully understood.

The following two sections focus on current understanding of the ablation plume interaction with liquids leading to the possible nanoparticle generation mechanisms. In Chapter 1.1.1., advancement of experimental techniques to probe phenomena occurred at different temporal stages of pulsed laser ablation in liquids to understand nanoparticle generation mechanism will be discussed. In Chapter 1.1.2, current computational and theoretical approaches to model pulsed laser ablation in liquids and corresponding interpretation of nanoparticle generation mechanisms will be discussed. Finally, the potential role of applying Molecular Dynamics (MD) to further the understanding of nanoparticle generation mechanisms in pulsed laser ablation in liquids is suggested with the description of computational model used in the dissertation in Chapter 1.2.

1.1.1. Process of pulsed laser ablation in liquids and experimental probing

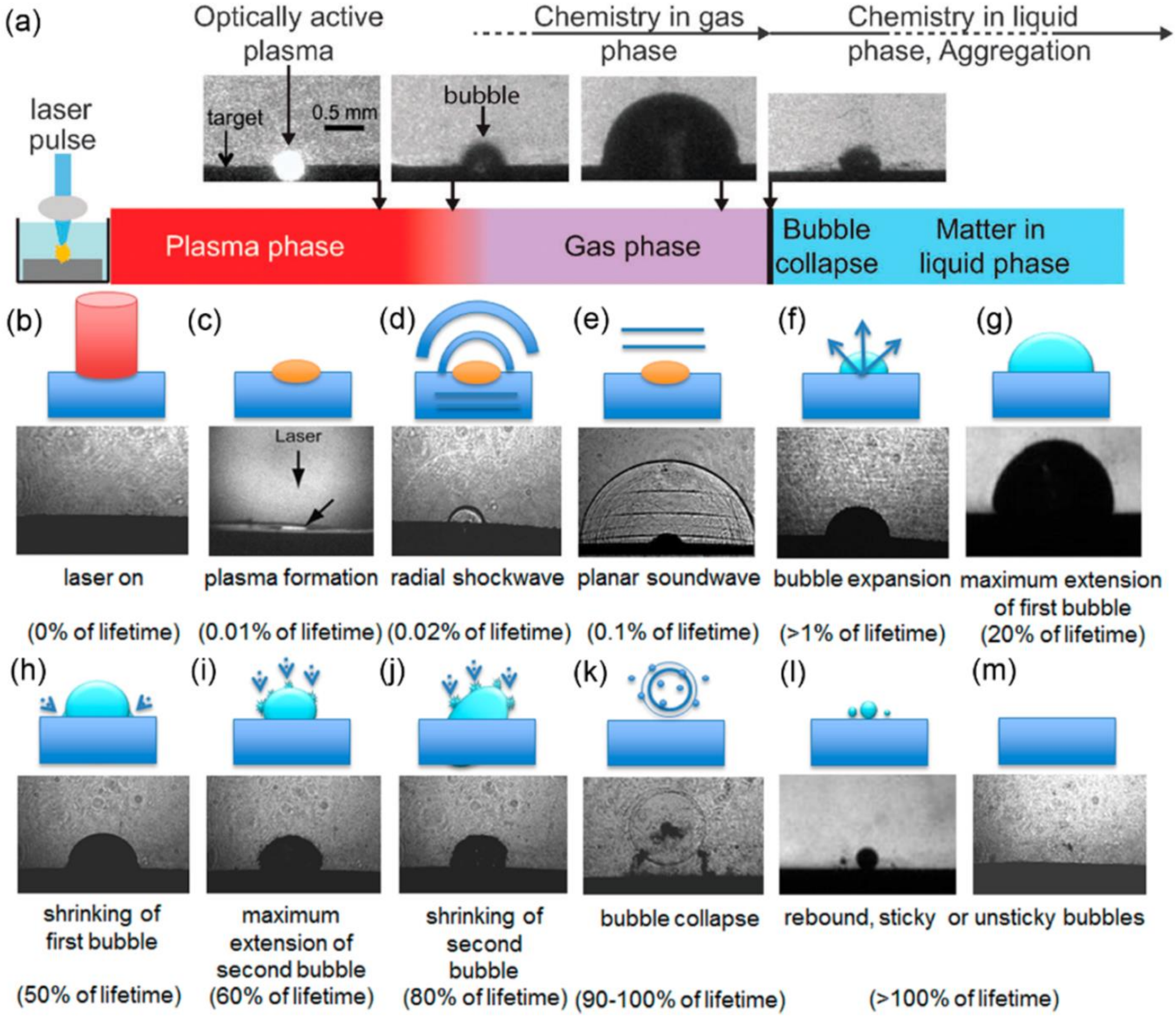

Figure 1.1. (a) the main sequential processes occure during pulsed laser ablation in liquids. (b)-(m) show the sketchs of cavitaition bubble dynamics (upper row) with the corresponding images recorded by shadowgraphs (lower row). Reprinted with permission from ref 11. Copyright 2017 American Chemical Society.

A general series of macroscopic processes that can be experimentally observed during pulsed laser ablation in liquids is shown in Fig. 1.1a. Plasma, Fig. 1.1c, can be generated when the target in liquids is irradiated by a laser pulse with high enough intensity, and its emission can be spectroscopically probed.[25, 43, 53] The plasma emission spectroscopy can provide the valuable information on the likely chemical reaction happens at the first tens of ns to a few us[50] and predict the possible final products. The initial plasma temperature can reach thousands of Kelvins with pressures on the orders of hundreds of pascals.[51] The liquid in contact with the plasma will be overheated quickly to form a thin layer of vapor surrounding the plasma, shown in Fig. 1.1d. The vapor not only expands toward the water to form cavitation bubble, but also toward the plasma to suppress the plasma expansion. The expansion of vapor layer toward surrounding liquids results in formation of cavitation bubble, shown in Fig. 1.1f and 1.1g. The study of the cavitation bubble dynamics itself is an expanding field that can be applied to energy conversion and surface processing.[54-57] For PLAL, cavitation bubble dynamics are believed to be a prominent piece of puzzles to understand the origin of nanoparticle generations. Dynamics of cavitation bubble can be observed via optical imaging techniques including shadowgraphy,[49, 58] stroboscopic videography,[52] X-ray radiography.[45] The first cycle of cavitation bubble expansion and collapse is normally observed as semi-spherical bubble with sharp interface, as shown in Fig. 1.1f-h, that can be adequately approximated by Rayleigh-Plesset theory.[49] However, the subsequent cycles of rebounce and final collapse often show cavitation bubbles with irregular shapes and divisions into “daughter bubbles”, as shown Fig. 1.1i-l. The temperature and pressure of the cavitation bubble have been modeled by van der Waals equations and Rayleigh-Plesset theory.[49, 58] The calculation shows that the high temperature and pressure conditions are only created during the initial plasma phase and the moment of bubble collapse. During the bubble expansion stage, the internal environment of the bubble is rather cold with pressure decreasing to close to external liquid conditions that is ideal to facilitate nanoparticle formation with highly non-equilibrium phases and structures.

Currently, the prevailing theory suggests that the ablated material is likely to be confined and trapped inside the cavitation bubble, while the cavitation bubble provides favorable low pressure and temperature conditions for nanoparticle nucleation, growth, coalescence and finally solidification.[51] However, the conventional optical methods cannot provide credible proofs of the theory, since the optically dense interface between the liquid and cavitation bubble blocks the means of optical detection. Recently, the novel use of small angle x-ray scattering (SAXS) to monitor nanoparticle growth and distribution is proved to be an effective technique to relate cavitation bubble dynamics to nanoparticle generation and growth.[44-47] In-situ SAXS can be used to scan different positions in the bubble with time delay, so the particle size distribution can be mapped out as function of time and position inside the bubble.[44-47] The results from SAXS reveal broad nanoparticle size distribution for nanosecond laser ablation in liquids,[7-8] and qualitatively agree with the theory of nanoparticle generation in cavitation bubble.

Signals yielded by SAXS show two distinctive peaks, representing two distinguishable size populations.[44-47] The first population is called primary particles, and has size distribution centered around 8-10 nm. The primary particles are detected starting at the early stage during first bubble expansion. Greater number of primary particles is detected near the bottom of the bubble, and its abundance decays as the scan moves toward the top of the bubble. Moreover, the average particle diameter is found to decrease with the bubble height. This decrease indirectly supports the classic nucleation and growth theory, where there are higher particle density and coalescence probability at region to the ablated target. The second population is called secondary particles, and has size distribution centered around 50 nm. The secondary particles have been speculated to mostly form through collisions and agglomeration of primary particles,[44] although the possibility of multiple pathways for generation of secondary particles have recently been considered as well.[46] Moreover, secondary particles sizes are highly variable, the size are changing rapidly during the whole bubble dynamic process, indicating that these secondary particles are not compact objects, but some forms of loose molten networks. While the interpretation of SAXS data provides first hand quantitative data on nanoparticle generation process in PLAL, other approaches are needed to understand the nanoparticle generation mechanisms from different perspectives. In particular, the atomic clusters and nanoparticles smaller than 5 nm cannot be detected with SAXS but may be responsible for the nanoparticle nucleation and growth in the ablation process as well as the slower growth and coarsening of nanoparticles in the colloidal solutions generated by PLAL.[59-60] Moreover, the primary particles detected at the early stage of the first bubble expansion are likely to be directly ejected from the irradiated target or formed during the first nanoseconds of the plume expansion, which is currently beyond the temporal resolution of SAXS. One needs to push beyond the current SAXS limits on the particle sizes and temporal/spatial resolution to observe the ablation phenomena in more details. Moreover, there is a need to resolve the thermodynamic states of the plume confined in the cavitation bubble to enable reliable theoretical description of PLAL. Computational modeling can play key roles in further exploring the initial non-equilibrium dynamics in PLAL.

1.1.2. Current theoretical/computational approaches and the potential role of Molecular Dynamics

Currently, the available theoretical and computational literature tackling nanoparticle generation mechanism of PLAL is scant; introduction of a spatial confinement and the interaction between the ejected plume and the surrounding medium add another layer of complexity to the description of pulsed laser ablation, which by itself is a complex and highly non-equilibrium phenomenon. As a result, the theoretical analysis of the nanoparticle formation by laser ablation in liquids[61] is largely based on semi-quantitative models that adopt the concepts developed for the plume expansion in a background gas to the much stronger confinement by a liquid environment, and describe the nanoparticle formation as a process of coalescence of clusters in a supersaturated solution formed by the mixing of the ablation plume and the liquid. The analysis in this case relies on the assumptions of the initial cluster size distribution in the solution, the temperature evolution in the plume-liquid mixing region, the thickness of the mixing region, and other parameters.

The difficulties of the theoretical analysis are shared by continuum-level computational approaches, where realistic modeling of phase transformations occurring under highly nonequilibrium conditions represents a daunting challenge. The first hydrodynamic simulations of PLAL[62-63] adopt a simplified representation of water environment as a thermally insulating, non-mixable overlayer described by a single-phase equation of state. The highly simplified representation of the water environment prevents the realistic description of some of the key processes, such as the formation of a layer of water vapor driving the expansion of the cavitation bubble, water-metal mixing and rapid cooling of the metal species in the mixing region. Moreover, the 1D nature of the model does not allow for the direct simulation of the nanoparticle generation. Nevertheless, the results of the first hydrodynamic simulations have provided important insights into the evolution of thermodynamic conditions and phase decomposition at the early stage of PLAL. Two main types of nanoparticle generation mechanisms depending on laser fluence are purposed by Povarnitsyn et al,[63] and discussed below.

The first nanoparticle generation mechanism, illustrated in Fig. 1.2a, is seen in low fluence regime. Multiple liquid layers are ejected due to spallation, and the spalled layers merge into one thick layer due to the deceleration of the front layer in contact with water. The merged layer is kept at metastable condition that is far away from the critical point, and explosive boiling does not occur. The metastable liquid layer is expected to breakdown into large size droplet due to thin liquid film instability[64] with diameters of tens of nanometers at a later time. The second mechanism, illustrated in Fig. 1.2b, is seen in high fluence regime, when top ejected layer undergoes phase explosion. A new thermodynamic phase with liquid and gas coexisting appears, and actively pushes the water overlayer above and the ejected liquid layer below. Since the density of the mixture is by one or two orders of magnitude less than that of the liquid phase, one can expect small nanoparticles come from the liquid-gas mixture. Even though such simplified representation of water cannot fully confirm aforementioned nanoparticle generation mechanism purposed from experimental observation, the results from these studies show that the confinement alone is likely to facilitate bimodal nanoparticle distribution.

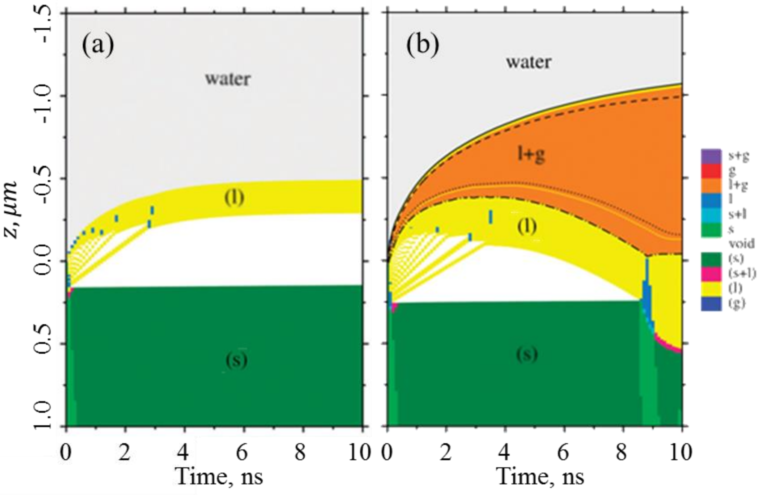

Figure 1.2. Spatial-temporal diagrams of water and gold marked by phases states of gold, predicted in continuum level modeling by Povarnitsyn et al.[63] (a) corresponds to gold target in water irradiated by a 200 fs laser pulse at an absorbed fluence of 2600 J/m^2, and (b) corresponds to that of an absorbed fluence of 5500 J/m^2. Adapted with permission from ref 63. Copyright 2013 Royal Society of Chemistry.

Under conditions when theoretical description and continuum-level modeling of PLAL are hindered by the complexity and highly nonequilibrium nature of laser-induced processes in liquids, the molecular dynamics (MD) computer simulation technique[65-66] can serve as a useful alternative approach, capable of providing atomic-level insights into the laser-induced processes. The main advantage of the MD technique is that no assumptions are made on the processes or mechanisms under study. The only input in the MD model is the interatomic interaction potential that fully defines the structure and thermodynamic properties of the material. The MD technique has indeed been successfully applied to simulations of laser melting, spallation and ablation of molecular systems, metals, and semiconductors in vacuum, as reviewed refs. 67-70. Moreover, since the resolution limit of MD is atomistic, one can clearly observe the intricate interaction between ablation plume and liquid including metal-liquid mixing, formation of nanoparticles and microstructure of the target. However, there have been no MD simulations of PLAL attempted so far. The high computational cost of the atomistic representation of both the target material and liquid environment combined with the relatively large time- and length-scales of processes responsible for the nanoparticle generation in PLAL have been discouraging the application of the MD technique to simulation of laser-materials interactions in liquid environment. The simulations of PLAL are enabled by the development of a computationally-efficient coarse-grained representation of liquid environment combined with the acoustic impedance matching boundary conditions that allow us to focus the computational efforts on the part of the system where the active processes of laser ablation, metal-liquid mixing, and nanoparticle formation take place. The details of computational model and its parameterization for simulation of laser ablation of metal in water environment are described in next section.

1.2. Computational model

The simulations reported in this dissertation are performed with a hybrid computational model combining a coarse-grained representation of liquid (parameterized for water), a fully atomistic description of laser interactions with metal targets, and acoustic impedance matching boundary conditions designed to mimic the non-reflecting propagation of the laser-induced pressure waves through the boundaries of the computational domain. A schematic representation of the computational system is shown in Fig. 1.3. A brief description of the main components of the computational model as well as details of the computational setup is provided below.

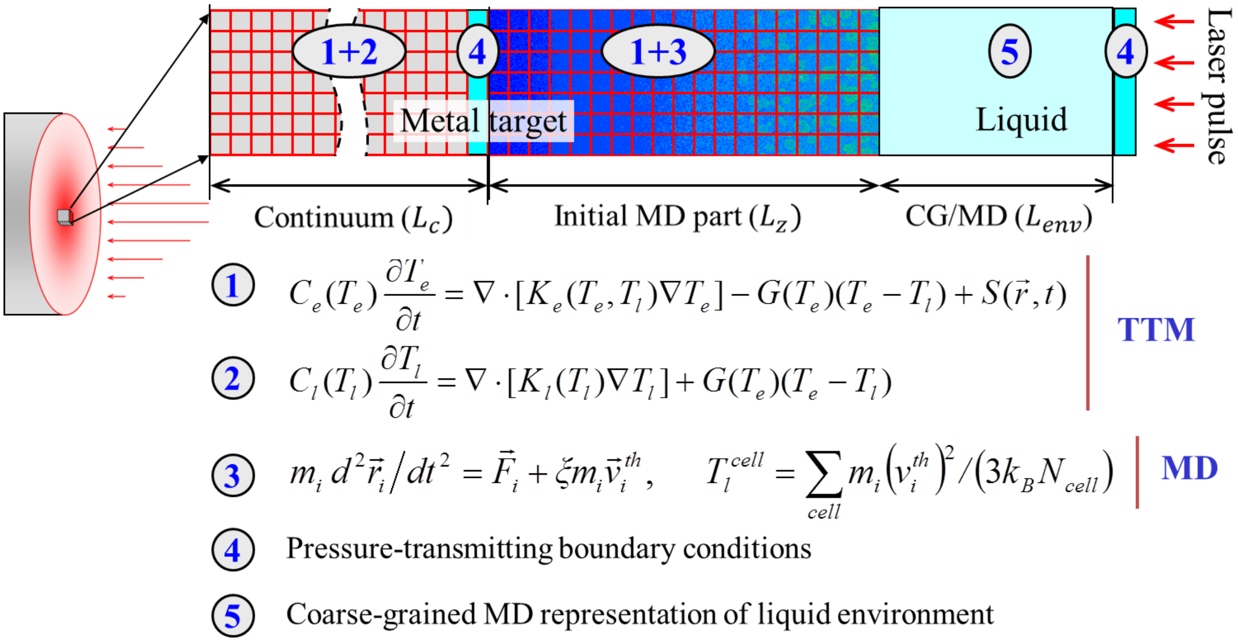

Figure 1.3. Schematic representation of the combined continuum coarse grained atomistic model for simulation of laser interaction with a metal target under spatial confinement. The abbreviated symbols in this figure are explained in section 1.3.1, 1.3.2, and 1.3.3. The dimensions of atomisic and continuum regions are not drawn to scale. The complete description of the combined TTM-MD method can be found in refs.71-72.

1.2.1. Principle of Molecular Dynamics

The MD technique is based on the numerical integration of Newtonian equations of motion for all atoms in the system, allowing the observation of time evolution of a system of interacting particles. MD has been actively applied in various fields of materials science, chemistry and biology, and detailed discussion of different types of applications can be found in several books dedicated to the technique.[65-66] Basically, the evolution of all particles in a system can be written in the form of a set of Newtonian equations of motion, Eqs. (3) without the coupling term, $\xi m_i \vec{v}_i^{th}$ in Fig. 1.3, where $m_i$and r_i are the mass and position of a particle i and F_i is the force acting on this particle due to the interaction with other particles in the system. The force acting on the i_{th} particle at a given time can be obtained from the interatomic interaction potential U, which is a function of the position of all particles. To solve the Newtonian equations of motion numerically, one only needs to define the initial conditions and the interatomic interaction potential. The direct output of the simulation is the position and velocity of all the particles as a function of time. The structural and thermodynamic parameters of the system can be derived based on the atomic trajectories.

The main advantage of the MD technique is that no assumptions are made for the processes or mechanisms under the study. The only input in the simulation is the interatomic interaction potential functions defining all the thermal and elastic properties of the target material, such as the lattice heat capacity, elastic moduli, coefficient of thermal expansion, melting temperature, volume and entropy of melting and vaporization, etc. Once the interatomic potentials are chosen and initial conditions are defined, the MD trajectories (positions and velocities) are solved numerically without any further assumptions. This advantage makes MD an ideal technique to explore the new physical phenomena and non-equilibrium process. Moreover, MD can provide atomistic-resolution of the process, providing complete information on the phenomena of interest. MD technique is proven to be capable of providing various atomic-level insights into laser-induced process for broad ranges of material systems[70, 73-78] including laser-induced thermoelastic deformation, melting and resolidification, generation of crystal defects,[79-87] photomechanical damage and spallation, and phase explosion.[71, 82, 88-94] A comprehensive review of the MD results on simulation of laser-material interaction in vacuum is available in refs. 67-69. However, the predictive power of MD comes with high computational costs, so the time and length scales of the simulations are limited. Nevertheless, the fast advancement in computing technology and infrastructure, including the progress of computer processing power, the adaption of graphic processing units,[95-96] development of efficient parallelization algorithms, supercomputer centers built for massive calculations,[97-98] have gradually pushed the time and length scale limitations of MD simulations.

Choice of Materials in the dissertation

From Chapter 2 to 7, the interatomic interactions in the MD part are modeled as Ag described by the embedded atom method (EAM) potential with the functional form and parameterization developed in ref. [99]. A cut-off function suggested in ref. [100] is added to the potential to smoothly bring the interaction energies and forces to zero at interatomic distance of 5.5 Å. Since this Ag EAM potential has been applied to study laser-metal interactions extensively by Computational Materials Group,[69, 88-89, 101-103] it has been continued to use in this dissertation to explore the effect of a liquid on laser-materials interactions. Although the potential is fitted to low-temperature values of the equilibrium lattice constant, sublimation energy, elastic constants, and vacancy formation energy, it also provides a good description of high-temperature thermodynamic properties of Ag[104] relevant to the simulation of laser-induced processes. In particular, the equilibrium melting temperature, T_m, determined in liquid–crystal coexistence simulations, is 1139 ± 2 K,[103] about 8% below the experimental values of 1235 K.[105] The threshold temperature for the onset of the explosive phase separation into liquid and vapor, T^*, determined in simulations of slow heating of a metastable liquid, is found to be ~3450 K at zero pressure and ~4850 K at 0.5 GPa.[101] The onset of the phase explosion can be expected at 10% below the critical temperature[106-108] and the values of T^* calculated for the EAM Ag material are not in conflict with the range of experimental values of the critical temperature of Ag spanning from 4300 K to 7500 K.[109] In Chapter 8, an EAM potential represents Cr[87] is used to establish the connection with our collaborator, Iaroslav Gnilitskyi from University of Modena and Reggio Emilia (UNIMORE) in Italy, who will also use Cr target for experiments.

1.2.2. Representation of laser interaction with metals

Although the MD method is capable of providing detailed information on the microscopic mechanisms of laser ablation, several modifications have to be made in order to apply the classical MD for simulations of laser interactions with metals. In particular, a realistic description of the laser coupling to the target material, the kinetics of thermalization of the absorbed laser energy, and the fast electron heat conduction should be incorporated into the MD technique. These processes can be accounted for by incorporating the MD method into the general framework of the two-temperature model (TTM)[110-111] commonly used in the simulations of short pulse lase interactions with metals. The idea of the combined TTM-MD model,[82, 88, 112] schematically illustrated in Fig. 1.3 is briefly explained below.

In the original TTM, the time evolution of the lattice and electron temperatures, T_l and T_e, is described by two coupled differential equations (Eqs. (1) and (2) in Fig. 1.3) that account for the electron heat conduction in the metal target and the energy exchange between the electrons and atomic vibrations. In the combined TTM-MD method, MD substitutes the TTM equation for the lattice temperature in the surface region of the target, where laser-induced structural and phase transformations take place. The diffusion equation for the electron temperature, T_e, is solved by a finite difference method simultaneously with MD integration of the equations of motion of atoms. The cells in the finite difference discretization are related to the corresponding volumes of the MD system, and the local lattice temperature, T_l^{cell}, is defined for each cell from the average kinetic energy of thermal motion of atoms. The electron temperature enters a coupling term, $\xi m_i \vec{v}_i^{\,th}$, that is added to the MD equations of motion to account for the energy exchange between the electrons and atomic vibrations. In this coupling term, ξ is a coefficient that depends on the instantaneous difference between the local lattice and electron temperatures as well as the strength of the electron-phonon coupling[72], $\vec{v}_i^{\,th}$, is the thermal velocity of the atom defined as $\vec{v}_i^{\,th} = \vec{v}_i - \vec{v}^{\,c}$, where $\vec{v}_i$ is the actual velocity of atom *i* and $\vec{v}^{\,c}$ is the velocity of the center of mass of a cell to which the atom *i* belongs. The expansion, density variation and, at higher fluences, disintegration of the irradiated target predicted in the MD part of the model are accounted for through the corresponding changes of the parameters of the TTM equation for electron temperature. The three-dimensional solution of the diffusion equation for T_e is used in simulations of laser spallation and ablation,[88, 113-114] where the dynamic material decomposition may result in lateral density and temperature variations.

In the continuum part of the model, beyond the surface region represented by the MD method, the electron heat conduction and the energy exchange between the electrons and the lattice are described by the conventional TTM equations, with L_c ~ 2-6 μm chosen to ensure negligible temperature changes at the bottom of the computational domain during the simulation time. A dynamic pressure-transmitting boundary condition[92, 115] is applied at the bottom of the MD part of the system (marked as ④ in Fig. 1.3) to ensure non-reflecting propagation of the laser-induced stress wave from the MD region of the computational system to the bulk of the target. The energy carried away by the stress wave is monitored, allowing for control over the total energy conservation in the combined model.[116]

In the simulations of laser interactions with thin films deposited on a substrate, the atomistic TTM-MD representation is extended to the whole metal film with thickness L_z and the boundary condition marked as ④ in the left part of Fig. 1.3 is modified to reproduce the elastic response of the substrate to the laser-induced pressure waves and the cohesion between the metal film and the substrate.[101, 117] The acoustic impedance matching boundary condition at the substrate-film interface is designed in this case to represent the partial propagation of the laser-induced pressure wave into the substrate, as well as the work of adhesion between the silica substrate and metal film.

The electron temperature dependences of the thermophysical material properties included in the TTM equation for the electron temperature (electron-phonon coupling factor G, the electron heat capacity Ce, and the heat conductivity K_e, see Fig. 1.3) are highly sensitive to details of the electronic structure of the material and can exhibit large deviations (up to an order of magnitude) from the commonly used approximations of a linear temperature dependence of the electron heat capacity and a constant electron-phonon coupling.[118-119] These deviations have important implications for quantitative computational analysis of ultrafast processes associated with fs laser interaction with metals[103, 112, 119-121] and are accounted for in the TTM-MD model.

Thermophysical properties of Ag (Used in Chapter 2-7)

The electron temperature dependences of the thermo-physical material properties included in the TTM equation for the electron temperature (electron-phonon coupling factor and electron heat capacity) are taken in the forms that account for the thermal excitation from the electron states below the Fermi level.[118] The electron thermal conductivity is described by the Drude model relationship, $K_e(T_e,T_l) = v^2 C_e(T_e)\tau_e(T_e,T_l)/3$, where $C_e(T_e)$ is the electron heat capacity, v^2 is the mean square velocity of the electrons contributing to the electron heat conductivity, approximated in this work as the Fermi velocity squared, v_F^2, and $\tau_e(T_e,T_l)$ is the total electron scattering time defined by the electron-electron and electron-phonon scattering rates, $1/\tau_e = 1/\tau_{e-e} + 1/\tau_{e-ph} = AT_e^2 + BT_l$. The value of the coefficient A, 3.57×10^6 s^{-1}K^{-2}, is estimated within the free electron model, following the approach suggested in ref. 122. The value of the coefficient B, 1.12×10^{11} $s^{-1}K^{-1}$ is obtained from the experimental value of the thermal conductivity of solid Ag at the melting temperature, 363 $Wm^{-1}K^{-1}$. [123]

1.2.3. Coarse-grained liquid

The direct application of the conventional all-atom MD representation of liquids in large-scale simulations of laser processing or ablation is not feasible due to the high computational cost. Thus, a coarse-grained representation of the liquid environment,[70, 124] where each particle represents several molecules, is adapted in this work. The coarse-graining reduces the number of degrees of freedom that have to be treated in the MD simulations and significantly increases the time and length scales accessible for the simulations. At the same time, however, the smaller number of the dynamic degrees of freedom results in a severe underestimation of the heat capacity of the liquid. To resolve this problem, the degrees of freedom that are missing in the coarse-grained model are accounted for through a heat bath approach that associates an internal energy variable with each coarse-grained particle.[125-127] The energy exchange between the internal (implicit) and dynamic (explicit) degrees of freedom are controlled by the dynamic coupling between the translational degrees of freedom and the vibrational (breathing) mode associated with each coarse-grained particle (the particles are allowed to change their radii, or to "breath" [124, 127]). The energy exchange is implemented through a damping or viscosity force applied to the breathing mode, which connects it to the energy bath with capacity chosen to reproduce the real heat capacity of the group of atoms represented by each coarse-grained particle. Effectively, the breathing mode serves as a "gate" for accessing the energy stored in the molecular heat bath.

The first implementation of the coarse-grained model with heat bath approach was recently developed for water and applied to simulations of laser interactions with water-lysozyme system.[127] Each coarse-grained particle in the model has a mass of 50 Da and represents about three real water molecules. The potential describing the inter-particle interactions is provided in ref. 127 and the parameters of the potential are selected to ensure a satisfactory semi-quantitative description of experimental properties of water. While one cannot expect the coarse-grained model to provide an accurate representation of all the structural and thermodynamic properties of water, the key physical properties predicted by the model, such as density, speed of sound, bulk modulus, viscosity, surface energy, melting temperature, critical temperature, and critical density, are found to not deviate from the experimental values by more than 25%, as can be seen from

Table 1.1. The room temperature density, ρ, and heat capacity, c_p, are fitted exactly through the selection of the equilibrium inter-particle distance and the capacity of the heat bath associated with each coarse-grained particle. The bulk modulus, K, is calculated from the pressure-volume dependence obtained in MD simulations and the speed of sound, c_s, is evaluated from the values of K and ρ. The melting temperature of the coarse grained "water", T_m, is determined in a constant-pressure and constant-energy liquid-crystal coexistence simulation and is about 21% higher than the experimental value. The critical temperature and density, T_c and ρ_c, are extrapolated from the results of constant-temperature and constant-pressure liquid-gas coexistence simulation from 300 to 500 K following the method of ref. 128. Note that the critical temperature listed in Table 1.1 is slightly lower than the value roughly estimated from the threshold temperature for the phase explosion and provided in ref. 127. Thermal conductivity, k, is evaluated by fitting the evolution of the temperature profiles in an elongated MD system with a heat source applied in the middle to the solution of the heat diffusion equation. The dynamic viscosity, η, is calculated with the Stoke-Einstein equation, using the values of the self-diffusion coefficient evaluated from the time dependence of the mean square displacement of coarse-grained particles in a MD simulation performed at 300 K. Finally, the surface energy, γ, is obtained based on the results of a liquid-gas coexistence simulation performed at 300 K. The details of testing of coarse-grained water physical parameters are provided in Appendix A1.

As shown in Fig. 1.3, the coarse-grained MD representation of the water environment is used only in a layer with thickness of L_{env} adjacent to the surface of the metal target. The thickness of this layer is chosen to include the region affected by the phase transformations induced in water by the interaction with hot metal surface and ablation plume. At the top of the coarse-grained MD region, a dynamic acoustic impedance matching boundary condition based on an imaginary plane approach[101] is applied to ensure nonreflective propagation of the pressure wave generated at the metal−water interface into the bulk of a thick water overlayer. This boundary condition is suitable for reproducing experimental conditions where the reflection of the pressure wave from the outer surface of the water overlayer does not have any significant effect on processes occurring in the vicinity of the irradiated metal surface.

The interactions between Ag atoms and the coarse-grained water particles are described by the Lennard-Jones (LJ) potential with the following length and energy parameters: σ = 1.92 Å and ε = 0.145 eV. The parameters are fitted to match the diffusion of metal atoms and small clusters in water predicted by the Stoke-Einstein equation at 300 K and calculated in constant-temperature and constant-volume MD simulations. Furthermore, the values of σ and ε are chosen to ensure that the values of the equilibrium O-Ag distance and the adsorption energy of water on a Ag surface predicted in *ab-initio* simulations[129-132] are roughly reproduced in the coarse-grained model. Note that, while it is possible to incorporate the description of chemical reactions into the framework of coarse-grained MD model,[70, 133-134] we have not included descriptions of oxidation or other chemical reactions[48] in the version of the model used in the present study.

properties of water	experiment	CG model	Δ, %
density, ρ, g/cm^3	1.0	1.0	0
heat capacity, c_p, J/(kg K)	4.2×10^3	4.2×10^3	0
bulk modulus, K, GPa	2.2	1.8	18
speed of sound, c_s, m/s	1483	1342	9
melting temperature, T_m, K	273	330	21
critical temperature, T_c, K	647	520	20
critical density, ρ_c, g/cm^3	0.322	0.398	24
thermal conductivity, k, W/(m K)	0.6	0.13	78
viscosity, η, cP	0.894	0.910	2
surface energy, γ, J/m^2	0.072	0.073	1

Table 1.1. Properties of the coarse-grained model parametrized for water and the corresponding experimental values. The values of ρ, c_p, K, c_s, k, η, and γ are listed for a temperature of 300 K. The experimental values are from ref [105].

1.3. Research Objectives

The main research objectives of the dissertation are to gain, through advanced computer modeling and theoretical analysis, a clear fundamental understanding of the mechanisms and kinetics of structural and phase transformations occurring in pulsed laser ablation in liquids, so that the emerging understanding of laser-induced processes could facilitate the intelligent design of new PLAL setups capable of controlled generation of nanoparticles and surface structures. The seven interrelated focus areas targeting this general objective are as follows:

1. ***Understand the fundamental microscopic dynamics at the interface between ablation plume and liquid environment leading to nanoparticle generation***

Experimental evidence suggests that liquid environment spatially confines the direct expansion of ablation plume, so subsequent nanoparticle generation takes place mostly within the cavitation bubble. However, the exact physical picture of initial highly non-equilibrium dynamics between ablation plume and liquid environment remains inaccessible for experimental probing and continuum level modeling. The understanding of the effect of liquid environment on the formation and expansion of ablation plume is the key to grasping the nanoparticle generation mechanisms and designing techniques to control nanoparticle size distribution. The unique advantage of atomistic modeling is in its ability to visualize the initial nonequilibrium processes with atomistic resolution. A series of MD simulations of Ag bulk target in water irradiated in the range of fluence above the phase explosion threshold in vacuum is performed to observe the ablation plume – water interaction and the subsequent nanoparticle generation. The results are presented in Chapter 4.3.3, 5, and 7.

2. ***Understand the effect of pulse duration on nanoparticle generation mechanisms and size distribution***

While the pulse duration is one of the common experimental parameters used to control nanoparticle size distribution, its fundamental role to nanoparticle generation mechanisms remains unknown. Clear methodology to achieve narrow nanoparticle size distribution by direct one-step PLAL is still intangible. Regardless of the pulse duration, a broad size distribution, where the often desired small nanoparticles (< 10 nanometers) coexist with larger ones (10s to 100s of nanometers), are typically obtained in PLAL experiments. However, with sufficient nanoparticle statistics and proper experimental setup that does not facilitate nanoparticle fragmentation through post-irradiation (*i.e.*, the flow chamber design and appropriate laser repetition rate prevent interaction of laser pulses with already generated nanoparticles), the effect of pulse duration on nanoparticle size distribution emerges as follows: bimodal nanoparticle size distribution becomes apparent for short laser pulse (< 100 picoseconds), and broad nanoparticle size distribution remains for nanosecond laser pulse. A series of MD simulations of Ag bulk target in water irradiated in the range of fluence above the phase explosion threshold is performed with pulse duration ranging from 10 picoseconds to 2 nanoseconds to explore the effect of the pulse duration on nanoparticle generation mechanisms. The explanation of bimodal size distribution for short pulse laser ablation in liquids is presented in Chapter 5. In chapter 7, the effect of the laser pulse duration explored by performing additional simulations with pulse durations of 400 picoseconds to 2 nanoseconds.

3. ***Explore the role of spatial energy confinement in thin film ablation in liquids and in vacuum***

While the conventional pulsed laser ablation in liquids is performed with bulk targets, using thin films as ablation targets can introduce new aspects to the process of laser ablation related to the spatial confinement of the deposited laser energy. It is known from ablation in vacuum or background gas that the energy confinement within the thickness of the film can not only reduce the ablation threshold, but also increase the fraction of nanoparticles in the plume. The resulting nanoparticle size distributions obtained in thin film ablation are narrower and more controllable than those observed in bulk target ablation. Hence, study thin film ablation in liquids can provide an alternative approach for more precise control of nanoparticle size distribution. Moreover, understanding the dynamics of thin film ablation in liquids can be extended to engineering alloy nanoparticles with multilayer ablation in liquids. A series of MD simulations for thin Ag film ablation in vacuum and water is performed to understand the effect of the water environment on laser – thin film interaction. The results of the simulations of thin film ablation in vacuum and in liquids are presented in Chapters 2 and 3, respectively. First results of a preliminary study of Ag-Cu multilayer ablation in water for generation of alloy nanoparticles are discussed in Chapter 9.1.

4. ***Study fast quenching and rapid crystallization of nanoparticles***

The highly nonequilibrium nature of the interaction between the ablation plume and liquid environment can facilitate synthesis of nanoparticles with unusual structure, shape, and composition. The kinetics of nanoparticles formation, rapid cooling, and solidification due to the interaction with water is investigated based on the performed MD simulations and described in Chapters 3, 5, 6 and 7.

5. *Investigate the effect of water environment on laser-induced surface structure*

For irradiation in vacuum or in air, the utility of short laser pulses for selective nanoscale engineering of surface microstructure has been demonstrated for various material systems. The results of previous simulations, however, suggest that the laser-induced generation of nanocrystalline layer on the surface of a pure Ag target is only possible in a narrow range of laser fluences close to the spallation threshold, when the generation sub-surface voids slows down the propagation of the resolidification front from the bulk of the target. This leads to an intriguing question on whether the presence of liquid environment could broaden the range of irradiation conditions that yield surface nanocrystallization and result in the formation of a nanocrystalline surface layer without the generation of sub-surface voids.

In addition to the possibility to subdue the sub-surface voids formation, another relevant question is whether the presence of liquid environment can stabilize highly expanded irradiated surface, thus facilitating formation of unique surface morphology. MD simulations of Ag bulk target in water irradiated with short pulse laser at fluences that correspond to regimes of 1) melting and re-solidification, and 2) photomechanical spallation are performed to investigate the confining and quenching effects of the liquid environment on the morphology and microstructure of surfaces generated by short pulse laser irradiation. The results are presented in Chapters 4.3.1 and 4.3.2.

6. *Explore the incubation effect introduced by the presence of sub-surface voids in pulsed laser ablation in liquids*

The results from Chapters 4.3.2. and 4.3.3. show that the presence of water can prevent direct materials ejection and stabilize large sub-surface voids. The subsequent irradiation of targets with large sub-surface voids can result in spatially localized energy deposition within the top surface layer and to dramatically reduce the ablation threshold. The reduction of the ablation threshold in multi-pulse laser irradiation regime is known as incubation effect. While the incubation effect caused by the presence of sub-surface voids in vacuum has been well-studied, the response of the target with subsurface voids to laser irradiation in a liquid environment, where the material expansion is suppressed by liquid confinement, has not been explored yet. A MD simulation of the second pulse irradiation is performed with initial configuration produced in a simulation discussed in Chapter 4.3.2, where the laser fluence was below the nanoparticle generation threshold in a single pulse laser irradiation in water. The results are presented in Chapter 6.

7. ***Investigation of the effect of water on generation of laser-induced periodic surface structures in single pulse irradiation regime***

While generation of laser-induced periodic surface structures (LIPSS) is traditionally done through repetitive irradiation of the same laser spot in the irradiation regime of melting and resolidification, there has been a recent demonstration of the formation of highly regular LIPSS (HR-LIPSS) in the single pulse ablative regime. Although the mechanisms leading to the HR-LIPSS formation in vacuum has been investigated computationally, it is imperative to understand whether the liquid environment can serve as an additional experimental parameter to control the structure of HR-LIPSS. A MD simulation of bulk Cr target in water irradiated with spatially modulated short pulse laser is performed, and the results are presented in Chapter 8.

2. Atomistic simulation of through thin film ablation in vacuum

2.1. Introduction

To investigate the effect of water confinement on nanoparticle generation for thin film ablation discussed in Chapter 3, the microscopic pictures of laser ablation in vacuum are established in this Chapter. Femtosecond (fs) laser ablation is proved to be an effective mean to nanoparticle generation, since a large fraction of ablated materials is shown to be nanoparticles.[135-136] Traditionally, bulk target is used to for fs laser ablation; however, it is difficult to generate nanoparticles with controlled-distribution because the ablation is highly dependent on the characteristic length of laser heating. This characteristic length corresponds to the diffusive penetration depth of photo-excited electrons, which is highly sensitive to the electron structure of the target material.[118] Moreover, due to different temperature and pressure conditions within the bulk target, mixed ablation mechanisms are common in bulk target that induces spatial segregation of different plume components.[88, 137] As compared to the conventional ablation of bulk materials, the use of thin films introduces new aspects to the nanoparticle generation in laser ablation. The energy confinement within the thickness of the film can reduce the laser fluence necessary for the ablation and results in the complete ablation of films with thickness below the characteristic length of laser heating.[138] The effect of spatial segregation is expected to be less apparent, and the nanoparticle distribution is narrower and more controllable.[139-141] To fully utilize the potential of fs-pulsed laser ablation of thin metal films, an improved understanding of the various factors affecting the structure and composition of nanoparticle generation is needed.

Typical thin film laser ablation can result in either unimodal nanoparticle size distribution with one nanoparticle peak on the orders of few to 10s nm[117, 135, 139, 141-143] or bimodal nanoparticle size distribution with one nanoparticle peak of small nanoparticles (around 10s nm) and another nanoparticle peak of large nanoparticles (on the orders of 100s nm).[117, 139, 142] By changing the laser fluence and film thickness, there can be transition between unimodal and bimodal nanoparticle size distribution.[117] For bimodal distribution, the large nanoparticles (on the orders of 100s nm) can be detected from the ICCD images of the plumes, but the small nanoparticles are invisible to the ICCD. Small nanoparticles are proven not to form by the condensation in the plume, since variation of the background gas pressure has almost no effect on the distribution; and they are not formed from splashing and stacking on the substrate as well.[117] The detailed laser ablation mechanisms and transition of these two distinctive nanoparticles distributions are poorly understood due to the limited applicability of traditional continuum-level models to the highly non-equilibrium processes induced by laser irradiation. The atomic-level molecular dynamics (MD) computer technique has proven to be a viable alternative since there is no implicit assumptions on the non-equilibrium processes during simulation. Our previous MD-TTM study[117] (Details are presented in Appendix A2) has shown that the small nanoparticles are most likely to be generated during the early stage along with the large nanoparticles as the laser-induced tensile stress separates the film into two molten layers with uneven thickness, and rupturing of the molten layers results in bimodal size distribution. In this chapter, *MD computer simulations will be used to obtain a detailed microscopic picture of the thin film ablation phenomenon to understand the thickness and fluence dependence of the ablation mechanisms responsible for different nanoparticle size distributions*. In addition to continue a more detailed investigation of the ablation mechanism contributing to bimodal size distribution, we also report two additional ablation mechanisms leading to unimodal size distribution and physical insight behind the transition between bimodal and unimodal nanoparticle size distribution.

2.2. Computational setup

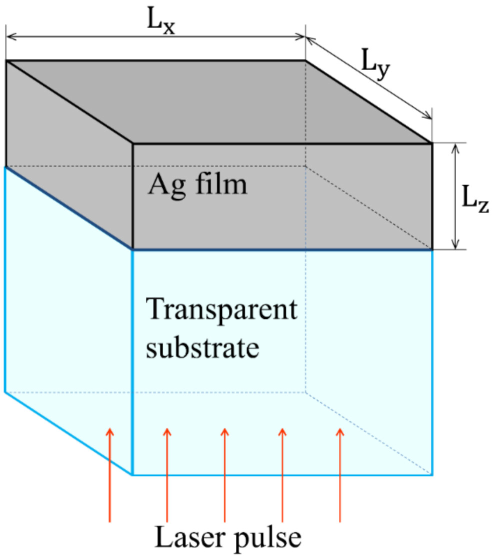

Figure 2.1. Schematic representation of the computational model for simulation of short pulse laser interaction with a thin silver film deposited on a transparent (silica) substrate. The grey

rectangular parallelepiped shows the initial location of the silver film represented by the TTM-MD model. L_x, L_y, and L_z correspond to the length of x, y, and z in Cartesian coordinate system. Lx and Ly are either 100 or 400 nm, while L_z is 5, 10 or 20 nm. The dynamic response of the substrate is not explicitly simulated but represented by an acoustic impedance matching boundary condition applied at the substrate-film interface (shown by blue plane). The laser pulse is directed from the bottom of the figure, through the transparent substrate. Periodic boundary conditions are applied in the lateral directions, perpendicular to the surface normal of the film.

The simulation reported in this chapter is performed with a classic TTM-MD model, containing a fully atomistic description of laser interaction with metal targets and acoustic impedance matching boundary conditions, designed to mimic the non-reflecting propagation of the laser-induced pressure waves through the boundaries of the computational domain. A complete description of the computational model is provided in Chapter 1.2, and below only parameters relevant to the computational setup of the simulation reported in this chapter are described.

The schematic representation of computational setup is shown in Fig. 2.1. The initial Ag film is represented as a fcc crystal with (001) orientation of the free surface. Four different MD computational systems were used in the modeling. The lateral dimensions of the first three systems are 100nm × 100nm, with the 5nm, 10nm and 20nm thickness; the total number of atoms in the systems is 2.8, 5.6, and 11.3 million, respectively. The last MD computational system has the lateral dimensions of 400nm × 400nm and thickness of 5nm; the total number of atoms in the system is 44.8 million. The periodic boundary conditions are applied in the directions parallel to the surface of the film and all systems are equilibrated at 300 K before applying laser irradiation. Before running the large-scale simulation, several test simulations are performed at different laser fluences for systems with smaller lateral dimensions of 4.1 nm × 4.1 nm (4800, 9600,19600 atoms for 5nm, 10nm and 20nm thickness respectively) to identify the range of laser fluences that correspond to different photo-mechanical thresholds.

The dynamic response of the silica substrate to the laser excitation of the metal film is not explicitly simulated in the model but represented by an acoustic impedance matching boundary condition applied at the substrate-film interface. This boundary condition is designed to represent the partial propagation of the laser-induced pressure wave into the substrate as well as work of adhesion between the silica substrate and Ag film. The detailed implementation is described in ref. [101].

The irradiation of the target with a 40 fs laser pulse is represented through a source term added to the equation for the electron temperature.[72] The source term simulates excitation of the conduction band electrons by a laser pulse with a Gaussian temporal profile and reproduces the exponential attenuation of laser intensity with depth under the surface. The optical absorption depth, 12 nm at laser wavelength of 800 nm,[144] is used in the source term of the TTM equation.[72, 86] The source term is corrected for thickness dependence to ensure that all the energy of the laser excitation is deposited in the film, leading to an almost uniform energy deposition throughout the film thickness. The results of the simulations are provided for the absorbed fluences; thus, the reflectivity and transparency of the surface is not defined in the model.

2.3. Results and discussion

2.3.1. Thickness dependence of ablation regimes

A series of small-scale simulations have been completed to predict the possible nanoparticle generation regimes. Fig.2.2a has shown the possible regimes with respect to the film thickness and absorbed fluences. For a given thickness, there are four possible regimes identified. From low to high fluence, a targeted film can go through intact, spallation, transition, and phase explosion regimes. Different regimes are predicted to give different patterns of nanoparticle distributions, which will be investigated in this chapter.

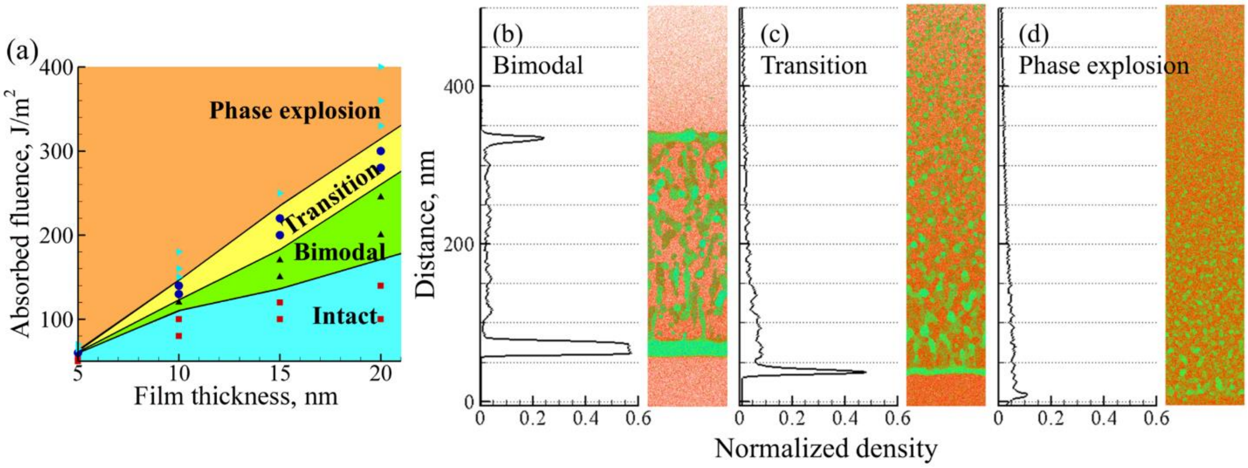

Figure 2.2. (a) shows thin film ablation regime plot based on a series of small scale simulations (the details of the small systems are described in section 2) The x-axis is film thickness and y-axis is the absorbed fluence. Four regimes are labeled with different colors with corresponding characteristic ablated plume density profile (plotted based on 20 nm Ag film irradiated by a 40 fs laser pulse with an absorbed fluence of 250 **(b)**, 300 **(c)**, and 360 **(d)** J/m^2 at 500 ps). The

corresponding flat views of the atomistic snapshots are shown along on the right side of each ablated plume density plot. The x-axis is the density normalized to the Ag density at 300 K and 0 GPa, and the y-axis is the distance from the initial surface of the substrate. Intact regime is colored with blue. Spallation regime is colored with green, and corresponding ablated plume density plot is shown in **(b)**. Transition regime is colored with yellow, and corresponding ablated plume density plot is shown in **(c)**. Phase explosion regime is colored with orange, and corresponding ablated plume density plot is shown in **(d)**.

Without venturing into the detailed analysis of the exact physical mechanism behind each regime, the definition of each regime is based on the ablated plume densities as shown with three representative samples in Fig.2.2b-d. The intact regime is not shown in the Fig.2.2, since it just corresponds to a targeted film remains intact with minor evaporation. In Fig. 2.2b, the spallation regime is represented by the 20 nm Ag film with the absorbed fluence of 245 J/m^2. The spallation regime shows that there are two distinctive peaks in the plumes, while the bottom peak has more atoms than that of the top peak. In between two peaks, there is uniform distribution of vapor atoms. In Fig. 2.2c, the transition regime is represented by the 20 nm Ag film with the absorbed fluence of 300 J/m^2. The transition regime shows that there is only one distinctive peak in the plume, and it locates at the bottom of the plume. This peak contains much less materials than that of the bottom peak from spallation regime. Above the peak, there is a steady decrease in plume density, as the distance from the initial surface increases. In Fig. 2.2d, the phase explosion regime is represented by the 20 nm Ag film with the absorbed fluence of 360 J/m^2. This regime shows that there is no distinctive peak in the plume, and the whole plume has steady decrease of plume density as the distance from the initial surface increases. Other results within the same regimes show the similar patterns in ablated plume density plots. Hence, we can define each regime based on the numbers of peaks observed in the plume density plots.

In Fig. 2.2, the boundary of each regime is roughly sketched out, based on the available results. These lines are semi-quantitative, and do not represent the exact regime-change conditions. However, these lines convey two main points. Firstly, as the thickness decreases, the fluence range of each regime decreases. The three lines in Fig. 2.2a collapses to a point as one extrapolating to small film thickness and the ranges of different regimes could become too small to be distinguished. In this study, 5nm Ag film is considered as the border thickness that one can barely observe the change of regimes. As shown in Fig. 2.2a, the shift between each regime is within 5 J/m^2 for 5nm, so experiments typically only capture one regime with such thickness.[117] The analysis for 5nm Ag film results will be separated from other results of thicker films in this chapter. Secondly, the boundary lines of different regimes are considered to be linear. Since the optical penetration depth is on the same order of the film thickness, the energy distribution with the film can be approximated as uniform. The amount of energy requires for each regime is generally assumed to be proportional to the thickness of the film. As the film thickness reaches the order of hundreds nm, the role of ballistic electrons cannot be ignored, and the energy distribution within the film will not be homogeneous.

The following structure of this chapter will be based on regimes. The detailed physical mechanism of each regime will be discussed with the corresponding nanoparticle distribution in chapter 2.3.2 and 2.3.3. Due to the convergence of each regime trend lines into 5nm, the investigation of 5 nm Ag film will be presented separately in chapter 2.3.4.

2.3.2. Spallation regime

Two large-scale simulations, 20nm Ag film irradiated by a 40 fs laser pulse at an laser fluence of 245 J/m^2 and of 10nm Ag film irradiated by a 40 fs laser pulse at an laser fluence of 120 J/m^2, to further explore the two peaks observed in plume density plot. Figs. 2.3 and 2.4 show the spatial evolution snapshots of 20nm Ag film irradiated by laser fluence of 245 J/m^2 and of 10nm Ag film irradiated by laser fluence of 120 J/m^2 respectively. Shown in Figs. 2.3 and 2.4, the film is separated into two molten layers with uneven thicknesses, and each layer was decomposing in different rates and moving with different velocities. These two molten layers correspond to the two peaks shown in the ablated plume density plot in Fig. 2.2b. The top molten layer has much smaller thickness and lower density than the bottom molten layer; moreover, it starts decomposition into droplets during the simulation time. The top molten layer completely breaks down into clusters around 1100 ps for both cases. Bottom molten layer remains intact throughout the 1.5 ns simulation time; however, it can be expected to be decomposed into larger droplets at the later timescale, as presented in Appendix A3 of liquid stability analysis. The foamy structure, formed between these two layers during the spallation process, decays into droplets with diameter less than 10 nm.

The analysis of the visual picture of the ablation process can be supplemented by consideration of the evolution of temperature, pressure, and density in the direction away from the substrate, shown in the form of contour plots in Fig. 2.5 for 20nm and 10 nm films, respectively. Laser energy is deposited during the laser pulse to the conduction band electrons, and the initial temperature increase is attributed to the rapid energy transfer from the hot electrons to the lattice. Since the film thickness is smaller than the effective deposition depth, the heating is homogeneous throughout the film. This fast heating is occurring under the condition of stress confinement, so high compressive stress can be generated. This condition can be expressed as $\tau_h \approx L_f / C_s$, where τ_h – the characteristic heating time which was determined for this set of simulations to be about 3.5 ps, L_f is the thickness of the film and C_s is the speed of sound which is 3650 m/s for Ag.

The relaxation of the stress results in the expansion of the film and generation of two tensile waves moving from the film boundaries to the center. However, the free expansion of the film in one of the directions is suppressed by the silica substrate, and the magnitude of the two tensile waves is different.[145] Hence, the combined maximum tensile stresses with the amplitude 0.66 GPa and 0.56 GPa for 20 nm and 10 nm films respectively generated after meeting the waves, is formed not in the center, but closer to the free boundary. The differences in film thickness affects the pressure waves travel time, the tensile stresses build up at around 16 ps for 20 nm and 8 ps for 10 nm film. The non-center tensile stress results in the uneven thickness of the two ejected molten layers. The top molten layer is thinner but travels with greater collective velocity, while the bottom molten layer is thicker and travels with smaller collective velocity as indicated on Fig. 2.5c and f. The observation of two ejected molten layers with different thickness and collective velocity has been experimentally verified through the use of time-resolved pump-probe microscopy and the measurement of Newton’s rings,[146] and the order of magnitude of the velocities are also agreed with experiments.

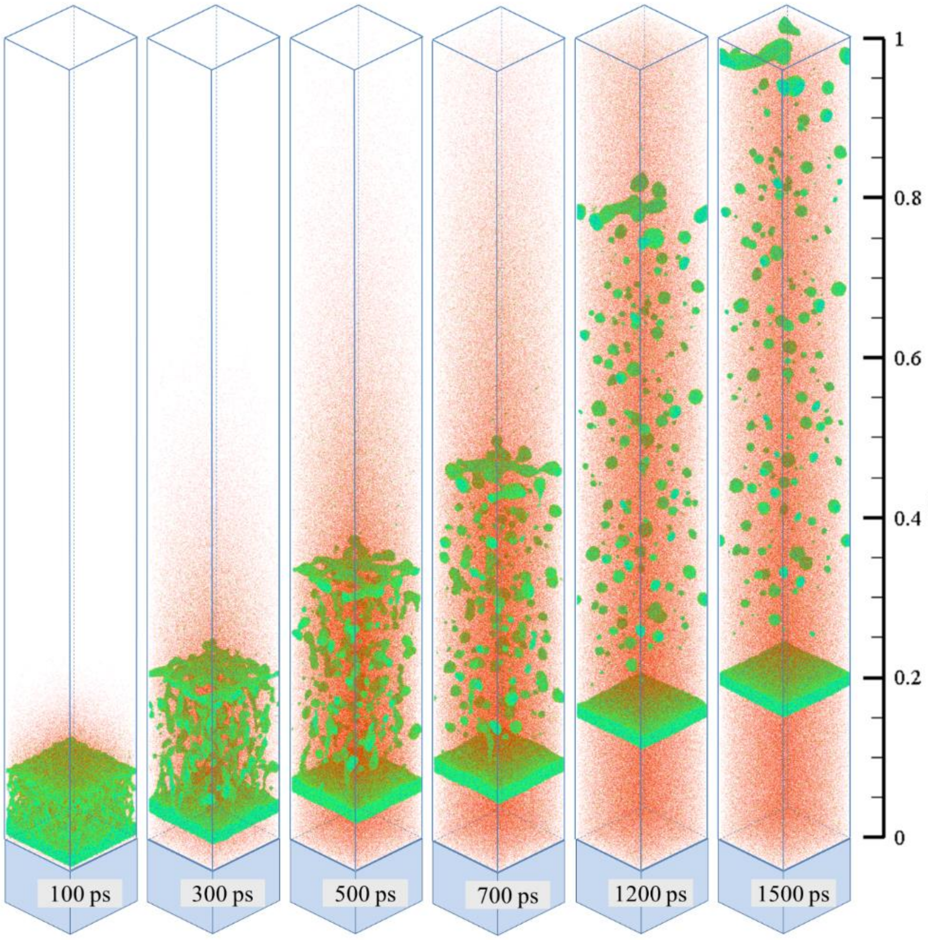

Figure 2.3. Snapshots of atomic configurations obtained in a TTM-MD simulation of laser ablation of a 20 nm Ag film irradiated by a 40 fs laser pulse at an absorbed fluence of 245 J/m^2 in vacuum condition. The irradiation conditions correspond to the spallation regime in vacuum. The location of the transparent substrate is shown by the blue rectangular parallelepipeds. The atoms are colored according to their potential energies, from green for molten Ag to red for vapor-phase Ag atoms.

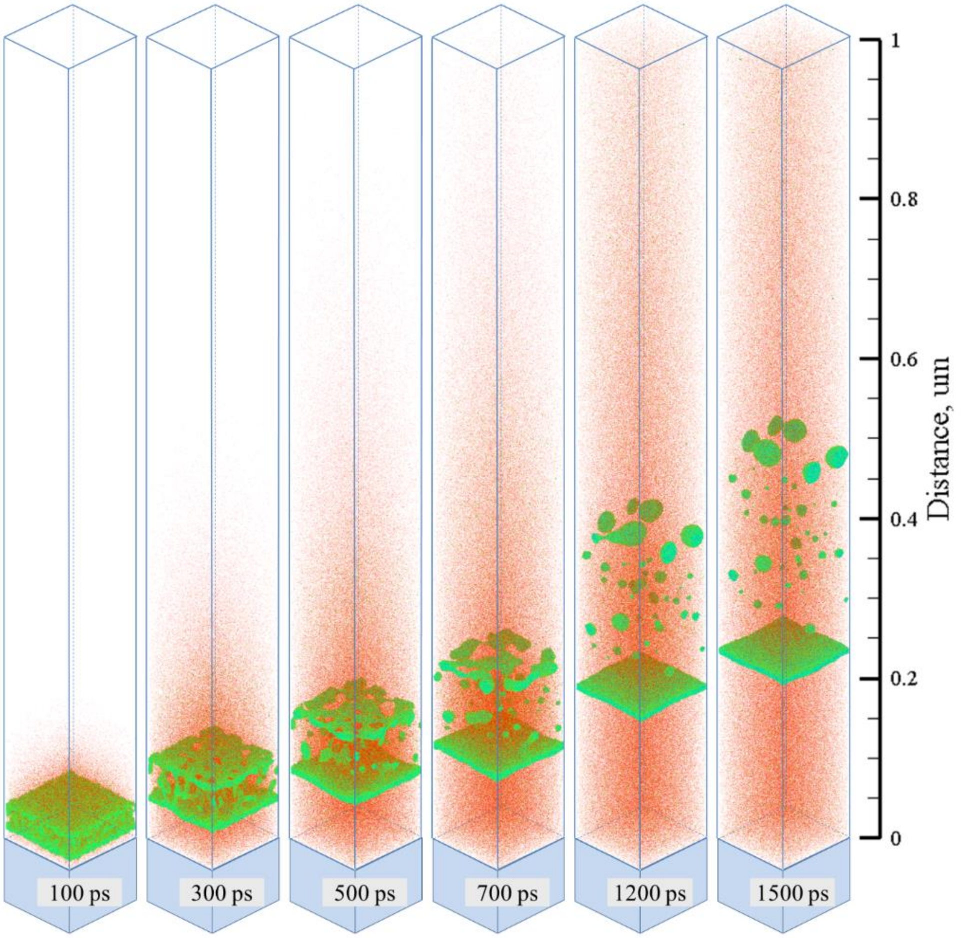

Figure 2.4. Snapshots of atomic configurations obtained in a TTM-MD simulation of laser ablation of a 10 nm Ag film irradiated by a 40 fs laser pulse at an absorbed fluence of 120 J/m^2 in vacuum condition. The irradiation conditions correspond to the spallation regime in vacuum. The location of the transparent substrate is shown by the blue rectangular parallelepipeds. The atoms are colored according to their potential energies, from green for molten Ag to red for vapor-phase Ag atoms.

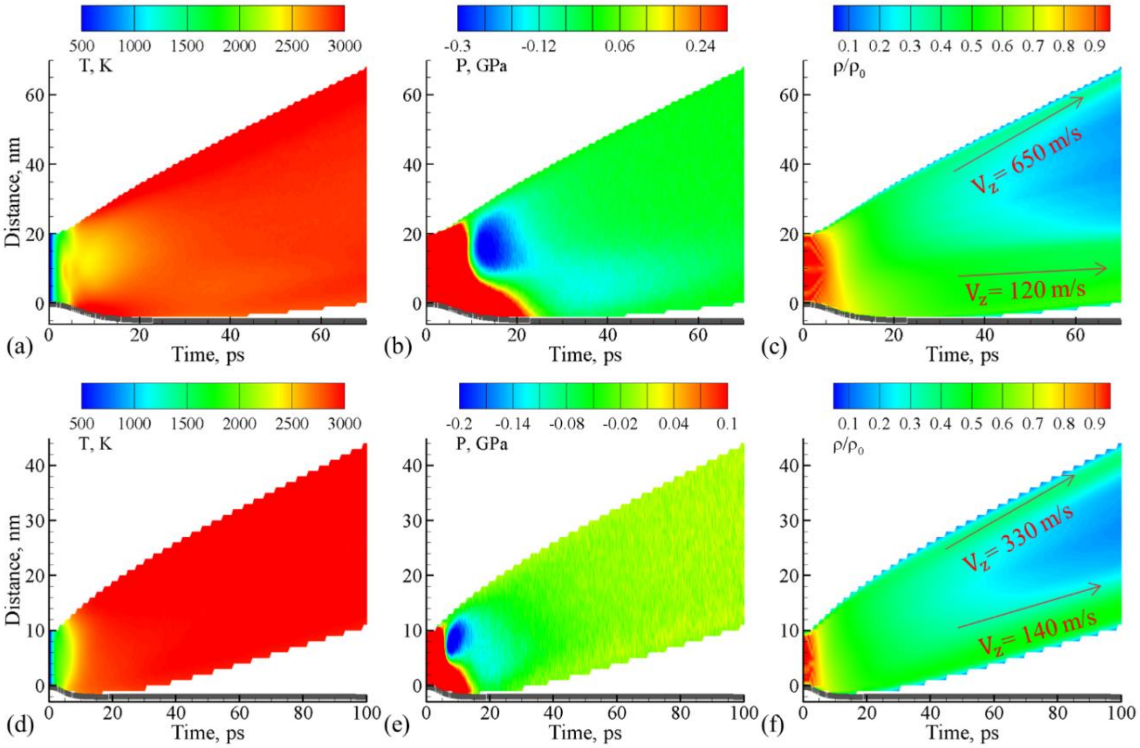

Figure 2.5. The contour plots of the initial spatial and time evolution in the direction away from the substrate in MD-TTM simulations performed for 20 nm Ag film irradiated by a 40 fs laser pulse at an absorbed fluences of 245 J/m^2 **(a,b,c)** and 10 nm film irradiated by a 40 fs laser pulse at an absorbed fluence of 120 J/m^2 **(d,e,f)**. Lattice temperature is colored in **(a,d)**, pressure is colored in **(b,e)**, and normalized density is colored in **(c,f)** labeled with the collective velocities of the spalled molten layers. The laser pulse is directed along the y axis from the bottom of the contour plots, through a silica substrate shown as a grey line.

Moreover, the tensile stress plays the role of cooling the film, as one can observe that lattice temperature of the region experiencing tensile stress is lower than those under compressive stress. Nevertheless, the average lattice temperature continues increasing during the electron-phonon relaxation which in Ag takes around 50 ps. During this process the maximum temperature does not reach the threshold of phase explosion; however, in the region where the tensile stress is localized the material exceeds the limit of cavitation, and the spallation process takes place. According to the data provided in ref. [105], it can be expected to have a cavitation threshold for the tensile stress 0.33 GPa at approximately 2600 K and that is in the agreement with the pressure and temperature contour plots in Fig. 2.5. The normalized density plots, Fig. 2.5c and f, confirm the formation of low density foamy structures observed in Figs. 2.3 and 2.4. The compressive stresses of lower part of the films retreat slowly since the onset of tensile stress, and tensile stresses extend to the lower part of the films. The disappearance of the compressive stresses is around 28 ps for 20 nm film and 14 ps for 10 nm film. Once the tensile stresses reach the lowest part of the film, it acts as the main force pulling the bottom molten layer away from the substrate, and the complete detachment of the silica substrate happens.

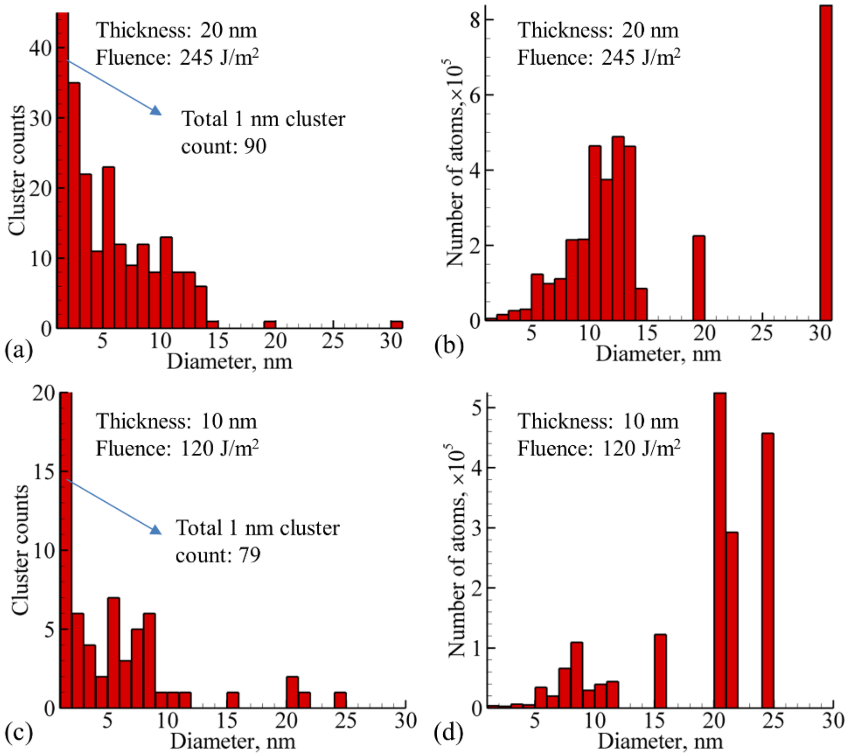

Figure 2.6. The results of the cluster analysis of the ablation plume generated in simulations performed for 20 nm Ag film irradiated by a 40 fs laser pulse at an absorbed fluences of 245 J/m^2 **(a,b)** and 10 nm Ag film irradiated by a 40 fs laser pulse at an absorbed fluence of 120 J/m^2 **(c,d)**. The numbers of nanoparticles of different diameter are shown on **(a,c)**; the numbers of atoms that belong to nanoparticles of different diameter are presented on the **(b,d)**. The bottom liquid layer that remains intact throughout the simulation is not taken into account during the analysis. The corresponding film thickness and absorbed fluence are labeled on each plot.

The results of the cluster analysis of 20nm and 10 nm cases are demonstrated in Fig. 2.6. This analysis has been performed at the moment of time 1.5 ns; only clusters with the diameter more than 1 nm (at least 30 atoms) are considered as stable clusters. For clusters with diameter less than 1nm, they are treated as vapors. For 20 nm film, 18.7 % of the total atoms are considered as vapor; and for 10nm film, the fraction of vapor atoms is 27.3 %. Under the similar unit input fluence, the lower vapor density of 20 nm film is due to the nature of pressure balance during plume expansion. Even though 20 nm film has twice more atoms than 10 nm film, the plume size is only about 1.3

times larger. Hence, 20 nm film can only have slightly more vapor atoms than 10 nm film in order to maintain the vapor pressure, resulting in the lower vapor concentration of the thicker films. At this moment, the bottom molten layer is not decomposed and the distribution of clusters does not contain particles with the size above 100 nm. For 20 nm, 48.6 % of total atoms belong to the bottom molten layer, and for 10nm, 41.6 % of total atoms belong to the bottom molten layer. Fig. 2.6 a and c demonstrates the distribution of the number of clusters; this representation is hard to track the lager clusters which are limited in numbers. In Fig. 2.6b and d the alternative histograms with the total number of the atoms in the clusters are provided. The top molten layer from 20 nm Ag film decomposes to two clusters with diameters of 19.4 nm and 30.1 nm, and the top molten layer from 10 nm Ag film decomposes to four clusters with diameters in the range from 20.2 to 24.6 nm. The formation of clusters on the orders of 20s nm is consistent with small peak of bimodal size distribution observed in experiments.[117] On the other hand, rupturing of bottom molten layer is capable of giving cluster size in diameter more than 100s nm providing a plausible source of large peak of bimodal size distribution observed in experiments.[117] Based on the liquid layer stability analysis in Appendix A3, cluster with diameter of 446 and 112 nm can come out of the bottom molten layer of 20 and 10 nm films, respectively. The liquid layer stability analysis gives the upper bound of the possible cluster diameter, since the theory assumes that there are no external factors affecting the rupture process. Nevertheless, the analysis indicates that one can expect the bottom molten layer breaks down into clusters with diameter on the order of hundreds of nanometers.

Cluster analysis of both 10 nm and 20 nm film show three distinct size groups of clusters from different part of the plume. The first group has cluster diameters within 15 nm mostly from the formation of the foam region during spallation. The second group has cluster diameters with diameter greater than 20 nm that from due to the rupture of top molten layers. The third group is from the bottom molten layers, and is predicted with cluster diameters on the orders of 100 nm via molten layer stability theory. However, in experiments, clusters from the first group are hard to be distinguished from cluster from the second group, since clusters from the first group are likely to be overlapped by larger clusters during the cluster collection process or consumed by ripening effect.

Although there are three distinct size groups of clusters observed in simulations, the diameter difference between each group becomes smaller as film becomes thinner with properly scaled laser fluence. Based on thin liquid layer stability analysis in Appendix A3, cluster diameter is proportional to the thickness to the power of 5/3. With the similar energy density input for laser, thicker film can have thicker molten layer that disintegrates into clusters with larger size distribution than thinner film. The insight from thin film instability theory agrees with experiment that the shrinking of two bimodal modes as thickness of the film become thinner, and the two modes collapse at some critical thickness.[117]

Both experimental and computational studies show that laser ablation of thin film is capable to produce the nanoparticles with diameters that are much larger (< 100s nm) or in comparable of the film thickness because of spallation of the film. To understand which parts of the film are responsible for large nanoparticles, the ID of atoms contributing to the large nanoparticles and molten layer are tracked back to the initial film prior to laser irradiation. Fig. 2.7a shows the normalized original atomic density of the bottom molten layer and two large clusters that decomposed from the top molten layers of the 20 nm Ag film. It indicates that the atoms for bottom molten layers are mostly coming from the bottom half of the film, while the atoms for the top two large clusters are mostly coming from the top 5 nm of the film. Fig. 2.7a also indicates that clusters formed from the foamy regions in the plume have atoms mostly coming from the middle part of the film. Hence, it is apparent in this case that different size groups of nanoparticles are coming from the different parts of the film. However, the segregation is only apparent along z-axis, the atomic movements along x and y-axis are random. The top views of the original atom positions of large clusters, Fig. 2.7a, show that periodic boundary conditions can restrict the size of the cluster of 30.1 nm, but not for the cluster of 19.4 nm. Fig. 2.7b shows the similar segregation for the 10 nm Ag film, and one can still observe the bottom molten layers and top large clusters are coming from different parts of the film. However, the segregation is less apparent, since the curves between bottom molten layers and top large clusters are overlapped for about 4 nm. Moreover, the top views of the top four large clusters, Fig. 2.7b, show that the periodic boundaries conditions do not affect cluster diameters. Two brief conclusions can be drawn from the comparison of Fig. 2.7a and 2.7b, Firstly, the segregation becomes more apparent with increase of the film thickness. Secondly, the restrictions of the periodic boundary conditions are mostly for the nanoparticles with diameters larger than 25 nm. Simulation with larger computational domain is needed to understand how much the random thermal diffusion in x and y directions are impeded, which will be discussed later in Chapter 2.3.4.

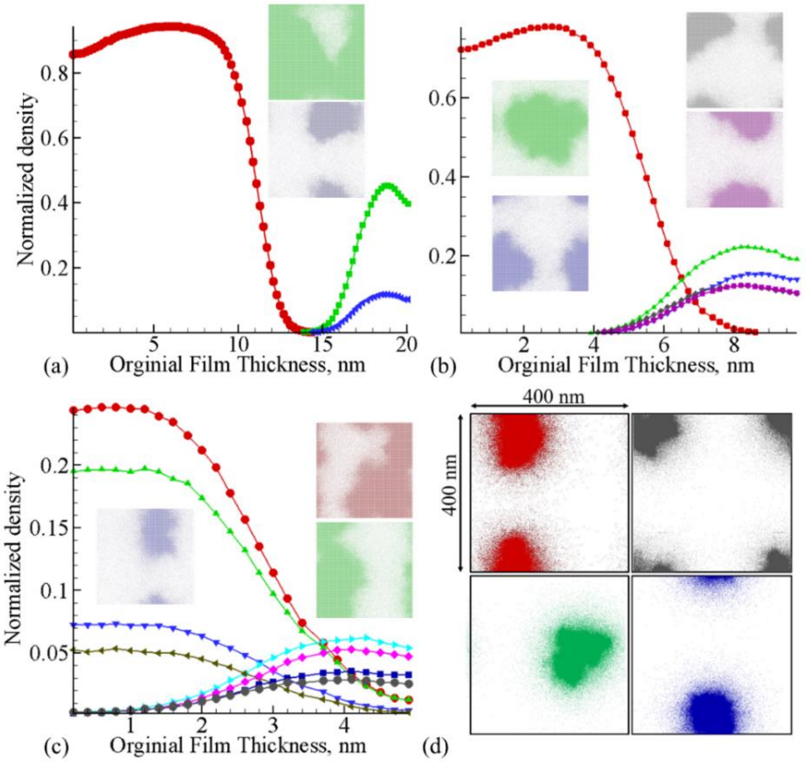

Figure 2.7. The normalized density plots of large clusters traced back to the film prior to laser irradiation is shown in **(a)** for 20 nm Ag film irradiated by a 40 fs laser pulse with an absorbed fluence of 245 J/m^2, **(b)** for 10 nm Ag film irradiated by a 40 fs laser pulse with an absorbed fluence of 120 J/m^2, and **(c)** for 5 nm Ag film irradiated by a 40 fs laser pulse with an absorbed fluence of 60 J/m^2. In **(a)**, the atoms from the bottom liquid layer (red lines) and the two largest clusters (green and blue lines) decomposed from the top liquid layer are traced back to their original positions. In **(b)**, the atoms from the bottom liquid layer (red lines) and the four largest clusters (other colors) decomposed from the top liquid layer are traced back to their original positions. In **(c)**, the 4 clusters decomposed from the bottom liquid layer and the 4 largest clusters decomposed form the top liquid layer are traced back to their original positions. Each atom position is summed along the film thickness, and normalized to the density of silver at 300 K and 0 GPa. The corresponding top views of the initial film with positions of atoms of the two largest clusters are shown in the smaller squares, each side of the square corresponds to 100 nm. The atoms inside the squares are colored based on the color of the lines for identification. In **(d)**, the top views of the original positions of 4 largest clusters generated in simulation of 600 × 600 × 5 nm film irradiated by a 40 fs laser pulse with an absorbed fluence of 60 J/m^2.

2.3.3. Transition and phase explosion regimes

For 20 nm Ag film irradiated by a 40 fs laser pulse at an with the absorbed fluence of 300 J/m^2 and 10 nm Ag film irradiated by a 40 fs laser pulse at an with the absorbed fluence of 130 and 140 J/m^2, the film spallation into two molten layers is not observed. It is clear to see from atomic snapshots, Figs. 2.8, 2.9 and 2.10, that the upper part of the film produces small and homogeneous size clusters with the size decrease in respect to the distance from the initial surface, while the lower part of the film forms a molten layer which decomposes slowly into large clusters of diameter on the orders of 10s nm. When the fluence goes beyond the range of the bimodal distribution region, a new nanoparticle generation mechanism, which can be considered as a transition between spallation and phase explosion (discussed later), sets in.

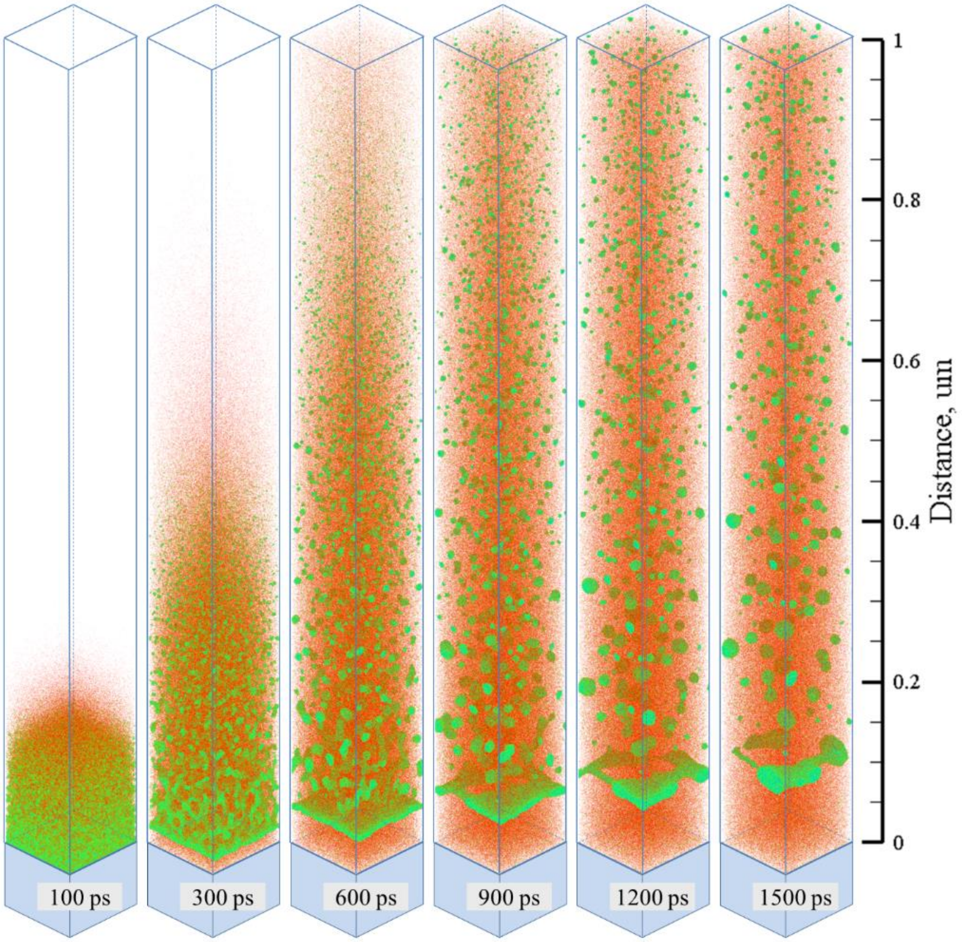

Figure 2.8. Snapshots of atomic configurations obtained in a TTM-MD simulation of laser ablation of a 20 nm Ag film irradiated by a 40 fs laser pulse at an absorbed fluence of 300 J/m^2 in vacuum condition. The irradiation conditions correspond to the spallation regime in vacuum. The location of the transparent substrate is shown by the blue rectangular parallelepipeds. The atoms are colored according to their potential energies, from green for molten Ag to red for vapor-phase Ag atoms.

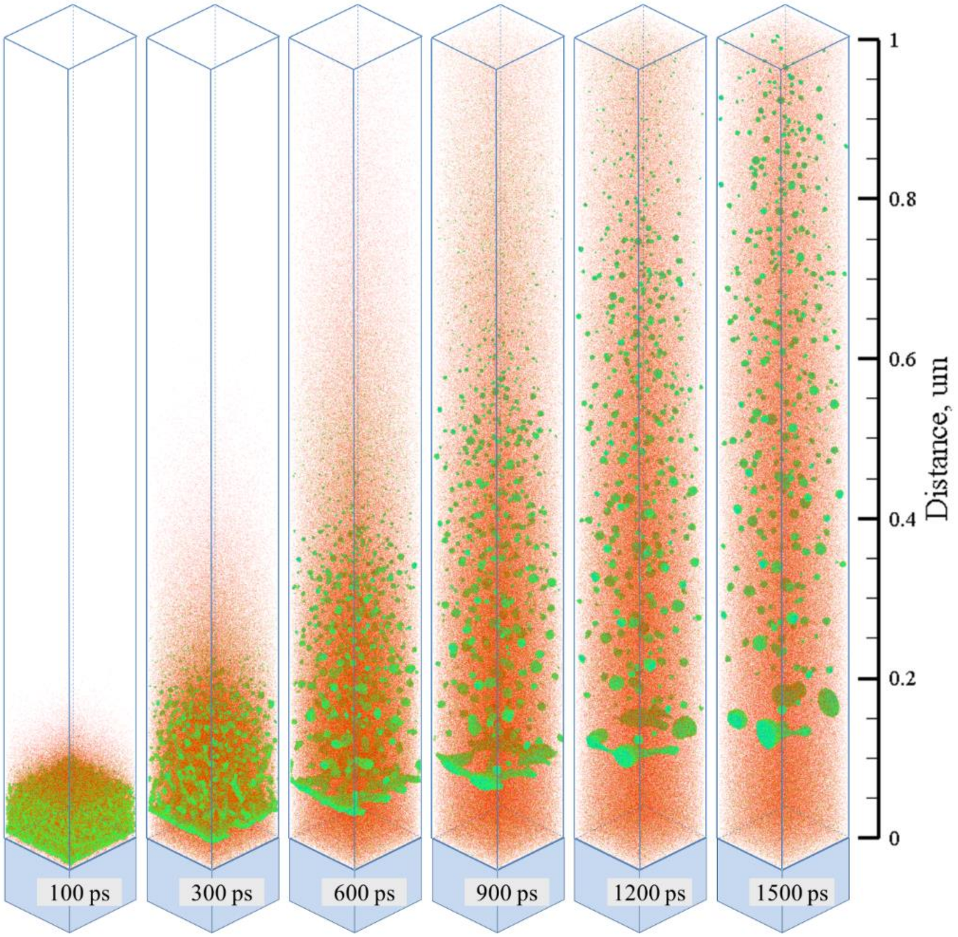

Figure 2.9. Snapshots of atomic configurations obtained in a TTM-MD simulation of laser ablation of a 10 nm Ag film irradiated by a 40 fs laser pulse at an absorbed fluence of 130 J/m^2 in vacuum condition. The irradiation conditions correspond to the spallation regime in vacuum. The location of the transparent substrate is shown by the blue rectangular parallelepipeds. The atoms are colored according to their potential energies, from green for molten Ag to red for vapor-phase Ag atoms.

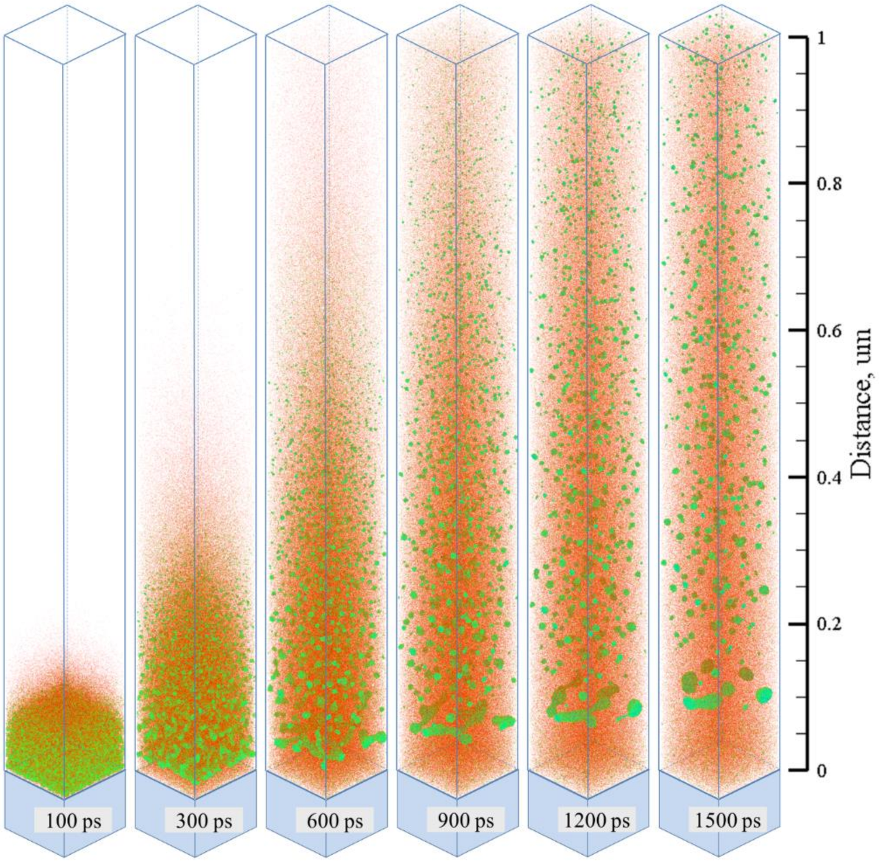

Figure 2.10. Snapshots of atomic configurations obtained in a TTM-MD simulation of laser ablation of a 10 nm Ag film irradiated by a 40 fs laser pulse at an absorbed fluence of 140 J/m^2 in vacuum condition. The irradiation conditions correspond to the spallation regime in vacuum. The location of the transparent substrate is shown by the blue rectangular parallelepipeds. The atoms are colored according to their potential energies, from green for molten Ag to red for vapor-phase Ag atoms.

The evolution of temperature, pressure, and density in the direction away from the substrate is shown in the form of contour plots in Fig. 2.11. The initial stage of the ablation process is similar to the previous case; the film is heated up almost homogeneously that builds the uniform compression under the stress confinement condition during the first 8 ps for 10 nm Ag films and 16 ps for the 20 nm Ag film as shown in the pressure contour plot, Fig. 2.11b, 2.11e, and 2.11h. For the case of 10 nm Ag film with absorbed fluence of 130 J/m^2, there is still weak tensile stress at the magnitude around 0.1 GPa forms at the upper part of the film, and the first frame (at 100 ps) of Fig. 2.9, shows the resemblance of spallation discussed earlier. However, while close, the film does not reach the cavitation threshold. (Temperature of the cavitation threshold at 0.1 GPa tensile stress is approximately 3200 K, but the lattice temperature during the onset of tensile stress is only around 3100 K.) The case of 10 nm Ag film with absorbed fluence of 140 J/m^2 and the case of 20 nm Ag film with absorbed fluence of 300 J/m^2 have similar pressure profiles, Fig. 2.11b and 2.11h, that there is no weak tensile stress appears on the upper part of the film. Lattice temperature of both cases (3380 K for 10nm Ag film with absorbed fluence of 140 J/m^2 and 3350 K for 20 nm Ag film with absorbed fluence of 300 J/m^2) reach the phase explosion threshold at zero pressure which is 3100 - 3450 K, and the upper part of the film undergoes the explosive decomposition. The normalized density plots, Fig. 2.11c, 2.11f and 2.11i, show that upper parts of the films have density decreasing drastically to almost less than 0.2 normalized densities within in 100 ps. The phase explosion creates a recoil pressure which keeps the bottom part in a molten state and provides the time to cool this layer below phase explosion temperature. Thus, the bottom part remains as a molten layer which is propelled away from the substrate by the vapor which forms near the interface. Eventually, the bottom layer decomposes into large clusters due to the thin layer instability.[64]

The results of the cluster analysis at 1.5 ns are demonstrated in Fig. 2.12. Due to the partial phase explosion, the vapor content, cluster with diameter less than 1 nm, in the plume is much higher than that of bimodal distribution regime. 20nm Ag film with absorbed fluence of 300 J/m^2 and 10 nm Ag film with absorbed fluence of 130 J/m^2 have similar ratio of vapor content to total atoms that are 39.6% and 40.3%, respectively, while the 10nm Ag film with absorbed fluence of 140 J/m^2 has much higher ratio of vapor content to total atoms of 49.3 %. For 10 nm film with absorbed fluence of 140 J/m^2, the bottom molten layer decomposes into 4 clusters with diameters ranging from 14.2 to 21.6 nm, while for 10 nm Ag film with absorbed fluence of 130 J/m^2, the bottom molten layer decomposes into 2 clusters with diameters 26.6 and 28 nm. For 20 nm Ag film, the bottom molten layer decomposes into a cluster with diameter around 39.8 nm that constitutes 1.9 million atoms.

By comparing 10 nm Ag films with the absorbed fluence of 130 and 140 J/m^2, the change of nanoparticle pattern is noticeable as fluence increases. The bottom molten layer of the absorbed fluence of 140 J/m^2 is thinner than the one of absorbed fluence of 130 J/m^2, resulting in the smaller sizes nanoparticles. The nanoparticle size difference from the bottom molten layer and vapor plume also shrinks when the absorbed fluence increases from 130 to 140 J/m^2; the overall nanoparticle size becomes smaller with higher vapor content as the fluence increases. One can expect that if the fluence increases further, there will be no presence of bottom molten layer, and the plume will be mostly vapor. This condition is similar to the traditionally known phase explosion, and will be discussed in the following paragraphs.

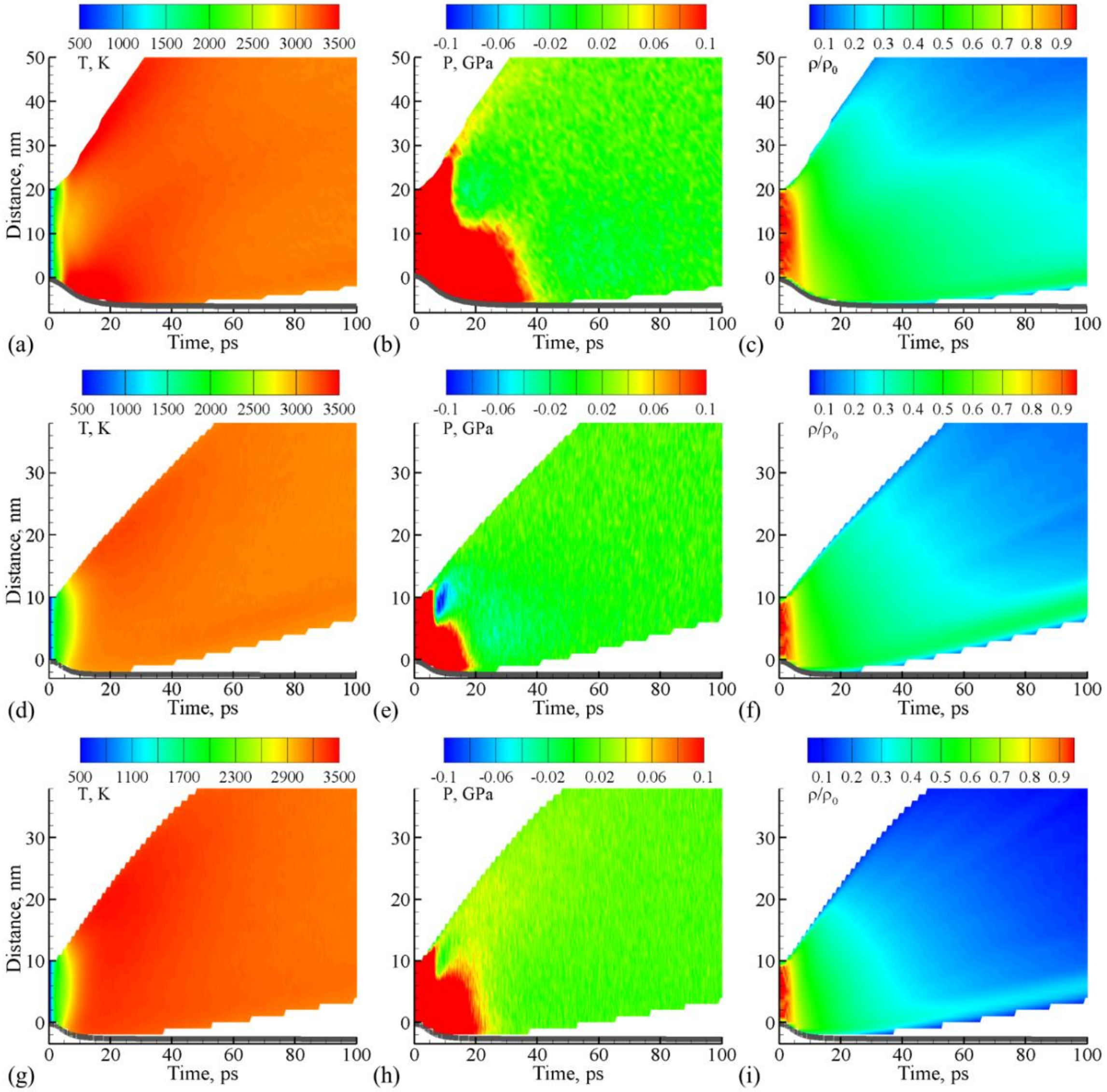

Figure 2.11. The contour plots of the initial spatial and time evolution in the direction away from the substrate in MD-TTM simulations performed for 20 nm Ag film irradiated by a 40 fs laser pulse at an absorbed fluences of 300 J/m^2 **(a,b,c)**, 10 nm Ag film irradiated by a 40 fs laser pulse at an absorbed fluence of 130 J/m^2 **(d,e,f)**, and 10 nm Ag film irradiated by a 40 fs laser pulse at an absorbed fluence of 140 J/m^2 **(g,h,i)**. Lattice temperature is colored in **(a,d,g)**, pressure is colored in **(b,e,h)**, and normalized density is colored in **(c,f,i)**. The laser pulse is directed along the y axis from the bottom of the contour plots, through a silica substrate shown as a grey line.

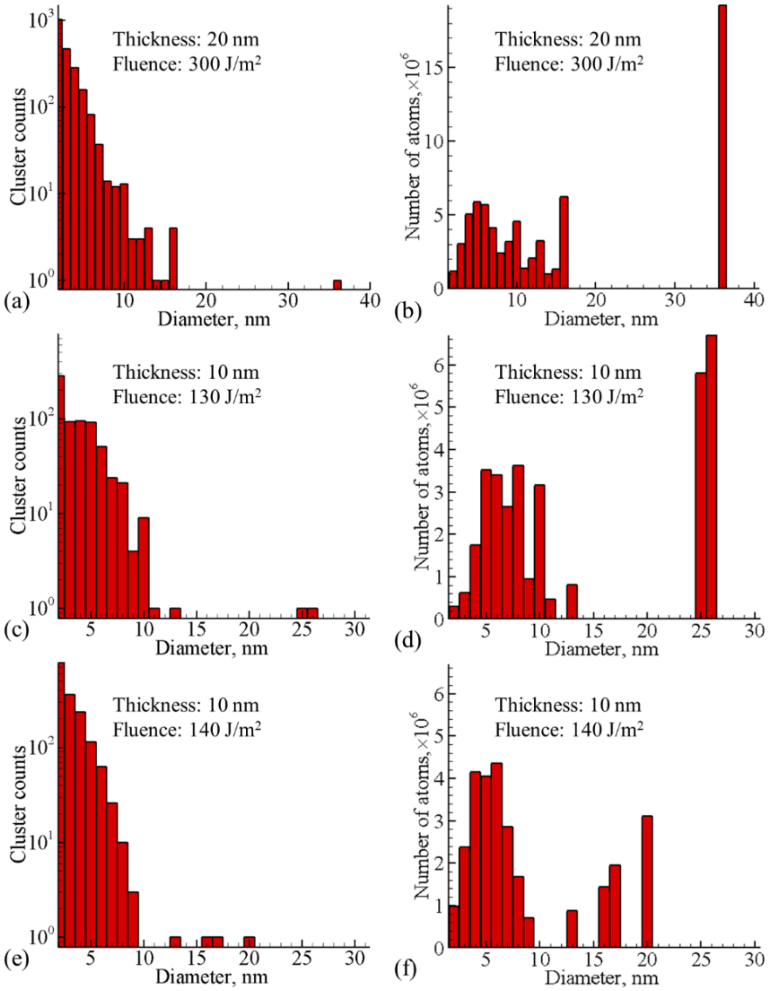

Figure 2.12. The results of the cluster analysis of the ablation plume generated in simulations performed for 20 nm Ag film irradiated by a 40 fs laser pulse at an absorbed fluence of 245 J/m^2 in vacuum condition **(a,b)**, 10 nm Ag film irradiated by a 40 fs laser pulse at an absorbed fluence of 130 J/m^2 **(c,d)**, 10 nm Ag film irradiated by a 40 fs laser pulse at an absorbed fluence of 140 J/m^2 **(e,f)**. The numbers of nanoparticles of different diameter are shown on **(a,c,e)**; the numbers of atoms that belong to nanoparticles of different diameter are presented on the **(b,d,f)**. The corresponding film thickness and absorbed fluence are labeled on each plot.

As the absorbed fluence increases further to 360 J/m^2 for the 20 nm Ag film, the snapshots, Fig. 2.13, show no formation of distinct molten layer during the simulation, and the plume is predominated with vapor and small droplets that decrease in size with respect to the distance from the initial surface. As shown in the temperature and pressure contour plots in Fig. 2.14 a and b, the laser fluence in this regime is high enough to bring the material far beyond the phase explosion temperature. Similar to the previous case, the explosive decomposition starts in the surface region and creates the recoil pressure on the order of 0.5 GPa which prevents the expansion of the bottom part initially. At pressure of 0.5 GPa, the phase explosion threshold is 4850 K[101] that is above the maximum temperature of the film which is only about 4600 K. However, the cooling of the material due to the explosive boiling and expansion is not enough to decrease the temperature of the bottom part below the phase explosion threshold at zero pressure which is 3450 K. Thus, the remaining part of the film disintegrates into the vapor droplet mixture when the recoil pressure becomes weaker.

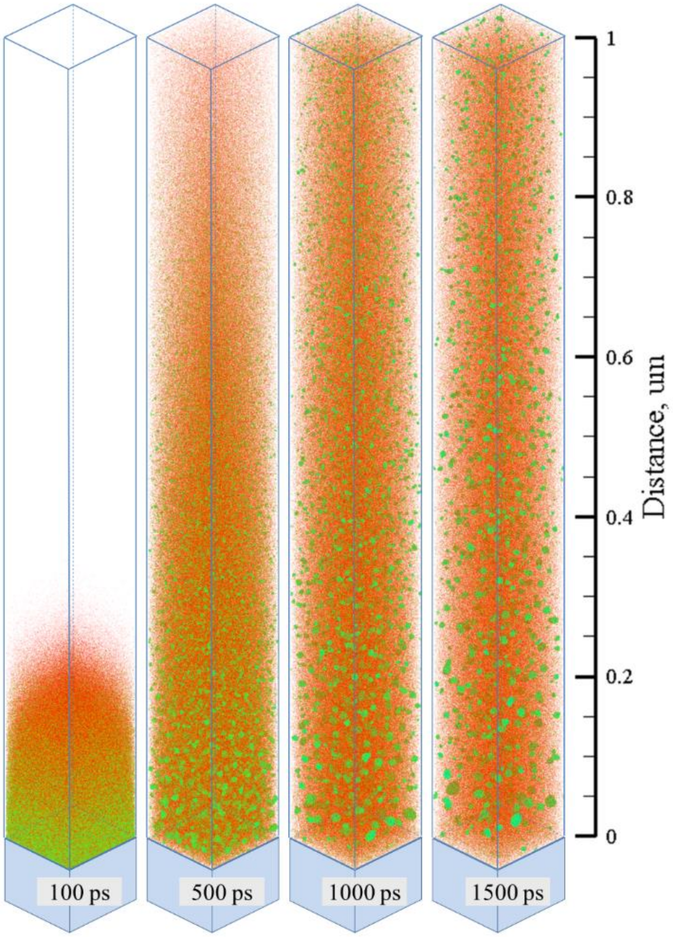

Figure 2.13. Snapshots of atomic configurations obtained in a TTM-MD simulation of laser ablation of a 20 nm Ag film irradiated by a 40 fs laser pulse at an absorbed fluence of 360 J/m^2 in vacuum condition. The irradiation conditions correspond to the spallation regime in vacuum. The location of the transparent substrate is shown by the blue rectangular parallelepipeds. The atoms are colored according to their potential energies, from green for molten Ag to red for vapor-phase Ag atoms.

The spontaneous decomposition of the overheated material into a mixture of vapor and molten droplets, observed in the simulations at high laser fluences, is consistent with the phase explosion mechanism predicted on the basis of the classical nucleation theory[107-108, 147] and confirmed in earlier simulations of laser ablation. It takes place simultaneously with the relaxation of the laser-induced compressive stress, resulting in a more vigorous material ejection and higher ablation yields as compared to a "pure" phase explosion, which is characteristic for longer pulses. The molten layer does not form at these conditions; thus, only small clusters can be produced as shown by cluster analysis in Fig. 2.15, and majority of atoms in the plumes, 59.9%, are vapors. Compared to the fluence of 300 J/m^2, the cluster distribution is narrower with more yielding concentrated for the smaller clusters for the fluence of 360 J/m^2.

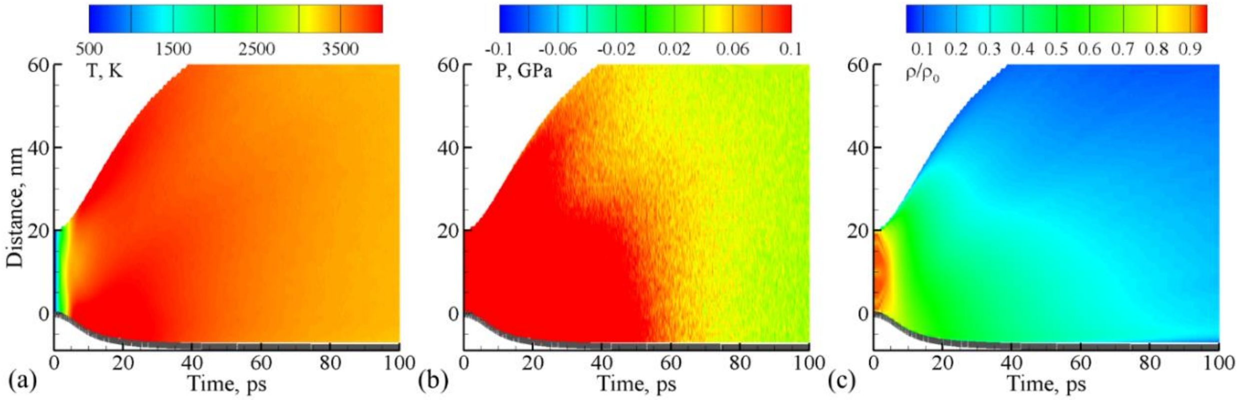

Figure 2.14. The contour plots of the initial spatial and time evolution of the lattice temperature, pressure, and normalized density in the direction away from the substrate predicted in MD-TTM simulation of laser ablation of a 20 nm Ag film irradiated by a 40 fs laser pulse at an absorbed fluence of 360 J/m^2. The laser pulse is directed along the y axis from the bottom of the contour plots, through a silica substrate shown as a grey line.

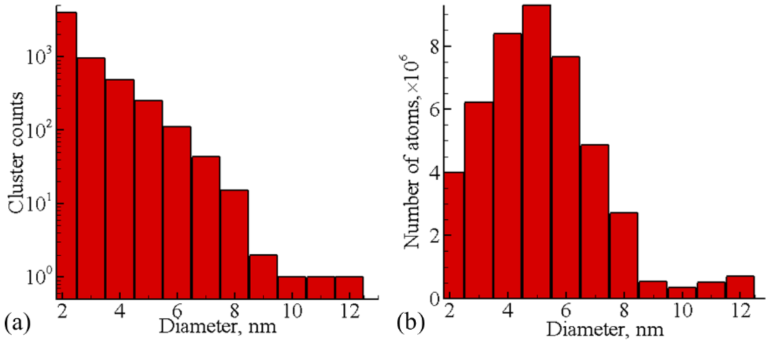

Figure 2.15. The results of the cluster analysis of the ablation plume generated in simulations performed for 20 nm Ag film irradiated by a 40 fs laser pulse at an absorbed fluence of 360 J/m^2 in vacuum condition. The numbers of nanoparticles of different diameter are shown on **(a)**; the numbers of atoms that belong to nanoparticles of different diameter are presented on the **(b)**.

2.3.4. Collapse of regimes

The distinctive fluences of each regime discussed above collapse as the Ag film thickness reduces to 5nm. In a series of MD simulations, it has been revealed that 5nm Ag film thickness can be considered as the boundary thickness which forms the bimodal distribution. As the film becomes thinner, stress confinement condition is weaker and both the maximum compressive and tensile stresses are reduced, so the formation of two molten layers is discouraged. Five different fluences have been tested, 50, 55, 60, 65, and 70 J/m^2. In the simulations with fluences 50 and 55 J/m^2, the fluence is not high enough to reach the cavitation threshold to spall the film, each film is detached and transferred as a single layer which can be decomposed into clusters of similar size at later time scale. However, the phase explosion takes place at the absorbed fluences of 65 and 70 J/m^2 that the whole films simultaneously decompose into the mixture of small droplets and vapors. Only at fluence of 60 J/m^2, ablation mechanism that is similar to spallation regime is observed. The narrow gap between the spallation and phase explosion regimes can be understood through the evolution of the temperature, pressure and the normalized density during the laser ablation of 5 nm Ag film at 60 J/m^2 in Fig. 2.16. While the tensile stress is around 0.02 GPa, the temperature is around 3200 K. For so small tensile stress, the cavitation threshold temperature is very close to the phase explosion onset; thus, there is only a very narrow gap between the spallation and phase explosion regimes.

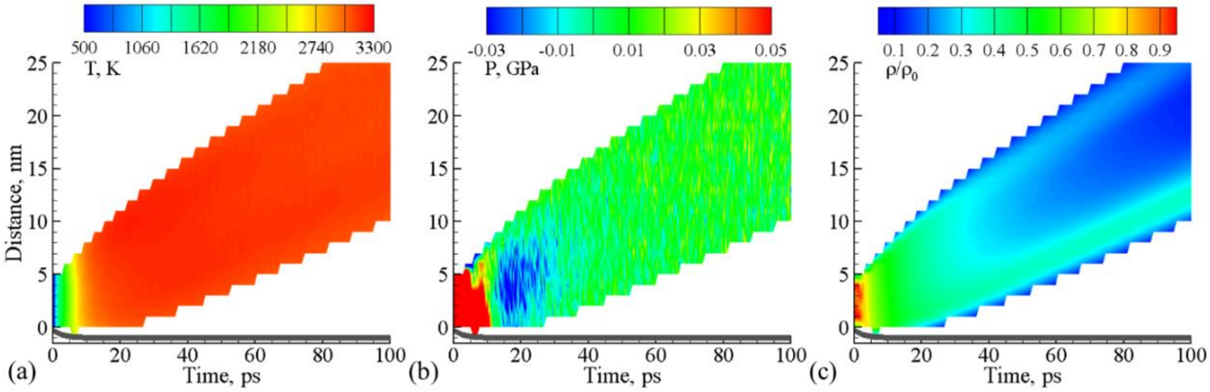

Figure 2.16. The contour plots of the initial spatial and time evolution of the lattice temperature **(a)**, pressure **(b)**, and normalized density **(c)** in the direction away from the substrate predicted in MD-TTM simulation of laser ablation of a 5 nm Ag film irradiated by a 40 fs laser pulse at an absorbed fluence of 60 J/m^2. The laser pulse is directed along the y axis from the bottom of the contour plots, through a silica substrate shown as a grey line.

The atomistic snapshots of 5nm Ag film irradiated by a 40 fs laser pulse at an absorbed fluence of 60 J/m^2 are shown in Fig. 2.17. The formation of two molten layers can be clearly identified at timeframe 100 and 300 ps in Fig. 2.17, and disintegration of these two molten layers is responsible for the different sizes of clusters. The results of cluster analysis shown in Fig. 2.18a and b show that the bottom molten layer forms 4 largest clusters range from 14.2 to 23.7 nm and the top molten layer forms the intermediate clusters range from 9.1 to 14.1 nm. The bottom molten layer forms larger clusters, since the partial confinement from the silica that prevents the effective evaporation and stabilizes the bottom molten layer. Even though laser-induced tensile stress can still cause spallation of 5nm Ag film into two molten layers, the size difference from the decomposition of two molten layers is sufficiently narrow and overall distribution resembles unimodal. Unlike the spallation regime observed from thicker films that constitutes low ratio vapor content (< 30 %), the ratio of vapor content calculated from 5nm Ag film with absorbed fluence of 60 J/m^2 is 42.8 %. While tracking the ID of large clusters back to original film, the segregation observed in 10 and 20 nm film discussed earlier disappears. Fig. 2.7c shows that clusters form from the bottom molten layers have atoms coming from the whole film, and clusters form from the top molten layers have atoms coming from the top 4 nm of the film. However, from the top views, the two largest clusters from the bottom molten layers are still affected by the periodic boundary conditions. To understand the effect of periodic boundary conditions to the nanoparticle size distribution, the last simulation is performed with 400 nm × 400 nm × 5nm film irradiated at an absorbed fluence of 60 J/m^2.

Fig. 2.19 shows the atomic snapshots of 400 nm × 400 nm × 5nm film irradiated by a 40 fs laser pulse at an absorbed fluence of 60 J/m^2. Similar to the results from 100 nm × 100 nm × 5nm simulation, two molten layers with uneven thickness form, and decompose in different rates. The results of cluster analysis in Fig. 2.18c and d show that the upper molten layer decomposes into clusters with diameters in the same range as the case of 100 nm × 100nm, but the maximum size of large clusters decomposed from the bottom molten layer increases to 30.3 nm, showing that periodic boundary conditions can influence the film disintegration and cluster formation if the lateral size is not enough. From Fig. 2.7d, the analysis of the clusters origin shows that the largest four clusters from 400 nm × 400 nm × 5nm film are not affected by the periodic boundary conditions, and the maximum distance an atom can travel laterally to join a cluster is about 200 nm. The vapor content is 43.2 %, similar to the simulation performed with lateral dimension of 100 nm x 100 nm. Hence, while slightly limited the size of large clusters from bottom molten layer, the 100 nm × 100 nm computational dimensions are large enough to provide the general trend of nanoparticle distribution pattern. From Fig. 2.18c and 2.18d, the larger lateral dimension provides more counting statistics for clearer nanoparticle distribution, the signature of unimodal distribution is much more pronounced than that of Fig. 2.18a and 2.18b. The collapse of different regimes as the film becomes ultra-thin also results in narrowing of nanoparticle size distribution into one mode. This observation agrees with typical unimodal nanoparticle size distribution when the film is below 5 nm.[117]

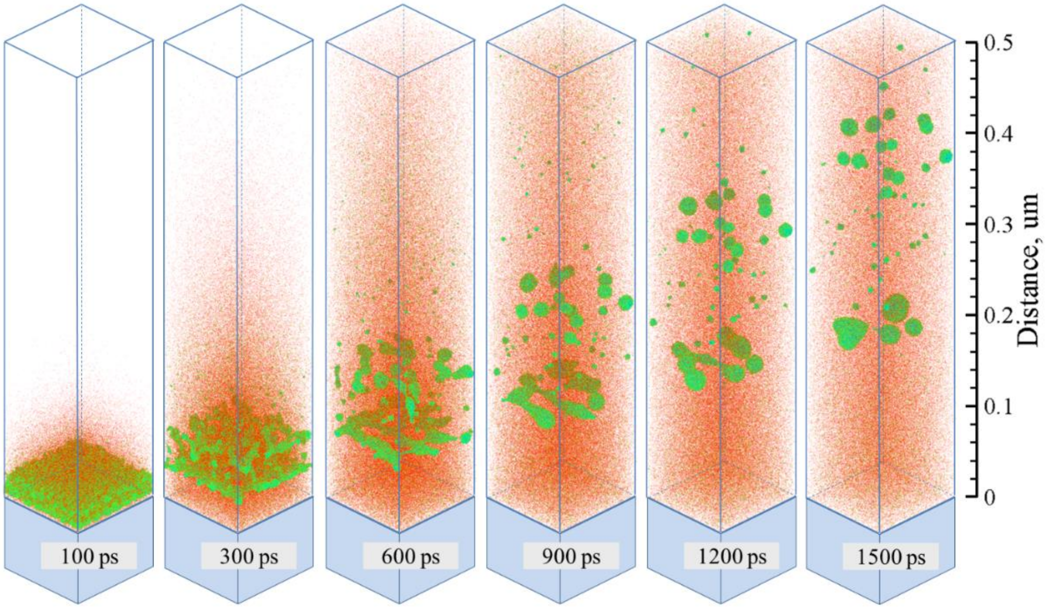

Figure 2.17. Snapshots of atomic configurations obtained in a TTM-MD simulation of laser ablation of a 5 nm Ag film irradiated by a 40 fs laser pulse at an absorbed fluence of 60 J/m^2 in vacuum condition. The irradiation conditions correspond to the spallation regime in vacuum. The location of the transparent substrate is shown by the blue rectangular parallelepipeds. The atoms are colored according to their potential energies, from green for molten Ag to red for vapor-phase Ag atoms.

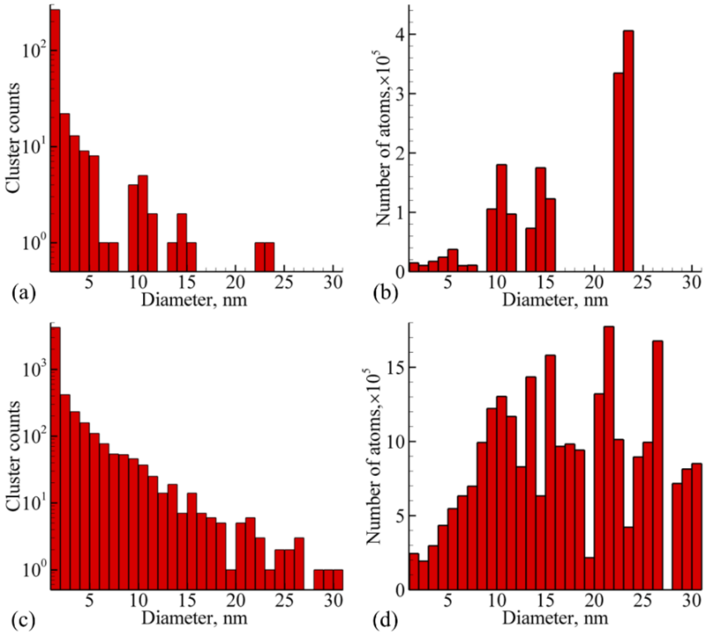

Figure 2.18. The results of the cluster analysis of the ablation plume generated in simulations performed for 5 Ag nm irradiated by a 40 fs laser pulse at an absorbed fluence of 60 J/m^2 in vacuum condition with lateral dimension of 100 nm **(a,b)** and 400 nm **(c,d).** The numbers of nanoparticles of different diameter are shown on **(a,c)**; the numbers of atoms that belong to nanoparticles of different diameter are presented on the **(b,d)**.

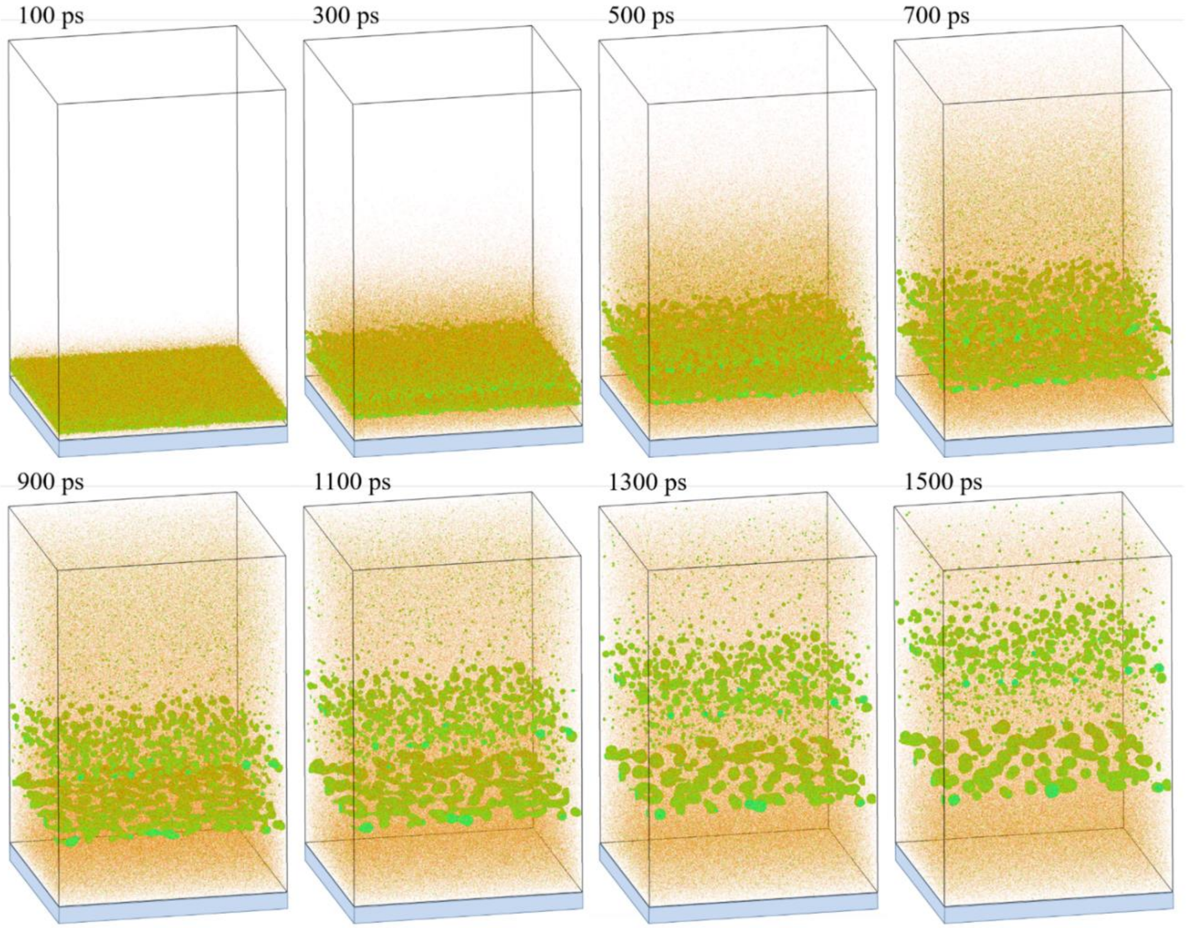

Figure 2.19. Snapshots of atomic configurations obtained in a TTM-MD simulation of laser ablation of a 400 nm × 400 nm × 5 nm Ag film irradiated by a 40 fs laser pulse at an absorbed fluence of 60 J/m^2 in vacuum condition. The irradiation conditions correspond to the spallation regime in vacuum. The location of the transparent substrate is shown by the blue rectangular parallelepipeds. The atoms are colored according to their potential energies, from green for molten Ag to red for vapor-phase Ag atoms.

2.4. Summary

Through the systematic investigation of thin film ablation in vacuum with different thickness and fluence, a map is constructed based on observed four distinctive ablation regimes (intact, spallation, transition, and phase explosion). Each regime corresponds to different characteristic laser-material interaction, and produces subsequently different nanoparticle distribution.

Spallation regime corresponds to laser induced tensile stress separates the film into two molten layers with uneven thickness decomposing in different rates. The eventual rupture of these two molten layers can give bimodal nanoparticle size distribution in experimental scale. Transition regime is identified as when upper part of the film undergoes phase explosion, while the lower part of the film decomposes slowly into clusters with size on the orders of 10s nm. Phase explosion regime is defined as the temperature of the whole film reaches beyond the thermodynamic stability of molten and undergoes phase explosion. Both transition and phase explosion regimes are expected to give unimodal nanoparticle size distribution in experiments, and the transition from bimodal to unimodal distribution can be achieved by control of fluence.

The distinction of different regimes rapidly collapses as the film becomes progressively thinner, as shown by series of simulations of ablation of 5 nm Ag films. While the weak tensile stress can still play the role to spall 5nm Ag film into two molten layer with uneven thickness, the resulting cluster distribution still resembles unimodal, as the spalled molten layers have insufficient thickness. The finding suggests that reduces the film thickness can be another alternative to control nanoparticle sizes toward unimodal distribution.

3. Atomistic modeling of nanoparticle generation in short pulse laser ablation of thin metal films in water

3.1. Introduction

With the finding of basic thin metal film-laser interaction in vacuum discussed in Chapter 2, the nature second step is to study the effect of water confinement to thin metal film-laser interaction and nanoparticle generation. Hence, the target in the simulations of laser ablation in this chapter is a thin Ag film deposited on a transparent silica substrate in water. The use of the thin film rather than a bulk metal target commonly used for nanoparticle production in PLAL is allowing us to perform the first exploration of the effects of the ablation plume confinement by liquid environment and nanoparticle formation mechanisms at a reduced computational cost. Moreover, the exploration of the role of the spatial confinement of the deposited laser energy within a thin metal film may provide ideas for achieving a more precise control over the size distribution of nanoparticles generated in PLAL.[148-149]

3.2. Computational setup

The simulation reported in this chapter is performed with a hybrid computational model combining a coarse-grained representation of liquid, a fully atomistic description of laser interaction with metal targets, and acoustic impedance matching boundary conditions, designed to mimic the non-reflecting propagation of the laser-induced pressure waves through the boundaries of the computational domain. A complete description of the computational model tailored for simulation of pulse laser interaction with Ag in water environment is provided in Chapter 1.2, and below only parameters relevant to the computational setup of the simulation reported in this chapter are described.

The simulations are performed for a 20 nm Ag film deposited on a transparent silica substrate and covered by water, as shown in Fig. 3.1. The initial film has fcc crystal structure and (001) orientation of the free surface. The periodic boundary conditions are applied in the directions parallel to the surface of the film and the dimensions of the computational system in these directions are 100 nm × 100 nm.

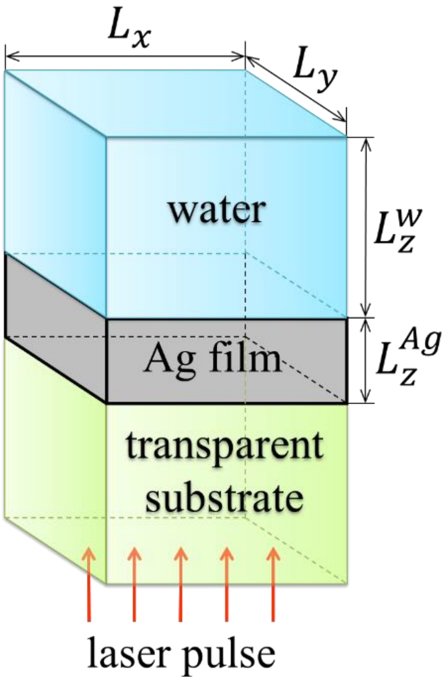

Figure 3.1. Schematic representation of the computational setup for simulation of short pulse laser interaction with a thin silver film in water deposited on a transparent silica substrate. The grey rectangular parallelepiped shows the initial location of the silver film represented by the TTM-MD model. The blue rectangular parallelepiped shows the initial location of the water represented by the coarse-grained MD model. The initial dimensions of the TTM-MD and coarse-grained MD parts of the system are $L_x = L_y = 100$ nm, $L_z^{Ag} = 20$ nm, and $L_z^w = 300$ nm. The elastic response of the substrate and the non-reflecting propagation of the laser-induced pressure wave in water environment are represented by acoustic impedance matching boundary conditions applied at the substrate-film interface and at the top of the coarse-grained MD part of the system. The laser pulse is directed from the bottom of the figure, through the transparent substrate. Periodic boundary conditions are applied in the lateral directions, perpendicular to the surface normal of the film.

The silica substrate is not represented with atomic resolution but introduced through a dynamic acoustic impedance matching boundary condition that accounts for the displacement of the metal-substrate interface in response to the thermal expansion and phase transformations occurring in the metal film. This boundary condition is designed to reproduce the transformation of a part of the energy deposited by the laser pulse into the energy of a pressure generated in the substrate, as well as the work of adhesion between the silica substrate and Ag film. The details of the implementation and parametrization of the boundary condition are described in ref. [101].

The water environment above the Ag film is represented by a combination of the coarse-grained MD model, described in Chapter 1.2.3, and a dynamic acoustic impedance matching boundary condition[101, 115, 150] that ensures non-reflective propagation of the pressure wave generated at the metal-water interface into the bulk of the water environment. This boundary condition is suitable for simulation of experimental conditions where reflection of the pressure wave from the surface of a thick water overlayer does not play any significant role in the generation of nanoparticle. The coarse-grained MD representation is used in a 300-nm-thick region of the water environment adjacent to the Ag film and the dynamic boundary condition is applied at the top of this region. The computational system consists of 11.3 million Ag atoms and 36.1 million coarse-grained particles representing water environment. The system is equilibrated at 300 K for 200 ps before applying laser irradiation.

The irradiation of the target with a 40 fs laser pulse is represented through a source term added to the equation for the electron temperature.[72] The source term simulates excitation of the conduction band electrons by a laser pulse with a Gaussian temporal profile and reproduces the exponential attenuation of laser intensity with depth under the surface. The optical absorption depth, 12 nm at laser wavelength of 800 nm,[144] combined with the effective depth of the “ballistic” energy transport, estimated to be about 56 nm for Ag,[89, 101-102] is used in the source term of the TTM equation.[72, 151] Since the ballistic range in Au exceeds the thickness of the films considered in this work, 20 nm, the reflection of the ballistic electrons from the back surface of the film results in a uniform distribution of the electronic temperature established on the time scale of electron thermalization. The effect of the ballistic energy transport and the finite size of the film are accounted for in the source term describing the laser irradiation,[72, 151] leading to an almost uniform energy deposition throughout the film thickness. The reflectivity of the surface is not defined in the model since the absorbed laser fluence rather than the incident fluence is used in the presentation of the simulation results.

3.3. Results and discussion

In this section, we report the results of two large-scale MD simulations of laser ablation of thin Ag films in liquid environment. Series of snapshots of atomic configurations generated in the course of the MD simulations are supplemented by the analysis of the evolution of thermodynamic parameters in response to the laser energy deposition and are used in the discussion of the characteristic features of laser ablation in liquids in Chapter 3.3.1 and 3.3.2. The distinct mechanisms of the nanoparticle formation in PLAL revealed in the simulations and the connection between the computational predictions and experimental observations are discussed in Chapter 3.3.3.

3.3.1. Visual picture of thin film laser ablation in liquid

The simulations discussed in this section are performed for 20 nm Ag films irradiated at absorbed laser fluences of 400 and 700 J/m^2. For irradiation in vacuum,[117] these fluences correspond to the regime of phase explosion,[71, 88, 106-108] when the entire Ag film undergoes an explosive decomposition into liquid droplets and vapor. The threshold for the phase explosion in vacuum is determined to be 310 J/m^2 for a 20 nm Ag film in a separate series of simulations. To provide a reference for the analysis of the effect of liquid environment on the ablation dynamics, snapshots of atomic configurations and a density contour plot are shown in Fig. 3.2 for a simulation performed for a 20 nm Ag film irradiated at an absorbed fluence of 360 J/m^2 in vacuum. At this fluence, the laser excitation and rapid equilibration between the excited electrons and lattice vibrations (electron-phonon coupling[118]) overheats the film material above the limit of its thermodynamic stability,[106-108] leading to an explosive release of vapor and ejection of a mixture of vapor and small liquid droplets. The ejected vapor-droplet mixture quickly expands away from the substrate, as can be seen from the snapshots in Fig. 3.2a and the rapidly dropping density in Fig. 3.2b.

The dynamics of the ablation plume expansion is strongly altered by the presence of the liquid environment, as can be seen from Figs. 3.3 and 3.4, where two series of snapshots of atomic configurations produced in the simulations of PLAL are presented along with normalized density distributions plotted for both silver and water. Even though the absorbed laser fluences in these simulations are higher than that in the simulation illustrated by Fig. 3.2, the expansion of a hot mixture of vapor and liquid droplets generated in the phase explosion of the superheated Ag film is meeting a stiff resistance from the water environment and is largely suppressed. While the expansion is stronger at 700 J/m^2, in both simulations the products of the film decomposition are rapidly decelerating and remain confined within hundreds of nanometers from the substrate during the first nanoseconds after the laser irradiation.

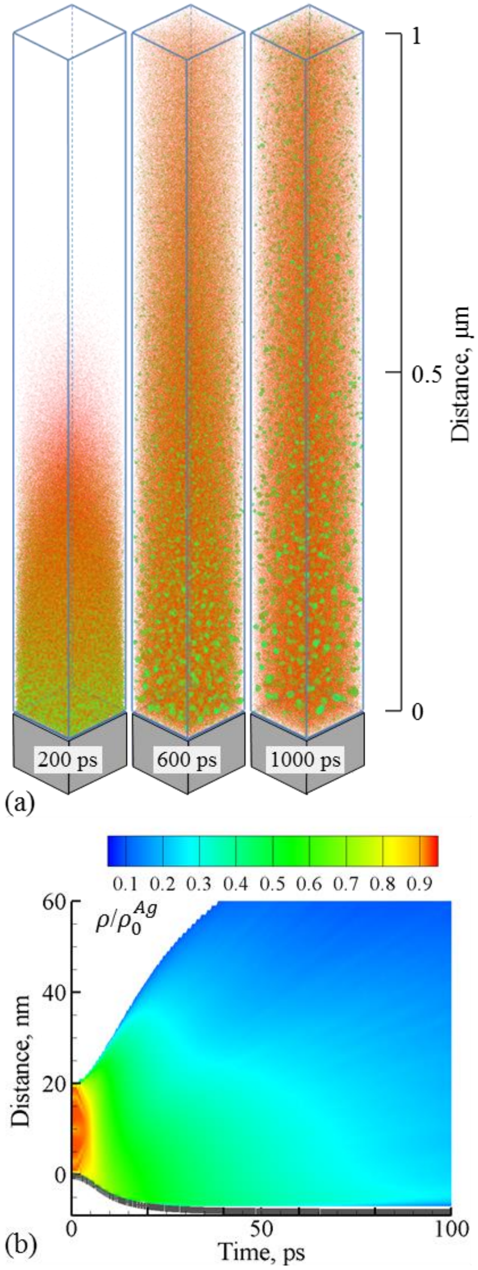

Figure 3.2. Snapshots of atomic configurations (a) and density contour plot (b) obtained in a MD simulation of laser ablation of a 20 nm Ag film in vacuum irradiated by a 40 fs laser pulse at an absorbed fluence of 360 J/m^2. The transparent silica substrate is represented in (a) by the grey rectangular parallelepiped. The Ag atoms are colored by their potential energies, so that the *green* atoms belong to liquid droplets and the *red* ones are the vapor-phase atoms. The density in (b) is normalized by the initial density of solid silver at 300 K, ρ_0^{Ag}.

The inspection of the density profiles plotted to the right from the snapshots in Figs. 3.3 and 3.4 reveals the formation of a dense front of the Ag plume near the interface with water by the time of 200 ps, with a sharper density peak observed in the simulation performed at a lower fluence of 400 J/m^2. The density values in the layers at the front of the expanding plume correspond to a strongly superheated liquid metal that can be expected to exhibit a limited stability as it interacts with compressed water layer. Indeed, the snapshots from the simulations show that the morphologies of the dense superheated layers (green layers in Figs. 3.3 and 3.4) undergo continuous evolution throughout the simulations. The fine roughness of the top surfaces of the layers exposed to the water environment can be seen already at 200 ps and is particularly pronounced in the simulation performed at the higher fluence, Fig. 3.4. The interfacial structures coarsen and decompose into large liquid regions on the timescale of nanoseconds. The important implications of the liquid layer decomposition for the nanoparticle formation are discussed in Chapter 3.3.3.

Another prominent process that plays an important role in the nanoparticle generation and, as discussed in Chapter 3.3.2, can be related to experimental observations of large, micrometers to millimeters, bubbles in PLAL,[43-47, 49, 51, 152] is the appearance and growth of a low-density Ag-water mixing region at the interface between the dense layer of the superheated liquid metal and the water environment. While in both simulations the initial fronts of the density profiles are relatively sharp and the metal-water mixing region does not exceed 30 nm at 200 ps, the mixing region steadily expands with time and reaches the thickness of about 100 nm by the time of 3 ns after the laser pulse. As discussed below, the expansion of the mixing region is driven by the rapid heating and vaporization of water that is brought in contact with the hot mixture of metal vapor, clusters, and droplets produced by the explosive decomposition of the irradiated film. The thermodynamic conditions in the mixing region are highly susceptible to the nucleation and growth of metal clusters and nanoparticles, which is clearly reflected in the snapshots, where a large number of small clusters can be seen to emerge in the mixing region on the timescale of just a couple of nanoseconds.

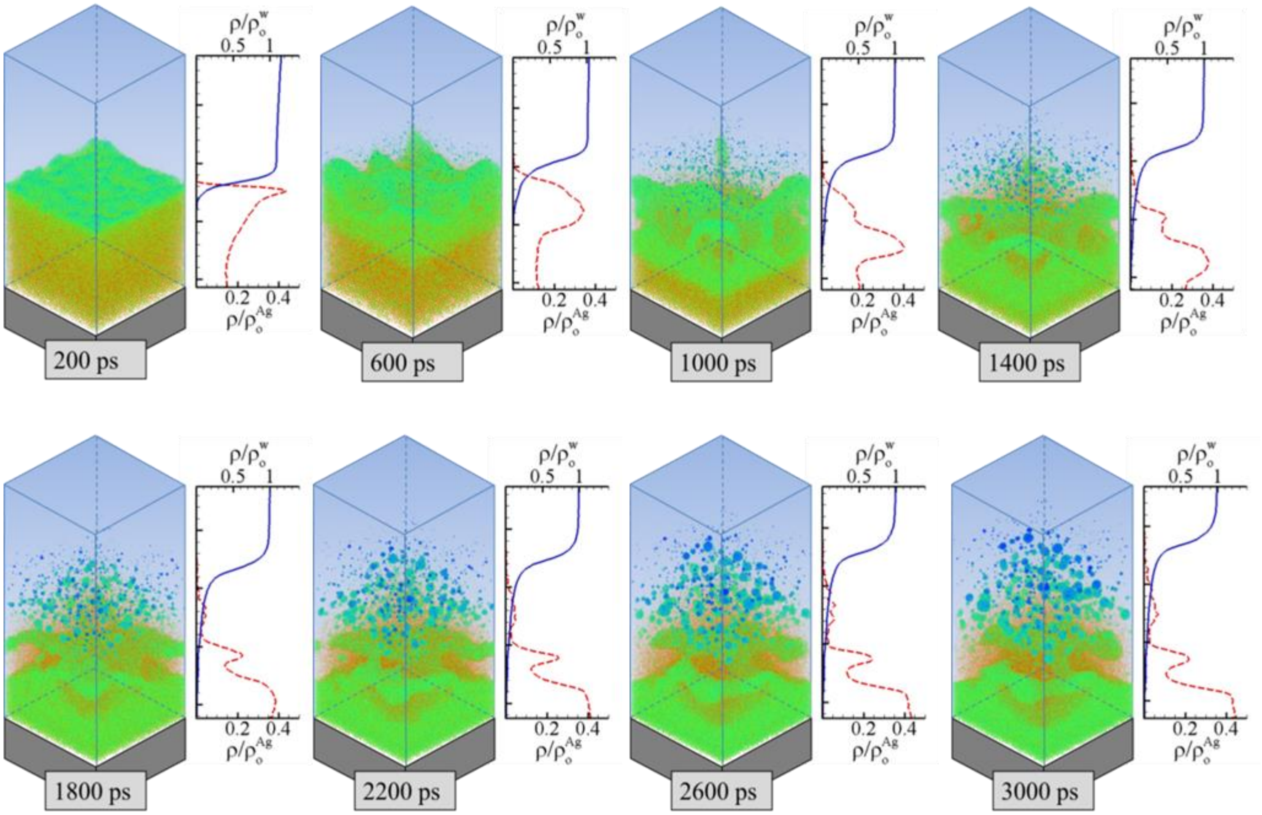

Figure 3.3. Snapshots of atomic configurations obtained in a MD simulation of laser ablation of a 20 nm Ag film in water irradiated by a 40 fs laser pulse at an absorbed fluence of 400 J/m^2. The transparent silica substrate is represented by the grey rectangular parallelepiped. A 200-nm-wide region above the substrate is shown in the snapshots. The Ag atoms are colored by their potential energies, in the range from -2.5 to -1.5 eV, so that the *blue* atoms belong to solidified nanoparticles and the *red* ones are the vapor-phase atoms. The water molecules are blanked to expose the nanoparticle formation, and the presence of water is shown schematically by the blue background. The degree of water-silver mixing is illustrated by density plots shown as functions of distance from the substrate for both water and silver on the right sides of the snapshots. The values of the water and silver densities in these plots are normalized by the initial densities of liquid water and solid silver at 300 K, $\boldsymbol{\rho_0^w}$ and $\boldsymbol{\rho_0^{Ag}}$, respectively.

3.3.2. Evolution of thermodynamic parameters

The analysis of the visual picture of the ablation process can be supplemented by consideration of the evolution of density, temperature, pressure, and collective velocity in the direction away from the substrate, shown in the form of contour plots in Figs. 3.5 and 3.6. The initial rapid expansion of the irradiated film undergoing an explosive decomposition into vapor and small droplets, the formation of a dense layer of hot metal plume pushing against the water environment, as well as the appearance and expansion of a low-density metal-water mixing region are the common features of the two simulations that can be seen in the contour plots. To facilitate the analysis, several distinct regions can be identified in the contour plots based on the evolving distributions of Ag and water. These regions are labeled in the density contour plots, Figs. 3.5a and 3.6a, and are defined and discussed below.

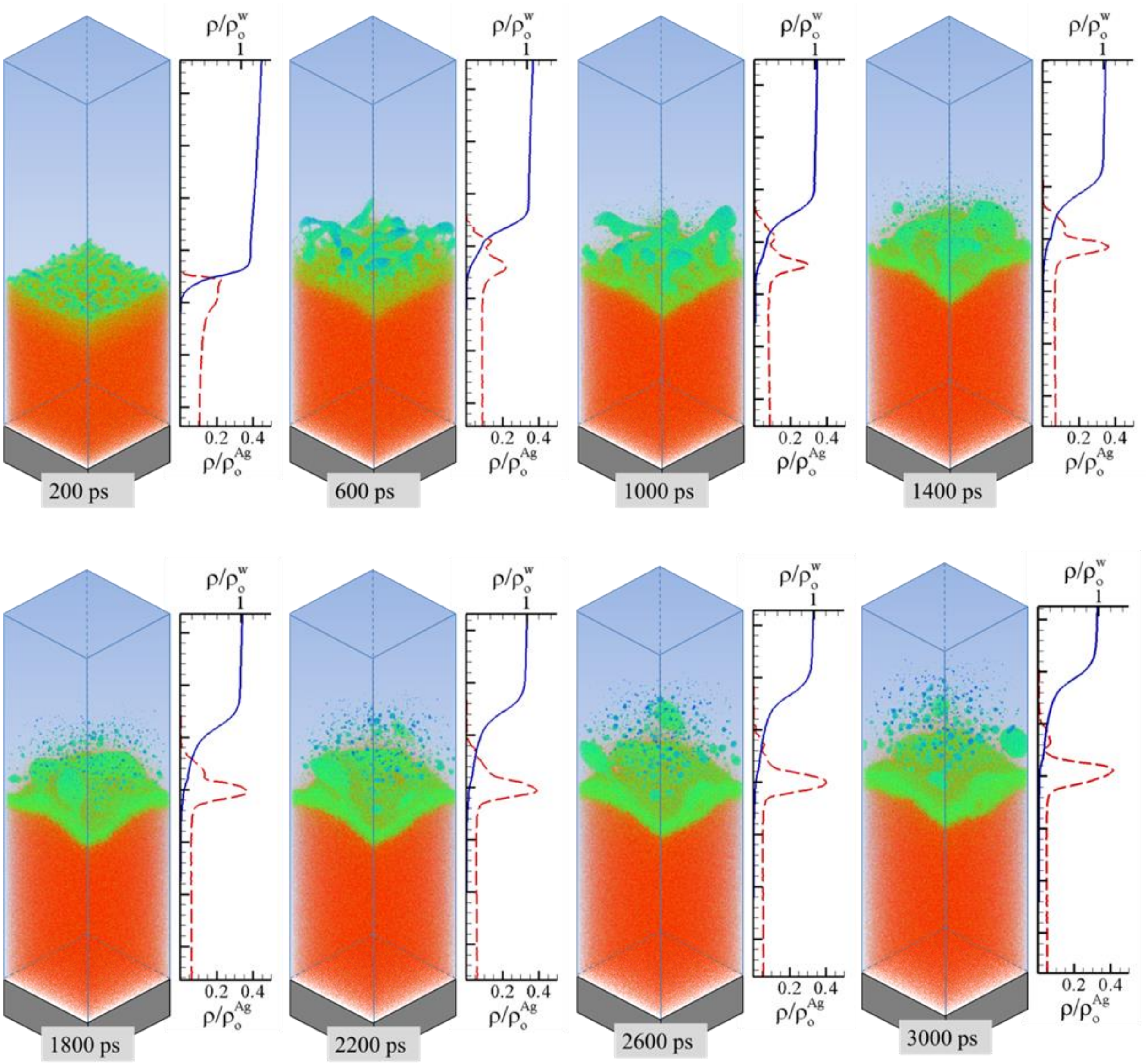

Figure 3.4. Snapshots of atomic configurations obtained in a MD simulation of laser ablation of a 20 nm Ag film in water irradiated by a 40 fs laser pulse at an absorbed fluence of 700 J/m^2. The transparent silica substrate is represented by the grey rectangular parallelepiped. A 350-nm-wide region above the substrate is shown in the snapshots. The Ag atoms are colored by their potential energies, in the range from -2.5 to -1.5 eV, so that the *blue* atoms belong to solidified nanoparticles and the *red* ones are the vapor-phase atoms. The water molecules are blanked to expose the nanoparticle formation, and the presence of water is shown schematically by the blue background.

The degree of water-silver mixing is illustrated by density plots shown as functions of distance from the substrate for both water and silver on the right sides of the snapshots. The values of the water and silver densities in these plots are normalized by the initial densities of liquid water and solid silver at 300 K, $\boldsymbol{\rho_0^w}$ and $\boldsymbol{\rho_0^{Ag}}$, respectively.

The first region is a low density region that appears in the vicinity of the silica substrate as a result of the rapid expansion of the metal film undergoing the phase explosion. It is defined as a region where the density of the products of the explosive film decomposition (a mixture of Ag vapor, atomic clusters, and small droplets) is below 20% of the initial density of the metal film. The second region is a dense part of the ablation plume that is generated due to the confinement of the plume expansion by the water environment. The interaction of this dense layer with water results in the formation of a complex protruding morphology of the top surface of the dense layer that can be seen in the snapshots in Figs. 3.3 and 3.4. The layer, therefore, can be subdivided into a more compact/uniform part (region 2) and a "terrain" region (region 3) where the liquid metal protrusions and large droplets are surrounded by supercritical water. The boundary between the second and third regions is defined as the location where the concentration of water exceeds 0.5 wt.% in the simulation performed at a fluence of 400 J/m^2 and 5 wt.% in the one performed at 700 J/m^2. The upper boundary of the terrain region is also defined by the water concentration and corresponds to 5 and 24 wt.% water in the lower and higher fluence simulations, respectively. The different thresholds used for identification of the second and third regions in the two simulations are chosen to match the visual identification of the "compact" and "terrain" parts of the dense metal layer from the simulation snapshots, Figs. 3.3 and 3.4, and are reflecting the stronger penetration of water into the layer at a higher fluence.

Above the "terrain" region, we observe an expanding low-density region (region 4 in the contour plots) where Ag atoms, clusters, and nanoparticles are suspended in water that is brought to the supercritical state by the interaction with the hot metal plume. The density of water in the lower part of this region is below 0.1 and 0.2 g/cm^3 in the simulations performed at 400 J/m^2 and 700 J/m^2, respectively, and the boundaries of the region are defined so that the concentration of water is ranging from 5 to 98 wt.% at 400 J/m^2, and from 24 to 98 wt.% at 700 J/m^2. Finally, the fifth region is defined as a water region where the concentration of Ag is below 2 wt.% and the water remains close to its initial density of 1 g/cm^3.

The most distinctive difference between the evolutions of different regions in the two simulations reported in this chapter is the dynamics of the dense Ag layer formed at the interface with the water environment (regions 2 and 3). At a lower fluence of 400 J/m^2, the dense liquid layer starts to drop down after 500 ps and redeposits to the substrate at ~1150 ps. At a higher fluence of 700 J/m^2, the molten layer is also decelerated by the resistance of the water environment but continues to float above the substrate on the timescale of the simulation. The difference in the layer dynamics can be explained by considering the difference in the thermodynamic conditions in the regions immediately adjacent to the superheated liquid layer, *i.e.*, in regions 1 and 4. As can be seen from the temperature contour plots, the levels of temperature and pressure in region 1 are substantially higher in the simulation performed at a higher fluence (note the difference in scales used for temperature and pressure in Figs. 3.5 and 3.6). As a result, the force exerted on the layer from the expanding region 1 is weaker in the lower fluence simulation and is quickly exceeded by the counterforce applied on the layer from region 4, where the expansion of heated supercritical water is fueled by the rapid energy transfer from the hot metal plume. The expanding Ag-water mixing region is able in this case to push the dense front of the plume down to the substrate while simultaneously pushing the overlaying water region in the upward direction. At a higher fluence of 700 J/m^2, a similar downward push from the emerging Ag-water mixing region meets stiffer resistance from the underlying gaseous region 1, where the emission and reflection of a compressive wave can be seen in the pressure and velocity contour plots shown in Figs. 3.6c and 3.6d. As a result, the position of the layer undergoes a series of weak oscillations while floating above the silica substrate.

3.3.3. Nanoparticle formation mechanisms

The results of the simulations discussed above make it possible to identify two distinct mechanisms of nanoparticle formation in laser ablation of metals in water environment. Both mechanisms are activated by the formation of the dense layer of superheated liquid metal at the water-plume interface at the early stage of the ablation plume expansion. The interaction of water with the hot metal layer brings an interfacial region of water to the supercritical state and results in the formation of a low density metal-water mixing region that rapidly expands and serves as a precursor for the formation of cavitation bubble at a later time. As the evaporation provides the main pathway for the hot molten layer to cool down, the layer serves as a continuous source of metal vapor supplied to the mixing region. The conditions in the mixing region are highly susceptible to the condensation of metal atoms into clusters and rapid growth of the atomic clusters into nanoparticles. Indeed, it can be seen from the contour plots in Figs. 3.5b and 3.6b that the average temperature in the mixing regions, while staying above the critical temperature of water, is close to and, in the upper part, even below the melting temperature of Ag. The rapid nucleation and growth of the nanoparticles is initiated on the very short timescale of just a few nanoseconds after the laser irradiation and is directly observed in the MD simulations. This constitutes *the first nanoparticle generation mechanism* predicted in the simulations, and further analysis of the kinetics of the nanoparticle formation through this mechanism is provided below.

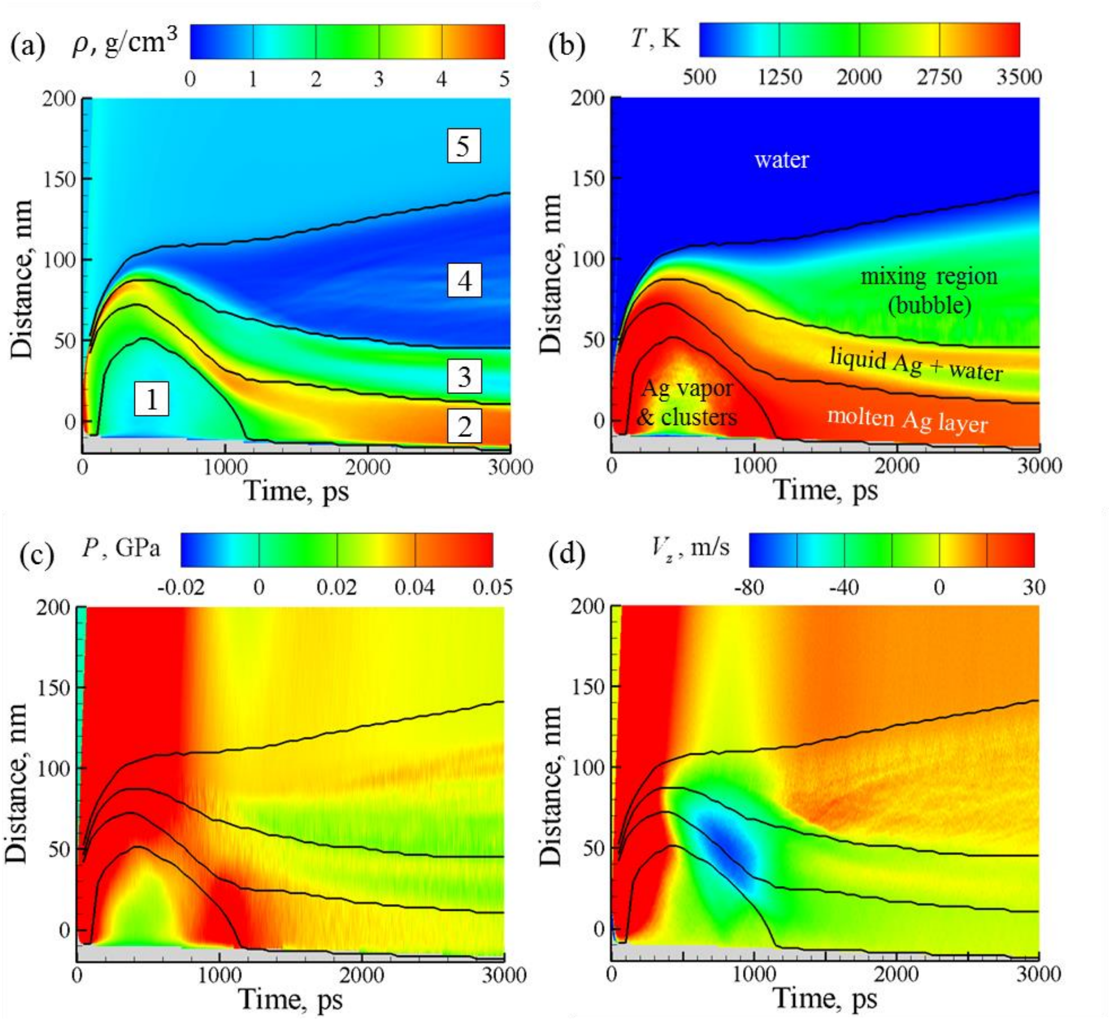

Figure 3.5. The contour plots of the initial spatial and time evolution of the density (a), lattice temperature (b), pressure (c), and collective velocity in the direction away from the substrate (d) predicted in a MD simulation of laser ablation of a 20 nm Ag film in water irradiated by a 40 fs laser pulse at an absorbed fluence of 400 J/m^2. The snapshots from the simulation are shown in

Fig. 3.3. The laser pulse is directed along the *y* axis from the bottom of the contour plots, through a silica substrate shown as a grey area. The black lines separate five distinct regions labeled by numbers in (a): Region 1 corresponds the gaseous mixture of Ag vapor and small clusters, region 2 is a compact superheated molten Ag, region 3 is a "terrain" of liquid Ag structures and droplets mixed with water, region 4 is a Ag – supercritical water mixing region where Ag nanoparticles form through condensation and growth, and region 5 is pure liquid water. The quantitative criteria used for identification of the regions are explained in the text.

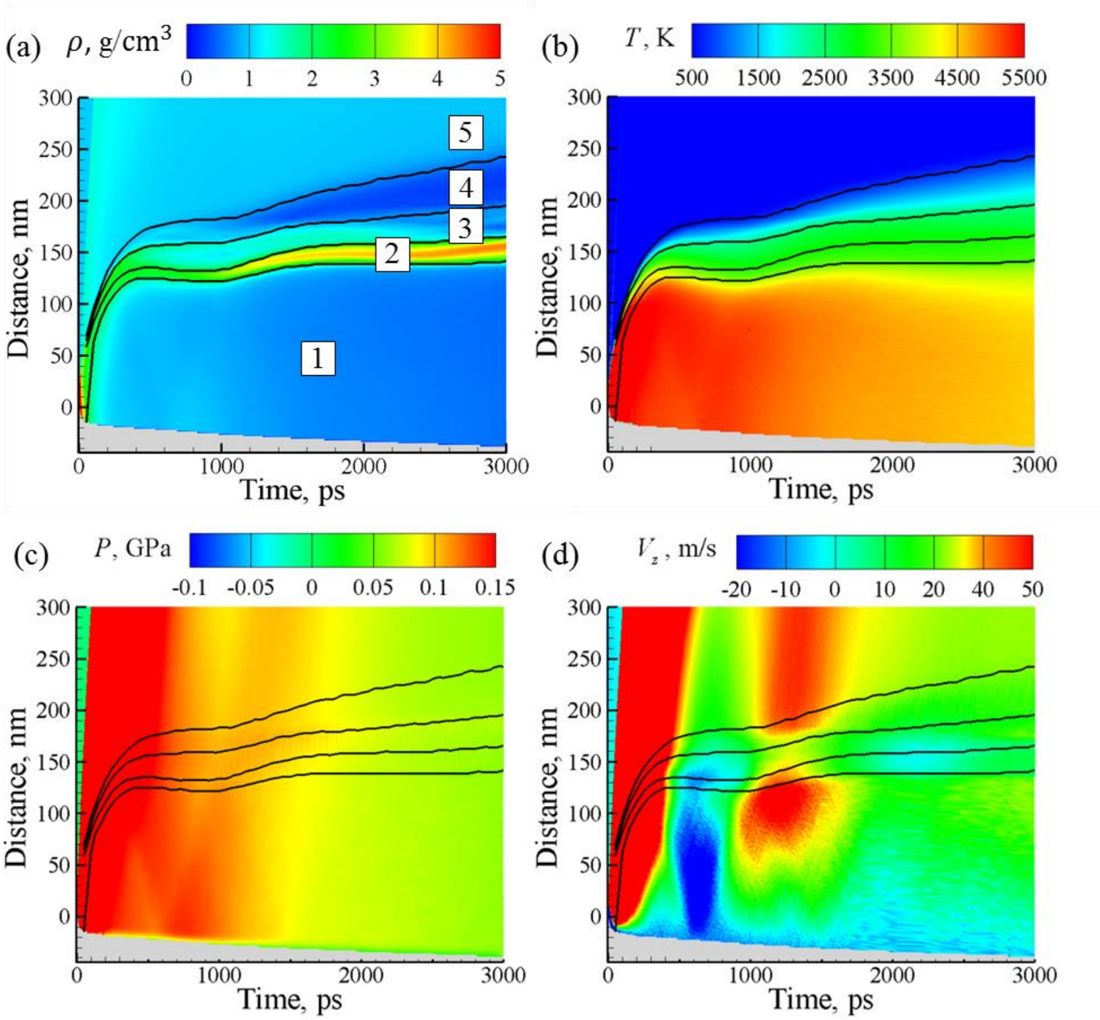

Figure 3.6. The contour plots of the initial spatial and time evolution of the density (a), lattice temperature (b), pressure (c), and collective velocity in the direction away from the substrate (d) predicted in a MD simulation of laser ablation of a 20 nm Ag film in water irradiated by a 40 fs laser pulse at an absorbed fluence of 700 J/m^2. The snapshots from the simulation are shown in Fig. 3.4. The laser pulse is directed along the *y* axis from the bottom of the contour plots, through a silica substrate shown as a grey area. The black lines separate five distinct regions labeled by numbers in (a): Region 1 corresponds the gaseous mixture of Ag vapor and small clusters, region 2 is a compact superheated molten Ag, region 3 is a "terrain" of liquid Ag structures and droplets mixed with water, region 4 is a Ag – supercritical water mixing region where Ag nanoparticles

form through condensation and growth, and region 5 is pure liquid water. The quantitative criteria used for identification of the regions are explained in the text.

The analysis of the evolution of sizes of the metal clusters and nanoparticles in the mixing region is performed with a cluster identification algorithm applied to atomic configurations generated in the two simulations between 300 ps and 3000 ps, with a 100 ps interval. Only the clusters detected above the molten layer (regions 3 and 4) are considered in the analysis, since these are the clusters that contribute to the generation of nanoparticles in the mixing region. The results of the analysis are presented in Figs. 3.7 and 3.8, where the cumulative numbers of Ag atoms present above the molten layer as individual atoms and small atomic clusters with diameter below 1 nm (less than 30 atoms) are shown separately from the larger clusters that we denote as nanoparticles. As the total number of atoms in the mixing region is steadily rising due to the evaporation from the superheated liquid layer, the number of individual atoms and small atomic clusters saturates in both simulations, Figs. 3.7a and 3.7b. This reflects the high rate of the nanoparticle growth that depletes the population of atoms and clusters faster than they are resupplied by the layer evaporation.

The evolution of the abundance of nanoparticles of different sizes is shown in Figs. 3.7c and 3.7d. The populations of nanoparticles with diameters less than 4-6 nm seem to plateau and even show signs of decline in the lower fluence simulation, Fig. 3.7c, as the smaller nanoparticles grow and coalesce into the larger ones. Indeed, the larger nanoparticles keep up the trend of cumulative number of atoms in the mixing region growing when the abundance of smaller nanoparticles go flat. As can be seen from the snapshots in Figs. 3.3 and 3.4, the larger nanoparticles are mostly found closer to the molten layer, where the higher density of atoms and other nanoparticles leads to the faster growth and higher probability of nanoparticle coalescence. Overall, the nanoparticle size distribution shifts to larger sizes as time progresses and nanoparticles grow and coalesce. The growth of the nanoparticles and broadening of the size distributions is further visualized by plotting the histograms of the amount of material contributing to nanoparticles of different sized at three moments of time, 1, 2, and 3 ns after the laser pulse, Figs. 3.7e and 3.7f.

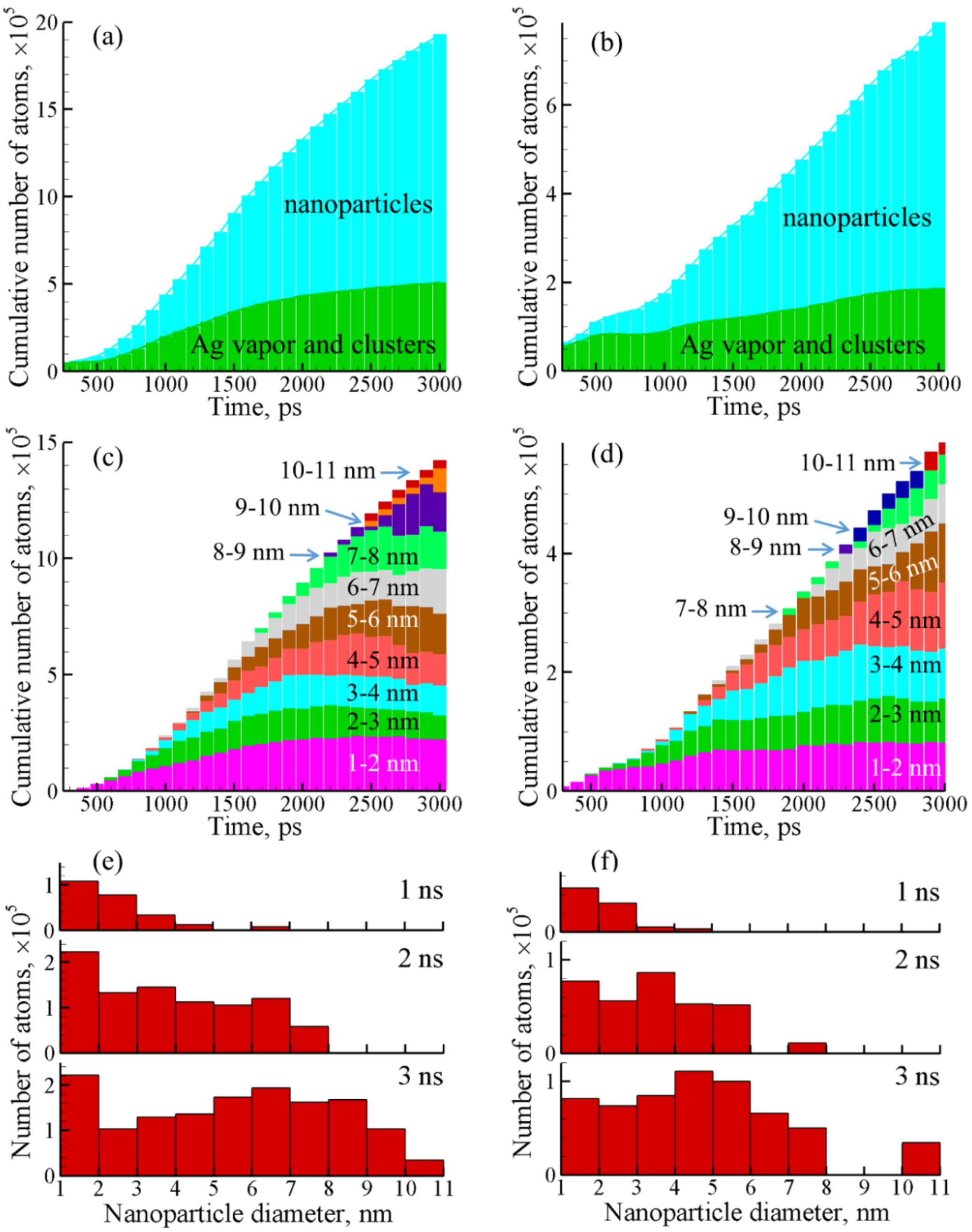

Figure 3.7. The results of the cluster analysis of the ablation plume generated in simulations performed at absorbed fluences of 400 J/m2 (a,c,e) and 700 J/m2 (b,d,f). The cumulative number of individual Ag atoms and small clusters with diameters less than 1 nm (green) and atoms that belong to Ag nanoparticles with diameters above 1 nm (blue) are shown in (a) and (b). The cumulative numbers of atoms that belong to nanoparticles of different sizes (above 1 nm) are shown in (c) and (d). The number of atoms in nanoparticles of different sizes (above 1 nm) are also shown as histograms for 1, 2 and 3 ns in (e) and (f). The analysis is applied only to the part of the plume above the molten layer, i.e., to the regions 3 and 4 in Figs. 3.5 and 3.6.

While the simulation performed at a fluence of 700 J/m^2 has stronger plume expansion, the subsequent vapor and clusters growth above the molten layer is substantially slower than that at 400 J/m^2. This observation can be related to the additional contribution to the rapid expansion of the mixing region coming in the lower fluence simulation from the downward motion and redeposition of the liquid layer. The wider mixing region facilitates the evaporation of the liquid layer that produces more than twice higher total number of Ag atoms as compared to the simulation performed at 700 J/m^2, Figs. 3.7a and 3.7b. At the same time, the mixing region generated at a fluence of 700 J/m^2 has a pressure of 0.064 GPa at the end of simulation, as compared 0.025 GPa in the same region in the lower fluence simulation. The difference in the values of pressure indicate that further expansion is likely to be more extensive at the higher fluence, which may lead to a higher final nanoparticle yield.

One important aspect of the nanoparticle generation mechanism predicted in the simulations is the rapid quenching of the metal vapor ejected into the water-metal mixing region. While the interaction between the hot metal vapor and water brings the water to the supercritical state, the same interaction cools the metal vapor and nanoparticles down to the temperature that can be sufficiently low to cause solidification of the nanoparticles. As one can observe from Figs. 3.3 and 3.4, the nanoparticles in the top part of the mixing region are colored blue, indicating the low level of potential energy. To clearly show the temperature of the nanoparticles generated by the end of the simulations, the final snapshots colored by local temperature are provided in Fig. 3.8. While the nanoparticles located closer to the superheated liquid layer are green and have temperatures that are about twice the melting temperature of Ag, marked as T_m in the temperature scale, the small blue nanoparticles in the top part of the mixing region are already below T_m and can be expected to be solid. Indeed, the enlarged views of two representative "blue" nanoparticles shown in Fig. 3.8 clearly demonstrate their (poly)crystalline structure. While the observation of the crystalline structure of Ag nanoparticles generated in the simulations is consistent with experimental results reported for PLAL of Ag targets,[153] the surprising prediction of the simulations is that the cooling of the metal vapor injected into the mixing region from the phase explosion temperature generated in the Ag film by the laser excitation down to the melting temperature of Ag takes less than 3 ns, resulting in the effective cooling rate on the order of 10^{12} K/s and producing solid nanoparticles at the very early stage of the ablation process. The ultrafast growth and quenching rates may result in the generation of nanoparticles with highly nonequilibrium metastable structures and phases.

The second mechanism of the nanoparticle generation that can be inferred from the simulation results is the disintegration of the superheated liquid layer itself, which can directly yield much larger, on the order of tens of nanometers, nanoparticles. While the timescale of the complete breakup of the liquid layer exceeds the timescales accessible to MD simulations, the first manifestation of this nanoparticle generation mechanism can be observed in the simulation snapshots, Figs. 3.3 and 3.4, where the morphology of the "terrain" region at the vapor-plume interface is gradually evolving towards the formation of individual large droplets. Indeed, the first droplet produced through this mechanism can already be observed in the last snapshot shown in Fig. 3.4. Although the temperature of this droplet, that consist of 354,455 atoms and has diameter of 22.8 nm, is more than twice the melting temperature of Ag at the time of its separation from the liquid layer (see Fig. 3.8), the rapid cooling in the mixing region can be expected to result in its eventual freezing into a solid nanoparticle.

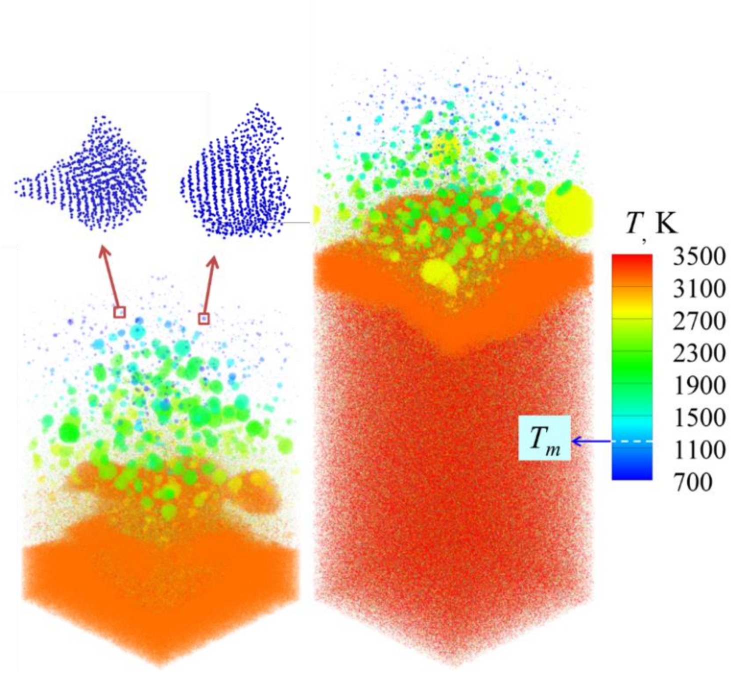

Figure 3.8. The snapshots of final configurations obtained for 3 ns after the laser pulse in simulations performed at absorbed fluences of 400 J/m^2 (left) and 700 J/m^2 (right). The atoms in the snapshots are colored by local temperature. The enlarged view of atomic structure of two crystalline nanoparticles located in the upper part of the mixing region (region 4 in Fig. 3.5) is shown in the left panel.

The decomposition of the thin superheated liquid layer into individual droplets may, in principle, be driven by the inherent thin film instability at high temperatures,[64, 88, 117] although the results of the simulations suggest that the interaction of the metal layer with the compressed supercritical water is playing the dominant role in defining the morphology to the "terrain" region and, eventually, the characteristic sizes of nanoparticles generated by the film breakup. The appearance of roughness at the interface between the metal layer and the supercritical water can be observed as early as 200 ps after the laser pulse, Figs. 3.3 and 3.4, and the interfacial morphology evolve rapidly as the metal layer is decelerated and, in the lower fluence simulation, pushed back to the substrate by the expansion of the supercritical water region during the first nanosecond of the ablation process. The development of the complex morphology of the interface between the higher density metal layer decelerated by the pressure from the lighter supercritical water (see Figs. 3.5a and 3.6a) can be attributed to the Rayleigh-Taylor instability of the interface between the accelerated fluid layers.[154-156] The morphological features of the interfacial region are finer in the higher fluence simulation (Fig. 3.4) as compared to the ones at the lower fluence (Fig. 3.3), which is related to more active initial mixing and lower viscosity at higher temperature leading to the higher spatial frequency of the interfacial features. Although the quantitative aspects of the nanoparticle generation through the breakup of a laser-generated superheated liquid induced by the Rayleigh-Taylor instability are still being investigated and will be reported elsewhere, this mechanism appears to be general (observed in the simulation of PLAL of bulk targets) and can be utilized for controlled nanoparticle generation and surface nanostructuring by laser ablation in liquid environment.

The computational prediction of the existence of two distinct mechanisms of nanoparticle formation in PLAL is consistent with experimental observations of bimodal nanoparticle size distributions [7-8] and can be related to the results of recent time-resolved SAXS probing of the cavitation bubble dynamics,[44-47] where two groups of nanoparticles with different characteristic sizes have been observed to emerge at different stages of the bubble evolution. The experimental observation of "primary particles," with the size distribution centered around 8-10 nm, can be related to the nanoparticles generated by the rapid condensation and growth in the expanding mixing region in the simulations. Indeed, the presence of the primary particles at the earliest stage of the cavitation bubble expansion, the higher population of the nanoparticles in the lower part of the bubble and the decrease of the nanoparticle abundance and size with increasing distance from irradiated surface are the experimental observations that are consistent with the nucleation and growth pathway of the nanoparticle formation predicted in the simulations.

The second group of nanoparticles, the so-called "secondary particles" with the size distribution of around 30-50 nm, are observed to appear at a later stage of the cavitation bubble evolution and are speculated to form through agglomeration of the primary particles during the bubble collapse.[44-47] While the MD simulations cannot provide information on the whole cavitation bubble dynamics, they offer an alternative plausible explanation of the origin of the secondary particles. The simulations predict that the secondary particles may appear through the formation of a dense layer of superheated liquid metal at the front of the ablation plume confined by the water environment, followed by disintegration of the molten layer facilitated by its interaction with the compressed supercritical water. The collapse of the bubble may simply disperse the large nanoparticles already formed through the molten metal layer disintegration, or it can actually cause the breakdown of the molten layer if it survives until this late stage of the cavitation bubble dynamics.

While the simulations reported in this chapter are performed for thin films, the discussion of the mechanisms of the nanoparticle generation revealed in the simulations is fully applicable to the ablation of bulk targets in a liquid environment. The first simulations performed for bulk targets, to be reported elsewhere, show that the dynamics of the ablation plume generated through the explosive disintegration of a top layer of the irradiated bulk target is very similar to the one discussed above for the thin film ablation. The confinement of the ablation plume by the water environment results in the formation of a dense layer of superheated metal at the water-plume interface, followed by the appearance and expansion of a metal - supercritical water mixing region and generation of two populations of nanoparticles through the condensation in the mixing region and disintegration of the liquid layer.

The results are also not specific for the femtosecond laser pulses, as the increase of the lattice temperature in the film is controlled by the timescale of the electron-phonon equilibration, $\tau_{e\text{-}ph} \sim$ 8 ps, defined as the time constant of the exponential decay of the energy of the excited electrons.[101] This time is comparable to the time needed for the mechanical relaxation (expansion) of the film, $\tau_m \sim L_f/C_s \approx 5.5$ ps, where $L_f = 20$ nm is the film thickness and $C_s \approx 3650$ m/s is the speed of sound in Ag. As a result, the heating takes place under conditions of partial stress confinement,[71, 82, 88,

[102] leading to a stronger initial expansion of the material undergoing the phase explosion.[71, 157] Any pulse duration that is shorter than $\tau_{e\text{-}ph}$ would produce results that very similar to the ones reported in this chapter. The increase of the pulse duration above $\tau_{e\text{-}ph}$ would allow for the film expansion during the laser heating, thus diminishing the contribution of photomechanical effects to the ejection of the plume and generation of nanoparticles.

3.4. Summary

An advanced computational model combining an atomistic description of laser interactions with metal targets, a coarse-grained representation of liquid (parameterized for water), and acoustic impedance matching boundary conditions designed for representation of a transparent substrate (parameterized for silica glass) and non-reflecting propagation of laser-induced pressure wave in the liquid environment is developed and applied for investigation of the mechanisms of nanoparticle generation in PLAL. First atomistic simulations of laser ablation of thin Ag films in water environment have provided detailed microscopic information on the unique characteristics of laser ablation in liquids and revealed two distinct mechanisms of nanoparticle formation in PLAL.

In contrast to the laser ablation in vacuum or a background gas, where nanoparticles can be directly produced via explosive decomposition of the superheated target material into a mixture of vapor, atomic clusters and droplets, the interaction of the ablation plume with liquid environment leads to a rapid deceleration of the ejected material and the formation of a dense superheated molten layer at the water-plume interface. The water in contact with the hot metal layer is brought to the supercritical state and transforms into expanding low density metal-water mixing region that serves as a precursor for the formation of a cavitation bubble at a later time. The conditions in the mixing region facilitate condensation of metal atoms into clusters and rapid growth of the atomic clusters into nanoparticles with maximum sizes barely exceeding 10 nm. The interaction of the growing nanoparticles with supercritical water provides a highly efficient cooling mechanism that produces an effective cooling rate for the metal vapor and clusters of up to 10^{12} K/s and results in solidification of nanoparticles located in the upper part of the mixing region on the timescale of nanoseconds.

In addition to the nanoparticles produced by the rapid nucleation and growth in the water-metal mixing region, the second mechanism of the nanoparticle generation identified in the simulations is the breakup of the layer of superheated molten metal accumulated at the plume-water interface. The preliminary analysis of the initial stage of the layer decomposition suggests that the emergence of complex morphological features in the interfacial region can be attributed to the Rayleigh-Taylor instability of the interface between the higher density metal layer decelerated by the pressure from the lighter supercritical water. The nanoparticles produced through the disintegration of the superheated liquid layer are larger than the ones produced through the condensation in the mixing region and have characteristic sized on the order of tens of nanometers.

The computational prediction of the two mechanisms of the nanoparticle generation yielding nanoparticles with different characteristic sizes is consistent with experimental observations of the bimodal nanoparticle size distributions produced by PLAL and can be related to the results of recent time-resolved SAXS probing of the cavitation bubble dynamics, where the appearance of two different nanoparticle populations is detected at different stages of the bubble evolution.

4. Effect of water environment on short pulse laser-materials interaction for bulk target in different irradiation regimes

4.1. Introduction

The investigation of laser-material interactions in water is extended to bulk metal targets in this chapter. The effects of water environment on three well-studied laser irradiation regimes corresponding to melting and solidification (chapter 4.3.1), photomechanical spallation (chapter 4.3.2), and phase explosion (chapter 4.3.3 and 4.3.4) of a surface region of the irradiated target in vacuum are discussed. The implications of the interaction of ablation plume with liquid environment on the formation of nanoparticles and morphology of resolidified surface are analyzed based on the simulation results.

4.2. Computational setup

The simulation reported in this chapter is performed with a hybrid computational model combining a coarse-grained representation of liquid, a fully atomistic description of laser interaction with metal targets, and acoustic impedance matching boundary conditions, designed to mimic the non-reflecting propagation of the laser-induced pressure waves through the boundaries of the computational domain. A complete description of the computational model tailored for simulation of pulse laser interaction with Ag in water environment is provided in Chapter 1.2, and below only parameters relevant to the computational setup of the simulation reported in this chapter are described.

The simulations are performed for a Ag bulk target covered by water, and the initial target has fcc crystal structure and (001) orientation of the free surface. The periodic boundary conditions are applied in the lateral directions, parallel to the surface of the target. The dimensions of the computational system in the lateral directions are 98.7 nm × 98.7 nm. The depth of the surface part of the Ag target represented with atomistic resolution, L_z in Fig. 1.3, and the corresponding number of Ag atoms are different in simulations performed at different absorbed laser fluences, namely, L_z = 200 nm (112 million Ag atoms) at F_{abs} = 85 mJ/cm^2 in chapter 4.3.1, L_z = 200 nm (112 million Ag atoms) at F_{abs} = 150 mJ/cm^2 in chapter 4.3.2, and L_z = 400 nm (224 million Ag atoms) at F_{abs} = 400 mJ/cm^2 in chapter 4.3.3. The thickness of the part of the water overlayer represented by the coarse-grained MD model is the same in the three simulations, L_{env} in Fig. 1.3, as 300 nm, which corresponds to 34 million coarse-grained particles. To match the experimental conditions, the dynamic acoustic impedance matching boundary conditions imposed at the top and bottom of the computational domain are designed to mimic non-reflecting propagation of the laser-induced pressure waves through the boundaries of the computational domain[101, 150]. These boundary conditions implicitly simulate a sufficiently thick liquid overlayer and metal target, so that reflections of the laser-induced pressure waves from the free surface of a thick liquid overlayer and the opposite side of the metal target do not play any significant role in the generation of nanoparticles and modification of surface structure.

The size of the TTM part of the system, L_{TTM} in Figure 1, is 2.5 μm, 3 μm, and 2.8 μm in the simulations discussed in chapters 4.3.1, 4.3.2, and 4.3.3, respectively. The thicknesses of the parts of the system represented with atomic and molecular resolutions, L_z and L_{env}, are chosen based on the results of back-of-the-envelope estimations of zones affected by the laser-induced phase transformations, followed by small-scale test simulations performed for systems with lateral dimensions of 5 nm × 5 nm. In order to highlight the effect of the liquid environment on the laser-induced processes, the simulations described in chapters 4.3.1, 4.3.2 and 4.3.3 are also performed in vacuum, *i.e.*, without the liquid overlayer but with otherwise identical computational setups and irradiation conditions.

The laser irradiation of the target is represented in the model through a source term added to the TTM equation for the electron temperature.[72] The source term describes excitation of the conduction band electrons by a laser pulse with a Gaussian temporal profile and reproduces the exponential attenuation of laser intensity with the depth under the surface. The optical absorption depth, 12 nm at laser wavelength of 800 nm[144], combined with the effective depth of the "ballistic" energy transport, estimated to be about 56 nm for Ag[101-102] is used in the source term of the TTM equation.[72, 151] The laser pulse durations, τ_L, defined as full width at half maximum of the Gaussian profile, is 100 fs in all reported simulations. The reflectivity of the surface is not defined in the model since the absorbed laser fluence, F_{abs}, rather than the incident fluence is used in the presentation of the simulation results.

All systems are equilibrated at 300 K for 300 ps before applying laser irradiation. The simulations are performed with a computationally-efficient parallel code implementing the combined TTM-MD – coarse-grained MD model, with a three-dimensional treatment of the electronic heat conduction in the TTM-MD part of the computational system.

The implementation of the model used in this work does not account for ionization of the ejected plume, as simple estimations based on the Saha-Eggert equation[158-159] suggest that the degree of ionization in the ablation plume is negligible under irradiation conditions applied in the simulations reported in this chapter. As a result, the nanoparticle formation through nucleation around ion seeds in "misty plasma" considered for high fluence nanosecond PLAL**Error! Bookmark not defined.**[51, 160] is not relevant to the milder irradiation conditions and short pulses considered in the present work.

4.3. Results and discussion

4.3.1. Effect of water on laser-induced melting and solidification

The simulation of laser-induced melting and resolidification of Ag target in vacuum, performed at τ_p = 100 fs and F_{abs} = 85 mJ/cm^2, has already been described in ref. [102], and only a brief summary of the results is provided here. The snapshots from the simulation are shown in Fig. 4.1a, where the atoms are colored by their potential energy, so that the melted and solid parts of the target can be easily distinguished. Laser excitation of the conduction band electrons followed by the rapid energy transfer from the hot electrons to the lattice through electron-phonon coupling leads to the superheating and melting of an about 70-nm-deep surface region of the target within the first tens of picoseconds after the laser pulse. Due to the fast heat conduction to the bulk of the target, the temperature of the liquid-solid interface drops below the equilibrium melting temperature of the EAM Ag material, T_m = 1139 K, and the melting gives way to resolidification by ~75 ps.

The melting and resolidification are occurring simultaneously with the generation and dynamic relaxation of laser-induced stresses that are illustrated in Fig. 4.2a. The rapid temperature increase in the surface region of the target takes place under conditions of stress confinement[71, 91, 157, 161] and results in a build-up of strong compressive stresses, as can be seen from Fig. 4.2a. The relaxation of the compressive stresses in the presence of the free surface of the target results in the generation of an unloading tensile wave marked by dashed arrows in Fig. 4.2a. The tensile stresses, shown by blue color in Fig. 4.2, are sufficiently strong to induce cavitation in the lower part of the melted region, with the appearance of small cavities already apparent in the snapshot shown for 100 ps in Fig. 4.1a.

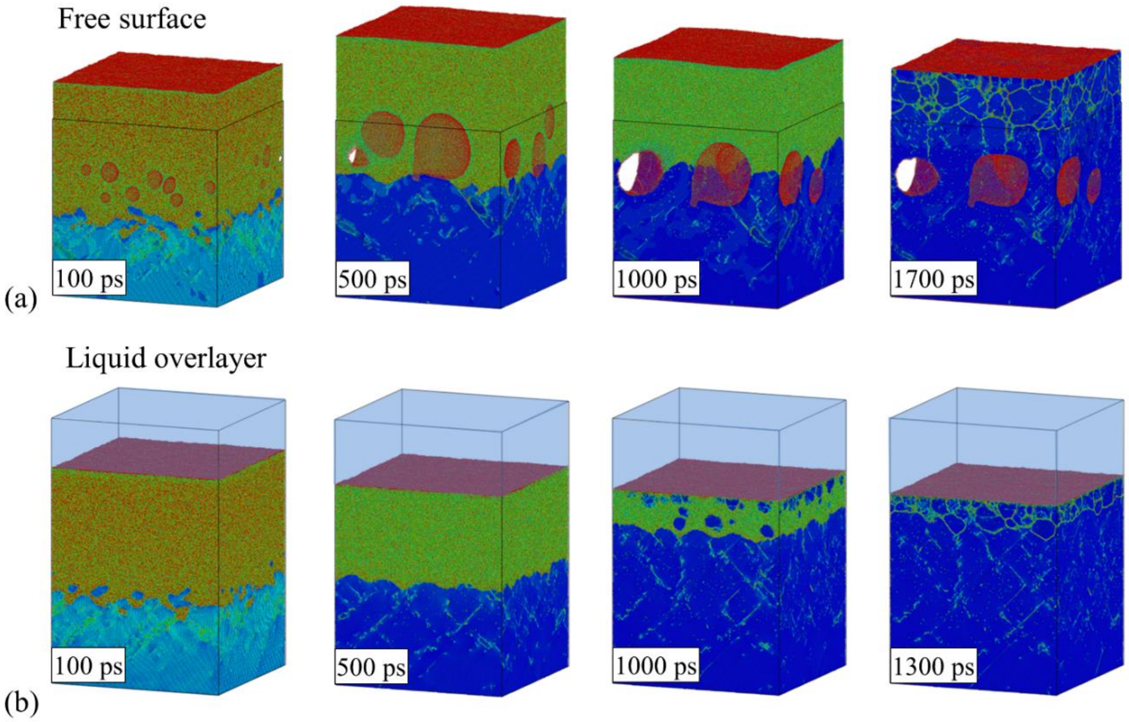

Figure 4.1. Snapshots of atomic configurations generated in TTM-MD simulations of laser irradiation of Ag targets in vacuum (a), and in water environment (b) with pulse duration of 100 fs and absorbed fluence of 85 mJ/cm^2. Only the regions that correspond to the top 100 nm parts of the targets before the irradiation are shown in the snapshots. The box in (a) outlines the initial position of the target before the irradiation, while boxes in (b) also includes parts of the overlayers extending up to 50 nm from the original surface. The atoms are colored by their potential energies, with the scale from −2.84 eV (blue) to −2.64 eV (red) chosen to ensure that the crystalline parts of the targets are blue, the melted regions are green, and the free surfaces are red. Crystal defects, such as vacancies, dislocations, stacking faults, and grain boundaries, can also be distinguished as regions with elevated potential energy. To reduce thermal noise in potential energies, the atomic configurations are quenched for 2 ps using the velocity-dampening technique.

The cavities grow, coalesce, and are eventually trapped by the solidification front advancing from the crystalline part of the target. The movement of the front of the epitaxial solidification can be followed in Fig. 4.3a, where the location of the front is shown by a black line. The presence of voids impedes the solidification front propagation, extends the time the top surface layer of the target remains in the molten state, and contributes to the generation of increasingly deep undercooling in the melted surface region. At about 1300 ps, when the surface temperature drops down to ~0.69 T_m, a massive nucleation of small crystallites is initiated throughout the deeply undercooled liquid region and results in the formation, within the next 400 ps, of a nanocrystalline layer with ultrafine grains featuring random crystallographic orientation and a high density of stacking faults and twin boundaries.[102] Similar to the solidification front propagation, the homogeneous nucleation of new crystallites leads to the release of the latent heat of melting and is reflected in a noticeable temperature increase in the surface region of the target, Fig. 4.3a.

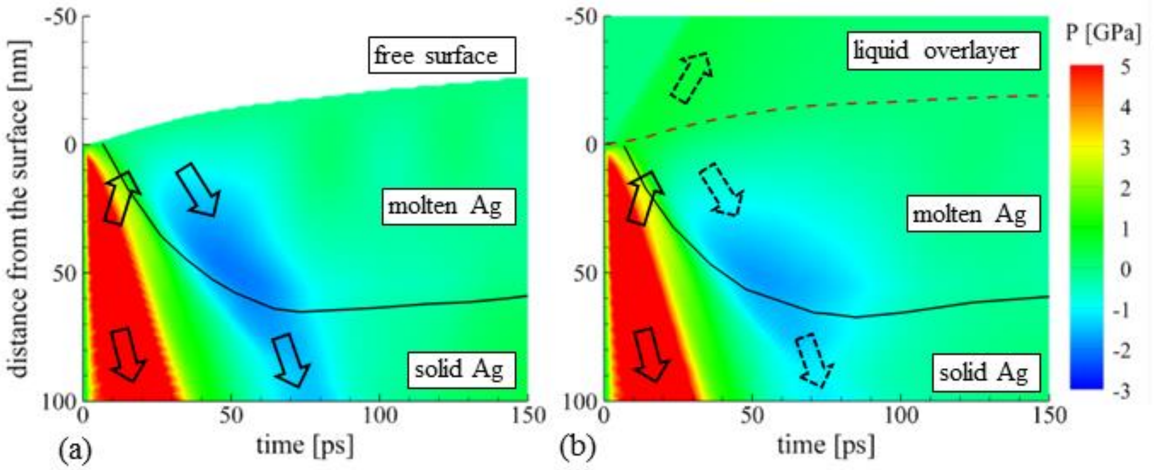

Figure 4.2. Contour plots of the spatial and time evolution of pressure in TTM-MD simulations of laser irradiation of Ag targets in vacuum (a), and in water environment (b). The targets are irradiated by 100 fs laser pulses at 85 mJ/cm^2. The laser pulse is directed along the vertical axis from the top of the contour plots. The solid black curves separate melted and solid parts of the Ag targets. The dashed red curve in (b) shows the position of the Ag-overlayer interface. The arrows schematically show the directions of the propagation of laser-induced pressure waves. The compressive waves, shown by the solid arrows, are generated by the fast laser heating of the surface regions of the targets and can partially propagate into the overlayers in (b), thus decreasing the amplitude of the unloading tensile waves shown by dashed arrows. The snapshots from the simulations are shown in Fig. 4.1.

The results of the simulations performed for targets with free surfaces suggest that it is difficult to expect generation of a nanocrystalline surface layer on a (001) Ag target without the concurrent formation of a sub-surface porous region that corresponds to an incomplete spallation conditions. This leads to the question on the possibility of using a liquid overlayer that could suppress the generation of sub-surface voids, contribute to the cooling of the metal target, and facilitate the surface nanocrystallization.

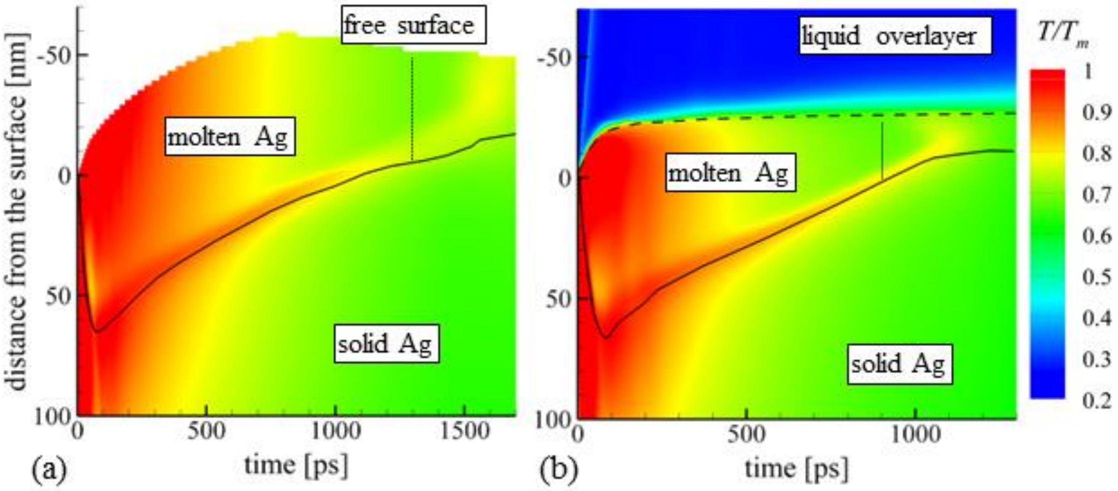

Figure 4.3. Contour plots of the long-term spatial and time evolution of temperature in TTM-MD simulations of laser irradiation of Ag targets in vacuum (a), and in water environment (b). The targets are irradiated by 100 fs laser pulses at 85 mJ/cm^2. The laser pulse is directed along the vertical axis from the top of the contour plots. The temperature scale is normalized by the melting temperature of EAM Ag, T_m. The maximum temperature reached in the Ag target is 1.60 T_m in (a), and 1.63 T_m in (b). The solid curves separate melted and solid parts of the Ag targets. The dashed curve in (b) show the position of the Ag-overlayer interface. The vertical dotted lines in (a) and (b) mark the times when the nucleation of the first crystallites is detected in the undercooled surface regions of the Ag targets. The snapshots from the simulations are shown in Fig. 4.1.

The large-scale simulation of laser interaction with a Ag target in liquid environment is performed with the same irradiation conditions as the first simulation in vacuum discussed above, where the generation of a nanocrystalline layer covering a porous sub-surface layer (Fig. 4.1a) is observed. The snapshots from the simulation are presented in Fig. 4.1b, while the pressure and temperature contour plots are shown in Figs. 4.2b and 4.3b, respectively. Two notable effects, apparent from the visual inspection of the snapshots, are (1) the absence of the sub-surface voids in the molten part of the target and (2) the onset of the nucleation of new crystallites near the surface of the target at the final stage of the solidification process. There two effects are discussed next.

The absence of the sub-surface voids can be explained based on the evolution of the laser-induced pressure illustrated in Fig. 4.2b. The generation of the initial compressive pressure is defined by the electron-phonon equilibration and rapid heating of the surface region occurring under conditions of the thermal and stress confinement,[71, 91, 157, 161] and is largely unaffected by the presence of the liquid environment. This is reflected in almost identical compressive parts of the pressure contour plots in Fig. 4.2a and 4.2b. The formation of the unloading tensile component of the pressure wave, however, is significantly affected by the liquid environment. Since the acoustic impedance of water is much lower than that of Ag, the relaxation of the compressive pressure results in the generation of both a compressive wave emitted into the water and a weaker, as compared to the simulation with free surface (Fig. 4.2a), tensile wave propagating into the bulk of the Ag target, as schematically shown by solid and dashed arrows in Fig. 4.2b. The reduced amplitude of the unloading tensile wave is not sufficient for the initiation of cavitation, which explains the absence of voids in the melted part of the target in Fig. 4.1b. Note that the suppression of the nucleation of subsurface voids has also been observed in earlier MD simulations of short pulse laser interactions with Ag targets performed under stronger spatial confinement by a solid silica overlayer,[101] while the reduction in the number of spalled layers was reported in hydrodynamic modeling of laser ablation of Al in water.[62]

The suppression of the void nucleation has important consequences for the kinetics of resolidification of the melted region. While the melting time and the maximum melting depth are very similar in the simulations performed in vacuum and in water environment, as can be seen from the similarity of the black curves showing the location of the liquid-crystal interface in Fig. 4.2a and 4.2b, the same black curves shown for a longer time in Fig. 4.3a and 4.3b clearly demonstrate the diverging resolidification behavior. The appearance of sub-surface voids not only increases the effective path the solidification front has to cover before it reaches the surface but also decreases the velocity of solidification front[102] when it passes the region with voids. In the simulation with water overlayer, Fig. 4.3b, after the initial rapid apparent advancement due to the solidification of a liquid-crystalline mixture formed by the end of the melting process, the velocity of the resolidification front reaches a steady level of ~63 m/s. In the case of the free surface, Fig. 4.3a, the velocity of the solidification front drops below 45 m/s when the front passes through the region with voids.

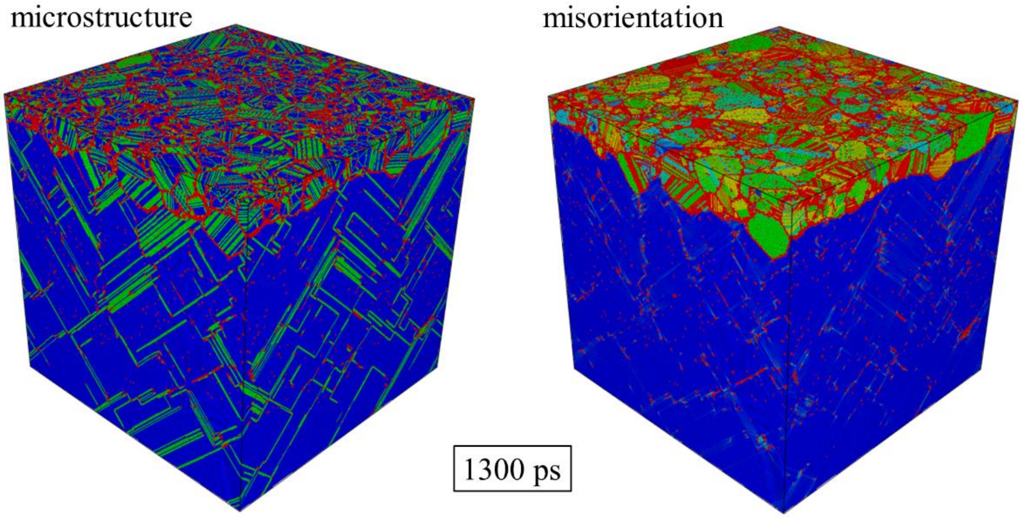

Figure 4.4. Snapshots of atomic configurations generated at the end of resolidification process in TTM-MD simulations of laser irradiation of Ag targets in water environment with pulse duration of 100 fs and absorbed fluence of 85 mJ/cm^2. The top 1 nm layers of the targets are blanked to expose the underlying defect structures. In the upper panels, the atoms are colored by their local structural environment, so that the fcc and hcp atoms are blue and green, respectively, and the red atoms have unidentified local crystal structure. With this coloring scheme, the single and double green layers on a blue background correspond to twin boundaries and stacking faults in the fcc structure, respectively. Unidentified atoms belong to grain boundaries, dislocation cores, and point defects. In the lower panels, the atoms are colored by the smallest angle between one of the <111> directions of the original fcc lattice and a <111> direction in the corresponding grain. The blue to red color scale corresponds to misorientation angles ranging from 0° to 30°.

The slowdown of the epitaxial solidification front by the sub-surface voids extends the time the top surface layer of the target remains in the molten state and allows it to reach a deeper undercooling. On the other hand, the reduced effective thermal conductivity of the porous sub-surface region slows down the cooling of the top layer. As a result, it takes about 1.3 ns for the top molten layer to cool down to 0.69 T_m, when and a massive homogeneous nucleation of new crystalline Ag grains is observed, Fig. 4.3a. In the presence of liquid environment, the surface cooling and the solidification front propagation proceed without the impediment from the voids and the rapid nanocrystallization is initiated much earlier, at ~900 ps, Fig. 4.3b. The nucleation and fast growth of multiple crystallites in the undercooled liquid region result in the formation of an about 18-nm-thick nanocrystalline surface layer with grains randomly oriented with respect to the crystallographic orientation of the Ag target. Similar to the targets with free surfaces discussed earlier, the rapid solidification under conditions of strong undercooling produces complex internal structure of individual grains characterized by a high density of stacking faults and twin boundaries, Fig. 4.4.

In addition to the thermal conduction to the bulk of the Ag target, the interaction with water provides an additional pathway for cooling of the Ag surface region. The efficiency of this channel is limited by the rapid superheating of water adjacent to the hot surface of the metal target and the formation of a low-density supercritical water layer with poor thermal conductivity. As a result, the total amount of the thermal energy transferred to the water overlayer by the end of the simulation is only ~2% of the energy deposited by the laser pulse. Nevertheless, this channel of cooling of the metal surface may play an important role defining the microstructure of resolidified surface.

4.3.2. Generation of subsurface voids through partial spallation in water

The simulations discussed in this section are performed for irradiation conditions that correspond to the regime of photomechanical spallation, when the dynamic relaxation of laser-induced stresses results in subsurface cavitation and ejection of molten layers or large droplets from the irradiated target.[71, 91, 157, 161] In particular, for the pulse duration of τ_L = 100 fs, the absorbed fluence applied in the simulations, F_{abs} = 150 mJ/cm^2, is about 50% above the spallation threshold in vacuum.[101-102, 162] The visual picture of the spallation process in vacuum is shown in Fig. 4.5. A large number of small subsurface voids can be seen to appear in the molten part of the target by the time of 100 ps. The voids are generated in a region where the strength of the unloading tensile wave generated due to the interaction of the laser-induced compressive stresses with the free surface of the irradiated target exceeds the limit of the dynamic stability of the metastable liquid against the onset of the cavitation.[67] The growth, coalescence and percolation of the voids result in the formation of complex foamy structure of inter-connected liquid regions connecting the bulk of the target with a ~28-nm-thick top liquid layer moving away from the target with an almost constant velocity of ~530 m/s, Figs. 4.5 and 4.7a. The foamy structure coarsens with time and eventually decomposes into individual droplets on the timescale of nanoseconds. The top liquid layer is expected to lose stability and decompose into larger droplets, estimated to have diameters from hundreds of nanometers to tens of micrometers.[67]

The presence of water environment has a profound effect on the dynamics of the spallation process, as can be seen from snapshots and the density contour plot shown in Fig. 4.6 and 4.7b.

While the multiple voids are still generated in a subsurface region of the target, partial propagation of the laser-induced pressure wave into the water overlayer reduces the strength of the unloading tensile wave and increases the thickness of the molten layer that is not affected by the void nucleation. Moreover, the resistance of the water environment to the outward motion of the surface layer decelerates the layer and, at about 1.35 ns after the laser pulse, reverses the direction of its motion back towards the target. The deceleration of the top layer under the water confinement makes it possible for the material that forms the expanding foamy structure in vacuum, Fig. 4.5, to join the top layer, resulting in a substantial thickening of the layer, Figs. 4.6 and 4.7b. This general picture of the spallation confined by a liquid environment is consistent with the results of earlier one-dimensional hydrodynamic simulations,[62-63] where the deceleration of the top spalled layer followed by merging of several spalled layers was predicted for femtosecond laser irradiation of Au and Al targets in water.

The resistance of the water environment to the outward motion of the top molten layer not only slows down the layer but also prevents its complete separation from the target. The conductive cooling through the remaining liquid bridge connecting the top layer to the bulk of the target, combined with an additional cooling due to the interaction with the water environment, brings the average temperature of the liquid layer down to the melting point of the EAM Ag, T_m = 1139 K,[100] by the time of 740 ps, and undercools the layer down to ~0.85 T_m by the end of the simulation at 1690 ps. The cooling of the molten layer is illustrated by Fig. 4.8, where the average temperature of the top 10-nm-thick part of the layer is plotted. To save computational time, the simulation was not continued beyond 1690 ps. Nevertheless, one can estimate, based on the cooling rate, the solidification front advancement, and the downward velocity of the top liquid layer, that the layer would solidify much before the redisposition to the substrate. The solidification is expected to mostly proceed through the epitaxial regrowth of the single-crystal target through the bridge into the top layer, with a possible additional contribution from the homogeneous nucleation of new crystallites in the strongly undercooled liquid layer. At the end of the simulation, the front of the epitaxial solidification is already passing through the bridge, as can be seen from the last snapshot shown for 1690 ps in Fig. 4.6 as well as from the contour plot in Fig. 4.7b, where the advancement of the solidification front is shown by the blue line. As has been demonstrated in earlier studies,[89, 102] a massive homogeneous nucleation of new crystallites can be expected when the temperature the EAM Ag material drops down to ~0.69 T_m. Using an extrapolation of the cooling curve in Fig. 4.8, one can estimate that this level of undercooling should be reached by ~4 ns, which sets the upper limit for the time needed for the complete resolidification of the target.

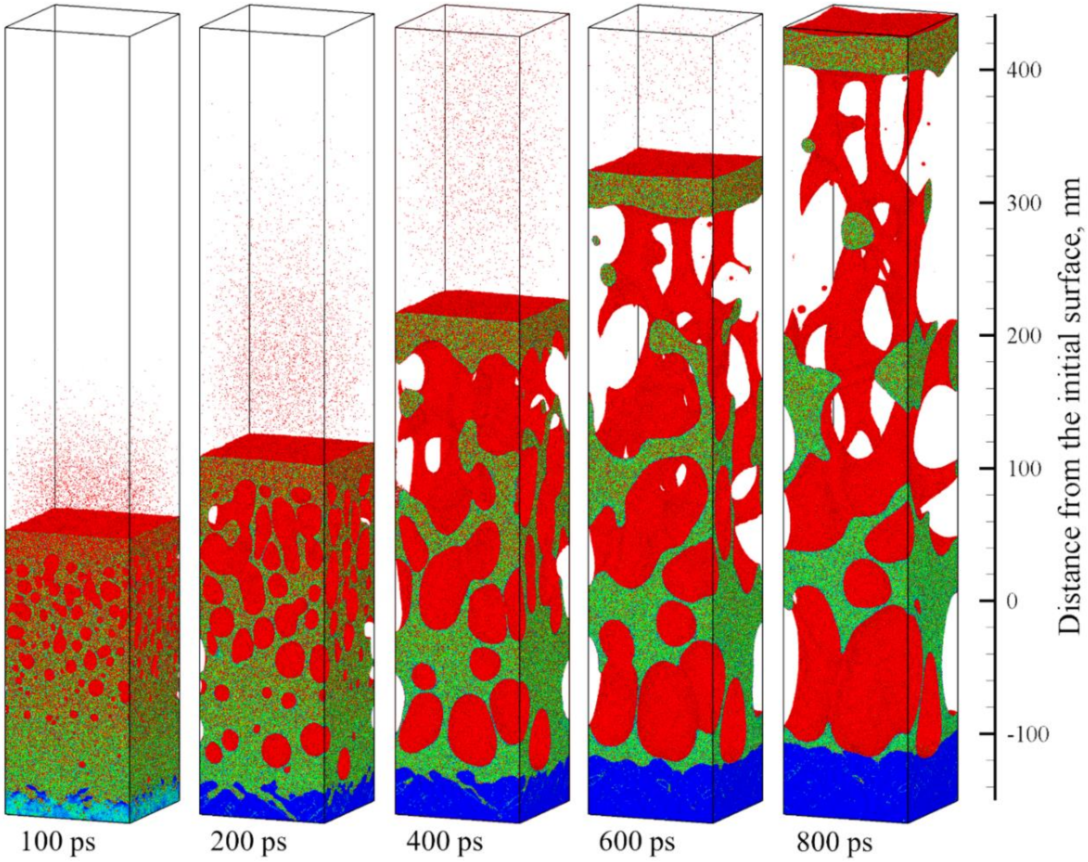

Figure 4.5. Snapshots of atomic configurations predicted in a simulation of laser spallation of a bulk Ag target irradiated *in vacuum* by a 100 fs laser pulse at an absorbed fluence of 150 mJ/cm^2. Only parts of the computational system from -150 to 443 nm with respect to the initial surface of the target are shown in the snapshots. The atoms are colored according to their potential energies, with the scale chosen so that the crystalline part of the target is blue, liquid Ag is green, and the top surface, internal surfaces of the voids, and vapor-phase Ag atoms are red.

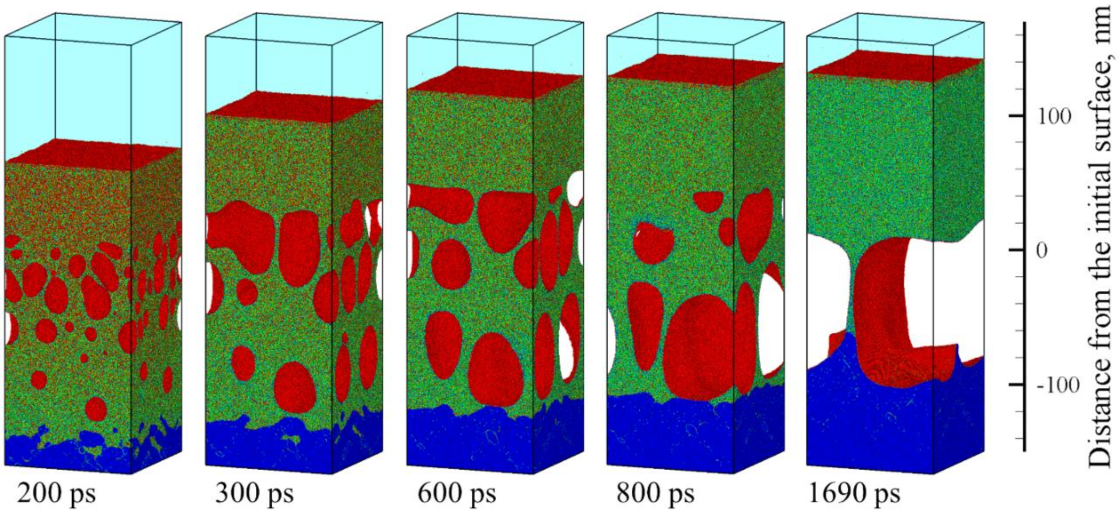

Figure 4.6. Snapshots of atomic configurations predicted in a simulation of an incomplete laser spallation of a bulk silver target irradiated *in water* by a 100 fs laser pulse at an absorbed fluence of 150 mJ/cm^2. Only parts of the computational system from -150 to 170 nm with respect to the initial surface of the Ag target are shown in the snapshots. The atoms are colored according to their potential energies: from blue for the crystalline part of the target, to green for liquid Ag, and to red for internal surfaces of the voids and water-Ag interface. The molecules representing water environment are blanked and the presence of water is illustrated schematically by a light blue region above the Ag target.

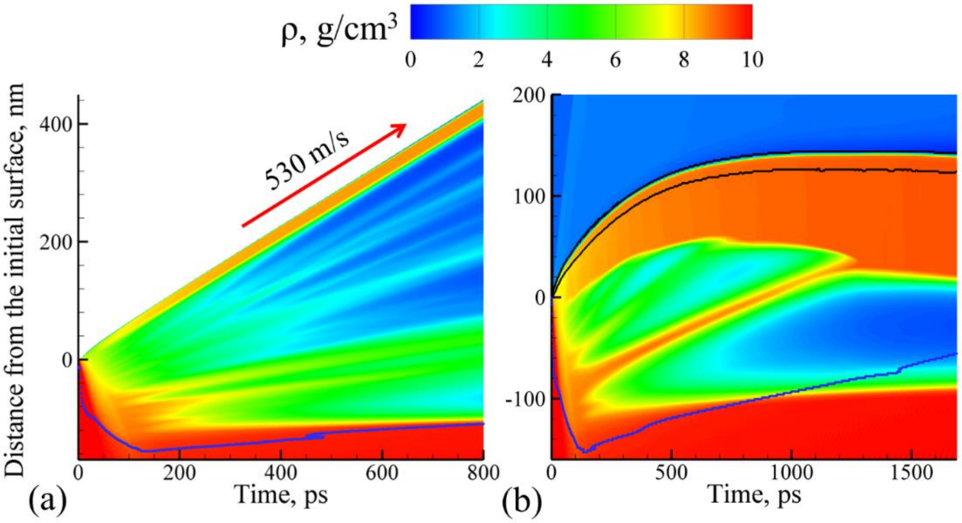

Figure 4.7. Density contour plots predicted in simulations of laser spallation of a bulk Ag target irradiated by a 100 fs laser pulse at an absorbed fluence of 150 mJ/cm^2 in vacuum (**a**) and in water (**b**). The blue line shows the location of the melting and solidification fronts. In (**b**), the two black lines outline the water-Ag mixing region defined as a region where both water molecules and Ag atoms are present. Snapshots from the simulations are shown in Figs. 4.5 and 4.6.

The computational prediction of the formation of large subsurface voids stabilized by the rapid cooling and solidification of the surface region has two important implications. First, the subsurface voids generated by the laser spallation confined by water are many times larger than the ones observed in simulations performed close to the spallation threshold in vacuum,[102] thus suggesting a strong effect of liquid environment on modification of surface morphology and microstructure. Second, the formation of a complex foamy structure of frozen walls and bridges connecting a thin surface layer to the bulk of the target can be expected to have a strong impact on the generation of nanoparticles in multipulse irradiation regime. The latter implication is considered in more detail in Chapter 6, where the results of a simulation of the second pulse irradiation of a target modified by the first pulse are discussed. The implication on the surface morphology is discussed below, in the remainder of this section.

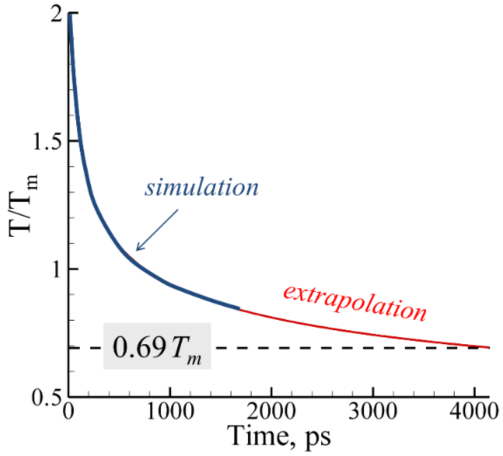

Figure 4.8. The evolution of the average temperature of a 10-nm-thick top surface layer of a Ag target irradiated in water by a 100 fs laser pulse at an absorbed fluence of 150 mJ/cm^2. The part of the curve colored blue is the data obtained in the simulation, while the part colored in red is the extrapolation beyond the time of the simulation. The snapshots and density contour plot from the simulation are shown in Figs. 4.6 and 4.7b, respectively.

While the subsurface cavitation and surface swelling produced by trapping of laser-generated voids by solidification front has been observed in both simulations and experiments performed in vacuum, [102, 163-166] the laser fluences resulting in the formation of subsurface voids cover a rather narrow range in the vicinity of the spallation threshold. For example, a recent atomistic simulation study of surface swelling of Ag surface irradiated in vacuum[102] shows the formation of subsurface voids and corresponding swelling of the surface by ~17 nm at an absorbed laser fluence of 85 mJ/cm^2. An increase of the fluence to 90 mJ/cm^2 leads to the separation/spallation of the layer and generation of frozen surface nanospikes rather than subsurface voids.[89] In contrast, the irradiation of an Ag target in water environment at an almost twice higher laser fluence, 150 mJ/cm^2, does not lead to the complete separation of the top layer. The solidification of the surface region in this case can be expected to produce much larger subsurface voids and the corresponding swelling of the irradiated area, Fig.4.9b.

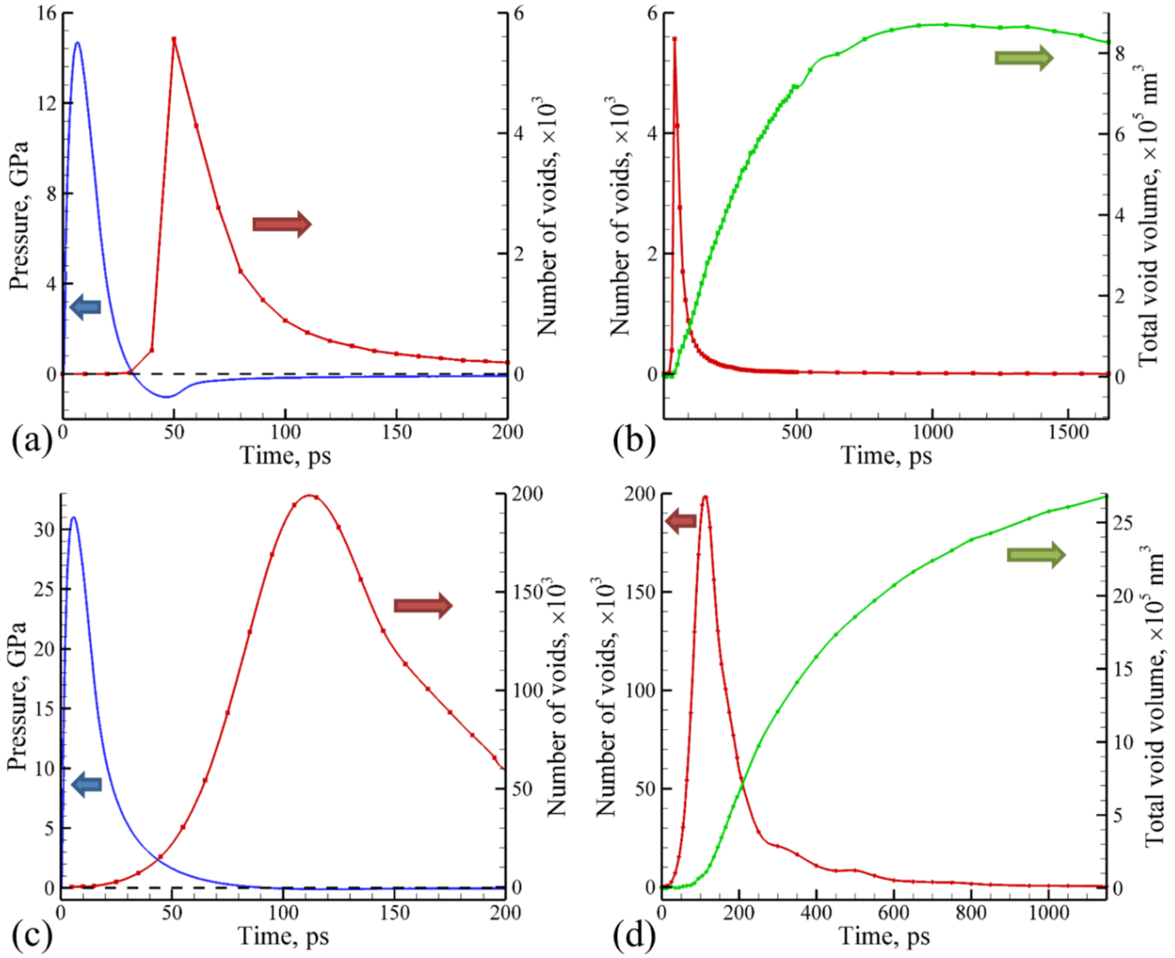

Figure 4.9. The evolution of pressure (blue curves in **a** and **c**), the total number of voids (red curves), and the total volume of all void (green curves in **b** and **d**) predicted in simulations of Ag targets irradiated in water by 100 fs laser pulses at absorbed fluences of 150 mJ/cm^2 (**a**,**b**) and 400 mJ/cm^2 (**c**,**d**). The pressure is averaged over a region between 10 and 60 nm under the initial surface of the Ag target, *i.e.*, the region where the voids are generated. The generation of voids is caused by the tensile stresses (negative pressure in **a**) generated in the subsurface region of the target in the lower fluence simulation (**a**,**b**) and by the internal release of vapor in the superheated molten region of the target (phase explosion) in the higher fluence simulation (**c**,**d**). The snapshots from the lower and higher fluence simulations are shown in Figs. 4.6 and 4.11, respectively; the

corresponding density contour plots are shown in Figs. 4.7b and 4.12b. The arrows show the connection between the curves and the corresponding y-axes.

Similar to the subsurface voids observed in simulations performed in vacuum, the voids and the large surface expansion produced in the simulation illustrated by Fig. 4.7 and 4.7b are driven by the relaxation of laser-induced stresses and can be described as incomplete spallation. This is apparent from Fig. 4.9a and 4.9b, where the evolution of the number and total volume of voids is plotted along with the pressure averaged over the subsurface region where the voids are generated. The sharp increase of the number of subsurface voids coincides with the time when the dynamic relaxation of the compressive stresses produced by the laser energy deposition put the subsurface region into tension, Fig. 4.9a. The number of voids generated in the expanding liquid region quickly drops as the voids coalesce and coarsen, while the total volume of voids continues to increase during the first nanosecond after the laser pulse. The maximum expansion in this simulation is more than twice larger than the one observed in the regime of subsurface void generation in vacuum,[102] and the analysis of the kinetics of the solidification process provided above indicates that much larger subsurface voids can be generated in the presence of liquid environment. Note that under experimental conditions the extent of the surface swelling can be substantially larger than in the simulations performed for a small region within the laser spot. The continuity of the top liquid layer extending beyond the lateral size of the computational cell used in the simulations can further stabilize the liquid layer and extend the range of fluences that correspond to the surface swelling regime.[88, 102]

In general, the computational prediction of the strong effect of the liquid environment on the generation of frozen surface structures is consistent with experimental observations of distinct surface morphologies generated in laser processing in liquids.[167-177] The detailed analysis of the subsurface structures, however, have not been reported for surfaces processed in liquids so far and the prediction of the enhanced generation of larger subsurface voids and surface foaming still awaits experimental confirmation.

4.3.3. Generation of hot metal layer in phase explosion under liquid confinement

The third set of the simulations, illustrated in Figs. 4.10-13, is performed at a higher absorbed laser fluence of 400 mJ/cm^2, which is about twice above the threshold fluence for the transition from spallation to phase explosion regimes of laser ablation in vacuum.[101] The visual picture of the phase explosion in vacuum is shown in Fig. 4.10. In contrast to the spallation regime, where the top part of the irradiated target remains in the liquid phase and is ejected as a thin liquid layer (Fig. 4.5), the material ejection is driven in this case by the rapid release of the vapor in the strongly superheated surface region. The very top layer of the target turns into a mixture of vapor and small atomic clusters freely expanding away from the target, while the internal release of vapor in the lower part of the target leads to the development of a fine cellular structure that rapidly decomposes into a mixture of small liquid droplets and vapor upon the expansion of the ablation plume. In the even deeper part of the plume, below the cellular structure, the propagation of tensile stresses leads to cavitation in the superheated liquid, and formation of large voids, which are almost free of vapor. The expansion of this region leads to the growth and coalescence of the voids and the formation of a foamy structure of interconnected liquid regions extending in the direction of the plume expansion. The clusters and droplets generated in the phase explosion of the top part of the target and the ones emerging from photomechanical cavitation and disintegration of the deeper region have different velocities and contribute to different parts of the ablation plume, thus leading to the segregation of the clusters of different sizes in the expanding plume.**Error! Bookmark not defined.**[88, 166]

The presence of liquid environment drastically alters the dynamics of the formation and expansion of the ablation plume generated in the phase explosion irradiation regime, as can be seen from the simulation snapshots and the density contour plot shown in Figs. 4.11 and 12b, respectively. The superheated molten metal that, in vacuum, undergoes an explosive decomposition into small droplets and vapor, is now confined by water and is collected into a dense hot layer that pushes the water away from the target. The temperature and pressure profiles, shown in Fig. 4.12c and 4.12d, indicate that the dense layer is initially brought into the supercritical state. The layer grows as the porous subsurface region of the Ag target expands, Fig. 4.11, and more melted and vapor phase Ag join the layer. The colder molten Ag joining the top layer from the bottom are largely responsible for the rapid decrease of the average temperature of the layer that can be seen from Fig. 4.12c.

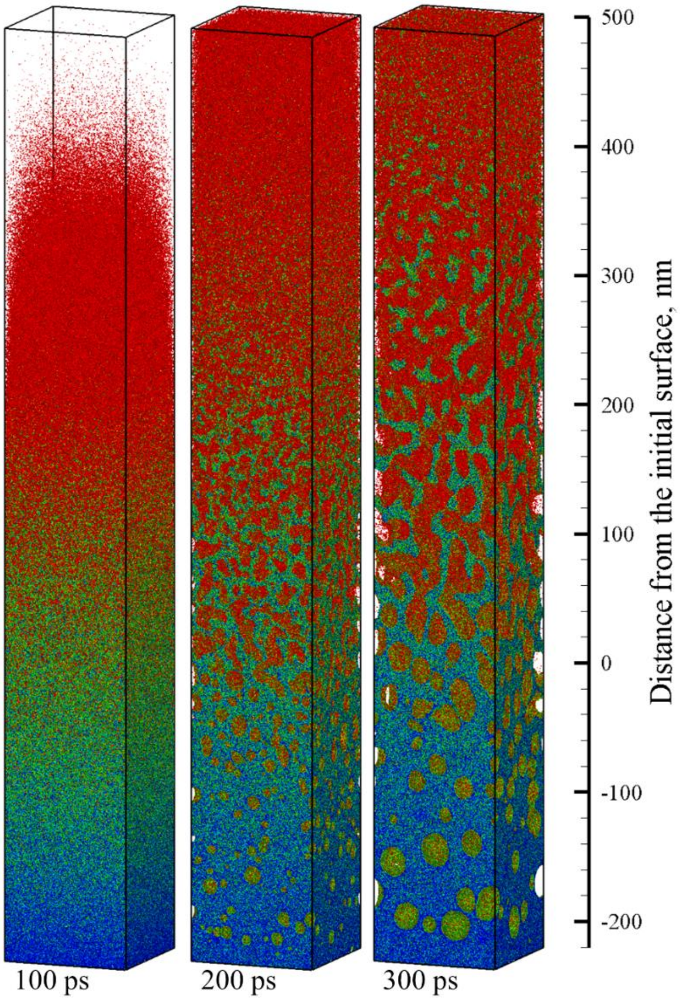

Figure 4.10. Snapshots of atomic configurations predicted in a simulation of a bulk Ag target irradiated *in vacuum* by a 100 fs laser pulse at an absorbed fluence of 400 mJ/cm^2. The irradiation conditions correspond to the regime of phase explosion. Only parts of the computational system from -220 to 500 nm with respect to the initial surface of the target are shown in the snapshots. The atoms are colored according to their potential energies, from blue for molten Ag to red for vapor-phase Ag atoms.

Note that despite the visual similarity of the subsurface void evolution in Figs. 4.6 and 4.11, the main driving forces behind the void generation in the two simulations are different, as can be clearly seen from Fig. 4.9a and 4.9c. In the spallation regime, at the absorbed fluence of 150 mJ/cm^2, the sharp increase of the number of subsurface voids coincides with the time when the tensile stress, depicted by a blue line in Fig. 4.9a, is generated in the corresponding region of the target. At the higher fluence of 400 mJ/cm^2, the superheated top layer confined by the water environment remains at positive pressure during the time when the sharp increase in the number of voids is observed, Fig. 4.9c. This suggests that, similarly to the simulation in vacuum discussed above and illustrated by Figs. 4.10 and 4.12a, the phase decomposition in the top part of the Ag target is mainly driven by the release of vapor and can be described as the explosive homogeneous boiling.[106-108] In contrast to the free expansion of the ablation plume in vacuum, however, the ejected material now accumulates into a hot layer at the interface with the water environment and exerts an outward force pushing the water away from the target, as shown in Figs. 4.11 and 4.12b-d.

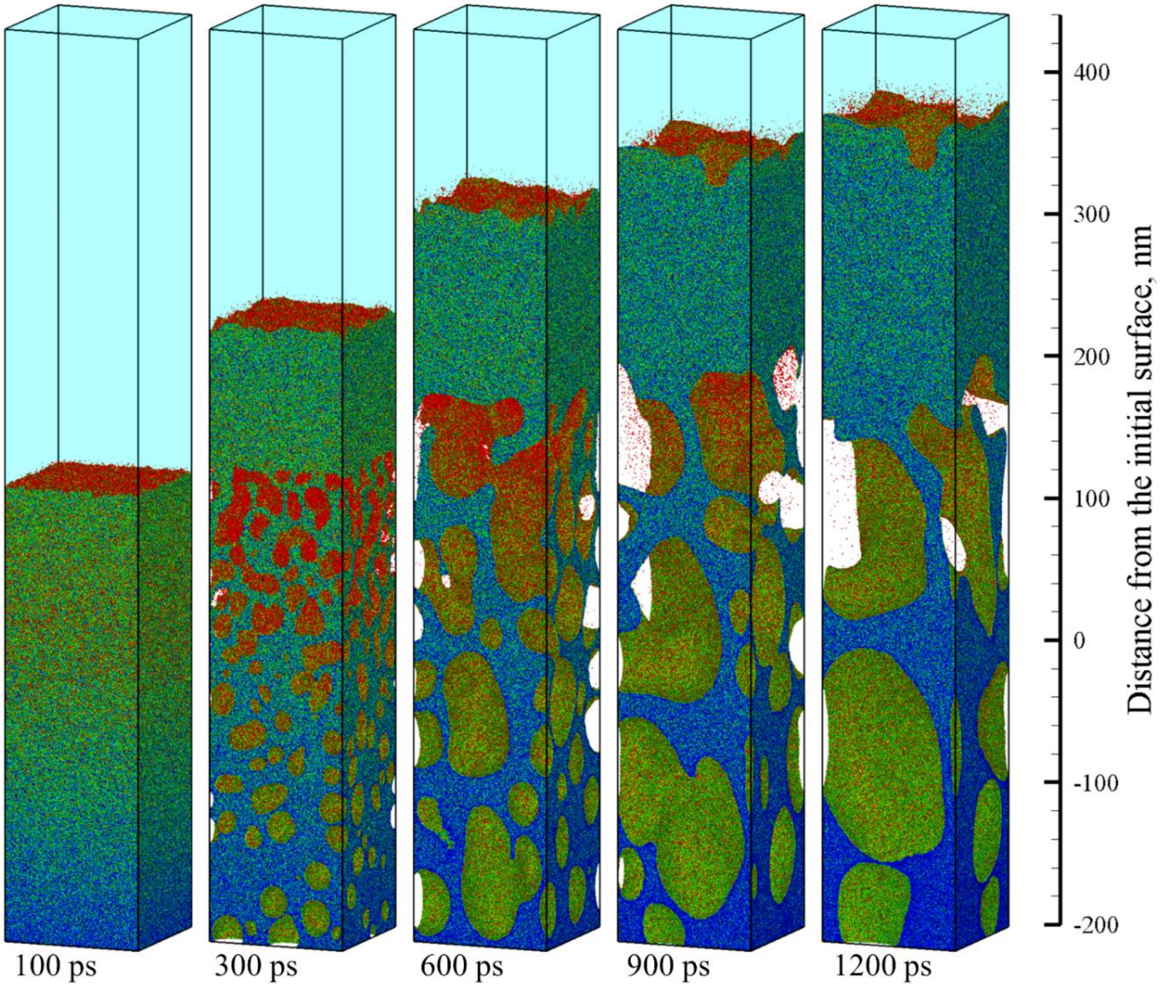

Figure 4.11. Snapshots of atomic configurations predicted in a simulation of a bulk Ag target irradiated *in water* by a 100 fs laser pulse at an absorbed fluence of 400 mJ/cm^2. The irradiation conditions correspond to the regime of phase explosion confined by the water environment. Only parts of the computational system from -220 to 450 nm with respect to the initial surface of the target are shown in the snapshots. The atoms are colored according to their potential energies, from blue for molten Ag to red for vapor-phase Ag atoms. The molecules representing water environment are blanked and the presence of water is illustrated schematically by a light blue region above the Ag target.

The water in contact with the hot metal layer formed by the ablation plume accumulation is rapidly heated to the supercritical state and provides an environment suitable for quenching and condensation of metal atoms emitted from the metal layer into the water. Note that while the temperature shown in the temperature contour plot for the water-Ag mixing region outlined by two black lines Fig. 4.12c is the result of averaging over water and Ag present in this region, the two components of the mixture are far from thermal equilibrium with each other. For example, the average temperatures of Ag and water present in the mixing region at a time of 600 ps are 2665 K and 1120 K, respectively. This lack of thermal equilibrium, combined with the relatively high pressure maintained in the mixing region by the dynamic metal-water interaction (Fig. 4.12d), keeps the thermodynamic conditions in the mixing region far from the ones required for the onset of thermal decomposition of water, as evaluated in calculation with software package FactSage.[178]

The large temperature difference between the water and metal in the mixing region, on the other hand, facilitates the rapid condensation, cooling and freezing of the metal nanoparticles. As has been shown in earlier simulations of thin film ablation in water,[179] the condensation of metal vapor in the mixing region leads to the formation and freezing of small (mostly $\leq$ 10 nm) nanoparticles on the timescale of several nanoseconds. The beginning of this process can already be seen in the last snapshots shown in Fig. 4.11. At a later time, beyond the time-scale of the simulation, the water-silver mixing region, outlined by two black lines in Fig. 4.12b-d is expected to grow and to evolve into a low-density vapor region (cavitation bubble) expanding under the action of water vapor pressure.

Although by the end of the simulation, 1.2 ns, the average temperature of the hot metal layer is below the limit of stability with respect to the phase explosion, it is more than twice higher than the melting point of Ag and is only 36% below the threshold for the phase explosion at zero pressure.[101] The layer may slowly cool down due to the interaction with water, evaporation and, if the bridges connecting the layer to the bulk of the target remain, through the heat conduction to the target. It is quite likely, however, that the hot metal layer would rupture and disintegrate into large liquid droplets due to the inherent instability of thin liquid films, [64, 117, 179] the dynamic interaction of the liquid metal layer with the expanding and collapsing vapor bubble, and the emergence of Rayleigh-Taylor instability at the metal-water interface. The latter mechanism is responsible for the rapid development of complex morphology of the metal-water interface that can be seen from snapshots shown in Fig. 4.11 and plays an important role in the layer decomposition. Therefore, the origin of the Rayleigh-Taylor instability is discussed in more detail in the next section.

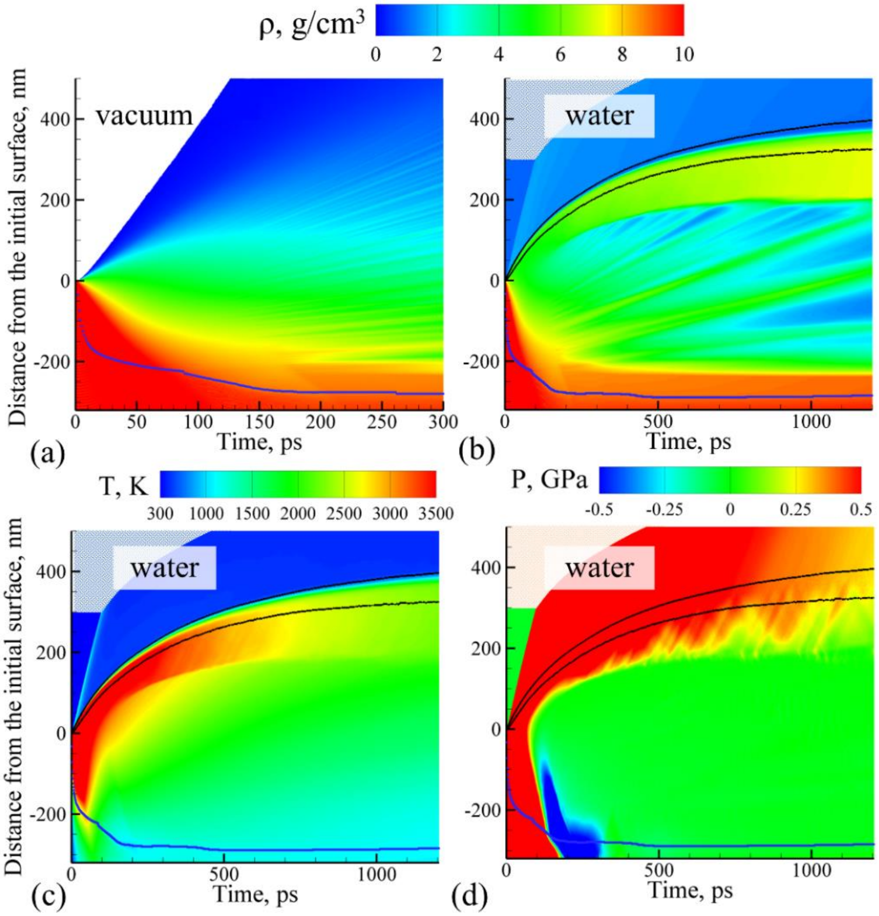

Figure 4.12. Density (**a**,**b**), temperature (**c**), and pressure (**d**) contour plots predicted in simulations of a bulk Ag target irradiated by a 100 fs laser pulse at an absorbed fluence of 400 mJ/cm^2 *in vacuum* (**a**) and *in water* (**b-d**). The blue line shows the location of the melting and solidification fronts. In (**b-d**), the two black lines outline the water-Ag mixing region defined as a region where both water molecules and Ag atoms are present. The blue (**b**,**c**) and red (**d**) dot background represents the presence of water beyond the pressure-transmitting boundary applied at the top of the water layer explicitly simulated with coarse-grained MD. Corresponding snapshots from the simulations are shown in Fig. 4.10 for (**a**) and Fig. 4.11 for (**b-d**).

The onset of the nucleation and growth of small nanoparticles in the metal-water mixing region and the likely breakup of the hot metal layer into large droplets represent two distinct mechanisms of the nanoparticle formation that are likely to yield nanoparticles of two different size ranges. This computational prediction is consistent with the observation of bimodal nanoparticle size distributions in femtosecond PLAL experiments,[7-8] where small nanoparticles with sizes less or around ten nanometers are found to coexist with larger (tens to hundreds of nanometers) ones. The high computational cost of large-scale atomistic simulations, the limited lateral size of the computational cell, and the relatively long timescales associated with both of the aforementioned mechanisms prevent us from directly observing the nanoparticle formation in the simulation discussed in this section. Faster generation of the nanoparticles through the same two mechanisms, however, have been observed in simulations of PLAL of thin films,[179] ablation of bulk targets at a higher fluence (to be reported in Chapter 5), and second pulse ablation of targets modified by the first pulse (discussed in Chapter 6).

4.3.4. Rayleigh-Taylor instability at the metal-water interface

One of the key processes that may lead (or contribute) to the disintegration of the molten metal layer generated due to the confinement of the ablation plume by the water environment is the development of Rayleigh-Taylor instability at the metal-water interface. The rapid deceleration of the denser metal layer by the pressure exerted from the lighter supercritical water creates conditions corresponding to the classical picture of the Rayleigh-Taylor instability, where the acceleration of the interface and density gradient have the same directions. The fastest growing wavelength λ_m and the characteristic time τ of the exponential growth of small perturbations in the Rayleigh-Taylor instability can be estimated based on the linear stability analysis applied to inviscid fluids:[154, 180]

$$\lambda_m = 2\pi\left[\frac{3\sigma}{(\rho_{ml}-\rho_w)G}\right]^{\frac{1}{2}} \qquad \text{Equation 4-1}$$

$$\tau = \left[\frac{2}{3}kAG\right]^{-\frac{1}{2}} = \left[\frac{2}{3^{\frac{3}{2}}}\frac{(\rho_{ml}-\rho_w)^{\frac{3}{2}}G^{\frac{3}{2}}}{(\rho_{ml}+\rho_w)\sigma^{\frac{1}{2}}}\right]^{-\frac{1}{2}} \qquad \text{Equation 4-2}$$

where $k = 2\pi/\lambda_m$ is the wave vector, $A = (\rho_{ml} - \rho_w)/(\rho_{ml} + \rho_w)$ is the Atwood number, ρ_{ml} and ρ_w are the densities of the heavier and lighter fluids (metal layer and supercritical water), σ is the interfacial tension, and G is the effective acceleration of the interface in the direction pointing into the heavier fluid.

In the simulation of PLAL discussed in the previous section, the deceleration of the metal layer by the water overlayer can be seen from the density contour plot shown in Fig. 4.12b. The deceleration is not constant, but rapidly changes from the maximum value of ~7×10^{12} m/s^2 recorded at 40 ps down to 1.6×10^{12} m/s^2 at 300 ps and then to 3.0×10^{11} m/s^2 by the end of the first nanosecond after the laser pulse. The densities of the compressed supercritical water, ρ_w, and the hot metal layer, ρ_{ml}, are also changing during the simulation. These changes, however, are relatively small and average values of $\rho_w = 1.2$ g/cm^3 and $\rho_{ml} = 7$ g/cm^3 are used in the estimations of λ_m and τ. The temperature dependence of the interfacial tension is also neglected, and the value of $\sigma = 0.09$ J/m^2 evaluated for the model Ag-water system at 1800 K using the test-area simulation method[181] is adopted in the estimations. Using these parameters in Eqs. (4-1) and (4-2), we obtain $\lambda_m = 33.9$ nm and $\tau = 85$ ps for the layer deceleration of 1.6×10^{12} m/s^2 at 300 ps and $\lambda_m = 78.3$ nm and $\tau = 297$ ps for the lower deceleration of 3.0×10^{11} m/s^2 at 1 ns.

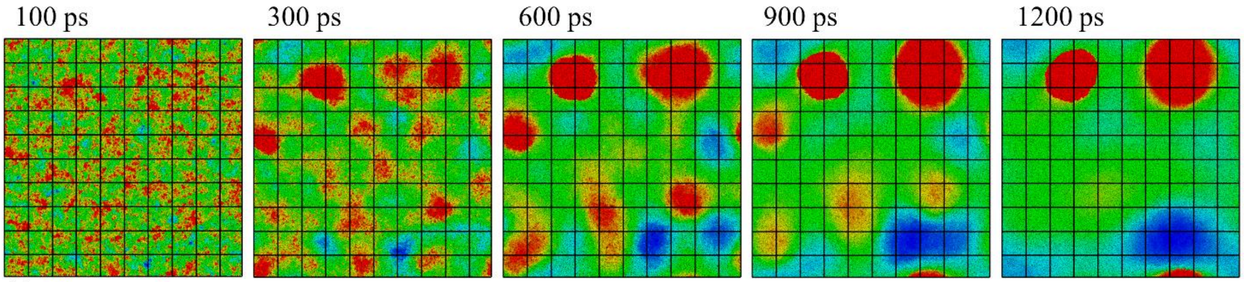

(a) **blue** to **red**: 5 nm 10 nm 20 nm 30 nm 40 nm

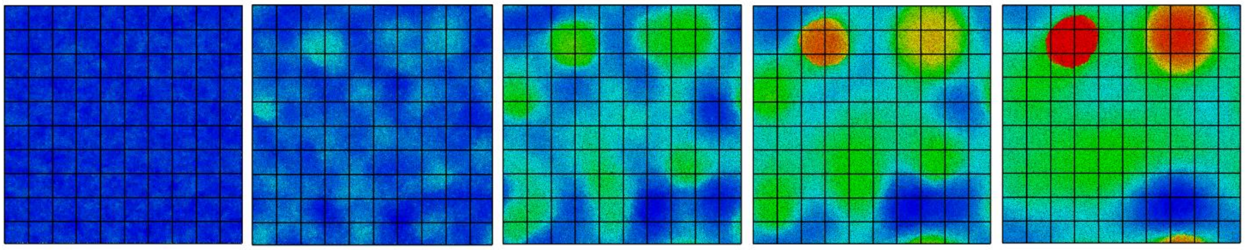

(b) **blue** to **red**: 50 nm in all frames

Figure 4.13. Topographic images of the interface between the hot metal layer and water shown for the simulation illustrated by snapshots in Fig. 4.11. The color shows the relative height of the topographical features, with different scales used for different times in (**a**) to highlight the evolving interfacial roughness. The same scale of 50 nm between red and blue regions is used in (**b**).

To compare the above estimations with the results of the simulation discussed in the previous section, the evolution of morphology of the interface is shown in Fig. 4.13 for the same moments of time for which the snapshots are shown in Fig. 4.11. In a semi-quantitative agreement with the theoretical estimations, the initial fine roughness of the interface with characteristic spatial dimension on the order of several nanometers appear as early as 100 ps and gradually evolves into a coarser interface morphology with characteristic length scale of several tens of nanometers. The observation of the emergence of the nanoscale interface morphology on the timescale of hundreds of picoseconds through the Rayleigh-Taylor instability is in agreement with the results of earlier

MD simulations[155-156] and is a clear indication that nanoscale hydrodynamic instability is likely to play an important role in the nanoparticle generation in PLAL. Indeed, in recent simulations of thin metal film ablation in liquids,[179] the Rayleigh-Taylor instability has been shown to result in disintegration of a molten metal layer and generation of large droplets. Another demonstration of the key role of the Rayleigh-Taylor instability in the generation of large metal nanoparticles in PLAL is provided in the next section.

Note that the initial development of the interface roughness due to the Rayleigh-Taylor instability and the subsequent nonlinear evolution of the interface morphology are sensitive to the viscosity, density ratio, and the variation of the acceleration of the two fluid layers. This sensitivity suggests that the characteristics of the nanoparticles generated through the Rayleigh-Taylor instability at the plume – liquid environment interface can be, to a certain extent, controlled by choosing the ablation target, liquid environment and irradiation parameters.

4.4. Summary

Large-scale atomistic simulations are used in this work to investigate the physical mechanisms and processes responsible for the modification of surface structure and generation of nanoparticles in short pulse laser interactions with bulk metal targets in a liquid environment. The simulations are performed with a computational model combining a coarse-grained representation of liquid (parameterized for water), a fully atomistic description of laser interactions with metal targets, and acoustic impedance matching boundary conditions designed to mimic non-reflecting propagation of the laser-induced pressure waves through the boundaries of the computational domain. The model is implemented in a computationally-efficient parallel code, which is used to perform a series of simulations of femtosecond pulse laser ablation and processing of bulk Ag targets. The results of the simulations performed in the irradiation regimes that correspond to melting, photomechanical spallation and phase explosion in vacuum have revealed strong effect of the liquid environment on the modification of surface regions of the irradiated targets and generation of nanoparticles of different sizes. The main findings of the computational study are summarized below.

1. *Suppression of sub-surface void nucleation and formation of nanostructured surface:* For irradiation conditions that corresponds to melting and re-solidification in vacuum, the presence of water environment suppresses the generation of strong tensile stresses

responsible for the formation of sub-surface voids, provides an additional pathway for cooling through the heat conduction, and facilitates the formation of nanocrystalline structure in a region of the metal target adjacent to the liquid. The nanocrystalline layers generated by laser processing of single-crystal Ag targets are characterized by a high density of stacking faults, twin boundaries, and point defects produced in the course of the rapid re-solidification. The strong effect of the liquid environment on laser-generated surface microstructure suggests a potential use of the spatial confinement in laser processing aimed at inducing surface nanocrystallization and achieving desired optical and mechanical properties of the surface.

2. *Generation of large subsurface voids and surface swelling*: For the irradiation conditions that correspond to the spallation regime in vacuum, the simulations performed in water predict that the interaction with water environment can prevent the complete separation of spalled molten layer from the target, resulting in the formation of much larger frozen-in subsurface voids as compared to ones observed in simulations performed close to the spallation threshold in vacuum. Moreover, the confinement by liquid environment can significantly broaden the fluence range for the formation of large subsurface voids, produce more extensive surface swelling, and result in the formation of unique surface morphologies.
3. *Phase explosion under liquid confinement – buildup of a hot metal layer at the front of the ablation plume*: The simulations performed at higher laser fluences, that correspond to the phase explosion regime in vacuum, reveal the accumulation of the ablation plume at the interface with the water environment and formation of a hot metal layer. The water in contact with the metal layer is brought to the supercritical state, expands, and absorbs metal atoms emitted from the hot metal layer. The expanding low density metal-water mixing region provides an environment suitable for rapid nucleation and growth of small metal nanoparticles and serves as a precursor for the formation of a cavitation bubble.
4. *Hydrodynamic instabilities and disintegration of the metal layer*: The hot metal layer generated due to the confinement of the ablation plume by the liquid environment has limited stability and can readily disintegrate into large (tens of nanometers) nanoparticles. The layer disintegration can be facilitated by Rayleigh-Taylor instability of the interface between the higher density metal layer decelerated by the pressure from the lighter supercritical water,

which creates an extensive nanoscale surface roughness of the interface on a timescale of hundreds of picoseconds.

Overall, the first atomistic simulations of laser ablation of bulk metal targets in water have provided important insights into the complex phenomenon of laser-materials interactions in liquid environment and revealed an array of mechanisms and processes that are unique for laser ablation in liquids. The emerging understanding of laser-induced processes is likely to facilitate the intelligent design of new PLAL setups capable of controlled generation of nanoparticles and surface structures characterized by unusual nonequilibrium structure and phase composition.

5. Two mechanisms of nanoparticle generation in short pulse laser ablation in liquids: The origin of the bimodal size distribution

5.1. Introduction

The production of clean colloidal solutions of nanoparticles through pulsed laser ablation in liquids (PLAL) has evolved over the last decade into a mature research field with a large and growing number of practical applications.[2, 11, 152, 182] While the challenges of increasing productivity and broadening the range of materials available for nanoparticle generation are successfully addressed in the ongoing exploration of the space of experimental parameters,[11, 40] the goal of achieving a narrow nanoparticle size distribution by direct one-step PLAL still remains elusive for many materials. In particular, the broad size distributions, where the desired small nanoparticles coexist with larger ones (tens to hundreds of nanometers), are commonly observed in PLAL experiments regardless of the pulse durations. However, for experiments performed with short (< 100 ps) laser pulses, bimodal nanoparticle size distribution[7, 183-185] becomes apparent, particularly when the nanoparticle statistic is sufficient and experimental setup does not facilitate nanoparticle fragmentation through post-irradiation (*i.e.*, the flow chamber design and appropriate laser repetition rate prevent interaction of laser pulses with already generated nanoparticles). In order to obtain certain nanoparticle sizes, additional steps such as centrifugation, laser post processing, or other methods have to be performed.[11] To fully utilize the potential of pulsed laser ablation in liquids for generation of nanoparticles with well-controlled structure, composition, and size distribution one needs to improve the understanding of the laser-induced processes responsible for the generation of colloidal nanoparticles. Such understanding can only emerge from simultaneous progress in time-resolved experimental probing, theoretical description, and computational modeling of laser-induced processes.

The experimental data on the nanoparticle generation in PLAL is mostly indirect and is based on analysis of the dynamics of cavitation bubble generated due to the interaction of the ablation plume with liquid environment. The cavitation bubble dynamics has been explored through various optical techniques including light scattering,[186] shadowgraphy,[51, 187] and stroboscopic videography.[52] The understanding of the connections between the nanoparticle generation mechanisms and cavitation bubble dynamics has recently been greatly advanced by the results of small angle X-ray scattering (SAXS) probing of the evolution of the nanoparticle size distribution with respect to time and position inside the bubble.[44-47] The experimental evidence suggests that cavitation bubble serves as a reaction chamber for the nanoparticle nucleation, growth, coalescence, and solidification, whilst two or more distinct nanoparticle populations may appear at different stages of the bubble expansion and collapse. The initial and perhaps most critical stage of the nanoparticle formation at the onset of the bubble generation and expansion, however, still remains beyond the temporal and spatial resolution of any of the experimental techniques.

The theoretical and computational treatments of laser – materials interactions in liquids have been hampered by the highly non-equilibrium nature of the laser-induced processes. The continuum-level modeling, in particular, while successful in providing initial insights into the effect of the spatial confinement on the ablation plume expansion and phase decomposition,[62-63] has been suffering from the lack of an adequate description of some of the key processes, such as vaporization of the liquid, mixing of the ablation plume with liquid environment, and generation of nanoparticles in the mixing region. The atomic-level molecular dynamics (MD) computational technique is suitable for exploring fast non-equilibrium phenomena and has been actively used for simulation of laser-materials interactions in vacuum, as reviewed in refs. 67-68, 188. The high computational cost of atomistic treatment of both the irradiated target and the liquid environment, however, has been hampering the extension of the domain of applicability of the MD technique to PLAL. New opportunities in this area has been provided by recent development of a computationally efficient coarse-grained representation of liquid environment[127, 179, 189] and advanced boundary conditions,[101] which led to the design of a hybrid atomistic – coarse-grained MD model capable of revealing the specific characteristics of laser-material interactions in liquids.[179, 190]

In this chapter, we report the results of a computational study supported by experimental observation aimed at revealing the mechanisms of nanoparticle formation in PLAL and explaining the origin of the bimodal nanoparticle size distributions. A large-scale MD simulation performed for a Ag target irradiated by a picosecond laser pulse in water provides important insights into the initial stage of the ablation plume formation and interaction with water environment, and predicts the existence of two distinct mechanisms of the nanoparticle formation, namely, the nucleation and growth of small nanoparticles in the metal-water mixing region and the formation of larger nanoparticles through the breakup of the superheated molten metal layer generated at the plume-water interface. The latter mechanism, involving injection of the large nanoparticles into liquid above the emerging bubble, is further supported by in the cavitation bubble imaging experiments, where small satellite bubbles surrounding the main cavitation bubble are observed upon single picosecond pulse irradiation and can be activated upon properly timed double pulse irradiation.

5.2. Computational and experimental methods

Computational method

The simulation reported in this chapter is performed with a hybrid computational model combining a coarse-grained representation of liquid, a fully atomistic description of laser interaction with metal targets, and acoustic impedance matching boundary conditions, designed to mimic the non-reflecting propagation of the laser-induced pressure waves through the boundaries of the computational domain. A complete description of the computational model tailored for simulation of pulse laser interaction with Ag in water environment is provided in Chapter 1.2, and below only parameters relevant to the computational setup of the simulation reported in this chapter are described.

The simulation reported in this chapter is performed for a Ag bulk target covered by water and irradiated by 10 ps laser pulse at an absorbed laser fluence of 600 mJ/cm^2. A schematic representation of the computational system used in the simulation is shown in Fig. 1.3. The computational system represents a small region within the laser spot and periodic boundary conditions are applied in the lateral directions, parallel to the surface of the target. The dimensions of the computational system in these directions are 49.4 nm × 49.4 nm. The depth of the surface part of the Ag target represented with atomistic resolution is 500 nm, which corresponds to 70 million atoms interacting via EAM Ag potential.[99] The heat transfer in the deeper part of the target is described by the TTM equations solved for lattice and electron temperatures down to the depth of 6 μm. The part of the water overlayer represented by the coarse-grained MD is 300 nm thick and consists of 8.5 million coarse-grained particles. To match the experimental conditions, the dynamic acoustic impedance matching boundary conditions imposed at the top and bottom of the computational domain are designed to mimic non-reflecting propagation of the laser-induced pressure waves through the boundaries of the computational domain.[101, 150] These boundary conditions implicitly simulate a sufficiently thick liquid overlayer and metal target, so that reflections of the laser-induced pressure waves from the free surface of a thick liquid overlayer and the opposite side of the metal target do not play any significant role in the generation of nanoparticles.

The laser irradiation of the target is represented in the model through a source term added to the TTM equation for the electron temperature.[72] The source term describes excitation of the conduction band electrons by a laser pulse with a Gaussian temporal profile and reproduces the exponential attenuation of laser intensity with the depth under the surface. The optical absorption depth, 12 nm at laser wavelength of 800 nm,[144] combined with the effective depth of the "ballistic" energy transport, estimated to be about 56 nm for Ag[101-102] is used in the source term of the TTM equation.[72, 151] The laser pulse durations, τ_L, defined as full width at half maximum of the Gaussian profile, is 10 ps. The reflectivity of the surface is not defined in the model since the absorbed laser fluence, F_{abs}, rather than the incident fluence is used in the presentation of the simulation results. The system is equilibrated at 300 K for 300 ps before applying laser irradiation. The simulation is performed with a computationally-efficient parallel code implementing the combined TTM-MD – coarse-grained MD model, with a three-dimensional treatment of the electronic heat conduction in the TTM-MD part of the computational system.

Experimental method

In all experiments a Fuego laser system from Time-Bandwidth with a pulse duration of 10 ps, a pulse energy of 120 μJ, and a wavelength of 1064 nm was used. The camera system for imaging of the cavitation bubbles was Phantom v1210 from Vision Research Inc.. The image refreshing rate was 240,300 fps at a resolution of 128 × 128 pixels.

The experiments are performed for Au rather than Ag targets used in the simulations. While the nanoparticle formation can be expected to be similar for both of the noble metals, the use of the more inert Au eliminates any contribution of oxidation during the ablation process, which is also not included in the simulation of Ag ablation. The pure water used for all experiments has a quality of 0.055 μS/cm and was adjusted to pH 8 to stabilize the nanoparticles with a sodium phosphate buffer (0.1 mM).

In both single-pulse and double-pulse experiments, a N-BK7 glass cubes (top open) with an outer dimension of 11 × 11 × 11 mm and a wall thickness of 2 mm were used. The gold target was attached to an inner sidewall of a glass cube. The liquid volume was 300 µl, while the liquid thickness between the gold target and the glass was 6 mm. After each pulse (or double-pulse), the chamber was moved 200 µm orthogonally to the laser beam and after several cleaning steps of the chamber, the liquid volume was changed. The laser beam was focused horizontally on the target by means of a focusing lens with a 100 mm focal length. The resulting focus had a diameter of 67 µm ± 5 µm and was determined by microscopy applying the zero-damage method[191]. This leads to a fluence of 3.4 J/cm² ± 0.51 J/cm². The incident fluence applied in experiment, when converted to the absorbed fluence through a TTM simulation performed with electron temperature dependent electronic heat capacity, electron-phonon coupling,[118] thermal conductivity[192] and reflectivity[193] is estimated to be between 1000 and 2000 mJ/cm^2 (see Supplementary Information for details of the calculations), *i.e.*, comparable to the fluence of 600 mJ/cm^2 used in the simulation of PLAL of Ag discussed in this chapter.

TEM images were obtained with a JEM-2200FS from JOEL USA, Inc.. A flow chamber (as described in more detail in ref. 194) was used for the long-term experiments (5 min). In this case, a liquid-flow volume of 60 ml/min and a liquid height of 5 mm was applied. The laser was set to a repetition rate of 200 kHz, with the other parameters are as described above. During the ablation, the chamber was moved by means of an *x-y* linear shifter at a speed of 20 mm/s in a filled square pattern (5 × 3 mm). The samples of the long-term experiments were analyzed by means of the analytical disc centrifuge DC 24000UHR from CPS Instruments, Inc.

5.3. Results and discussion

5.3.1. Computational prediction of two nanoparticle generation mechanisms

The simulation, illustrated in Figs. 5.1-5, is performed at an absorbed laser fluence of 600 mJ/cm^2, which is about three times above the threshold fluence for the transition from spallation to phase explosion regimes of laser ablation of Ag in vacuum.[89, 102] In the phase explosion regime, the main driving force responsible for the material ejection is the rapid release of vapor in a strongly superheated surface region of the target.[88] In vacuum, the explosive release of vapor drives the decomposition of the superheated region of the target into vapor, atomic clusters, and small droplets. Deeper into the target, the propagation of unloading wave generated due to the expansion of the top part of the target induces cavitation in the molten material and may result in the ejection of larger droplets through a process commonly referred to as photomechanical spallation.[71, 91, 161] The presence of liquid environment drastically alters the ablation dynamics. All the material that, in vacuum, freely expands away from the target as a mixture of small liquid droplets and vapor, is now confined by water and is collected at the plume-water interface into a dense hot molten layer, as shown in Fig. 5.1.

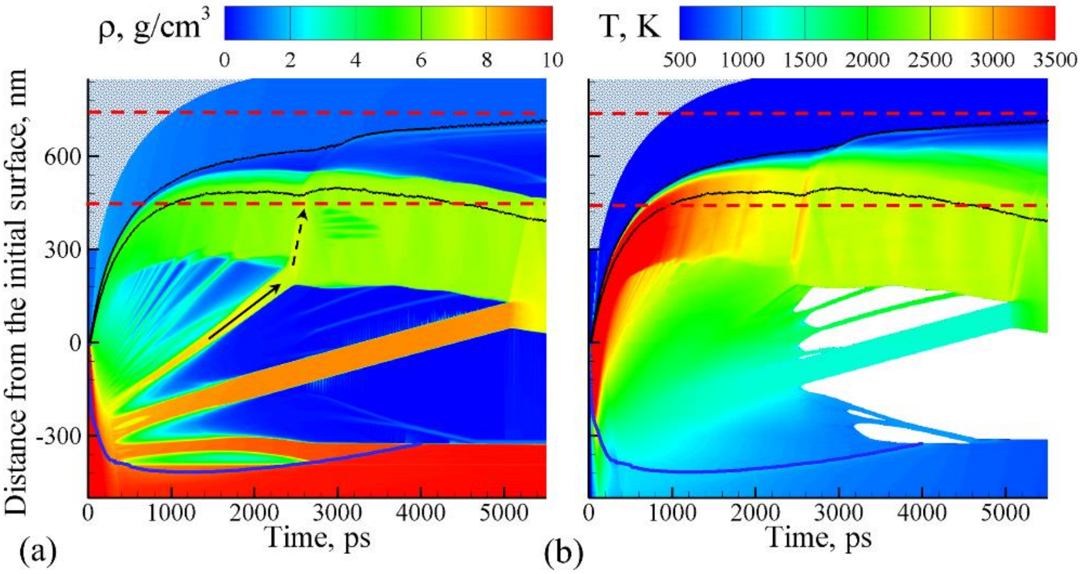

Figure 5.1. Density (a) and temperature (b) contour plots predicted in atomistic simulation of laser ablation of a bulk silver target irradiated in water by a 10 ps laser pulse at an absorbed fluence of 600 mJ/cm^2. The blue line shows the location of the melting and solidification fronts. The two black lines outline the water-Ag mixing region defined as a region where both water molecules and Ag atoms are present. The blue dot background represents the presence of water beyond the pressure-transmitting boundary applied at the top of the water layer explicitly simulated with coarse-grained MD. The two dashed red lines outline the region for which snapshots of atomic configurations are shown in Fig. 5.3.

The molten layer rapidly grows in thickness and cools down as more Ag droplets originating from deeper and colder parts of the target join it. At the same time, water in contact with the hot metal layer is brought into supercritical state and starts to expand, exerting additional downward pressure on the metal layer. The interaction with the water overlayer results in a rapid deceleration of the layer, with magnitude of the deceleration being as high as ~6.3×10^{12} m/s^2 at the initial stage of the plume-water interaction, at 100 ps, and decreasing down to ~7.4×10^{11} m/s^2 by 500 ps. This rapid deceleration directed from the lighter supercritical water to the higher density metal layer creates conditions for the development of the nanoscale Rayleigh-Taylor instability[154, 180] at the decelerated interface. The results of earlier MD simulations combined with quantitative analysis of the fastest growing wavelength and the characteristic time of the exponential growth of small perturbations in the Rayleigh-Taylor instability generated at comparable levels of interface acceleration[24] (or equivalent gravitational field[155-156]) predict the emergence of the nanoscale interface morphology on the timescale of hundreds of picoseconds. These predictions are consistent with the results of present simulation, where the initial nanoscale roughness of the metal-water interface emerges within the first ~500 ps after the laser pulse, shown in Fig. 5.2 and evolves into a deep trough (single finger of the Rayleigh-Taylor instability) by the time of 2,000 ps, as can be seen in the first snapshot shown in Fig. 5.3.

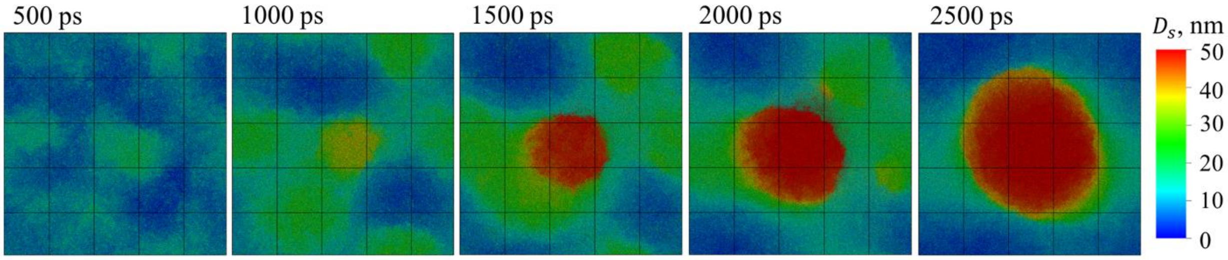

Figure 5.2. Topographic images of the interface between the hot metal layer and water shown for different times in the simulation illustrated by snapshots in Figure 5.3. The color shows the relative height of the topographical features from the surface.

The roughening of the interface between the hot metal layer and the supercritical water is also reflected in the shape of the metal-water mixing region that is outlined by two black lines in Fig. 5.1. The mixing proceeds not only by active evaporation of Ag atoms into the low-density supercritical water region that serves as a precursor of the cavitation bubble observed in PLAL experiments, but also by the penetration of water into the metal layer roughened by the Rayleigh-Taylor instability. The roughening of the metal-water interface combined with the general limited stability of thin liquid films[64,117] may result in eventual partial or complete disintegration of the metal layer leading to the generation of large nanoparticles in the lower part of the low-density metal-water region, as has been observed in a recent simulation of laser ablation of a thin Ag film in water.[179] The results of the present simulation, however, suggest an alternative scenario in which the large nanoparticles can be directly injected into the high-density colder water region located *above* the low-density mixing region. This scenario is illustrated in Fig. 5.3 and is described next.

As mentioned above, the metal layer formed at the interface with the water environment is growing through the addition of new metal droplets or layers joining it from below. As time progresses, these droplets/layers become larger and colder, as they originate from deeper regions of the target and are ejected with the assistance of photomechanical processes. The backside impact of the material joining the hot molten layer can induce pressure pulses in the layer that are sufficiently strong to interfere with rough metal-water interface and result in the emission of metal nanojets into the low-density mixing region. As an example of the sequence of processes leading to the nanojetting, we can consider the collision of a spalled layer ejected from a relatively deep part of the target (the trajectory of this layer is marked by a solid arrow in Fig. 5.1a) with the molten layer accumulated at the metal-water interface. The collision occurs at ~2,600 ps and produces a pressure pulse (marked by the dashed arrow in Fig. 5.1a) that can be identified from the transient densification of the molten metal layer (Fig. 5.1a) and the corresponding temperature spike due to the rapid adiabatic compression[72] (Fig. 5.1b). The interaction of the pressure pulse with the metal-water interface roughened due to the Rayleigh-Taylor instability leads to the emission of a nanojet that rapidly emerges from the metal layer between 2.7 and 3 ns, and disintegrates into three large nanoparticles with diameters on the order of tens of nanometers by the time of 5 ns, Fig. 5.3.

The origin of atoms that end up in each of the three nanoparticles is shown in the right frames of the pairs of snapshots shown in Fig. 5.3. As can be seen from these snapshots, the atoms that contribute to the large nanoparticles are mostly located within the trough region of the molten metal layer before the backside impact, suggesting that the roughness of the interface plays an essential role in the formation of the nanojet. Indeed, the dynamics of material redistribution from the troughs of the interface to the nanojet are consistent with conclusions of theoretical analysis of the Richtmyer-Meshkov instability produced when a shock wave impinges a roughened interface between materials of different density.[195,196]

The formation and subsequent rupturing of the nanojet not only produces three large nanoparticles but also launches two of them past the low-density mixing region directly into dense and relatively cold water environment. The boundary between the low-density mixing region and dense water environment is defined at water density of 0.6 g/cm^3 and marked in the atomistic snapshots shown in Fig. 5.3 by black dashed squares. The process of jetting that crosses the boundary at ~3,000 ps can be seen in Fig. 5.3 from both the snapshots and the water and Ag density profiles shown next to the corresponding snapshots. Two of the green peaks that correspond to the Ag nanoparticles in the density profiles appear in the region where the water density is comparable to its liquid state density and the metal atoms and small clusters produced through evaporation from the hot metal layer are absent. These two nanoparticles do not have net velocity with respect to water and can be expected to move along with the surrounding water as the low-density mixing region expands into a cavitation bubble.

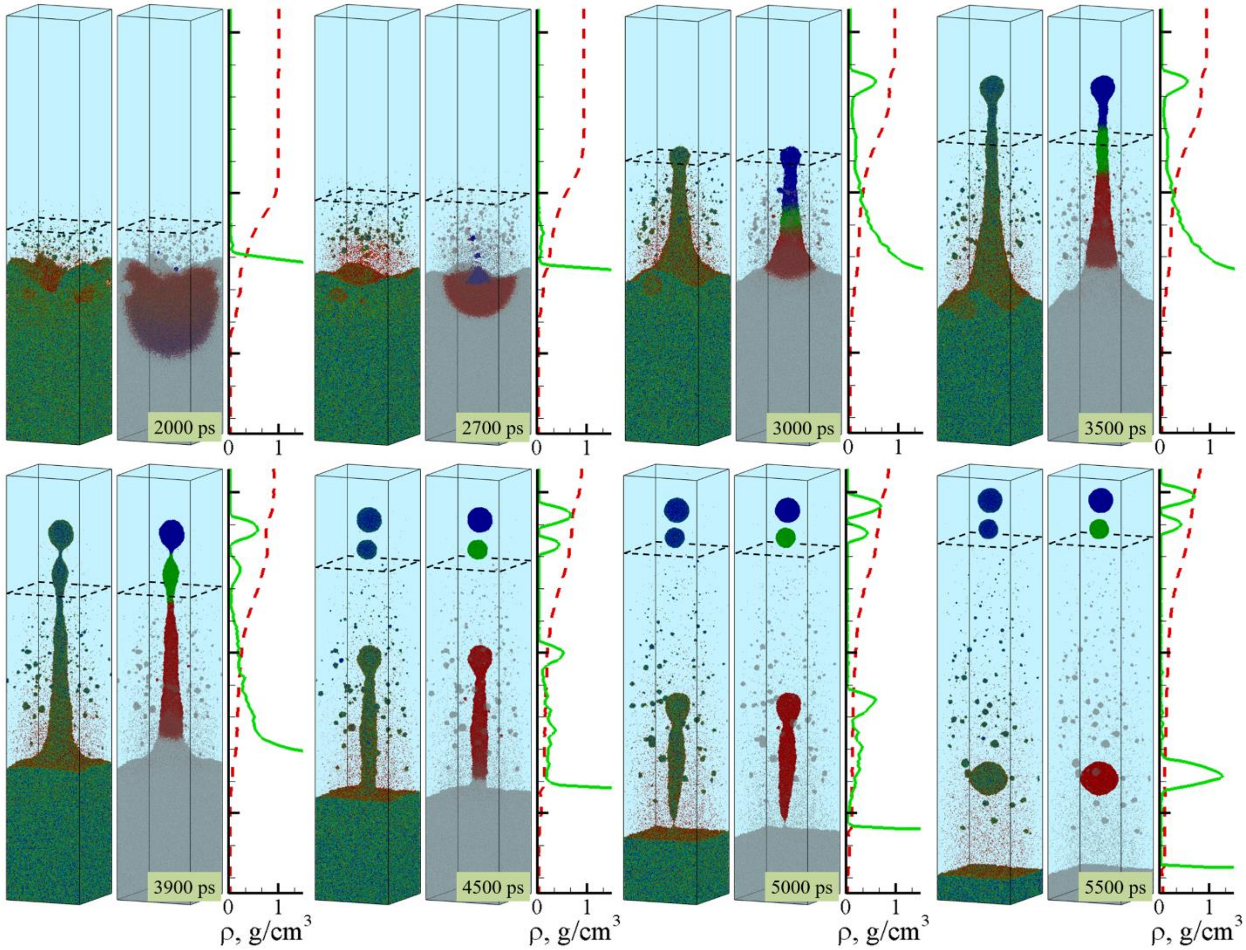

Figure 5.3. Snapshots of atomic configurations and density distribution predicted in atomistic simulation of laser ablation of a bulk silver target irradiated in water by a 10 ps laser pulse at an absorbed fluence of 600 mJ/cm^2. Only parts of the computational system from 450 to 715 nm with respect to the initial surface of the silver target are shown in the snapshots. Two representations of atomic configurations are shown for each moment of time. On the left side of the paired snapshots, the atoms are colored according to their potential energies, from blue for the crystalline nanoparticles, to green for molten Ag, and to red for individual Ag atoms. On the right side of the paired snapshots, the atoms are colored based on IDs of three nanoparticles generated through the rupture of the liquid spike (each color except grey corresponds to atoms that end up in one of the three nanoparticles). The molecules representing water environment are blanked and the presence

of water is illustrated schematically as a light blue region above the Ag target. The degree of water-silver mixing is illustrated by density plots shown as functions of distance from the substrate for both water and silver on the rightmost sides of the snapshots; the red dashed line represents water density distribution, and green solid line represents Ag density distribution. The black dashed squares in the atomistic snapshots show approximate positions of the diffuse "boundary" between the dense water and low-density mixing region defined here as the position where water density is 0.6 g/cm^3.

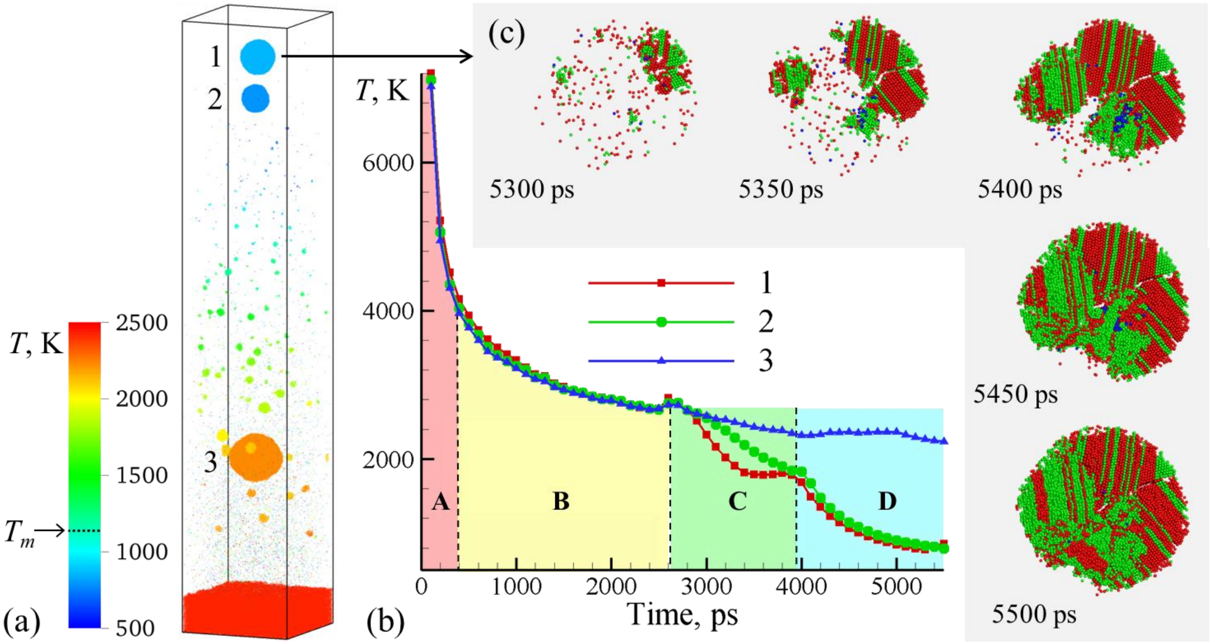

Figure 5.4. (a) Snapshot of the final configurations obtained for 5.5 ns after the laser pulse in a simulation of a bulk Ag target irradiated in water by a 10 ps laser pulse at an absorbed fluence of 600 mJ/cm^2. Only parts of the computational system from 450 to 715 nm with respect to the initial surface of the Ag target are shown in the snapshots. The atoms in the snapshot are colored by local temperature. (b) The time dependence of the average temperature of atoms generated through the rupture of the liquid spike shown in Figure 5.3. (c) The process of crystallization in the topmost nanoparticle ejected from the liquid spike. The atoms are colored according to their local structural environment, so that the fcc, hcp, and bcc atoms are colored green, red, and blue, respectively, while the atoms that belong to the melted parts of the nanoparticles, crystal defects and free surfaces are blanked.

The injection of the large liquid droplets into the dense water environment makes a strong impact on their cooling rate and solidification. The thermal history of material contributing to the three nanoparticles produced from the disintegration of the nanojet is shown in Fig. 5.4b, where four stages of cooling can be distinguished. The initial sharp temperature drop from the level exceeding the critical temperature of Ag (stage marked as **A** in Fig. 5.4b) corresponds to the explosive phase decomposition of the superheated surface region of the irradiated target into vapor and liquid. The material that experienced the phase decomposition is accumulated at the interface with the water environment, forms a hot molten layer that further cools down mostly due to the colder Ag originating from deeper parts of the target joining the layer (stage **B** in Fig. 5.4b). The time of ~2,600 ps is when the pressure pulse generated by the impact from a spalled layer initiates the active hydrodynamic flow leading to the nanojet formation. Following the initial temperature spike related to the transient compression of the material, the nanojet is generated and the temperature starts to drop (stage **C** in Fig. 5.4b). At this stage, the temperature trajectories calculated by averaging over atoms contributing to the three droplets start to diverge, with the top part of the nanojet (colored blue and green in the right frames of the pairs of snapshots shown in Fig. 5.3) cooling faster due to more vigorous expansion and interaction with colder water environment. The final stage **D** in Fig. 5.4b starts with disintegration of the nanojet into individual droplets. The disintegration itself leads to the surface energy minimization (and corresponding increase in the thermal energy) as the droplets attain spherical shape, which shows up as plateaus or even small transient increases in the temperature profiles. Following the separation from the nanojet, the droplets continue to cool due to the interaction with the surrounding water. At this stage, the thermal trajectories of the two droplets injected into dense water environment and the one left behind in the low-density precursor of the cavitation bubble sharply diverge. While the lowest nanoparticle located near the hot molten layer cools slowly and its temperature remains above 2000 K at the end of the simulation, the two upper nanoparticles experience an effective cooling rate of ~7×10^{11} K/s during stage **D** of the simulation and reach temperature as low as 30% below the equilibrium melting temperature of Ag.

The rapid quenching to the conditions of deep undercooling triggers the onset of solidification in the topmost nanoparticle, which proceeds through the nucleation of several crystallites at ~5250-5300 ps followed by their rapid growth and complete solidification of the nanoparticle within the following 200 ps, as shown in Fig. 5.4c. The structural analysis of the nanoparticle performed for different moments of time during the solidification reveals the transient appearance of small domains of body centered cubic (bcc) structure (blue atoms that can be seen between 5350 and 5450 ps) as well as cross-nucleation of face centered cubic (fcc) and hexagonal close packed (hcp) regions with ⟨111⟩fcc//⟨0001⟩hcp orientation relationship (green and red atoms in Fig. 5.4c). The resulting ultra-fine grained polycrystalline structure of the nanoparticle featuring multiple stacking faults, twin boundaries and platelets of metastable hcp structure illustrates the possibility of the generation of nanoparticles with highly non-equilibrium metastable structures, defects,[197] and phases under the conditions of extreme quenching rates that can be realized in PLAL.[3, 35] Although the topmost nanoparticle (nanoparticle #1 in Fig. 5.4a) was the coldest one during most of the duration of stage **D** in Fig. 5.4b, the reheating due to the release of the latent heat of solidification brings its temperature above the second smaller nanoparticle (nanoparticle #2 in Fig. 5.4a) by the end of the simulation. Structural analysis of the second nanoparticle reveals the appearance of a small nucleus of the crystal phase at the end of the simulation and one may expect that this nanoparticle would solidify within the following 100-200 ps if the simulation would be continued.

The third and largest nanoparticle generated through the nanojet disintegration (nanoparticle #3 in Fig. 5.4a) is located in the low-density part of the metal-water mixing region, where it coexists with numerous small nanoparticles generated through the nucleation and growth from Ag atoms that are continuously evaporating from the hot metal layer. As seen from Fig. 5.1b, the temperature in the mixing regions, while staying above the critical temperature of water, is close and, in the upper part, even below the melting temperature of Ag. As a result, the vapor Ag atoms rapidly condense forming small nanoparticles on a timescale of just several nanoseconds after the laser irradiation. The kinetics of the nanoparticle formation through the nucleation and growth in the mixing region is illustrated by Fig. 5.5. This nanoparticle generation mechanism has also been observed in recent atomistic simulations of laser ablation of Ag films and bulk targets in water,[179, 190] and is consistent with the results of time-resolved SAXS measurement[44-47] suggesting that the "primary" particles with diameter less than 10 nm are likely to form through the condensation from the vapor phase at the initial stage of the cavitation bubble expansion.[44]

The computation prediction that larger nanoparticles, in the size range of tens of nanometers, can also be generated during the first nanoseconds after the laser irradiation, however, might not be directly associated with the whole fraction of so-called "secondary" particles identified in SAXS experiments.[11-14] This secondary fraction is likely to consist of agglomerates and large spherical nanoparticles that cannot be differentiated in-situ[46]. Moreover, the SAXS experiments have been performed with nanosecond laser pulses, and the ablation process may proceed rather differently as compared to the picosecond ablation. In the nanosecond PLAL, the secondary particles have been speculated to mostly form through collisions and agglomeration of primary particles,[44] although the possibility of multiple pathways for generation of secondary particles have recently been considered as well.[46] Indeed, first results of MD simulations performed with longer, sub-ns to ns, laser pulses (to be reported in Chapter 7) suggest that the generation of large nanoparticles through the formation and decomposition of a dense metal layer at the ablation plume – water environment interface is also activated in the nanosecond PLAL.

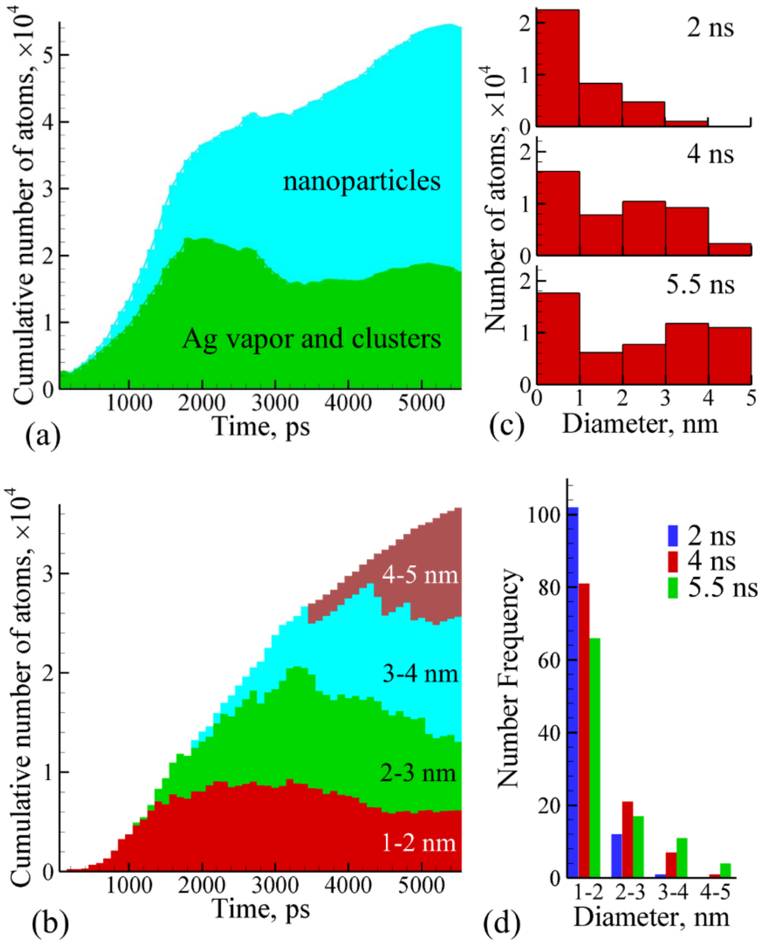

Figure 5.5. The results of the cluster analysis of the ablation plume generated in atomistic simulation of laser ablation of a bulk silver target irradiated in water by a 10 ps laser pulse at an absorbed fluence of 600 mJ/cm^2. The cumulative number of individual Ag atoms and small clusters with diameters less than 1 nm (green) and atoms that belong to Ag nanoparticles with diameters above 1 nm (blue) are shown in (a). The cumulative numbers of atoms that belong to nanoparticles of different sizes (above 1 nm) are shown in (b). The number of atoms in nanoparticles of different sizes (above 1 nm) are also shown as histograms for 2, 4 and 5.5 ns in (c). The number of nanoparticles of different sizes is also shown for the same moments of time in (d).

Neither in the nanosecond PLAL experiments nor simulations, however, the nanoparticles are detected beyond the cavitation bubble boundary. The computational prediction that, in the picosecond PLAL, the large nanoparticles generated through the cascade of hydrodynamic instabilities can be directly ejected and embedded in the dense water region beyond the cavitation bubble boundary, marked schematically by dashed squares in Fig. 5.3, goes against the commonly accepted view that the nanoparticles are generated and confined within the cavitation bubble and are only released into liquid environment when cavitation bubble collapses.[47, 51] At the same time, the computational prediction of the injection of large nanoparticles into the dense water environment suggests a unique feature of the picosecond PLAL. In order to support this intriguing computational prediction, a series of specially designed single and double pulse cavitation bubble imaging experiments are performed and reported in the next section.

5.3.2. Experiments: Cavitation bubble dynamics and nanoparticle size distributions

(Experiments are performed by Dr. Bilal Gökce and Prof. Stephan Barcikowski's groups from University of Essen-Duisburg, Germany)

Time-resolved measurements of the laser-induced cavitation bubble dynamics have been actively used in investigations of nanosecond PLAL,[43, 45, 49, 52, 58, 186] and have provided important, albeit mostly indirect, information on the nanoparticle formation mechanisms. There have been, however, few imaging measurements reported on cavitation bubbles induced by picosecond PLAL,[198] although ps PLAL comes with certain advantages such as a higher nanoparticle productivity[41]. In this chapter, we report first results of time resolved imaging of cavitation bubbles generated by a single and double 10 ps laser pulse irradiation of a Au target in water. The nanoparticle size distributions are also analyzed and the insights into the mechanisms of the nanoparticle generation in picosecond PLAL obtained in the experiments are related to the computational predictions.

The emergence of a cavitation bubble following a single 10 ps laser pulse irradiation is shown for the first 12 μs of the bubble expansion in Fig. 5.6a. The cavitation bubble exhibits unique features that have not been observed in nanosecond PLAL, where the bubble boundaries tend to be sharp and smooth.[45, 49, 52] The bubble in Fig. 5.6a exhibits rough and seemingly diffuse boundary, and most uniquely, numerous "microbubbles" protruding out of the boundary of the main cavitation bubble. The rough interface, which is already apparent at 3 μs after the laser pulse, gradually evolves into a well-defined semispherical main bubble surrounded by several satellite microbubbles, some of which can still be seen as late as 20 µs after the pulse (first frame in Fig. 5.6b).

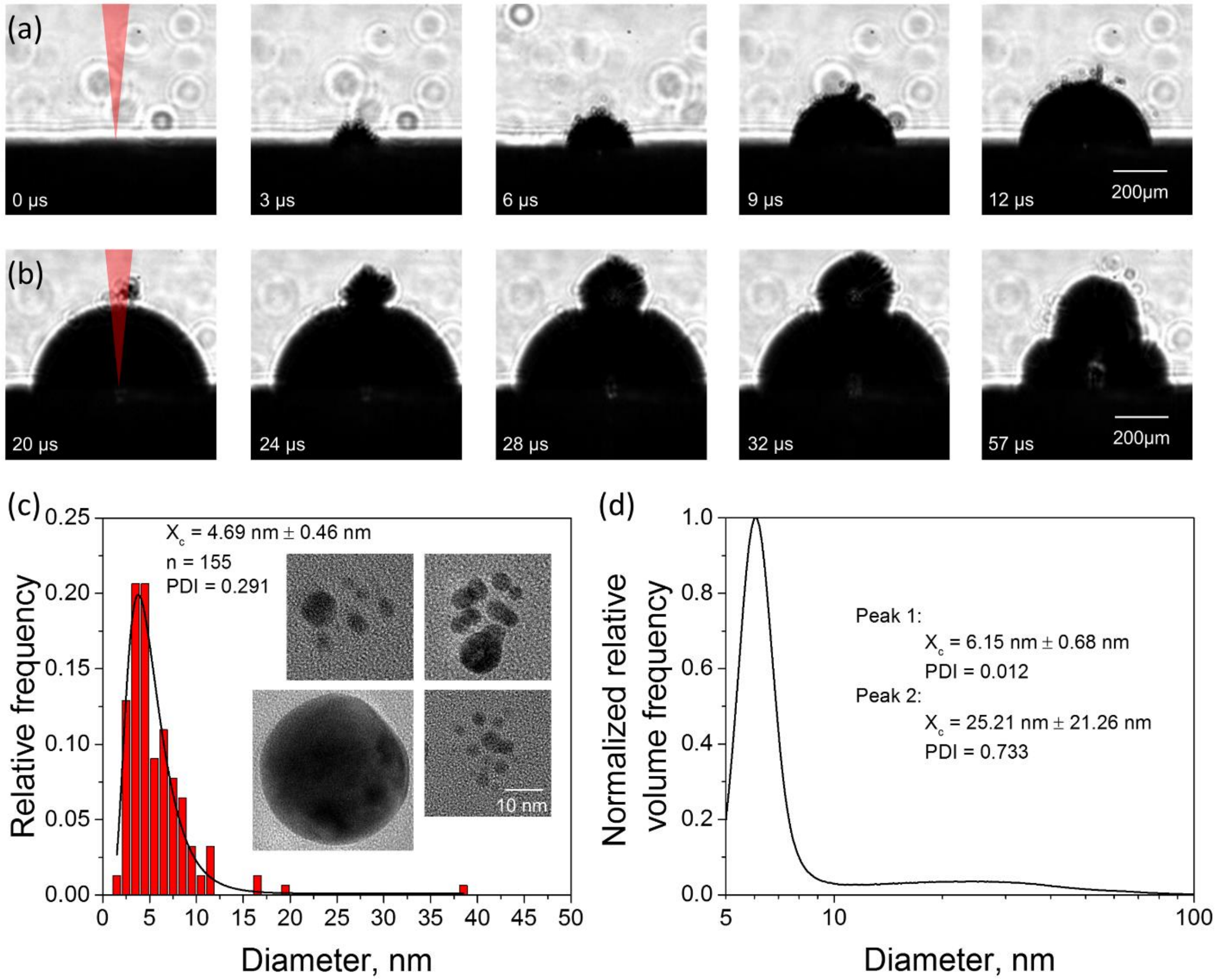

Figure 5.6. Experimental results on the cavitation bubble dynamics and generation of nanoparticles in PLAL of Au targets irradiated by 10 ps laser pulses in water at an incident fluence of 3.4 J/cm² ± 0.51 J/cm² and laser wavelength of 1064 nm. (a) Images of a cavitation bubble with rough boundary (satellite microbubbles) generated by a single laser pulse irradiation taken at regular intervals during the first 12 µs after the laser pulse. (b) Images of the cavitation bubble dynamics modified by a second pulse applied at 20 µs after the first one, *i.e.*, during expansion of the first cavitation bubble. The first four images are separated from each other by 4 µs, and the fifth image is taken 25 µs after the fourth image, *i.e.*, during the shrinking phase. (c) Size distribution of Au nanoparticles obtained from analysis of TEM images, with several representative images shown as insets. The scale bar is common for all insets and corresponds to 10 nm. (d) Nanoparticle size distribution obtained through analytical disc centrifugation measurement for nanoparticle solution produced under the same experimental conditions as in (c) but for a continuous ablation with a repetition rate of 200 kHz. Volume frequency is shown to increase the visibility of the second mode.

The appearance of the satellite micro-sized bubbles surrounding the main cavitation bubble may be related to the injection of the large nanoparticles into the dense water region above the precursor of the cavitation bubble observed in the simulations. The question on how the existence of large nanoparticles beyond the boundary of the cavitation bubble can show up as microbubbles in the imaging experiments, however, still remains open. As clearly demonstrated in the simulation discussed above, the nanoparticles embedded into the dense water environment are expected to cool down below the melting temperature and solidify on the timescale of nanoseconds. The cooling rate is ensured by the suppression of the formation of an insulating vapor layer around the hot nanoparticles by the high curvature of the nanoparticle-water interface,[51,52] and complete thermal equilibration between the nanoparticles and the surrounding water can be expected within a few tens of nanoseconds. The nanoparticles, therefore, cannot be expected to serve as sustained heat sources acting to support microscale vapor bubbles on the microsecond timescale. One possible explanation of the satellite microbubbles is that the metal nanoparticles can serve as heterogeneous nucleation sites lowering the nucleation barrier for vapor nucleation in a hot water layer surrounding the expanding cavitation bubble. An alternative explanation is that the nanoparticles embedded into the water environment at the initial stage of the cavitation bubble formation are clustering over time into loose aggregates that are sufficiently large to become visible in the cavitation bubble imaging experiments, which have a spatial resolution of 6.14 μm.

Given the ambiguity with association of the satellite microbubbles with metal nanoparticles, the origin of the satellite microbubbles can be further investigated in double pulse stroboscopic videography experiment, illustrated in Fig. 5.6b. Here, the second pulse is applied 20 μs after the first one, when the main cavitation bubble is still expanding and a cluster of satellite microbubbles is clearly visible near the top of the main bubble. The irradiation by the second pulse leads to the appearance of a secondary cavitation bubble that originates at the location of the satellite microbubbles. This observation can be interpreted as an evidence in favor of the presence of large nanoparticles beyond the boundaries of the main cavitation bubble. Such nanoparticles could absorb laser light from the second pulse, heat the surrounding water, and result in the emergence of the secondary cavitation bubble[199-200]. As time progresses, the secondary bubble expands, interacts and merges with the main cavitation bubble, thus drastically altering the overall cavitation bubble dynamics.

The combination of the single and double pulse cavitation bubble imaging results indicates that, in agreement with computational predictions, large (~ 10-20 nm) nanoparticles and eventually their agglomerates can be implanted into water environment beyond the boundary of the cavitation bubble during picosecond PLAL. An additional connection to the simulation results can be provided through analysis of the nanoparticle size distributions. For the single pulse experiment, the distribution obtained from analysis of TEM images of is shown, along with several representative TEM images, in Fig. 5.6c. The distribution shows a peak with maximum at ~4 nm and several larger nanoparticles with sizes extending up to 38 nm. To obtain a statistically reliable distribution, continuous ablation under the same conditions as in the single pulse experiment discussed above is performed for 5 minutes at a reputation rate of 200 kHz, and the analytical disc centrifugation is used for the nanoparticle analysis. The volume frequency of hydrodynamic nanoparticle diameter distribution obtained in this experiment, Fig. 5.6d, has clear bimodal character, with the first and second peaks reaching the maxima at ~6 nm and ~25 nm, respectively.

The experimental size distributions shown in Fig. 5.6c and 5.6d are in a good quantitative agreement with the results of the simulations, where the distribution of small nanoparticles generated through the nucleation and growth in the metal-water mixing region peaks around 4 nm, shown in Fig. 5.5, and the large nanoparticles produced through the nanojet disintegration have diameters of 12 nm, 15 nm, and 19 nm. The size of the large nanoparticles in the simulation may be affected by the relatively small lateral size of the computational system, which only allows for the emission of a single nanojet. Under experimental conditions, the particles ejected from neighboring nanojets may coalesce, while the nanoparticles that end up in the low-density region (*e.g.*, nanoparticle #3 in Fig. 5.4a) may grow with time by consuming the surrounding Ag atoms and clusters.

5.4. Summary

Atomistic modeling of picosecond laser ablation of Ag in water combined with cavitation bubble imaging experiments performed for Au targets provide new insights into the mechanisms of nanoparticle formation in PLAL and reveal a complex sequence of processes responsible for generation of two distinct size groups of nanoparticles, thus explaining the origin of the commonly observed bimodal nanoparticle size distribution.

The results of a large-scale atomistic simulation, performed at a laser fluence three times above the phase explosion threshold in vacuum, provide convincing evidence of the critical role the formation of a transient hot molten metal layer at the interface with water environment plays in the nanoparticle generation. The water in contact with the hot metal layer is brought to the supercritical state and expands into a low-density metal-water mixing region that serves as a precursor for the formation of a cavitation bubble. The thermodynamic conditions in the low-density mixing region are amenable to rapid nucleation and growth of small (below 10 nm) nanoparticles from Ag atoms that are continuously evaporating from the hot metal layer. In addition to serving as a source of Ag atoms for condensation of small nanoparticles in the mixing region, the hot molten layer itself has limited stability and can readily disintegrate into larger (10 -20 nm) nanoparticles through series of hydrodynamic instabilities. In particular, rapid deceleration of the molten metal layer by pressure exerted by supercritical water leads to Rayleigh-Taylor instability of the interface and produces extensive nanoscale interfacial roughness on a timescale of hundreds of picoseconds. The impact from new metal droplets or spalled layers joining the hot molten layer at a later time can further destabilize the interface by inducing Richtmyer-Meshkov instability of the roughened interface. The latter can lead to the formation of nanojets launching large metal droplets past the low-density mixing region directly into dense and relatively cold water environment.

The direct injection of large nanoparticles into liquid beyond the cavitation bubble boundary predicted in the simulation is directly confirmed in the cavitation bubble imaging experiments, where small satellite microbubbles surrounding the main cavitation bubble are observed upon single pulse irradiation of an Ag target. The formation of secondary bubbles originating from the satellite microbubbles upon properly timed second pulse irradiation further confirms the association of the microbubbles with large nanoparticles. The nanoparticle size distributions obtained in experiments through the analysis of TEM images and analytical disc centrifugation show the presence of both small (less than 10 nm) and large (tens of nm) nanoparticles, and are consistent with the distributions predicted in the simulation. The good quantitative agreement between the simulation and experiment supports the association of the two groups of nanoparticles with two distinct mechanisms of the nanoparticle formation, *i.e.*, the nucleation and growth of small nanoparticles in the metal-water mixing region and generation of larger nanoparticles through the breakup of the superheated molten metal layer generated at the plume-water interface.

6. Incubation effect of laser ablation in liquids on nanoparticle generation with the presence of sub-surface voids

6.1. Introduction

The results of the simulations discussed in section 4.3.2 predict that the final structure of a surface region of a target irradiated in the regime of spallation confined by liquid environment, below the threshold for nanoparticle formation, is essentially a thin metal layer loosely connected to the bulk of the target by thin walls and bridges, similar to the configuration shown for a partially solidified target in the last snapshot in Fig. 4.6. The formation of porous surface morphology is also possible at higher fluences, in the phase explosion regime discussed in section 4.3.3, when the hot metal layer generated at the front of the ablation plume (*e.g.*, Fig. 4.11) does not disintegrate into nanoparticles but cools down due to the interaction with liquid environment and heat conduction to the bulk of the target. The irradiation of such targets by a subsequent laser pulse would result in spatial localization of the deposited laser energy within the top surface layer of the target and may lead to a substantial reduction of the threshold fluence for the generation of nanoparticles. Thus, the presence of large subsurface voids can facilitate generation of nanoparticles in the multipulse irradiation regime at fluences that do not produce nanoparticles upon irradiation with a single pulse, leading to the so-called incubation effect. The incubation effect has been extensively studied for vacuum conditions[163, 201-204] and, as shown in a recent computational study[102], the generation of sub-surface voids may be one of the mechanisms responsible for the incubation. The response of a target with sub-surface voids to the irradiation in a liquid environment, when the material expansion is suppressed by the presence of the liquid overlayer, however, has not been investigated so far. To explore the effect of the presence of subsurface voids on the microscopic mechanisms of pulsed laser ablation in liquids, a sample mimicking a frozen film connected to the bulk of the target by thin bridges is constructed based on the predictions of the simulations discussed sections 4.32 and 4.3.3.

6.2. Computational setup

The simulation reported in this chapter is performed with a hybrid computational model combining a coarse-grained representation of liquid, a fully atomistic description of laser interaction with metal targets, and acoustic impedance matching boundary conditions, designed to mimic the non-reflecting propagation of the laser-induced pressure waves through the boundaries of the computational domain. A complete description of the computational model tailored for simulation of pulse laser interaction with Ag in water environment is provided in Chapter 1.2, and below only parameters relevant to the computational setup of the simulation reported in this chapter are described.

The simulations are performed for a Ag bulk target covered by water, and the initial target has fcc crystal structure and (001) orientation of the free surface. The periodic boundary conditions are applied in the lateral directions, parallel to the surface of the target. The dimensions of the computational system in the lateral directions are 98.7 nm × 98.7 nm. The depth of the surface part of the Ag target represented with atomistic resolution, L_z in Fig. 1.3, and the corresponding number of Ag atoms is 280 nm (126 million Ag atoms) at F_{abs} = 300 mJ/cm^2. The thickness of the part of the water overlayer represented by the coarse-grained MD model, L_{env} in Fig. 1.3, is 300 nm, which corresponds to 34 million coarse-grained particles. The size of the TTM part of the system, L_c in Fig. 1.3, is 2.9 μm. To match the experimental conditions, the dynamic acoustic impedance matching boundary conditions imposed at the top and bottom of the computational domain are designed to mimic non-reflecting propagation of the laser-induced pressure waves through the boundaries of the computational domain.[101, 150] These boundary conditions implicitly simulate a sufficiently thick liquid overlayer and metal target, so that reflections of the laser-induced pressure waves from the free surface of a thick liquid overlayer and the opposite side of the metal target do not play any significant role in the generation of nanoparticles and modification of surface structure.

The laser irradiation of the target is represented in the model through a source term added to the TTM equation for the electron temperature.[72] The source term describes excitation of the conduction band electrons by a laser pulse with a Gaussian temporal profile and reproduces the exponential attenuation of laser intensity with the depth under the surface. The optical absorption depth, 12 nm at laser wavelength of 800 nm,[144] combined with the effective depth of the “ballistic” energy transport, estimated to be about 56 nm for Ag[101-102] is used in the source term of the TTM equation.[72, 151] The laser pulse durations, τ_L, defined as full width at half maximum of the Gaussian profile, is 100 fs. The reflectivity of the surface is not defined in the model since the absorbed laser fluence, F_{abs}, rather than the incident fluence is used in the presentation of the simulation results. The system is equilibrated at 300 K for 300 ps before applying laser irradiation. The simulations are performed with a computationally-efficient parallel code implementing the combined TTM-MD – coarse-grained MD model, with a three-dimensional treatment of the electronic heat conduction in the TTM-MD part of the computational system.

The implementation of the model used in this work does not account for ionization of the ejected plume, as simple estimations based on the Saha-Eggert equation[158-159] suggest that the degree of ionization in the ablation plume is negligible under irradiation conditions applied in the simulations reported in this chapter. As a result, the nanoparticle formation through nucleation around ion seeds in "misty plasma" considered for high fluence nanosecond PLAL**Error! Bookmark not defined.**[51, 160] is not relevant to the milder irradiation conditions and short pulses considered in the present work.

6.3. Results and discussion

6.3.1. Visual picture of laser-materials response to sub-surface voids

The results of the simulation are illustrated by a series of snapshots shown in Fig. 6.1, which reveal rich dynamics of the superheated material undergoing an explosive decomposition into liquid and vapor. The deposition of laser energy is largely localized within the top thin layer that covers the underlying void. The superheated layer undergoes phase explosion and expands in both directions, as schematically shown by the two arrows on the density contour plot in Fig. 6.2a. Similar to the simulation discussed in section 4.3.3, the upward expansion of the top part of the film is decelerated by the water environment, and the products of the phase explosion (Ag vapor and small clusters) are accumulated at plume – water interface and form a hot metal layer. The downward expansion of the bottom part of the film results in a rapid collapse of the void within the first ~40 ps after the laser pulse, and is followed by formation of two vortexes on both sides of the thin wall that connected the initial top layer with the bulk of the target, as depicted in Fig. 6.3. The heating and lateral compression of the thin wall by the colliding vortexes rapidly melts and accelerates the wall material in the vertical direction, leading to the disintegration of the wall by ~ 1 ns (Fig. 6.1). The rebound of the hot plume from the wall leads to the formation of low-density vapor regions near the wall by 200 ps (Figs. 6.1 and 6.3) and accumulation of the material in the central part of the original void (snapshot for 500 ps in Fig. 6.1). The net results of the complex material flow dynamics illustrated in Fig. 6.3 is the overall upward acceleration (rebound) of the lower part of the plume from the bulk of the target, as shown by the lower arrow in Fig. 6.2a.

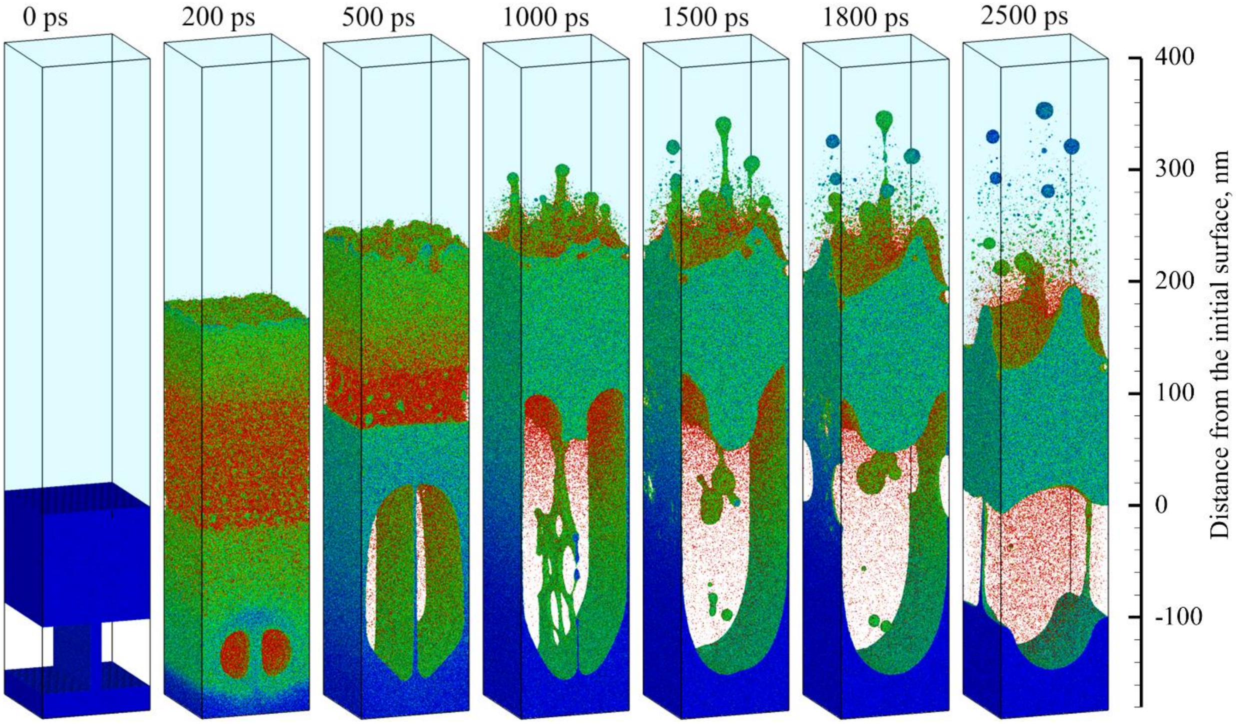

Figure 6.1. Snapshots of atomic configurations predicted in a simulation of a bulk Ag target with a subsurface void irradiated *in water* by a 100 fs laser pulse at an absorbed fluence of 300 mJ/cm^2. The irradiation conditions correspond to the regime of phase explosion confined by the water environment. Only parts of the computational system from -180 to 400 nm with respect to the initial surface of the target are shown in the snapshots. The atoms are colored according to their potential energies, from blue for solid Ag to green for molten Ag, and to red for vapor-phase Ag atoms. The molecules representing water environment are blanked and the presence of water is illustrated schematically by a light blue region above the Ag target.

The rebounded material moves up and eventually makes an impact to the floating molten layer formed by accumulation of the upper part of the phase explosion plume at the interface with the water environment. The impact occurs at ~800 ps and results in the formation of several nanojets or spikes rapidly extending into the water environment. These spikes elongate toward the colder water region and rupture to produce large droplets/nanoparticles with diameters on the order of tens of nanometers. A total of eight large nanoparticles are formed through the breakup of multiple liquid nanojets, with some of the nanojets producing more than one nanoparticle, as can be seen from the snapshots in Fig. 6.4 that are focused on the metal-water interface and the time span when the nanojets are generated. The diameters and the corresponding numbers of atoms in the eight large nanoparticles at a time of 2.5 ns are as follows: 15.8 nm (119,909 atoms), 14.3 nm (89,496 atoms), 13.1 nm (67,936 atoms), 12.3 nm (57,349 atoms), 11.1 nm (41,683 atoms), 11.0 nm (40,799 atoms), 10.0 nm (30,761 atoms), and 9.8 nm (29,073 atoms).

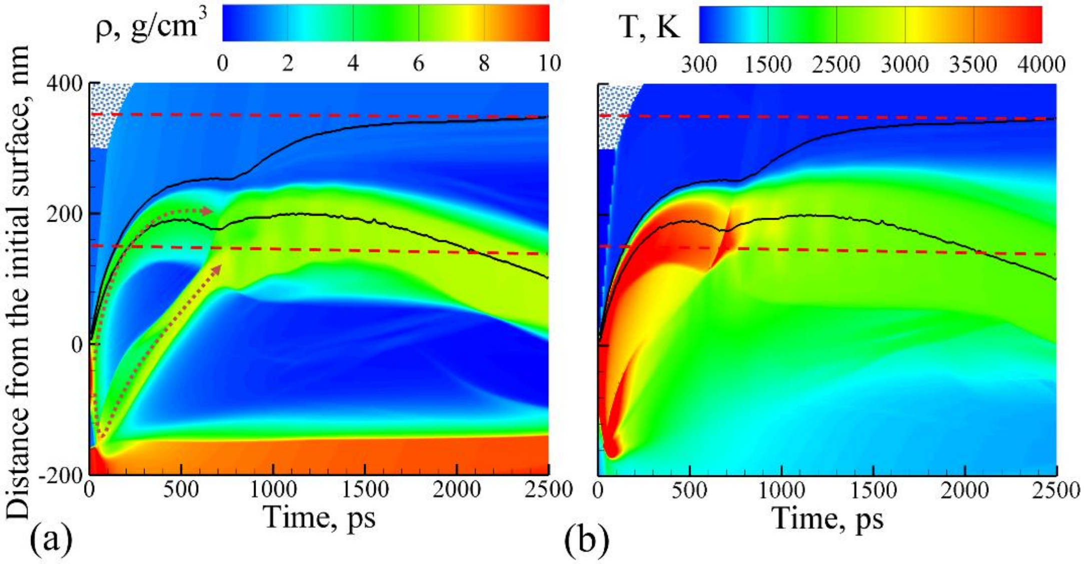

Figure 6.2. Density (**a**) and temperature (**b**) contour plots predicted in a simulation of a bulk Ag target with a subsurface void irradiated *in water* by a 100 fs laser pulse at an absorbed fluence of 300 mJ/cm^2. The two black lines outline the water-Ag mixing region defined as a region where both water molecules and Ag atoms are present. The blue dot background in the upper left corners of the plots represents the presence of water beyond the pressure-transmitting boundary applied at the top of the water layer explicitly simulated with coarse-grained MD. The two dashed orange arrows in (**a**) show schematically the colliding trajectories of the hot molten layer generated at the interface with water environment and a colder molten layer approaching it from the bottom. The two horizontal dashed red lines outline the region for which snapshots of atomic configurations are shown in Fig. 6.1.

The lower row of snapshots in Fig. 6.4 shows the origin of atoms that end up in each of the eight nanoparticles. It can be seen that before the impact from the rebounded material, all the atoms that contribute to the large nanoparticles are already present inside the liquid layer and are mostly located within the trough regions of the layer, suggesting that the roughness of the interface plays an essential role in the formation of the nanoparticles. Moreover, consideration of an overlap of the shapes of the interface before and after the rebounded materials impact (700 and 1100 ps, respectively), shown in Fig. 6.5, clearly demonstrates that the liquid spikes are jetting out from the trough areas of the interface.

As discussed in section 4.3.4, the initial roughness of the water-metal interface is produced through the Rayleigh-Taylor instability of the interface undergoing strong deceleration directed from the lighter supercritical water toward the heavier hot metal layer. By applying analysis described in section 4.3.4 and using the values of deceleration and densities measured at 500 ps after the laser pulse in Eqs. (4-1) and (4-2), the wavelength and timescale of the Rayleigh-Taylor instability are estimated to be $\lambda_m = 64.2$ nm and $\tau = 200$ ps. These values are in a reasonable semi-quantitative agreement with the interface roughness that can be seen in the snapshots shown for 200 and 500 ps in Fig. 6.1.

With the formation of roughened water-metal interface serving as the first step in the generation of large nanoparticles, the second step is the emission of nanojets induced by the backside impact of the rebounded material. The formation of the nanojets can be described in terms of Richtmyer-Meshkov instability that occurs when a shock wave impinges a roughened interface between materials of different density.[195] The shock-driven inversion of the initial surface perturbations and formation of spikes extending into lower-density medium have been analyzed theoretically[196, 205] and investigated in atomistic and hydrodynamic simulations.[206-208] The location of the nanojets and the dynamic material redistribution from the troughs of the interface to the nanojets are consistent with the results of the prior studies. Finally, the extension of the nanojets results in the separation of droplets in a process that can be attributed to the capillary (Plateau-Rayleigh) instabilities driven by the surface tension,[209-210] with water environment certainly playing an important role in defining the dynamics of the nanojets extension and separation of the droplets.

6.3.2. Two nanoparticle generation mechanisms

The new mechanism of the nanoparticle generation revealed in the simulation and discussed above demonstrates that the nucleation and growth from the vapor phase, which is also observed in this simulation (see discussion below and Fig. 6.6), is not the only possible channel of the nanoparticle generation at the early stage of PLAL. While the cascade of the hydrodynamic instabilities responsible for the ejection of the eight nanoparticles into the water environment in the present simulation may look somewhat exotic, the results of the simulations performed for other systems suggest that it is not unique to the target with subsurface voids. In particular, a similar phenomenon has also been observed in a simulation of high fluence short pulse laser ablation of a void-free bulk Ag target in water (to be reported elsewhere) where a spalled layer coming from the deeper part of the target and joining the hot metal layer formed at the interface with the water environment provides the external impact that leads to the jetting and generation of large nanoparticles. Moreover, the roughening of the metal-water interface through the Rayleigh-Taylor instability combined with the general limited stability of thin liquid films[64, 88, 117]may result in direct production of large nanoparticles, as have been observed in a recent simulation of laser ablation of a thin Ag film in water.[179]

As mentioned above, another general mechanism of nanoparticle generation observed in the simulation is the nucleation and growth from the Ag vapor in the low-density mixing region generated due to the interaction of water with the hot metal layer and evaporation of Ag atoms from the metal layer. The expanding metal-water mixing region is outlined by two black lines in Fig. 6.2. As seen from Fig. 6.2b, the average temperature in the mixing regions, while staying above the critical temperature of water, is close and, in the upper part, even below the melting temperature of Ag. Hence, the vapor Ag atoms rapidly condense forming small nanoparticles (up to several nanometers in diameter) on a very short timescale of just several nanoseconds after the laser irradiation. Moreover, some of the nanoparticles located in the upper part of the mixing region solidify on the timescale of the simulation, 2.5 ns. The kinetics of nanoparticle formation through the nucleation and growth in the mixing region is illustrated in Fig. 6.6 and discussed below.

The analysis of the evolution of sizes of the metal clusters and nanoparticles in the mixing region is performed with a cluster identification algorithm applied to atomic configurations generated in the simulation between 100 ps and 2500 ps, with a 100 ps interval. The eight large nanoparticles separated from the liquid jets are not considered in this analysis. The evolution of the cumulative number of Ag atoms present above the liquid layer as individual atoms (vapor) and small atomic clusters with the diameter below 1 nm (less than 30 atoms) as well as the larger clusters that we denote as nanoparticles is shown in Fig. 6.6a. While the total number of Ag atoms in the mixing region steadily increases due to the continuous evaporation from the hot molten metal layer, the number of atoms in the Ag vapor and atomic clusters stays at an approximately the same level starting from 1 ns, and the increase in the total number of Ag atoms in the mixing region is largely sustained by the growing populations of nanometer-scale nanoparticles. Note that the number of vapor-phase atoms and atomic clusters shows an apparent drop at around 800 ps, when the mixing region undergoes a transient compression due to the impact of the rebounded material from backside of the hot metal layer, Fig. 6.2. The compression makes some of the ejected metal atoms rejoin the metal layer, as suggested by the small temporal drop of the total number of Ag atoms in the mixing region, but also facilitates the condensation of vapor and coalescence of clusters into the nanoparticles.

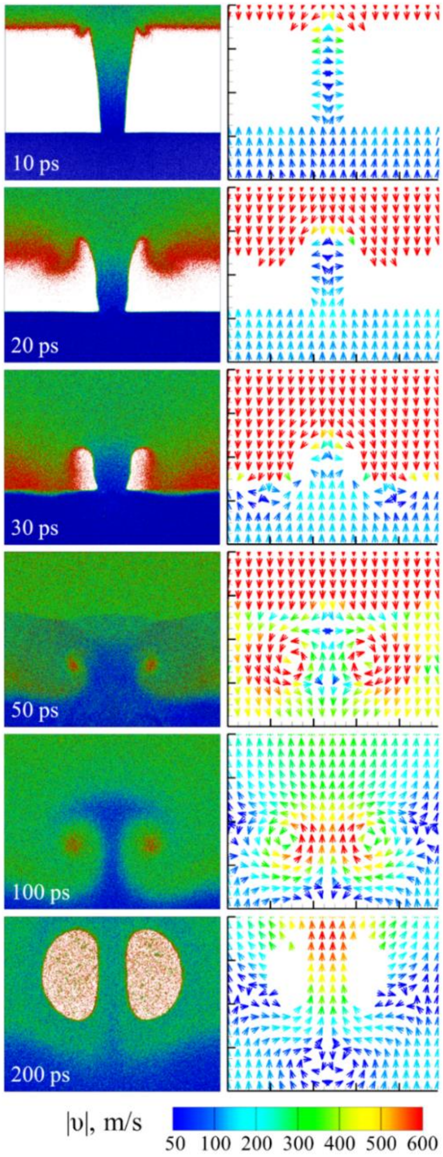

Figure 6.3. Snapshots of atomic configurations (left column) and fields of the material flow velocities (right column) highlighting the void collapse and vortex formation in a simulation of a bulk Ag target with a subsurface void irradiated *in water* by a 100 fs laser pulse at an absorbed

fluence of 300 mJ/cm^2. Only parts of the computational system from -100 to -180 nm with respect to the initial surface of the target are shown. The atoms in the snapshots are colored according to their potential energies, from blue for molten Ag to red for vapor-phase Ag atoms. The magnitude of the flow velocities is shown by color with scale provided at the bottom of the figure.

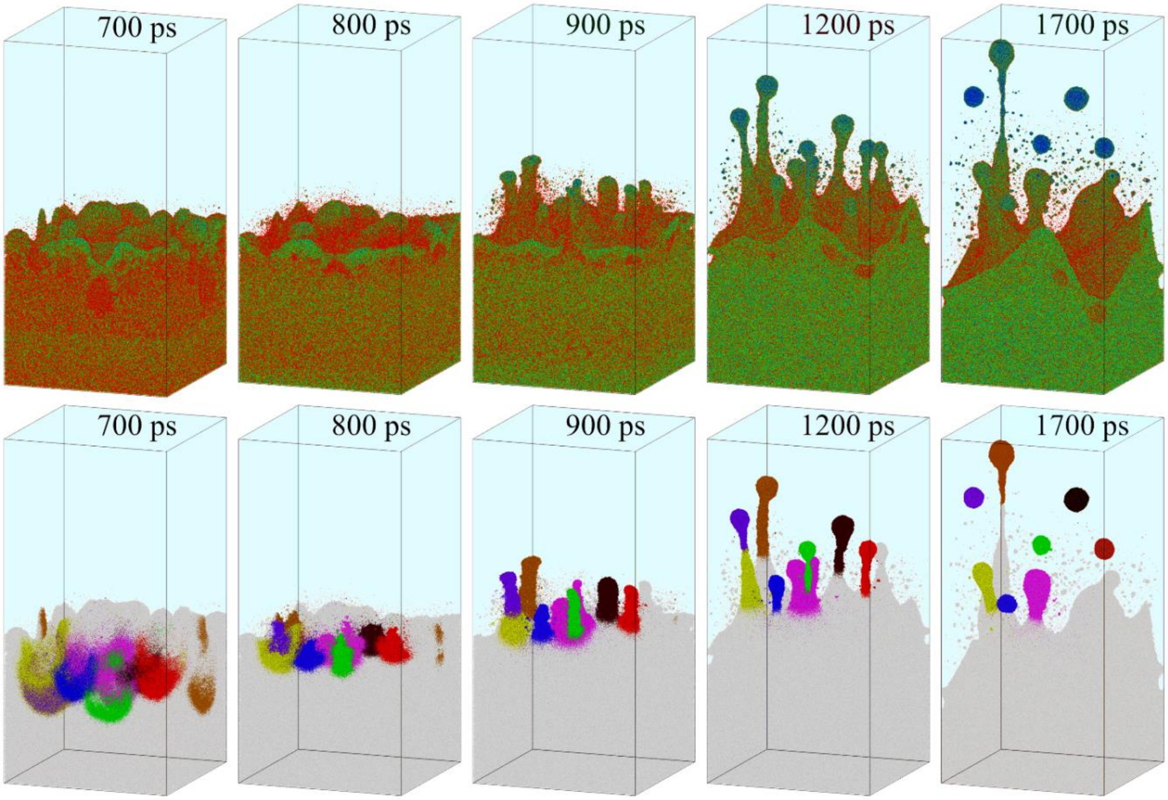

Figure 6.4. Snapshots of the evolution of the hot metal layer – water interface predicted in a simulation of a bulk Ag target with a subsurface void irradiated *in water* by a 100 fs laser pulse at an absorbed fluence of 300 mJ/cm^2. The snapshots are shown for a part of the computational system from 150 to 350 nm with respect to the initial surface of the target and for a time interval when several large (10s of nm in diameter) nanoparticles are ejected from the hot metal layer into the water environment. In the upper row (**a**), the atoms in the snapshots are colored according to their potential energies, from green for molten Ag to red for individual Ag atoms. In the lower row (**b**), the atoms are colored by nanoparticle ID defined by the contribution of atoms to one of the eight large nanoparticles ejected into the water environment via the Rayleigh-Taylor instability (each color except grey corresponds to atoms that end up in one of the eight nanoparticles). The molecules representing water environment are blanked in all snapshots.

Overall, the nanoparticle size distribution broadens and shifts to the larger sizes as time progresses, as can be seen from the nanoparticle size distributions shown in Fig. 6.6b and 6.6c. While the growth of the nanoparticles is still ongoing at the end of the simulation, the size of the nanoparticles generated through the nucleation and growth in the metal-water mixing region can be expected to mostly remain below 10 nm. This size is consistent with experimental observation of the generation of small (< 10 nm) nanoparticles in femtosecond laser ablation of gold[7] and silver[153] targets in pure water. An inspection of the enlarged view of the metal-water mixing region shown in Fig. 6.7a indicates that the largest nanoparticles formed through the nucleation and growth are mostly found in the middle part of the mixing region, where the sufficiently low temperature of the water environment and the high Ag vapor concentration provide the optimum conditions for condensation into Ag nanoparticles.

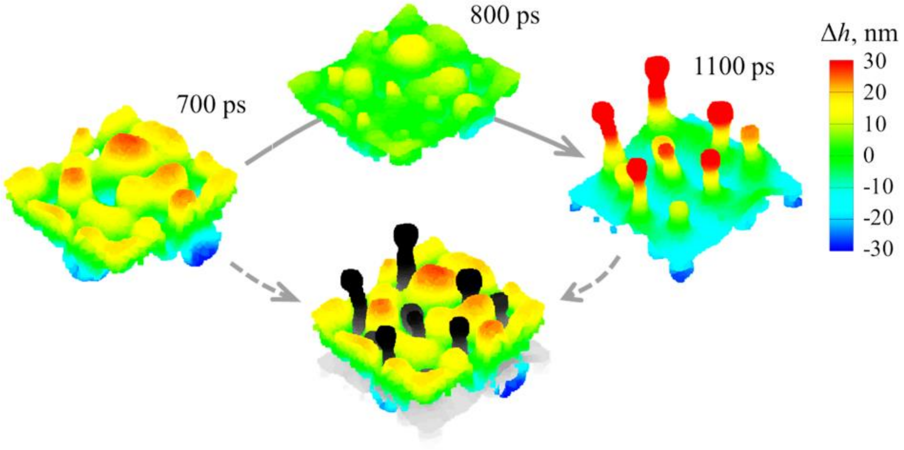

Figure 6.5. The result of the surface reconstruction performed for the hot metal layer – water interface that can be seen in the snapshots in Figs. 6.1 and 6.4. The overlapped view of two surfaces reconstructed for 700 ps and 1100 ps is shown in lower part of the figure, with the surface for 1100 ps colored using grey scale.

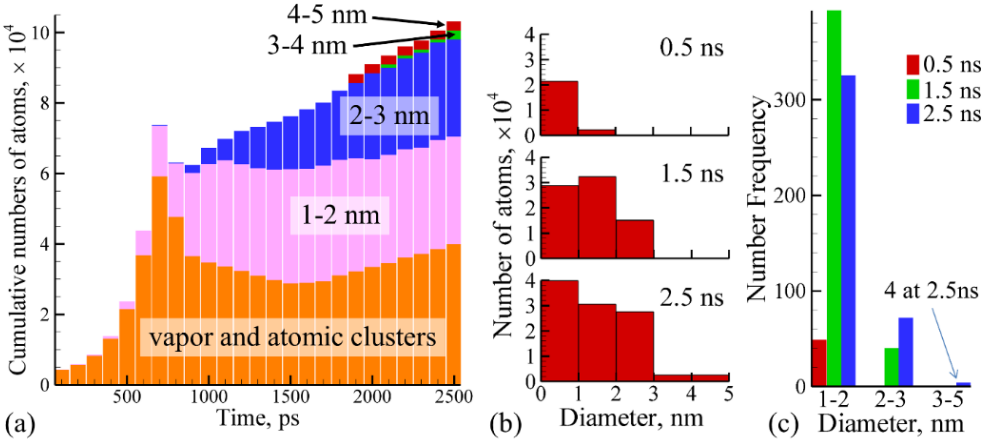

Figure 6.6. The results of the cluster analysis applied to the Ag content of the Ag-water mixing region generated in a simulation of a bulk Ag target with a subsurface void irradiated *in water* by a 100 fs laser pulse at an absorbed fluence of 300 mJ/cm^2. The cumulative number of individual Ag atoms and small clusters with diameters less than 1 nm (orange) and the cumulative numbers of atoms that belong to nanoparticles of different sizes (above 1 nm) are shown in (**a**). The number

of atoms in atomic clusters and nanoparticles of different sizes are shown as histograms for 0.5, 1.5 and 2.5 ns in (**b**). The number of nanoparticles of different sizes is also shown for the same moments of time in (**c**).

An important characteristic of the nanoparticle generation in PLAL, common to both mechanisms revealed in the simulations, is the rapid quenching of the nanoparticles inside the water-metal mixing region. The interaction between the hot metal vapor and water not only brings the water to the supercritical state, but also rapidly cools the metal vapor and nanoparticles down to the temperature that can be sufficiently low to cause solidification of large nanoparticles. As one can see from Fig. 6.7a, the small nanoparticles in the upper part of the mixing region are colored blue, indicating the low level of potential energy that is characteristic of the crystalline state. Indeed, similarly to the small nanoparticles generated through the nucleation and growth in the earlier simulation of PLAL of a thin Ag film,[179] the small nanoparticles in the upper part of the mixing region are found to crystallize within the first nanoseconds after the laser pulse.

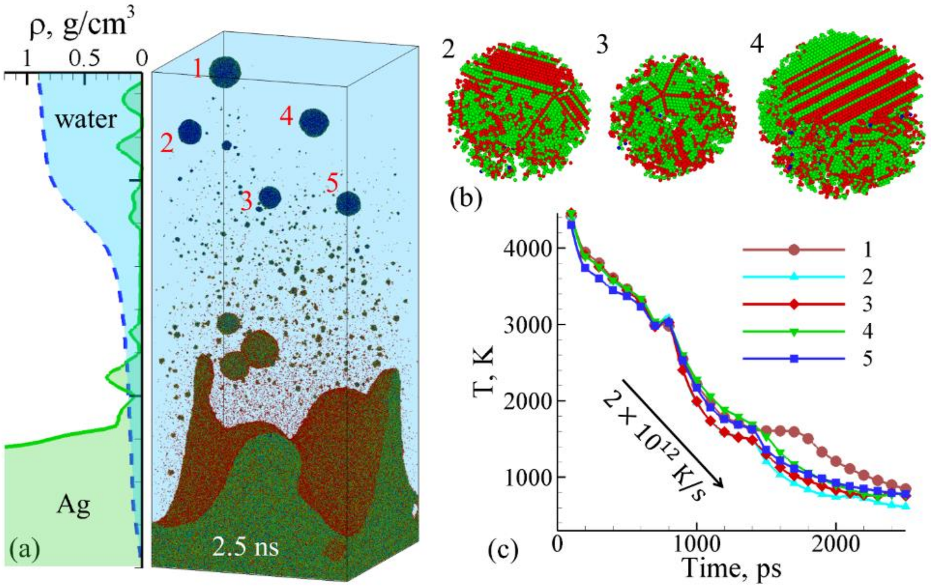

Figure 6.7. (**a**) Snapshot of a part of the final atomic configuration (from 120 to 350 nm with respect to the initial surface of the target) and the corresponding plots of water and silver densities (red dashed and green solid curves, respectively) in the simulation illustrated by Figs. 6.1-6. The atoms in the snapshot are colored by their potential energies, from blue for solid Ag to green for molten Ag, and to red for vapor-phase Ag atoms. The molecules representing water environment are blanked in the snapshot. Five out of eight large (10s of nm) nanoparticles generated via Rayleigh-Taylor instability had already crystallized by the end of the simulation and are indexed in the snapshot. The structure of three of these five nanoparticles are shown in (**b**), where the atoms are colored according to their local structural environment, so that the fcc, hcp, and bcc atoms are green, red, and blue, respectively, while the atoms that belong to the crystal defects and

surfaces are blanked. The time dependence of the average temperature of atoms that end up in the five nanoparticles indexed in (**a**) is shown in (**c**).

The larger nanoparticles produced from the droplets separated from the nanojets also experience a very rapid quenching and solidification. Indeed, the five of the nanoparticles labeled as 1 to 5 in Fig. 6.7a are already solidified by the end of the simulation. The nanojets generated through the Richtmyer-Meshkov instability of the roughened interface are launching the droplets past the low-density part of the mixing region directly into the denser and colder water environment, as can be seen from the density plots shown in Fig. 6.7a. The droplets then quickly cool and solidify through the interaction with water. The thermal history of the material contributing to the five nanoparticles injected into the dense water region is shown in Fig. 6.7c, where the effective cooling in excess of 10^{12} is observed. The high cooling rate is enabled by the suppression of the formation of an insulating vapor layer around the hot droplets by the high curvature of the droplet-water interface, the effect that has been demonstrated in MD simulations of heat transfer from hot nanoparticles to a surrounding liquid.[211-212] As a result, very high heat fluxes from the hot droplets to the water environment can be sustained, the metal droplets can be strongly undercooled, and the crystallization of the nanoparticles can be activated within just several hundreds of picoseconds. Similar timescale of crystallization has recently been reported in MD simulations of the solidification of ZnO nanoparticles in a liquid environment.[213]

The structural analysis of the frozen nanoparticles reveals polycrystalline structure with multiple stacking faults, twin boundaries and pentagonal twinned domains, as well as platelets metastable hcp structure, as illustrated by the structure of three nanoparticles shown in Fig. 6.7b. Similar complex nanostructure has been observed in a frozen nanospike generated in a simulation of laser spallation of an Ag target[89] and attributed to the highly nonequilibrium nature of the rapid nucleation and growth of new crystallites take place under conditions of deep undercooling,[89, 102] along with the low stacking-fault energy of Ag.[214] The polycrystalline structure has also been experimentally observed in Ag nanoparticles generated in femtosecond pulse laser ablation of a solid Ag target in water,[153] *i.e.*, for conditions similar to the ones used in the present simulations. In general, the ultrafast quenching and solidification rates suggest that PLAL can be an effective technique to generate nanoparticles with highly nonequilibrium metastable structures and phases.

The computational prediction of the existence of two distinct mechanisms of nanoparticle formation is consistent with experimental observations of bimodal nanoparticle size distributions in femtosecond PLAL[7-8] and can be related to the results of recent time-resolved SAXS probing of the cavitation bubble dynamics,[44-47] where two groups of nanoparticles, with different characteristic sizes have been observed to emerge at different stages of the bubble evolution. The SAXS experiments are performed with nanosecond laser pulses, where the formation of the hot molten metal layer at the interface with the liquid environment and the corresponding production of larger "secondary particle" nanoparticles through the breakup of the molten layer still need to be verified in the simulations. Nevertheless, the "primary particles" with sizes below 10 nm are likely to be generated through the same mechanism as the small nanoparticles in the simulations, *i.e.*, the rapid nucleation and growth in the expanding mixing region. The recent experimental conformation that the primary nanoparticles are present at the earliest stage of the cavitation bubble expansion[46] is providing an additional support to this association between the computational predictions and experimental observations.

6.4. Summary

The generation of subsurface voids or, at higher fluences, an extended porous surface morphology can strongly modify the processes induced by subsequent laser pulses applied to the same area on the target. Spatial localization of the deposited laser energy within the top surface layer partially insulated from the bulk of the target by the subsurface voids is shown to result in a substantial reduction of the threshold fluence for the explosive material disintegration and generation of nanoparticles. The reduction of the threshold for the material ablation and nanoparticle generation can be related to the incubation effect in the multipulse laser ablation in liquids.

While the ablation plume is confined by water and forms a metal molten layer, the water in contact with ablation plume is heated up beyond supercritical states. The expansion of superheated water results in low-density vapor region between plume and water interface. Ag vapor atoms can evaporate from the metal molten layer to low-density vapor region to nucleate and grow as nanoparticle less than 10 nm. The decelerated metal molten layer by the pressure from supercritical water induces nanoscale surface roughness on the surface metal molten layer on the timescale of hundreds of picoseconds. Moreover, the backside impact of the rebounced material joining the hot molten layer at a later time can induce Richtmyer-Meshkov instability of the roughened interface and result in the formation of nanojets launching large droplets through the low-density mixing region directly into denser and colder water environment. The rupturing of nanojets produces nanoparticle on the orders of 10s nm, and the ones located in dense water experiences fast quenching that crystalline on the timescale of nanoseconds. The nanoparticle distribution observed in the simulation shows bimodality that agrees with typical femtosecond PLAL experiments.

7. The effect of pulse duration on nanoparticle generation mechanisms in pulsed laser ablation in liquids

7.1. Introduction

Pulse duration has known to be one of the key parameters to optimize nanoparticle productivity in PLAL[11, 40] for advanced industrial applications. To further utilize the potential of PLAL for various applications, a fully-tunable narrow nanoparticle size distribution is also necessary. However, broad nanoparticle size distributions with diameters ranging from few to hundreds of nanometers are commonly reported[2] regardless pulse duration and ablated target. In order to obtain desirable narrow nanoparticle size distribution for advanced applications, time consuming post-irradiation processes have to be carried out.[11] Interestingly, with sufficient statistics and proper experimental setup that prevents simultaneous post-irradiation, the characteristic difference in nanoparticle size distributions between short (< 100 ps) and long (ns) laser pulse emerges: bimodal size distribution (one peak < 10 nm, and another peak on the orders of 10s nm) becomes apparent[7, 183-185] for short laser pulse, but overall nanoparticle size distribution stays broad for long laser pulses. It is clear that pulse duration plays an important role not only to productivity but also to underlying nanoparticle generation mechanisms resulting in different characteristic groups of nanoparticles. Hence, to adequately engineer desirable properties of nanoparticles in PLAL, it is imperative to understand the physical origin of pulse duration dependent nanoparticle size distribution and the underlying difference in nanoparticle generation mechanisms leading to nanoparticles with different characteristic size groups.

The pulse duration dependent metal-laser ablation mechanisms have been studied in details both in vacuum and background gas.[71] For short pulse, the fast laser energy deposition not only leads to sharp temperature rises, but also buildup of strong compressive stress under the stress confinement condition[72, 88, 91, 114, 161] followed by generation of a tensile stress due to material relaxation towards the target surface and photomechanical spallation. The contribution of thermo-elastic stress can significantly increase the ablation efficiency and change the compositions of ejected plume at laser fluences beyond the threshold of onset of phase explosion.[107-108, 215] While the pulse duration extended beyond the conditions of stress confinement or into nanosecond regime, the ablation is predominated by explosive boiling[107-108, 215] with contribution from expulsion of molten materials through recoil pressure.[144] While well-developed, the fundamental knowledge obtained from laser-metal interaction in vacuum cannot be directly applied to PLAL. The recent series of MD simulations of pulsed laser ablation in liquid performed in the irradiation regimes corresponding to photomechanical spallation and phase explosion in vacuum[190] show that liquid environment induces strong effect on surface modification of irradiated target and nanoparticle generation of different characteristic sizes. Two nanoparticle generation mechanisms have been proposed based on the simulation results and provide a convincing connection to commonly observed bimodal nanoparticle size distribution. The first mechanism is the nucleation and growth of small nanoparticles in a low-density metal-ware mixing region (precursor of cavitation bubble in experiments) that produces nanoparticle with characteristic size less than 10 nm.[179, 190] The second mechanism is the disintegration of a dense molten layer at plume-water interface either through thin liquid layer instability or a cascade of hydrodynamic instabilities resulting in nanoparticle with characteristic sizes on the order of 10s nm.[190] While previous MD simulations focus on short pulse (femtosecond and picosecond) laser ablation in liquid,[179, 190] the first effort to explore the microscopic phenomena of the long pulse laser ablation (sub-nanosecond to nanosecond) in liquids with MD simulations is presented in this chapter. The goal of the study is to understand the effect of pulse duration on dynamics of ablation plume-water interaction and nanoparticle generation

The chapter is organized as follows. A brief description of the computational model and parameters of the computational setup is provided in Chapter 7.2. The difference in microscopic pictures of ablation plume-water interaction of large-scale simulations performed at 10 ps and 400 ps is described in Chapter 7.3.1. The mechanisms and kinetics of nanoparticle generation mechanisms for long pulse irradiation are discussed in Chapter 7.3.2. The investigation of microscopic picture of ablation plume-water interaction is extended to 1 and 2 ns in Chapter 7.3.3. A summary of the computational predictions is provided in Chapter 7.4.

7.2. Computational setup

The simulation reported in this chapter is performed with a hybrid computational model combining a coarse-grained representation of liquid, a fully atomistic description of laser interaction with metal targets, and acoustic impedance matching boundary conditions, designed to mimic the non-reflecting propagation of the laser-induced pressure waves through the boundaries of the computational domain. A complete description of the computational model tailored for simulation of pulse laser interaction with Ag in water environment is provided in Chapter 1.2, and below only parameters relevant to the computational setup of the simulation reported in this chapter are described.

One large scale and three small scale simulations are performed with Ag bulk targets covered by water in this chapter. A schematic representation of the computational system used in the simulation is shown in Fig. 1.3. The computational system represents a small region within the laser spot and periodic boundary conditions are applied in the lateral directions, parallel to the surface of the target. The dimension of the computational system in these directions are 49.4 nm × 49.4 nm for large scale simulation, and 4.9 nm × 4.9 nm for small scale simulations. The depth of the surface part of the Ag target represented with atomistic resolution is 500 nm, which corresponds to 70 million Ag atoms for large scale simulation, and 0.7 million for small scale simulations.

The heat transfer in the deeper part of the target is described by the TTM equations solved for lattice and electron temperatures down to the depth of 6 μm. Three and one dimensional treatments of the electronic heat conduction in the TTM-MD part of the computational system are applied for large scale and small simulations, respectively. The part of the water overlayer represented by the coarse-grained MD is 300 nm thick and consists of 8.5 million coarse-grained particles for large scale simulation, and 85 thousand coarse-grain particles for small scale simulation. All systems are equilibrated at 300 K for 300 ps before applying laser irradiation. The absorbed laser fluences and pulse duration are F_{abs} = 600 mJ/cm^2, τ = 400 ps in the large scale simulation, and F_{abs} = 600 mJ/cm^2, τ = 1 ns, F_{abs} = 800 mJ/cm^2, τ = 1 ns and F_{abs} = 600 mJ/cm^2, τ = 2 ns for the three small scale simulations. To match the experimental conditions, the dynamic acoustic impedance matching boundary conditions imposed at the top and bottom of the computational domain are designed to mimic non-reflecting propagation of the laser-induced pressure waves through the boundaries of the computational domain.[101, 150] These boundary conditions implicitly simulate a sufficiently thick liquid overlayer and metal target, so that reflections of the laser-induced pressure waves from the free surface of a thick liquid overlayer and the opposite side of the metal target do not play any significant role in the generation of nanoparticles.

The laser irradiation of the target is represented in the model through a source term added to the TTM equation for the electron temperature.[72] The source term describes excitation of the conduction band electrons by a laser pulse with a Gaussian temporal profile and reproduces the exponential attenuation of laser intensity with the depth under the surface. The optical absorption depth, 12 nm at laser wavelength of 800 nm,[144] combined with the effective depth of the "ballistic" energy transport, estimated to be about 56 nm for Ag[101-102] is used in the source term of the TTM equation.[72, 151] The reflectivity of the surface is not defined in the model since the absorbed laser fluence, F_{abs}, rather than the incident fluence is used in the presentation of the simulation results.

The implementation of the model used in this work does not account for ionization of the ejected plume, as simple estimations based on the Saha-Eggert equation[158-159] suggest that the degree of ionization in the ablation plume is negligible under irradiation conditions applied in the simulations reported in this chapter. As a result, the nanoparticle formation through nucleation around ion seeds in "misty plasma" considered for high fluence nanosecond PLAL**Error! Bookmark not defined.**[51, 160] is not relevant to the milder irradiation conditions in the present work.

7.3. Results and discussion

7.3.1. Microscopic pictures of ablation plume-water interaction

Since the results of the simulation of Ag bulk target in water ablated with 10 ps laser at an absorbed fluence of 600 mJ/cm^2 is reported in Chapter 5, in the current chapter we provide only a brief summary. Fig. 7.1 illustrates formation of large nanoparticles through emission and decomposition of a liquid jet, dynamics of material expansion in short pulse laser ablation in water, and the microstructure of a nanoparticle rapidly quenched in the liquid environment. While an absorbed fluence of 600 mJ/cm^2 is three times above the phase explosion threshold for 10 ps laser irradiation in vacuum, the rapidly released vapor and liquid droplets from the irradiated target surface are collected as a dense molten layer at the plume water interface, as shown in Fig. 7.1a and 7.1b. The water in contact with the molten layer is heated up to supercritical conditions and expands forming a low-density region with suitable thermodynamic conditions that allow Ag atoms evaporate from the dense molten layer to condense and form small nanoparticles (< 10 nm). The dense molten layer is subjected to a series of hydrodynamic instabilities producing large nanoparticles (tens of nm). The molten layer surface is significantly roughened when the rapid deceleration of the ablation plume triggers Rayleigh-Taylor instability, shown in first frame of Fig. 7.1a. The subsequent impact of the spalled layer from the deeper part of the target to the backside of the molten layer (Fig. 7.1b, arrow) causes Richtmyer-Meshkov instability, and a nanojet comes out from the trough area of the molten layer surface. Eventually, the nanojet ruptures into three large nanoparticles (tens of nm); the two large nanoparticles, embedded in the dense water beyond the low-density mixing region, are rapidly quenched below the melting point of Ag and crystallized on timescale of several nanoseconds (Fig. 7.1c). Overall, the simulation suggests two distinctive nanoparticle generation mechanisms that can be related to the bimodal nanoparticle size distribution commonly observed in experiments for short pulsed laser ablation in liquids.

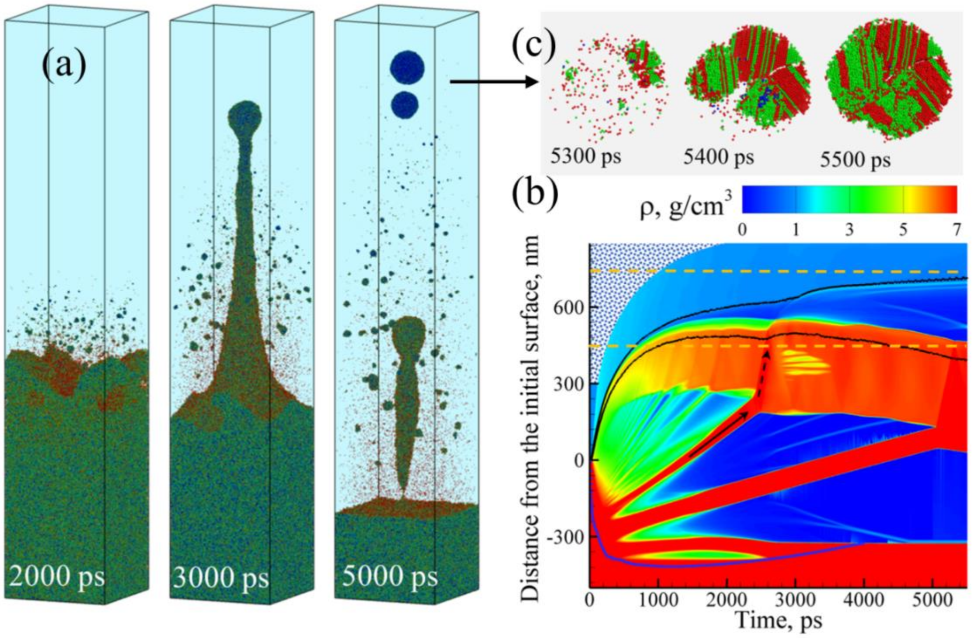

Figure 7.1. (a) Snapshots of atomic configurations and (b) density contour plot predicted in atomistic simulation of laser ablation of a bulk silver target irradiated in water by a 10 ps laser pulse at an absorbed fluence of 600 mJ/cm^2. Only parts of the computational system from 450 to 715 nm with respect to the initial surface of the silver target are shown in the snapshots. The molecules representing water environment are blanked and the presence of water is illustrated schematically as a light blue region above the Ag target. In (b), the blue line shows the location of the melting and solidification fronts. The two black lines outline the water-Ag mixing region

defined as a region where both water molecules and Ag atoms are present. The blue dot background represents the presence of water beyond the pressure-transmitting boundary applied at the top of the water layer that is explicitly simulated with coarse-grained MD. The two dashed yellow lines outline the region for which snapshots of atomic configurations are shown in (a). The solid and dashed arrows show the trajectory of a spalled layer and a pressure pulse generated by collision of this layer with the molten metal layer accumulated at the interface with water environment, respectively. The two yellow-dash lines in (b) shows the part of the computational system (a) is plotted from. The process of crystallization in the topmost nanoparticle ejected from the liquid nanojet is shown in (c). The atoms are colored according to their local structural environment, so that the fcc, hcp, and bcc atoms are colored green, red, and blue, respectively, while the atoms that belong to the melted parts of the nanoparticles, crystal defects, and free surfaces are blanked.

The results of ablation of Ag bulk target in water with a longer, 400 ps, laser pulse at an absorbed fluence of 600 mJ/cm^2 are illustrated in Figs. 7.2-4. The visual picture illustrated by atomistic snapshots in Fig. 7.2 is distinctively different from one obtained from the simulation performed at 10 ps (Fig. 1a). Instead of observing a dense molten layer at the plume front during plume expansion, as described with Fig. 7.1, a mixture of Ag vapor and liquid droplets is formed, as shown in Fig. 7.2 and density contour plot in Fig. 7.3a. The density difference at the plume fronts in simulations performed at 10 and 400 ps can be understood by comparing the effect of laser heating on the Ag target. When the laser pulse duration becomes longer, there is more time for the metal system to redistribute deposited laser energy through thermal conduction and stress wave. While the maximum temperature and pressure in simulation performed with 10 ps laser pulse reaches as high as ~ 12000 K and ~38 GPa, the maximum temperature and pressure in the simulation performed with 400 ps laser pulse is only ~ 8000 K and ~4.8 GPa. The effective thermal conduction to the bulk and reduced level of thermal-elastic stress result in a “gentler” ablation observed in simulation performed with 400 ps laser pulse. While in the simulation performed at 10 ps laser pulse the maximum expansion of the plume reaches the height of 550 nm above the initial surface, and the ablation depth is 325 nm, in the simulation performed for 400 ps the maximum expansion of the plume is only 460 nm with target ablated down to 186 nm. As the result of “gentler” ablation, the effect of vapor and liquid droplet accumulation at the water-plume interface due to water confinement is weaker, so a dense molten layer does not form during the plume expansion stage. Comparing Figs. 7.1b and 7.3a, while the plume front density for simulation performed at 10 ps goes up to ~ $6 g/cm^3$, the plume front in the simulation performed at 400 ps only reaches a density ~ 3.5 g/cm^3 and constitutes with Ag vapor and liquid droplet mixtures.

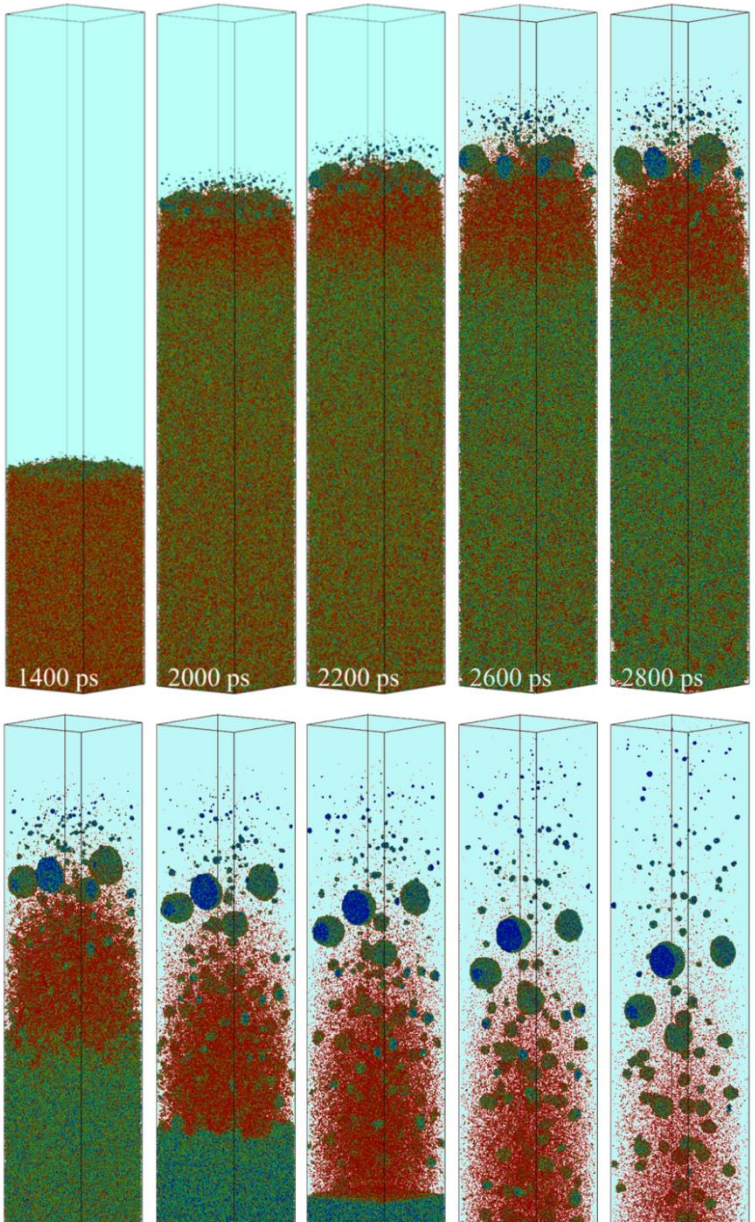

Figure 7.2. Snapshots of atomic configurations predicted in a simulation of a bulk Ag target irradiated *in water* by a 600 ps laser pulse at an absorbed fluence of 600 mJ/cm^2. The irradiation conditions correspond to the regime of phase explosion confined by the water environment. Only parts of the computational system from 195 to 535 nm with respect to the initial surface of the target are shown in the snapshots. The atoms are colored according to their potential energies, from blue for molten Ag to red for vapor-phase Ag atoms. The molecules representing water

environment are blanked and the presence of water is illustrated schematically by a light blue region above the Ag target.

During the initial expansion of the laser plume, the tip of low-density plume front is mixed with the water, as shown by two black lines in Fig. 7.3a and 7.3b. To emphasize the effect of mixing toward microscopic evolution of the plume front, the density and temperature profile in the vicinity of plume-water interface are shown in Fig. 7.3c with corresponding region highlighted in Fig 7.3a. The mixing profiles, Fig. 7.3c, show that the tip of the Ag plume mixed with water has lower density and temperature than unmixed part of the plume front. As the result of cooling by water, a thin transient liquid layer is condensed at plume-liquid interface (Fig. 7.2), where the cooling is the most significant. The formation of this thin transient layer can also be identified from the appearance of a higher density peak adjacent to the dense water from the Ag density profile in Fig. 7.3c

While the metal is cooled down by water in the mixing region, the water in contact with the hot metal is heated up to supercritical states, and water-Ag mixture undergo expansion in both directions and formation of a low-density mixing region above and below the high density layer (R1 and R2 in Fig. 7.3, respectively). Similar to the observation form the simulation of 10 ps laser pulse, hot Ag vapor atom evaporated from the ablation plume can condense to form small nanoparticles, which are readily observed in the first timeframe of Fig. 7.2. The hot water-Ag mixture does not only press up the cold water, but also pushes down the ablation plume. During the downward motion of the ablation plume, the thin transient liquid layer disintegrates, and three large clusters with diameters on the orders of 10s nm are formed. The spatial trajectory of the transient liquid layer and subsequent averaged positions of three large clusters are marked as the black dot lines on Fig. 7.3a and 7.3b. When the ablation plume is pushed downwards, a rapid formation of nanoparticles due to spinodal decomposition of Ag-water mixture is observed in the expanding R2 region, as shown in Fig.7.2. The plume, moving downwards, joins with the material ejected from the deeper part of the target, and a dense molten layer gradually forms after ~ 3100 ps. By extending the pulse duration, the ablation plume-water interaction is altered that results in new pathways of nanoparticle generation. The mechanisms and kinetics of nanoparticles formation for the simulation performed with 400 ps pulse will be discussed in more details in the next section.

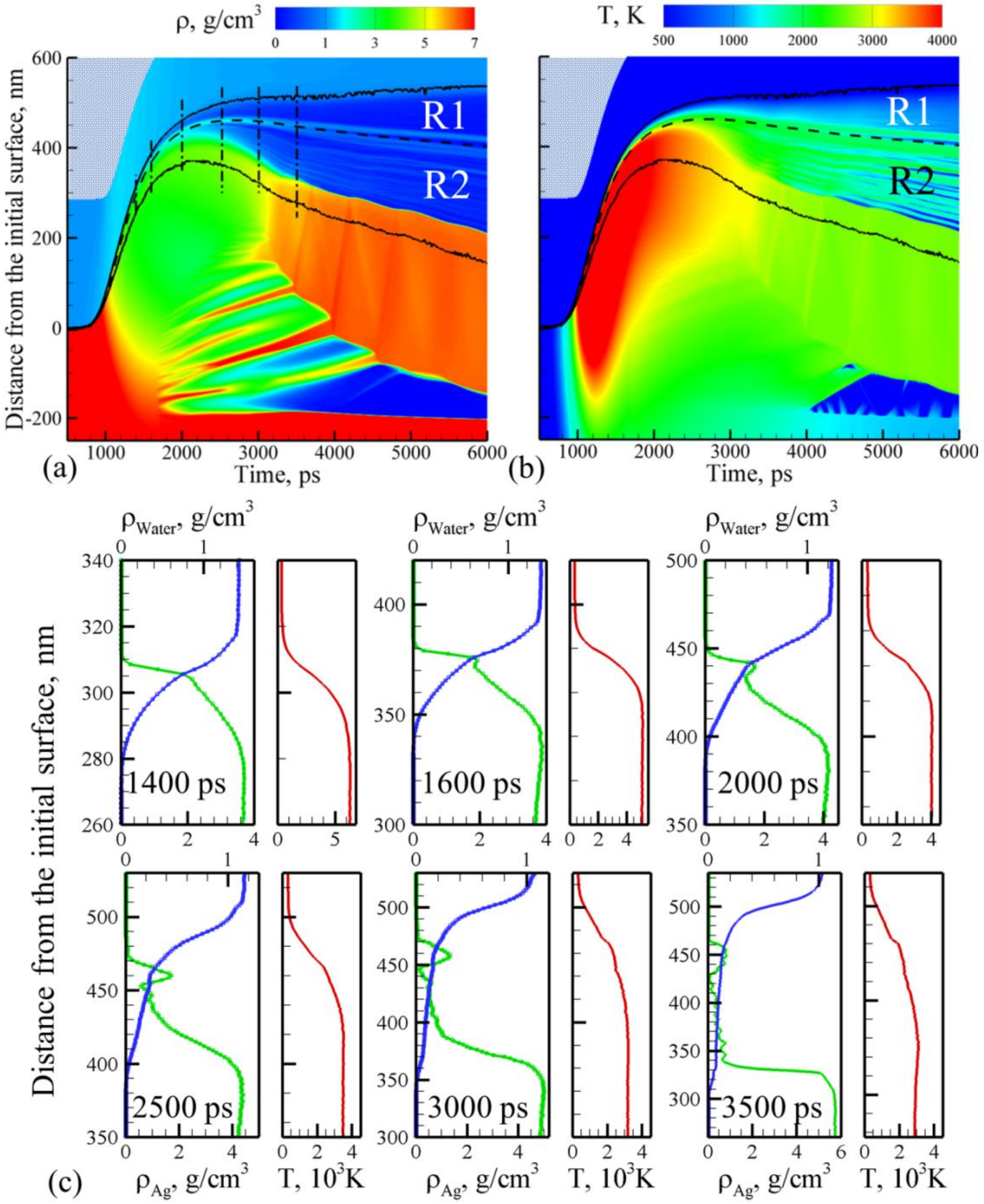

Figure 7.3. Density (a) and temperature (b) contour plots predicted in atomistic simulation of laser ablation of a bulk silver target irradiated in water by a 10 ps laser pulse at an absorbed fluence of 600 mJ/cm^2. The two black lines outline the water-Ag mixing region defined as a region where both water molecules and Ag atoms are present. The blue dot background represents the presence of water beyond the pressure-transmitting boundary applied at the top of the water layer that is explicitly simulated with coarse-grained MD. The blackdashed line show the trajectory of the transient liquid layer and the averaged position of three large nanoparticles ruptured from it. (c) shows the density profiles for water (blue line) and Ag (green line) at the region marked on (a) with dash dot lines along with the temperature profile on the right side.

7.3.2. Nanoparticle generation mechanisms

Three groups of nanoparticles with distinctive characteristic size are generated at different stages in different parts of the ablation plume. As mentioned in the last section, three largest particles with final diameters 16.5 nm (134239 atoms), 14.3 nm (87593 atoms), and 12.5 nm (59382 atoms) are produced from a rupture of a thin transient Ag layer caused by the thin liquid layer instability[64, 117] around ~ 2800 ps. This observation is in agreement with the early MD simulations of PLAL[179, 190] where a thin liquid layer located at the front of the plume can produce nanoparticles on the orders of 10s of nanometers. The position of the layer and the average position of nanoparticles produced after the layer rapture (Figure 3a and 3b, black dotted line) are used to delimitate remaining two groups of nanoparticles, and the results of cluster analysis performed for these groups are shown in Fig. 7.4.

The temporal evolution of the first group of nanoparticles, which are formed in the low density region marked as R2 in Fig. 3, is shown in Fig. 7.4b, d, and f. These particles are formed after a expansion of Ag-water mixture that results in cooling down and spinodal decomposition. The evolution of cumulative number of atoms within R2 region is shown in Fig. 7.4b, and the trend is explained as following. The nanoparticle in R2 actively grows in abundance and size within 2.5-3.5 ns while the region is cooled down. At ~ 3.5 ns, the abundance of nanoparticles in R2 reaches the maximum value when the Ag vapor and liquid droplet mixture at the plume front gradually densifies to form a dense molten layer due to cooling and continuous material accumulation from the deeper part of the target. After 3.5 ns, the overall abundance of nanoparticles in R2 decreases slowly and saturating toward 6 ns, as the continuous downward expansion of Ag-water mixture forces coarsening and merging some fraction of nanoparticles with the dense molten layer. Noticeably, the decrease of the nanoparticle population is mostly resulted by nanoparticles with size less than 4 nm, while larger nanoparticles consume the smaller nanoparticles and grow in size. The nanoparticle distributions at 3, 4.5, and 6 ns are shown in Fig. 7.4d and f in units of the number of atoms and number frequency. While both Fig. 7.4d and f show broadening of the distribution due to coarsening, the majority of nanoparticles form in R2 is shown to be less than 10 nm.

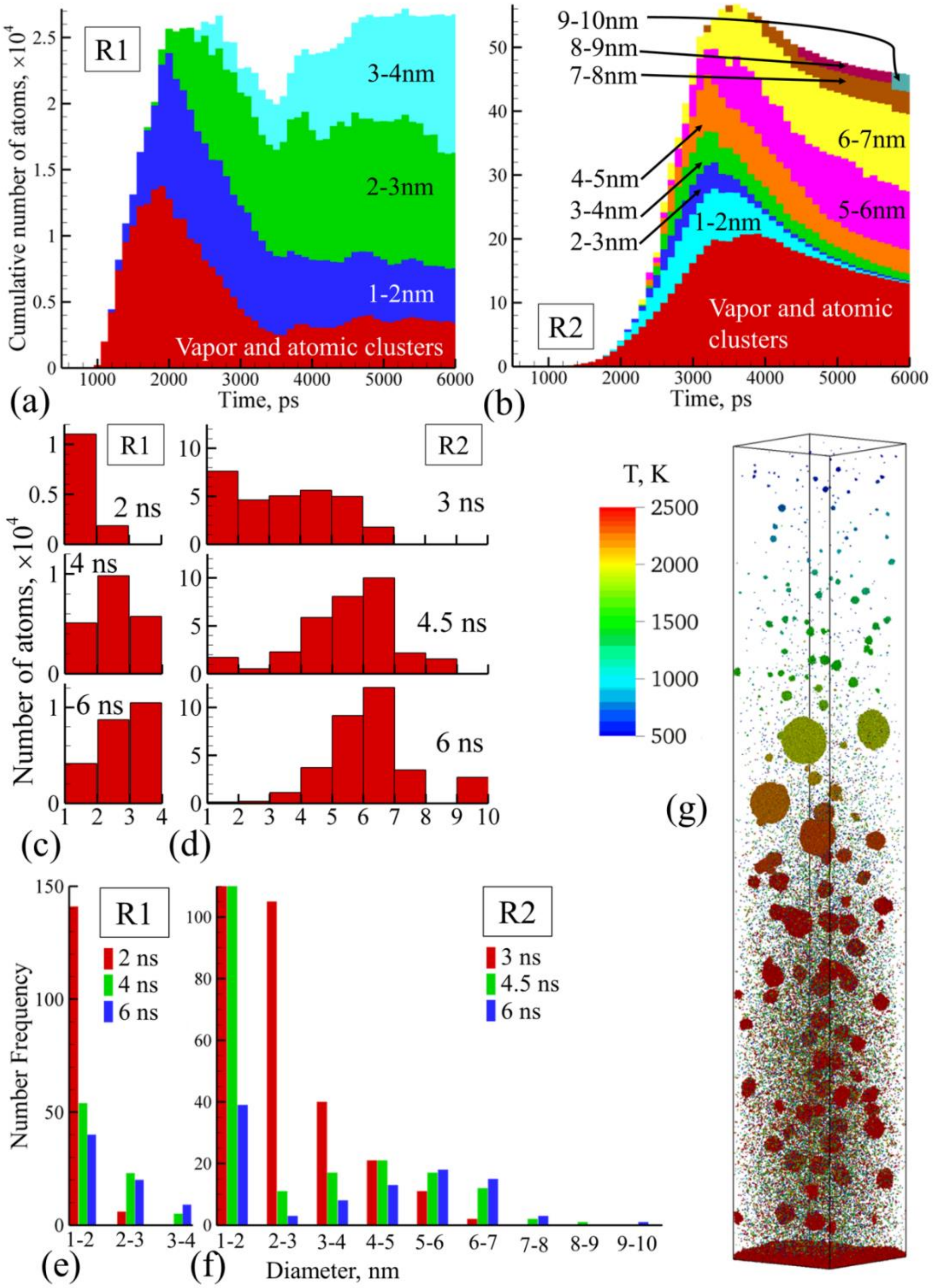

Figure 7.4. The results of the cluster analysis of the ablation plume generated in atomistic simulation of laser ablation of a bulk silver target irradiated in water by a 400 ps laser pulse at an absorbed fluence of 600 mJ/cm^2. The cumulative numbers of atoms that belong to individual Ag atoms/atomic clusters and nanoparticles of different sizes (above 1 nm) are shown in (a) in R1 region and (b) in R2 region (Fig. 7.3). The number of atoms in nanoparticles of different sizes (above 1 nm) are also shown as histograms for 2, 4 and 6 ns in (c) for R1 region, and 3, 4.5, 6 in (d) for R2 region. The number of nanoparticles of different sizes is also shown for the same moments of time in (e) for R1 region, and (f) for R2 region. Snapshot of the final configurations

obtained for 6 ns after the laser pulse in a simulation of a bulk Ag target irradiated in water by a 600 ps laser pulse at an absorbed fluence of 600 mJ/cm^2 colored by local temperature.

The second group of nanoparticle is located above the black dot line in the low-density mixing region marked as R1 in Fig.7.3. The nanoparticles in R1 are formed through condensation of the Ag vapor followed by nucleation and growth. They are observed starting at early stage of the plume expansion starting around ~ 1 ns, when the thin transient layer has not yet formed and detached from the plume front, as can be readily seen from 1400 and 2000 ps timeframes in Fig. 7.2. This nanoparticle generation mechanism has been already discussed based on the results of the simulations of pulsed laser ablation in water[179,190] and is considered as a common route of nanoparticle generation mechanism for pulsed laser ablation in liquids, regardless the pulse duration and target geometry. The kinetics of nanoparticle formation in R1 is shown in Fig. 7.4a, c, and e. The evolution of cumulative number of atoms within R1 is illustrated in Fig. 7.4a, and the trend is explained as following. While the abundance of nanoparticles in R1 region increases from 1 to 2.6 ns, it decreases from 2.7 to 3.5 ns and increases again after 3.5 ns. This unusual trend of nanoparticle abundance evolution can be explained with consideration of the whole ablation plume dynamics with water. Since the nucleation and growth of nanoparticles in R1 requires sources of vapor Ag atoms from the front of the plume, the downward motion of the ablation plume happening at ~ 2.5 ns effectively increases the path that vapor Ag atoms has to travel to R1. Moreover, the active generation of nanoparticles in R2 within 2.7 - 3.5 ns captures the evaporated Ag atoms from the ablation plume. However, while the nanoparticle population in the R2 region starts to saturate, and the dense molten layer is formed at around ~ 3.5 ns, R2 stops to compete the vapor Ag atom sources with R1 region, and the abundance of nanoparticles in R1 region starts to grow again afterwards. As shown in Fig. 4c and 4e, the size of nanoparticles in the region R1 is below 4 nm, and the cumulative number of atoms in this region is approximately 20 times less than the number of nanoparticles in R1 (Fig. 7.4a and b).

The results of simulation also show the importance of location-dependent cooling of nanoparticles, as illustrated in Fig. 7.4g. The temperatures of nanoparticles are spread across the low-density mixing region. While the nanoparticles located near the dense molten layer remain at the temperature above 2500 K, the nanoparticles on the top of the low-density mixing region adjacent to the dense cold water are rapidly quenched below the melting point of Ag. However, the fast quenching of large nanoparticles (10s of nm) is not observed in this simulation in contrast to the simulation performed for 10 ps laser pulse, where large nanoparticles are formed by a cascade of hydrodynamic instabilities, ejected into dense water, rapidly quenched by the surrounding water, and crystallized within 5.5 ns (Fig. 1c). The large nanoparticles formed through rupture of the thin transient layer in the simulation performed for 400 ps laser pulse stay in the middle of the low-density mixing region and have the temperature above ~ 1900 K until the end of the simulation.

7.3.3. Laser ablation in liquids: nanosecond regime

As demonstrated in the previous section, extension of the pulse duration from 10 to 400 ps dramatically changes the dynamics of the ablation plume in water. To further the investigation of the effect of the pulse duration on dynamics of the plume, a series of small scale simulations is performed at nanosecond (in Fig. 7.5). The density and temperature contour plots obtained in the simulation of ablation of Ag bulk target in water environment by a 1 ns laser pulse at an absorbed fluence of 600 mJ/cm^2 are shown in Fig 7.5a and b. Due to even slower heating, the maximum lattice temperature and pressure are only ~ 5000 K and ~2 GPa. The maximum expansion of the plume reaches the height of 390 nm above the initial surface, and after that the ablated material is quickly pushed back to the substrate. The ablation plume consists of the Ag vapor and liquid mixtures (colored in green in Fig. 7.5a), and the subsequent plume dynamics is similar to the simulation performed for 400 ps pulse. A thin transient liquid layer is formed at the plume-water interface due to the effective cooling of the plume surface from water. The mixing of water with Ag below the transient liquid layer also results in rapid nucleation of the Ag nanoparticles, and the superheated water in contact with the plume expands upward forming a low-density mixing region with appropriate thermodynamics conditions for nanoparticle nucleation and growth. Unlike the simulation performed at 400 ps, the formation of a dense molten layer is completely suppressed, and low-density ablation plume is deposited back to the substrate during expansion based on results of small-scale simulation performed at 1 ns. Increasing the absorbed fluence to 800 mJ/cm^2, the maximum lattice temperature and pressure increases to ~ 8000 K and ~2.5 GPa, respectively, leading to more vigorous generation of Ag vapor and liquid mixtures at the plume front and stronger expansion, as shown in Fig. 7.5c and 7.5d. However, the overall dynamics of the ablation plume is similar to the simulation performed for 1ns laser pulse with absorbed fluence of 600 mJ/cm^2, and the three nanoparticle generation mechanisms described in Chapter 7.3.2 can be recalled from Fig. 7.5c.

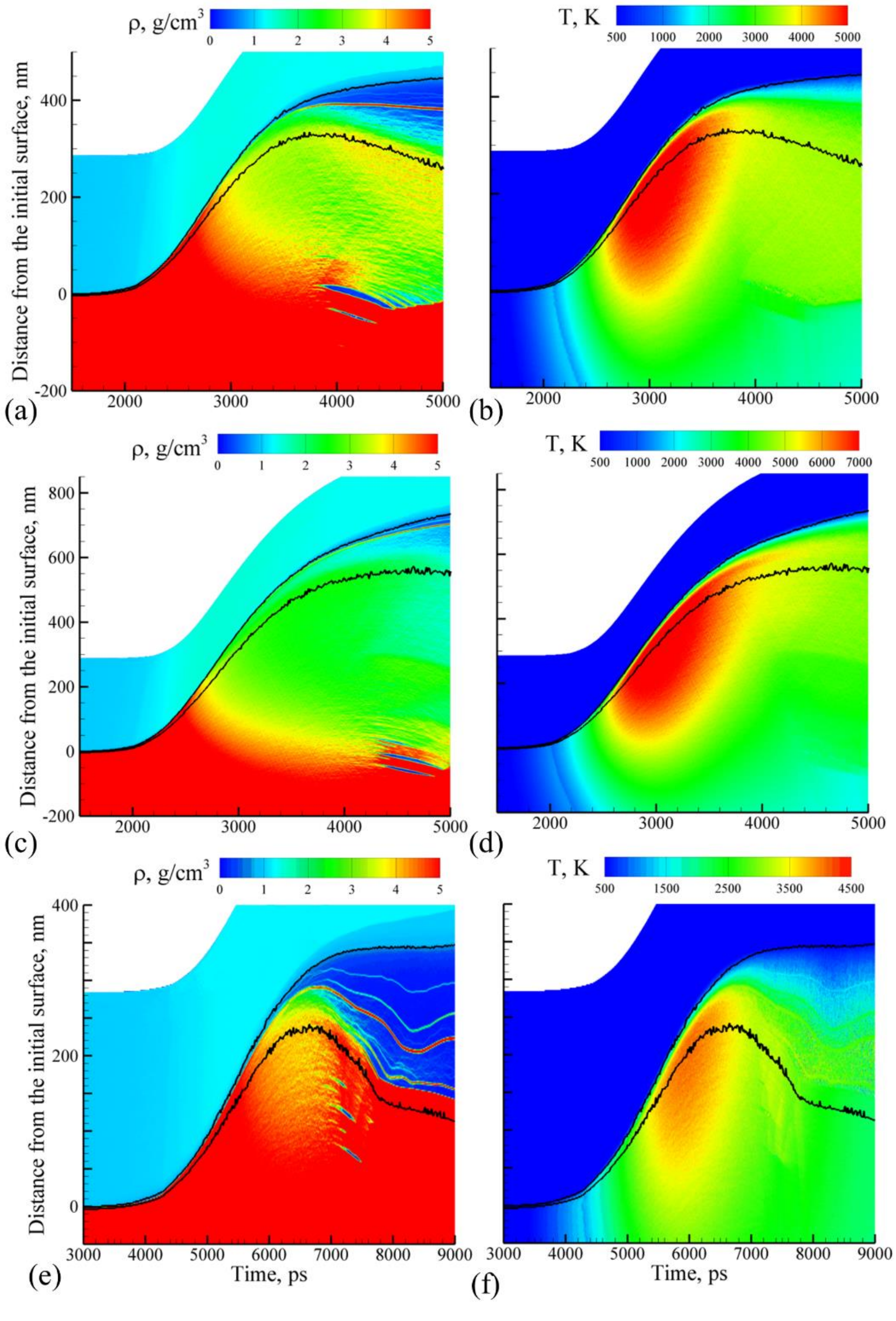

Figure 7.5. Density (a) and temperature (b) contour plots predicted in atomistic simulation of laser ablation of a bulk silver target irradiated in water by a 1 ns laser pulse at an absorbed fluence of 600 mJ/cm^2. Density (c) and temperature (d) contour plots predicted in atomistic simulation of laser ablation of a bulk silver target irradiated in water by a 1 ns laser pulse at an absorbed fluence

of 800 mJ/cm^2. Density (e) and temperature (f) contour plots predicted in atomistic simulation of laser ablation of a bulk silver target irradiated in water by a 2 ns laser pulse at an absorbed fluence of 600 mJ/cm^2. The two black lines in each figure outline the water-Ag mixing region defined as a region where both water molecules and Ag atoms are present.

The last simulation performed at an absorbed fluence of 600 mJ/cm^2 further extends the pulse duration to 2 ns. The corresponding density and temperature contour plots are shown in Fig. 7.5e and f. The maximum lattice temperature and pressure only reaches ~ 4000 K and ~1.3 GPa due to even slower laser heating. The plume only expands to maximum height of 290 nm and is rapidly deposited back to the substrate within 1 ns after the maximum expansion. While the Ag vapor and liquid plume has significantly smaller portion and shorter life span compared to the simulation performed for laser durations 400 ps and 1 ns, three nanoparticle generation pathways observed for are still observable based on Fig. 7.5e.

Based on the series of simulations performed at 600 mJ/cm^2 with pulse duration ranging from 10 ps to 2 ns, the following trends can be concluded. As the pulse duration extends beyond the conditions of stress confinement, the overall plume expansion decreases, the dense molten layer does not form at the plume-water interface during the initial expansion after laser excitation, and Ag vapor and liquid droplets are predominated at plume front. Based on the trend observed so far, one can predict that there is a threshold pulse duration when the plume of Ag vapor and liquid droplets mixture do not form, and the laser heating only results in mild expansion of the heated Ag target surface. Thus, beyond this threshold pulse duration, the only one expected nanoparticle generation pathway is the evaporation of Ag atoms into the low-density region followed by nucleation and growth of nanoparticles. While the simulations performed below the plasma generation regimes, the trend of reduced ablation plume size as pulse duration becomes longer is agreed with the pulse duration effect on ablation efficiency observed in experiments.[216-218]

The observation of a broad nanoparticle size distribution from the simulation is in agreement with the series of time-resolved SAXS experiments probing the process of nanoparticle generation within cavitation bubbles that indicate two groups of nanoparticles with different characteristic sizes appear at different stages of bubble evolution.[44-47] The experimental evidence suggests that the cavitation bubble provides suitable thermodynamic conditions for metal vapor species to nucleate and grow to form “primary particles” with characteristic diameter less than 10 nm. The mechanism of “primary particles” formation is directly supported by the MD simulations of vapor

Ag atom nucleation and growth in low-density mixing region. Nevertheless, the origin of "secondary particles" with characteristic diameters on the orders of 10s nm is less clear. While the signal of "secondary particles" cannot be differentiated in-situ as agglomerates or large spherical nanoparticles, it has been speculated to form through collisions and agglomeration of primary particles at later stage of bubble evolution. However, the recent SAXS experiments[44-47] indicate that "secondary particles" can also be detected at an early stage of bubble expansion,[46] suggesting multiple pathways for generation of secondary particles. The formation of thin transient liquid layer at plume-water interface consistently observed in simulations performed from 400 ps to 2 ns laser pulses offers a plausible connection to the origin of the secondary nanoparticles. The agglomerates reported in SAXS can be related to the thin transient liquid layer observed in simulations that can rupture to large nanoparticles on the orders of 10s nm.

7.4. Summary

A series of atomistic simulations is applied in this work to study the effect of pulse duration on the dynamics of ablation plume-water interaction and generation of nanoparticles in pulsed laser ablation of bulk metal targets in a liquid environment. The series of simulations is performed with a computational model combining a coarse-grained representation of liquid (parameterized for water), a fully atomistic description of laser interactions with metal targets, and acoustic impedance matching boundary conditions designed to mimic non-reflecting propagation of the laser-induced pressure waves through the boundaries of the computational domain.

The comparison of large-scale simulations performed for 10 ps and 400 ps laser pulse on Ag targets shows that the dynamics at the plume front dedicates the subsequent possible nanoparticle generation mechanisms. For simulation performed at 10 ps, the strong effect of stress confinement and rapid accumulation of ablated material results in formation of a dense molten layer at the plume-water interface. Cascades of hydrodynamic instabilities results in disintegration of the molten layer to from large nanoparticles (10s of nm), while the growing low-density region at the plume-water interface allows nucleation and growth of small nanoparticles (< 10 nm). For the simulation performed at 400 ps laser pulse, slow laser heating results in "gentler" ablation, so dense molten layer does not form during plume expansion, and the plume front remains as mixture of ejected vapor and liquid droplets. Mixing with water induces effective cooling of the plume front that facilitates two nanoparticle generation pathways. The top of the plume front that experiences the strongest quenching forms a thin transient liquid Ag layer that can rupture to generate large nanoparticles (10s nm). While below the transient liquid Ag layer, the Ag-water mixture expands and cools down resulting in formation of Ag nanoparticle through spinodal decomposition. Moreover, similar to simulation performed at 10 ps, the nucleation and growth of nanoparticles within the expanding low-density mixing region at the plume-water interface is also observed, showing the common nanoparticle generation mechanism regardless of pulse duration.

Simulations that extend pulse duration to nanosecond regimes show a consistent trend of changing ablation plume front from a dense molten layer to low-density Ag vapor and liquid mixtures. The three nanoparticle generation mechanisms observed in simulation performed at 400 ps are evident in simulations performed with 1 and 2 ns laser pulses. The series of MD simulations explain the origin of broad nanoparticle size distribution commonly observed for nanosecond pulses. Moreover, pulse duration is appeared to be an effective experimental parameter to control the dynamics at plume front that has strong influence on nanoparticle generation mechanisms and corresponding nanoparticle size distributions.

The fundamental difference between short and long pulse laser ablation in liquid in the nanoparticle generation mechanisms is whether significant fraction of ejected materials can be accumulated at plume-liquid interface. However, pulse duration is not the only key experimental parameter that can change the plume dynamics, and there are other intrinsic materials parameters affecting the dynamics at plume front, including but not limited to, the compressibility of liquid, optical and thermal properties of materials.

7.5. Macroscopic schematic of pulsed laser ablation in liquids

A graphical schematic (Fig. 7.6) is illustrated to connect the microscopic findings based on atomistic modeling of bulk Ag target irradiated in water (Chapter 4 – 7) to the macroscopic picture of dynamics between ablation plume and liquid at expansion stage of the cavitation bubble. The schematic does not consider complex hydrodynamic flow inside the cavitation bubble and generation of plasma, but simply confer the insight gained from Chapter 4 – 7 graphically to general audience. The discussion of the graphical schematic is based on laser pulse duration.

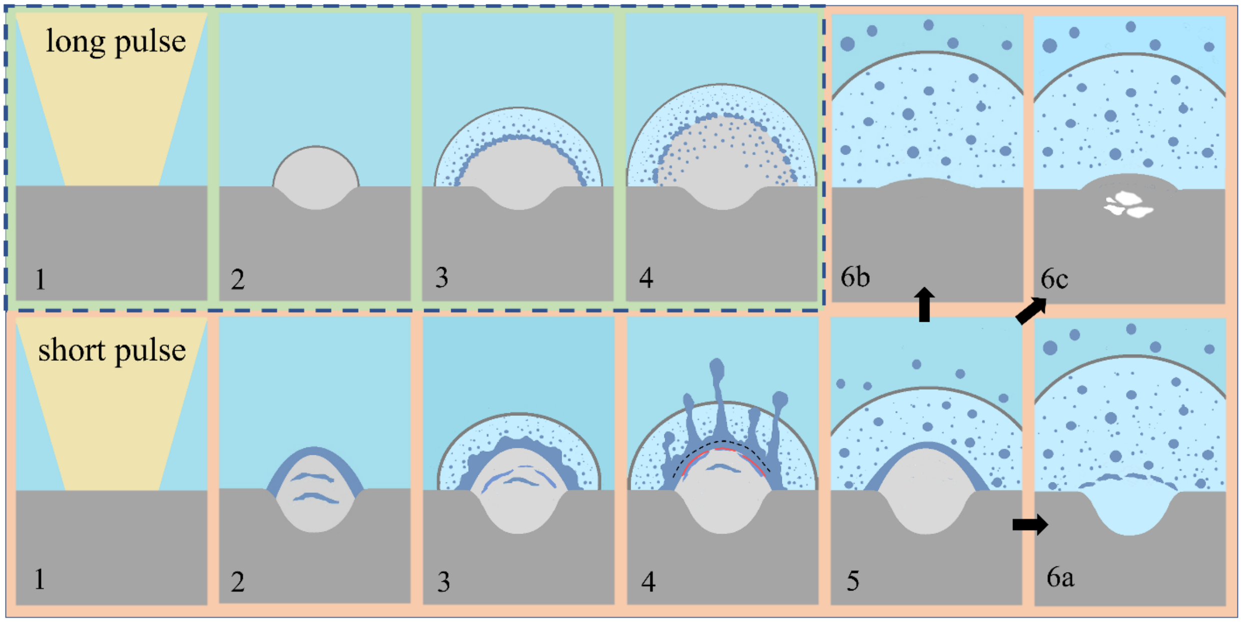

Figure 7.6. The schematic sequence for long laser pulse (in nanosecond regime) is shown in the dashed box with light green background, and the schematic sequence for short laser pulse (in picosecond and femtosecond regime) is shown with the light orange background. The water is colored with blue, and metal target is colored with grey. The ablation plume is colored with light grey, while the cavitation bubble is colored with light blue. The metal liquid layers and nanoparticles are colored with dark blue.

Long laser pulse (nanosecond regime):

For long laser pulse ablation, the surface of the irradiated target undergoes phase explosion results in rapid generation of mixture of vapor and small liquid droplet. However, the expansion of vapor and small liquid droplet mixture is confined by the water environment. (green frame 2 in Fig. 7.6) The water in contact with the ablation plume is heated up beyond supercritical state, and undergoes expansion to form cavitation bubble. The top part of the ablation plume is quenched by water resulting in formation of thin transient metal liquid layer. Metal vapor atoms evaporate into the cavitation bubble to form nanoparticle through nucleation and growth with characteristic size less than 10 nm. (green frame 3 in Fig. 7.6) The thin transient metal liquid layer ruptures into nanoparticles with characteristic size of 10s nm due to thin liquid layer instability. Diffusion of water into deeper part of the ablation plume results in rapid quenching of the plume and massive nucleation of nanoparticles. (green frame 4 in Fig. 7.6)

Short laser pulse (picosecond and femtosecond regime):

For short laser pulse, the condition of stress confinement results in a more vigorous ejection of ablated materials. While the top surface of the irradiate target undergoes phase explosion that generates mixture of vapor and small liquid droplets, colder liquid layers are generated in the deeper part of the irradiated target due to photomechanical spallation. The contribution of thermos-elastic stress facilitates accumulation of ablated materials at the interface between ablation plume and water to form a thick metal molten layer. (orange frame 2 in Fig. 7.6) Nanoscale surface roughness develops at the molten layer due to the Rayleigh-Taylor instability when the higher density metal molten layer is decelerated by the lower density water. The water in contact with the molten layer is heated up beyond supercritical state to form a cavitation bubble. The vapor atoms from the metal molten layer can nucleate and grow in the cavitation bubble to form small nanoparticle with diameter less than 10 nm. (orange frame 3 in Fig. 7.6) The subsequent back-side impact of the spalled liquid layer to the metal molten layer induces Richtmyer-Meshkov instability, so nanojets appear and extend from the trough area of the molten layer surface. The nanojets can grow beyond the boundary of cavitation bubble into the dense water environment. (orange frame 4 in Fig. 7.6) The eventual rupturing of the nanojets forms large nanoparticles with characteristic size on the orders of 10s nm, and some large nanoparticles are embedded beyond the cavitation bubble boundary. (orange frame 5 in Fig. 7.6) Three possible scenario can happen to the metal molten layer: a) The molten layer can disintegrate to large nanoparticle due to thin liquid layer instability. (orange frame 6a in Fig. 7.6) b) The molten layer can deposit back the target. (orange frame 6b in Fig. 7.6) c) The molten layer can freeze while moving back to the target, leading to the large voids formation that can induce strong incubation effect during multi-pulse laser irradiation. (orange frame 6c in Fig. 7.6)

8. Effect of liquid environment on single-pulsed ablative generation of laser induced periodic surface structures and nanoparticle generation

8.1. Introduction

Generation of laser-induced periodic surface structure (LIPSS) has promising applications in surface wettability,[219] tribology,[220] and optics.[221] The physical mechanisms of LIPSS formation are known through the interference of the incident laser and surface electromagnetic waves to create periodic absorption patterns. The main disadvantage of LIPSS inhibiting broad usage in practical application is the long processing time, since the formation of LIPSS requires repetitive irradiation by thousands of laser pulses in the regime of surface melting or mild ablation. Recently, the demonstration of highly regular LIPSS (HR-LIPSS) through a single pulse ablation shows a viable alternative strategy to compete to other industrial surface processing methods.[222-223] In contrast to the traditional LIPSS processing in low fluence regime just above the melting or mild ablation threshold, the laser fluence applied for formation of HR-LIPSS is significantly above the ablation threshold. The recent joint experimental and computational study shows that the mechanism of HR-LIPSS formation is based on redistribution of a mixture of vapor and liquid droplets in ablation plume in a course of spatially modulated laser ablation that leads to formation of a high-density region evolving into a protrusion captured by solidification.[224]

While the development of pulsed laser ablation in liquids (PLAL) has been heavily focused on generation of colloidal nanoparticles, there are numbers of experimental studies showing the potential of PLAL to control surface morphology and microstructure.[167-170] However, the fundamental mechanisms responsible for laser-assisted surface nanostructuring in liquids remain unclear, so the initial demonstration of promising results cannot be transited to a general technique for surface engineering. The recent MD simulations on the modification of surface nanostructure via PLAL shows that liquid environment can not only suppress the nucleation of subsurface voids and facilitate formation of a nanocrystalline surface in irradiation regime of melting and re-solidification,[225] but also help the irradiated target to stabilize surface swelling and capture large subsurface voids in irradiation regime of photomechanical spallation.[190] The goal of this paper is to investigate the effect of liquid environment on HR-LIPSS formation. A rich interplay between spatial modulated energy deposition and interaction between an ablation plume and water is capable not only dramatically change the HR-LIPSS structure, but also shed more light on nanoparticle generation with PLAL.

8.2. Computational setup

The simulation reported in this chapter is performed with a hybrid computational model combining a coarse-grained representation of liquid, a fully atomistic description of laser interaction with metal targets, and acoustic impedance matching boundary conditions, designed to mimic the non-reflecting propagation of the laser-induced pressure waves through the boundaries of the computational domain. A complete description of the computational model is provided in Chapter 1.2, and below only parameters relevant to the computational setup of the simulation reported in this chapter are described. A schematic representation of the computational system is shown in Fig. 8.1. The computational setup is designed and parametrized for a bulk Cr target covered by water and irradiated by a femtosecond laser pulse.

The initial Cr target has bcc crystal structure and (001) orientation of the free surface. The periodic boundary conditions are applied in the lateral directions, parallel to the surface of the target. The initial dimensions of the TTM-MD domain are 260 nm × 43 nm × 140 nm, which corresponds to 131 million Cr atoms. The interatomic interactions are described by the embedded atom method (EAM) potential parametrized for Cr.[87] Above the Cr bulk target, a layer of coarse-grained water with thickness of 300 nm and total of 37.4 million atoms is added. The course interaction between Cr and water is LJ potential; ε is fitted based on the experimental contact angle[226-227] between Cr and water, and σ is the averaged equilibrium distance between coarse-grained water and EAM Cr. At the top of the coarse-grained water layer, a dynamic acoustic impedance matching boundary condition based on an imaginary plane approach[101] is applied to ensure nonreflective propagation of the pressure wave generated at the metal–water interface into the bulk of a thick water overlayer. This boundary condition is suitable for reproducing experimental conditions where the reflection of the pressure wave from the outer surface of the water overlayer does not have any significant effect on processes occurring in the vicinity of the irradiated metal surface.

The electronic heat transfer in the deeper part of the target, where no structural changes take place in response to the laser irradiation, is described by the conventional TTM. The depth covered by the TTM is chosen to be 2.5 μm to ensure a negligible temperature change at the bottom of the computational system by the end of the simulation. A new Langevin Non-Reflecting Boundary (LNRB) condition[224] is imposed at the bottom of the TTM-MD part. The LNRB condition ensures nonreflecting propagation of laser-induced non-planar pressure wave into the bulk of the target, mimicking the elastic response of an infinitely thick target. This approach is suitable for simulation of experimental conditions where the reflection of the pressure waves from the back surface of the irradiated target does not have any significant effect on processes occurring in the vicinity of the irradiated surface. The detail implementation of LNRB boundary condition is reported in ref. 224. Before laser irradiation, the system is thermalized at 300 K for 300 ps.

The thermophysical properties of Cr entering the TTM equations are as follows. The electron heat capacity of Cr is approximated as $C_e = \gamma T_e$ with γ = 194 Jm^{-3}K^{-2}.[228] Constant values of the electron-phonon coupling factor, $G = 4.2 \times 10^{17}$ Wm^{-3}K^{-1}, [229] and the lattice heat capacity in the TTM part of the model, $C_l = 3.23\times10^6$ Jm^{-3}K^{-1},[105] are assumed in the calculations. The temperature dependence of the electron thermal conductivity is approximated by the Drude model relationship, $K_e(T_e,T_l) = v^2 C_e(T_e)\tau_e(T_e,T_l)/3$, where $C_e(T_e)$ is the electron heat capacity, v^2 is the mean square velocity of the electrons contributing to the electron heat conductivity, approximated in this work as the Fermi velocity squared, ${v_F}^2$, and $\tau_e(T_e,T_l)$ is the total electron scattering time defined by the electron-electron scattering rate, $1/\tau_{e-e} = A{T_e}^2$, and the electron-phonon scattering rate, $1/\tau_{e-ph} = BT_l$, so that $1/\tau_e = A{T_e}^2 + BT_l$. The value of the coefficient A = 2.66×10^6 K^{-2}s^{-1} is estimated within the free electron model[122]. Similar to ref.162, the coefficient B is described as a function of the lattice temperature and the phase state of the material, so that the experimental temperature dependence of thermal conductivity of Cr under conditions of electron-phonon equilibrium[123] is reproduced for both solid and liquid states. In particular, this description accounts for the two-fold drop of thermal conductivity as the temperature increases from 300 K to the melting point.

The absorption of laser energy is represented through a source term added to the TTM equation for the electron temperature.[72] The source term has a temporal Gaussian profile corresponding to 200 fs pulse and accounts for the exponential attenuation of the deposited laser energy with depth. The optical absorption depth of Cr is equal to 9.6 nm at the wavelength 258 nm.[230] The absorbed laser fluence is spatially modulated along the *x* direction to represent the periodic absorption pattern generated by the interference of the incident laser wave and surface electromagnetic wave. The period of the sinusoidal modulation is 260 nm, which matches the size of the computational cell in *x* direction, while the maximum and minimum absorbed fluences are 2000 to 3000 J/m^2, which corresponds to 20% modulation of the laser energy deposition with respect to the average level of 2500 J/m^2.

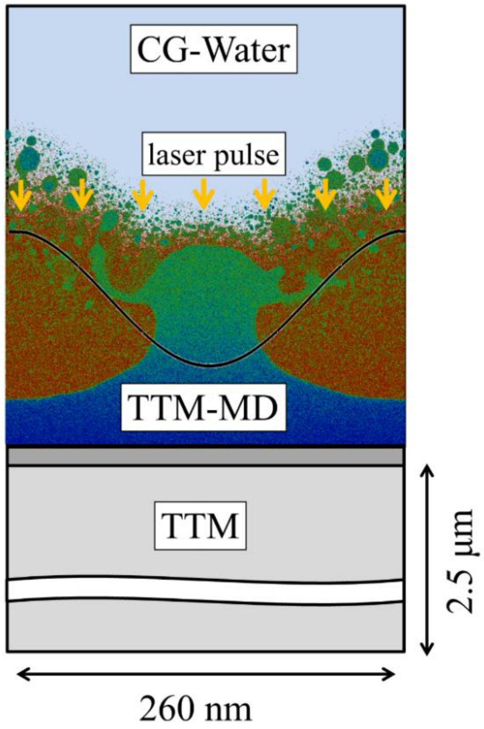

Figure 8.1. Schematic representation of the computational setup used in the simulation of single pulse ablative LIPSS formation with water environment. An atomistic snapshot from the simulation at 500 ps after the laser irradiation is used as background in the representation of the atomistic (TTM-MD). Only parts of the computational system from -60 nm with respect to the initial surface of the Cr target are shown in the snapshot. The molecules representing water environment are blanked, and the presence of water is illustrated schematically by a light blue region that labeled as CG-water. The atoms are colored according to their potential energies, from blue for molten Ag to red for vapor-phase Ag atoms. The black curve shows schematically the modulation of the laser energy deposition along the *x* direction. The continuum part of the model, and dimensions of the atomistic and continuum regions are not drawn to scale.

8.3. Results and Discussion

The laser irradiation produces a spatially modulated energy deposition with average fluence of 2500 J/m^2, while the lowest fluence is 2000 J/m^2 and the highest fluence is 3000 J/m^2. The deposited energy is above the phase explosion threshold of 1500 J/m^2 for Cr ablated with 200 fs pulse. The same irradiation condition applied in vacuum results in the formation of LIPSS with single pulse. The mechanism of the LIPSS formation with single pulse laser ablation is reported in ref. 224, only a brief summary is provided here with illustration in Fig. 8.2. The series of atomistic snapshots, in Fig. 8.2a, shows the visual process of HR-LIPSS formation after laser irradiation. While the whole plume expands upward after laser excitation, the modulated energy deposition induces strong lateral temperature and pressure gradients. Since the peripheral area has higher energy input, a stronger vapor pressure at the periphery drives the vapor and liquid droplets toward the central part, as shown in Fig. 8.2b, where it evolves into a liquid wall with the maximum height ~600 nm. The top part of the wall disintegrates into droplets while the base of the wall solidifies on the timescale of 2 ns. As shown in Fig. 8.2c, the final surface microstructure at 2.1 ns is a solid protrusion with height ~100 nm containing a high concentration of defects.

Introducing a liquid environment above the Cr target drastically changes the dynamics of ablation plume generated in the phase explosion regime, as can be seen from atomistic snapshots in Fig. 8.3. The interaction between ablation plume and water is illustrated in Figs. 8.4, 8.5 and 8.6, where the density profile with velocity vectors, concentration of water, and temperature are presented. The initial upward plume expansion is confined to be within ～150 nm from the initial target surface by the water environment. The plume expansion results in mixing of water at the tip of the plume, the initial narrow mixing region due to plume expansion can be observed on Fig. 8.4b, as the green region. The Cr in this thin mixed layer is quenched rapidly (Fig. 8.4c) and condenses to from a transient liquid layer, which can be seen on atomistic snapshots, Fig. 8.3, and density profile, Fig. 8.4a. While the top part of the plume is cooled down effectively, the water in contact with Cr plume is heated up to the supercritical state. The expansion of the supercritical water results in formation of a low-density water vapor region that is a precursor to a cavitation bubble observed in experiments. A thin water vapor layer, which undergoes expansion in simulation time, can readily be observed during plume expansion, as shown in density profile in Fig. 8.4a. Cr vapor atoms can evaporate into the expanding low-density water vapor region and condense forming nanoparticles (Fig. 8.3). Nanoparticle generation through nucleation and growth in low-density region is observed ubiquitously in previous MD simulations[179, 190] on PLAL, and the computational prediction is consistent with the experimental SAXS study of primary nanoparticle formation.[44-47]

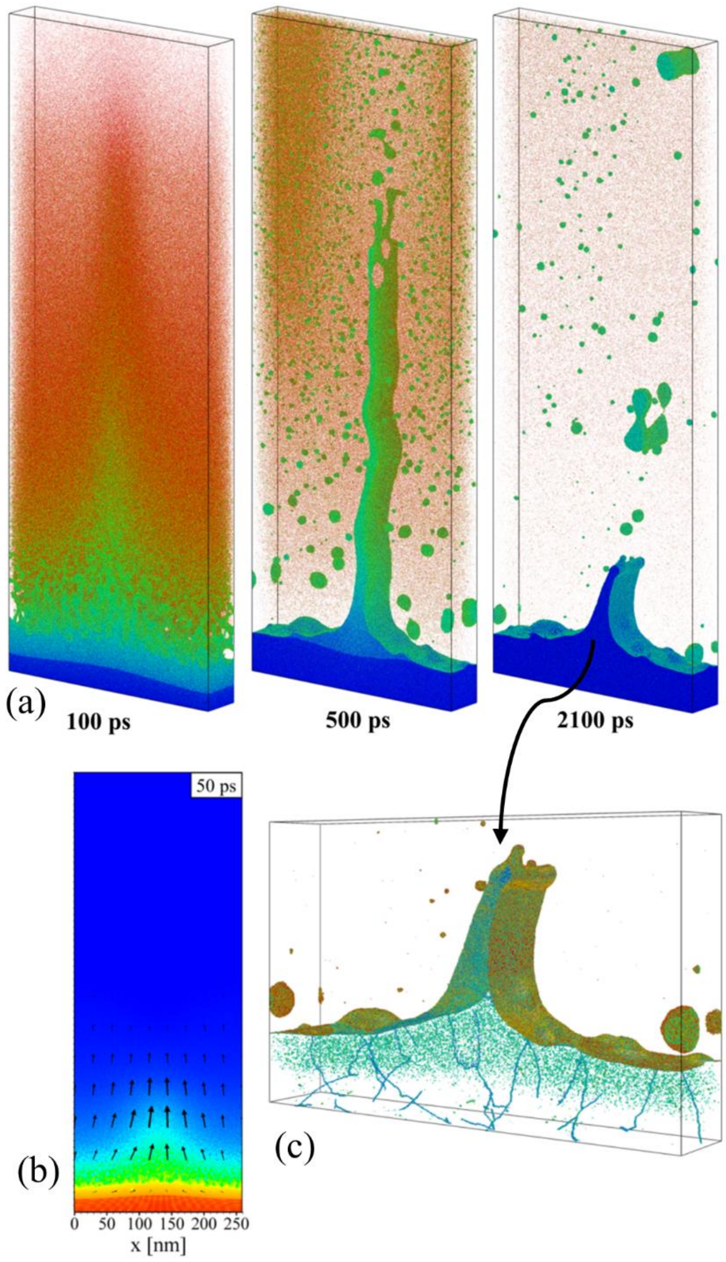

Figure 8.2. (a) Snapshots of atomic configurations predicted in a simulation of a bulk Cr target irradiated *in vacuum* by a 200 fs laser pulse at an averaged absorbed fluence of 250 mJ/cm^2 with 20% of energy modulation Only parts of the computational system from -80 nm to 600 nm with respect to the initial surface of the Cr target are shown. The atoms are colored according to their

potential energies, from blue for solid Cr, green for liquid Cr, to red for vapor-phase Cr atoms. (b) The dynamics of material redistribution at the initial stage of the ablation process. The background corresponds to density distribution with arrows show relative magnitude of material flux density (c) The defect structures of the final microstructure produced after complete resolidification of the target at 2100 ps. Only parts of the computational system from -80 nm to 80 nm with respect to the initial surface of the Cr target are shown. The BCC Cr atoms and single vacancies are blanked. The plot is colored based on potential energy with light-blue to dislocation cores, light-green to vacancy clusters, and green-yellow-red mixture to free surfaces.

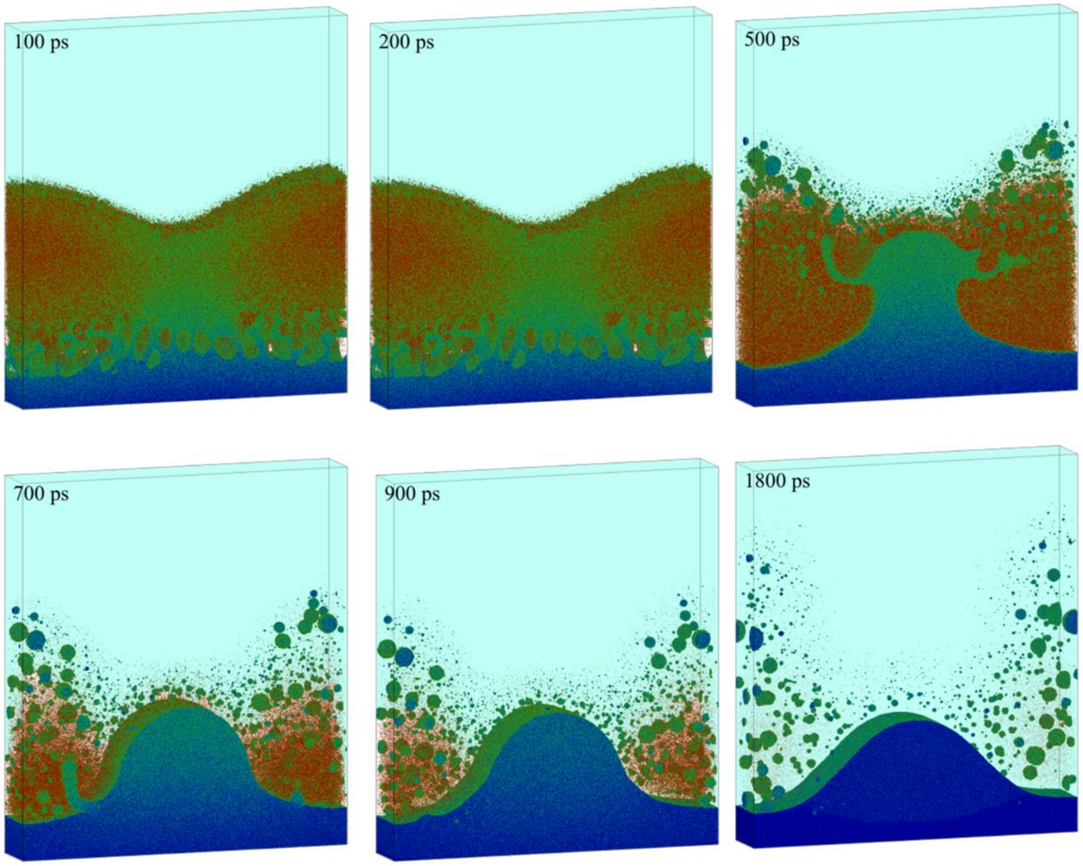

Figure 8.3. Snapshots of atomic configurations predicted in a simulation of a bulk Cr target irradiated *in water* by a 200 fs laser pulse at an averaged absorbed fluence of 250 mJ/cm^2 with 20% of energy modulation. Only parts of the computational system from -60 nm with respect to the initial surface of the Cr target are shown in the snapshot. The atoms are colored according to their potential energies, from blue for molten Ag to red for vapor-phase Cr atoms. The molecules representing water environment are blanked and the presence of water is illustrated schematically by a light blue region above the Cr target.

In addition to formation of thin transient liquid layer through upward expansion and mixing with water, the strong lateral pressure gradients due to the pulse energy modulation results in collective motion of Cr vapor and liquid droplets toward the center, shown by the vector field in

Fig. 8.4a. However, instead of formation of a liquid wall with thickness diminishing gradually above the initial surface, as seen for ablation in vacuum in Fig. 8.2a, the liquid wall formed during ablation in water shows a wing-like transient Cr liquid layer at the plume-water interface. This wing-like layer at the top part of the liquid wall is formed because the water confinement forces the ejected Cr atoms to branch out to the peripheral area. The corresponding velocity vectors are shown in Fig. 8.5a, so the wing-like transient Cr liquid layer, extending from the liquid wall, shows decreasing thickness from the center toward peripheral area.

Due to the confinement by water, the plume is reflected downward by its own vapor pressure, and the process of re-deposition back to the substrate starts after ~200 ps. The process of ablation plume re-deposition is highlighted in Fig. 8.5. The downward motion coupled with the lateral pressure gradient pushing the Cr vapor and liquid droplets toward the liquid wall leads to increase the thickness of the wall and formation of a liquid protrusion. The downward motion also facilitates the diffusion of water into the mixture of Cr vapor and liquid droplets, as shown from the sequence of concentration profile in Fig. 8.5b, e and h. The Cr mixing with water results in fast quenching of the Cr ablation plume that can be seen in the sequence of temperature profiles in Fig. 8.5c, f, and i. The quenching induces a massive nucleation of Cr nanoparticles from the mixture of Cr vapor and liquid droplets. Moreover, during the downward movement of the plume, Cr transient liquid wings disintegrate to large nanoparticles on the orders of 10s nm, as shown in Fig. 8.3, due to thin liquid layer instability[64] that is in agreement with previous MD simulations.[117, 179]

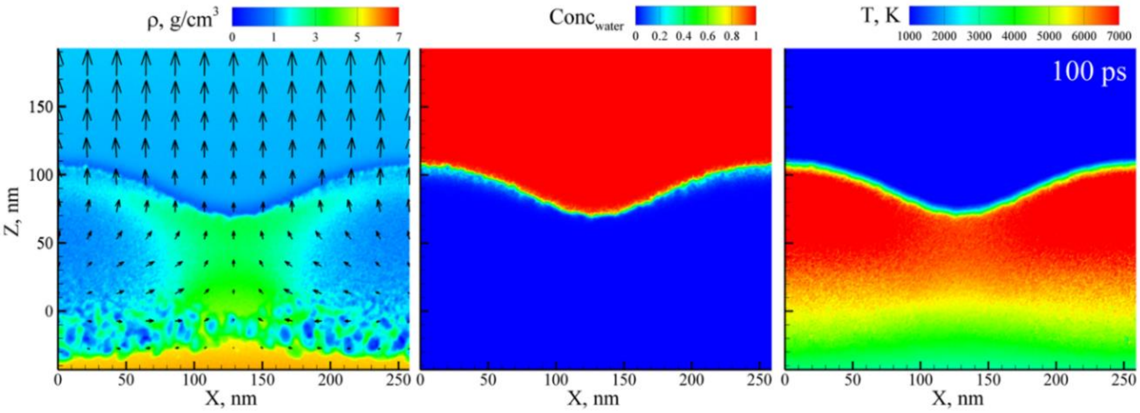

Figure 8.4. The initial expansion of ablation plume predicted in a simulation of a bulk Cr target irradiated *in water* by a 200 fs laser pulse at an averaged absorbed fluence of 250 mJ/cm^2 with 20% of energy modulation. The plots are colored with (a) density and velocity vectors, (b) water concentration, and (c) temperature of the ablation plume plotted at 100 ps. Only parts of the

computational system from -43 nm to 193 nm with respect to the initial surface of the Cr target are shown. The size of the velocity vector reflects its magnitude.

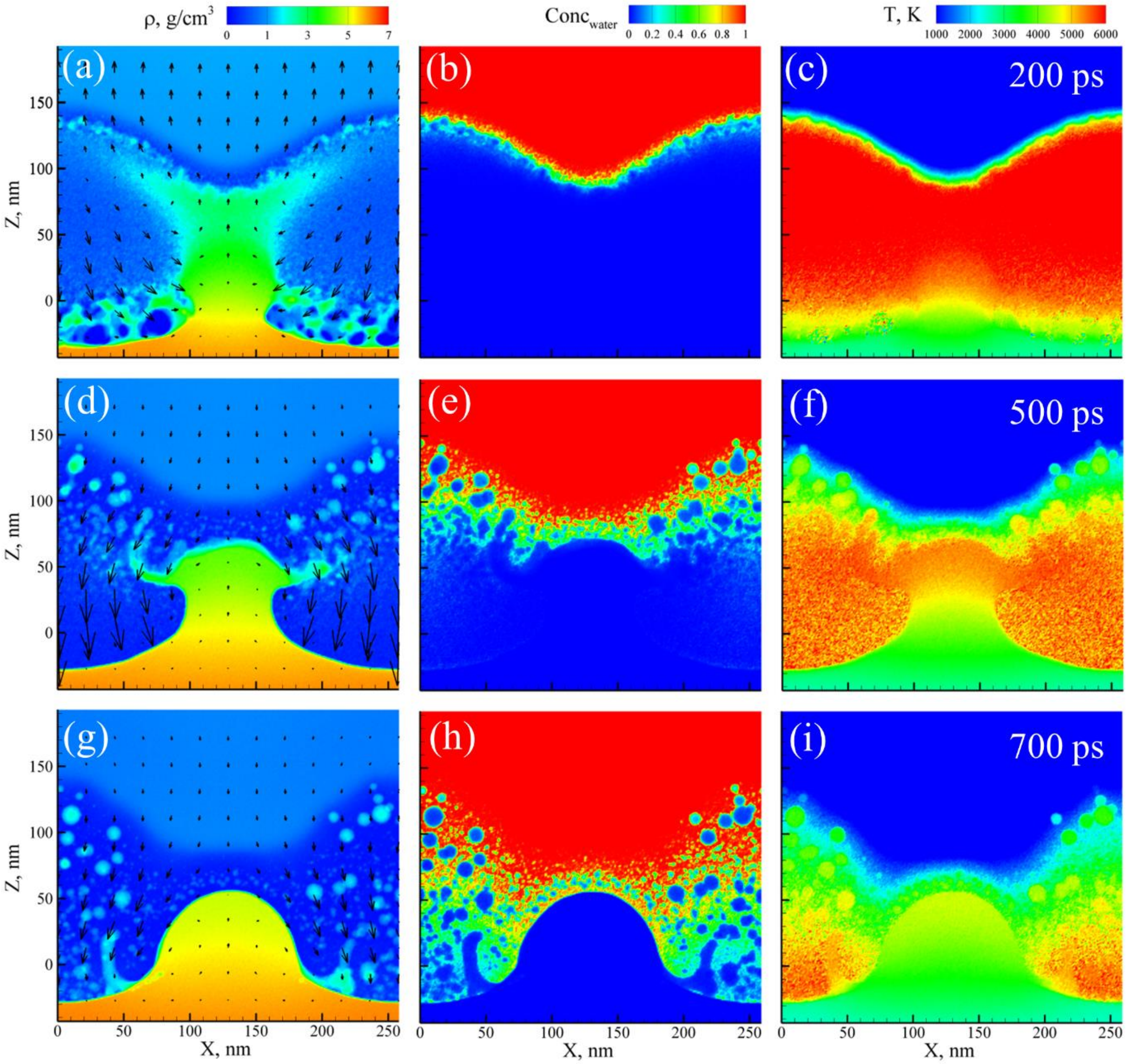

Figure 8.5. The re-deposition process of ablation plume predicted in a simulation of a bulk Cr target irradiated *in water* by a 200 fs laser pulse at an averaged absorbed fluence of 250 mJ/cm^2 with 20% of energy modulation. The plots are colored with (a,d,g) density and velocity vectors, (b,e,h) water concentration, and (c,f,i) temperature at 200, 500, and 700 ps, respectively. Only parts of the computational system from -43 nm to 193 nm with respect to the initial surface of the Cr target are shown. The size of the velocity vector reflects its magnitude, and the size is scaled up by 1.67 times from the vector magnitude in Fig. 8.4.

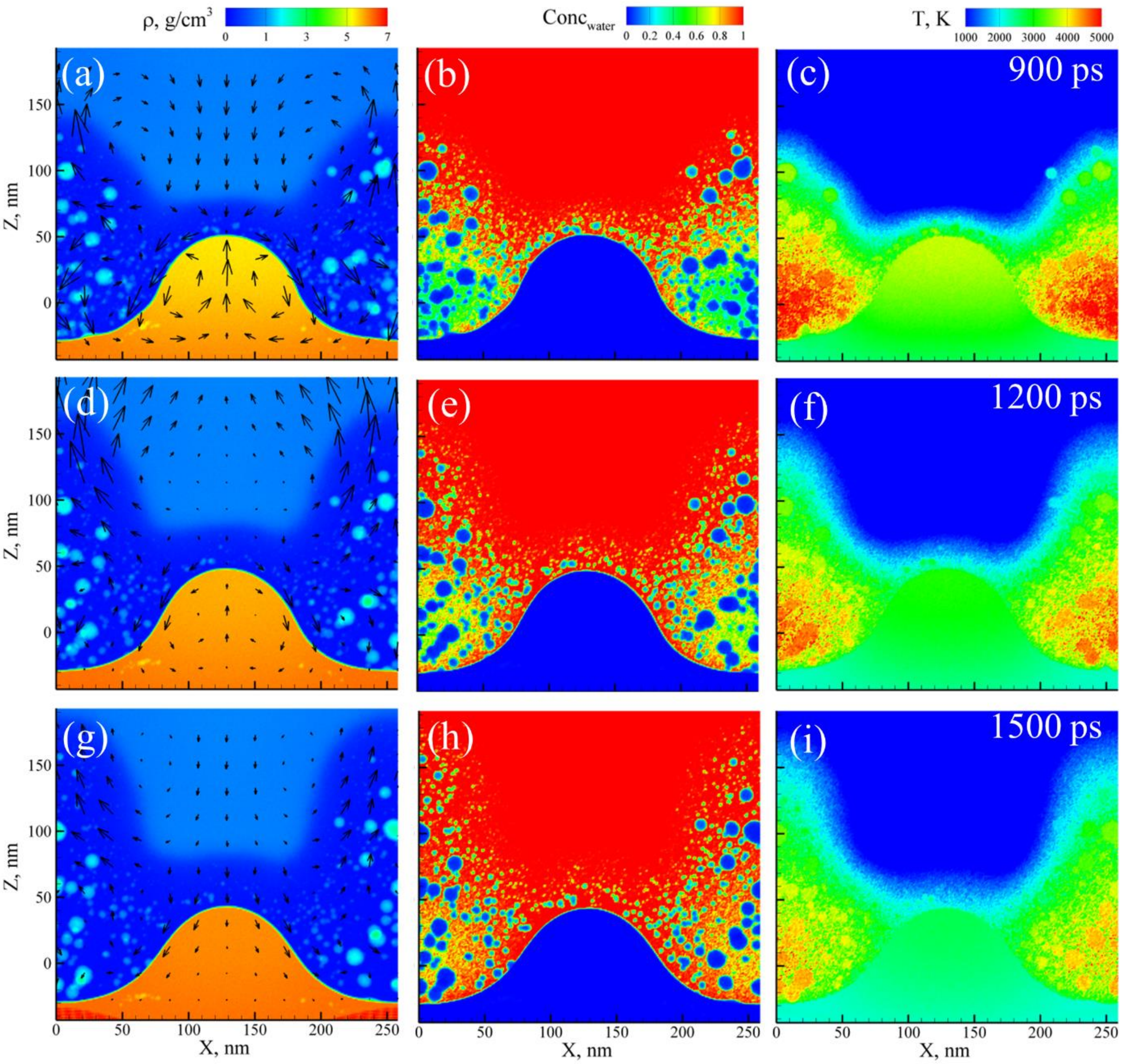

Figure 8.6. The materials flow after liquid wall redepostion predicted in a simulation of a bulk Cr target irradiated *in water* by a 200 fs laser pulse at an averaged absorbed fluence of 250 mJ/cm^2 with 20% of energy modulation. The plots are colored with (a,d,g) density and velocity vectors, (b,e,h) water concentration, and (c,f,i) temperature at 900, 1200, and 1500 ps, respectively. Only parts of the computational system from -43 nm to 193 nm with respect to the initial surface of the Cr target are shown. The size of the velocity vector reflects its magnitude, and the size is scaled up by 13.3 times from the vector magnitude in Fig. 8.4.

While part of the wing-like transient liquid layers disintegrates to large nanoparticles, part of wing-like transient liquid layer is deposited back to the substrate along with the ablation plume. The shape of liquid wall evolves into a semi-spherical bump as it deposited back to the substrate, shown on the sequence of density profile in Fig. 8.5a, d and g. Two vortexes are formed within the semi-spherical bump, as shown in Fig. 8.6a and d. The redeposition results in embedding of water atoms into the substrate, since the re-deposited Cr liquid droplets are mixed with water. Moreover, the vortex flow also keeps the water atoms from escaping the sub-surface. The trapping of liquid species on the substrate surface shows a potential advantage of applications in surface hyper-doping and nanostructuring.

The formation of semi-spherical bump facilitates the lateral flow of Cr-water mixture along the semi-spherical hill to the peripheral area, which can be seen from Fig. 8.5g. The lateral flow collides on the peripheral side, resulting in formation of two vortexes on the periphery near the plume-water interface driving the upper part of ablation plume upwards again around ~ 900 ps (Fig. 8.6 a, d and g). The dynamics of peripheral vortexes result in expansion of low-density mixing region and fast cooling that facilitates the nucleation of small nanoparticles via Cr vapor atom condensation. After approximetly 1500 ps, the complex materials flow observed due to the initial energy modulation dissipates. The cluster analysis performed at 1800 ps (Fig. 8.7) shows a broad nanoparticle size distribution with nanoparticle range from 1 to 18 nm. While Fig. 8.7a shows the conventional number frequency, an alternative representation with *y*-axis as number of atoms in corresponding nanoparticle size is depicted in Fig. 8.7b to highlight the presence of large nanoparticles. While the largest group of nanoparticles is generated through the disintegration of thin liquid layer, smaller nanoparticles are formed through either vapor atom condensation or fast quench of Cr plume by water mixing.

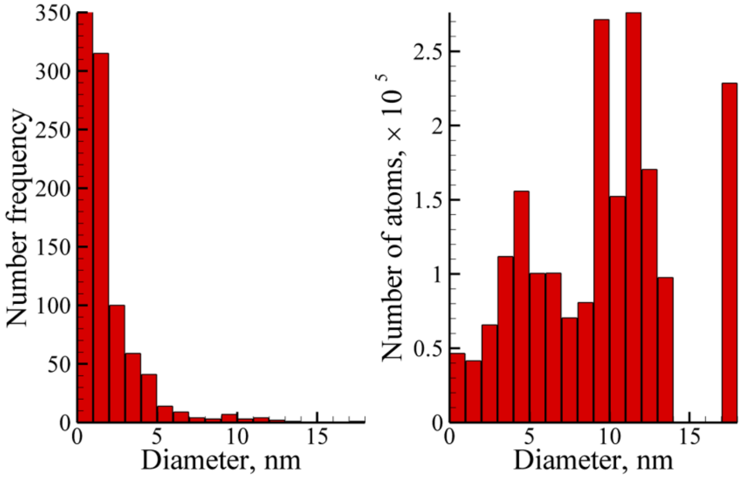

Figure 8.7. The results of the cluster analysis of the ablation plume generated in the simulation of laser ablation of a bulk Cr target irradiated in water by a 200 fs laser pulse at an averaged absorbed

fluence of 250 mJ/cm^2 with 20% of energy modulation at 1.8 ns (a) shows the number of nanoparticles of different sizes. (b) shows the number of atoms for nanoparticles of different sizes.

For the simulation performed in vacuum, the final solidified structure is a thin wall around ~ 100 nm in height, shown in Fig. 8.2c, but the confinement by water environment results in semi-spherical bump with high ~ 50 nm. Although the top of the semi-spherical bump is still remained in liquid state at 1.8 ns, its temperature is close to melting point of Cr. Based on the extrapolation of the advancement of solidification front, one should expect the complete solidification within the following 1 ns. The finding suggests that liquid environment can be an effective experimental parameter to engineer the LIPSS in single pulse regime.

8.4. Summary

Large-scale atomistic simulation is applied to investigate the effect of liquid environment to the mechanisms of single-pulse ablative generation of periodic surface structure. The simulation is performed with a hybrid computational model combining a coarse-grained representation of liquid (parameterized for water), a fully atomistic description of laser interactions with metal targets, and acoustic impedance matching boundary conditions designed to mimic non-reflecting propagation of the laser-induced pressure waves through the boundaries of the computational domain.

The simulation shows the modulated energy deposition results in strong lateral pressure and temperature gradients that initially facilitate accumulation of ejected Cr vapor and liquid droplets toward the center and formation of a liquid wall. A low-density vapor region is formed due to the heating of water in contact with the ablation plume, so Cr atoms evaporate to this region and condense into nanoparticles. The spatial confinement by water prevents the further expansion of ablation plume and facilitates wing-like transient liquid structure connecting to the liquid wall at the plume-water interface. The subsequent downward motion of the ablation plume results in significant mixing with water, and fast quench of the plume induces massive nanoparticle nucleation. The re-deposited Cr liquid wall evolves into a semi-spherical bump with height ~50 nm. Water atoms are embedded and trapped below the Cr surface, hinting the possibility of applications in hyperdoping with water-assisted laser ablation. The protruding surface morphology also facilitates complex liquid flow and vortex formation that further enhance the expansion of low-density vapor region. The simulation has not only confirmed the nanoparticle generation mechanisms in PLAL reported earlier from other MD simulations[179, 190] but also has revealed that liquid environment can be a practical experimental parameter to fine-tune surface morphology and structure in laser processing.

9. Future directions

It has been demonstrated that the hybrid computational model combining a coarse-grained representation of liquid environment, a fully atomistic description of laser interactions with metal targets, and acoustic impedance matching boundary conditions applied in this dissertation is a viable computational technique to explore research questions in the field of pulsed laser ablation in liquids. This chapter delineates the potential research topics in pulsed laser ablation in liquids that can be investigated with atomistic simulations.

9.1. Generation of alloy nanoparticles with metastable structure and chemical supersaturation

Alloy nanoparticles have attracted ever increasing interest due to their tunable catalytic,[231-232] magnetic[233-234] and optical properties[235-236] through change of alloy compositions and structures.[237] Compared to chemical or biological synthesis, alloy nanoparticle synthesized through pulsed laser ablation in liquids show superior physical properties due to its ligand free surface.[20] Pulsed laser ablation in liquids has proven to be able to synthesis alloy nanoparticles with thermodynamically forbidden composition and structures for board range of alloy systems (e.g., Au-Fe,[233, 236, 238-240] Au-Ni,[235, 241] Au-Co,[242] Ag-Au,[243] Ag-Cu,[244] and Ag-Fe[234]). Types of liquid environments used in laser ablation of bulk alloy target have proven to be a key factor to engineer the structure (tunable from core-shell to homogeneous) and compositions.[236, 238, 240] Moreover, pulsed laser melting of colloidal solution of two pre-prepared nanoparticles has also been demonstrated as another viable alternative with unique advantage of synthesis immiscible alloy system when desirable homogeneous compositions of bulk alloy for direct one-step ablation is difficult to obtain.[235, 241-243]

Recently, the novel use of multi-layers (Au-Fe) as an ablation target in liquids[245] to synthesize alloy nanoparticles has provided new perspectives not only to the control of alloy composition and structure but also to fundamental understanding of ablation plume-liquids interaction. Based on systematic ex-situ observation of ablated products, a two-stage ablation process with the concept of “sacrificial layer” has been proposed. A nanometer-thick molten layer, “sacrificial layer”, is speculated to form between ablation plume and liquid interface at early stage of ablation process to react with solution species and protect the underlying ablation plume from reacting with solution species. Moreover, since the “sacrificial layer” is mainly composed from the top surface of multi-layers, the chemical process of ablation can also be engineered. Ablation of multi-layers in liquids in expected to drastically expand the range of synthesizable alloy systems by PLAL, especially toward complex multicomponent alloy nanoparticles.

The experimental speculation of floating molten layer between ablation plume and liquid interface is observed and discussed in the Chapter 3, and it is shown that the metal molten layer prevents the further water diffusion into the hot metal vapor plume below. Preliminary large-scale simulations of thin Ag-Cu multi-layers ablation in water are showing the promising results of the role of sacrificial layer to control characteristics of alloy nanoparticle, and its briefly discussed below.

Fig. 9.1 shows atomistic snapshots of simulation performed for Ag-Cu multilayer ablation in water. The initial sample configuration is 10 nm of Cu film above 10 nm Ag film (lateral dimensions are 100 × 100 nm) deposited on silica substrate irradiated with 100 fs pulse at absorbed fluence of 100 $\mathrm{mJ/cm^2}$. The laser irradiation brings both metals above threshold for phase explosion in vacuum; however, the expanding mixtures of metal vapor and liquid droplets are confined by water environment. The deceleration of ablation plume by water confinement results in accumulation of mixture of metal vapor and liquid droplets into a metal molten layer that shown clearly from the density peak at 1 ns in Fig. 9.1; the metal molten layer mostly constitutes with Cu atoms due to the initial spatial order of layer deposition that can be related to experimental prediction of sacrificial layer.[245] The Cu-rich molten layer shields the Ag atoms from diffusing into the low-density vapor region at plume-water interface. Hence, the initial small nanoparticles observed in simulation are predominated by Cu. The disintegration of the molten Cu layer weakens the barrier of Ag upward diffusion, and small fraction of Ag nanoparticles starts to appear in the low-density vapor region during the simulation. Moreover, the composition of Ag atoms in the molten layer increases during the simulation, and disintegration of molten layer results in large nanoparticles, shown at 3 ns in Fig. 9.1, composed of Ag and Cu. Changing the spatial order of Cu and Ag shows the similar overall dynamics (reported elsewhere) suggests the multi-layer can be an effective sample setup to control alloy nanoparticle sizes and compositions.

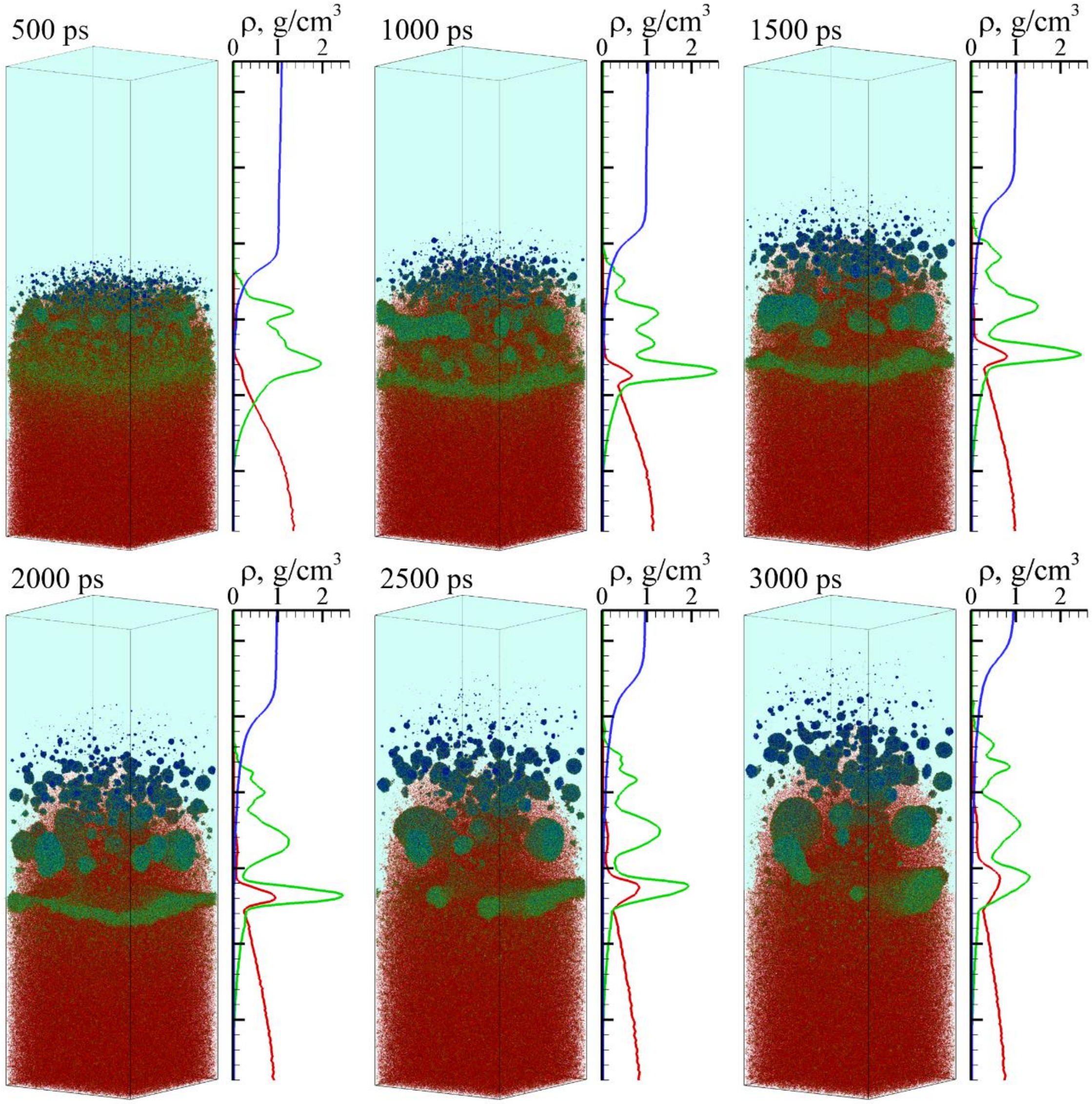

Figure 9.1. Snapshots of atomic configurations obtained in a MD simulation of laser ablation of a 10 nm Cu film above 10 nm Ag film deposited on silica substrate in water. The film is irradiated by a 100 fs laser pulse at an absorbed fluence of 100 $\mathrm{mJ/cm^2}$. Only parts of the computational system from 30 to 340 nm with respect to the initial surface of silica substrate shown in the snapshots. The atoms are colored by potential energies range from dark blue as solid, green as liquid to red as vapor atoms. The water molecules are blanked to expose the nanoparticle formation, and the presence of water is shown schematically by the blue background. The degree of water-silver mixing is illustrated by density plots shown as functions of distance from the substrate for both water (blue) Cu (green) and Ag (red) on the right sides of the snapshots.

The investigation of the metal alloys will be extended to silicon targets, leading to the exploration of the hyperdoping of laser-generated nanoparticles (or "quantum dots") for potential applications in optoelectronic devices. The substitutional doping of semiconductor nanoparticles is difficult to achieve due to the large supersaturation associated with just one dopant atom.[246-247] [248] The ultrafast cooling and solidification rates realized in PLAL hold a promise of incorporation of high concentration of dopants into the frozen nanoparticles, although the mechanisms responsible for the dopant incorporation into the lattice in the course of rapid melting and resolidification are still unexplored.

First simulations of hyperdoping of Si will be performed for doping of Au, due to the availability of Au-Si potential[249] already implemented in the code, and then extended to boron[250] and phosphorus.[251] Two methods of hyperdoping of Si nanoparticles will be investigated. In the first method, the targets produced by implanting the dopant at different concentrations will be used in the simulations and the degree of solvation of the dopant atoms in the nanoparticles generated by PLAL will be studied. In the second approach, the dopant will be dissolved in liquid[252] and the ability of the nanoparticles to capture the dopant atoms from the liquid environment during the nucleation and growth will be studied in the simulations.

9.2. Fundamental physical parameters controlling nanoparticle size distribution

The results discussed in Chapter 3, 5, 6 and 7 show the characteristic nanoparticle generation mechanisms are influenced by the dynamics of ablation plume-water interaction. The finding reveals the possibilities to control nanoparticle size distribution through changing relevant experimental parameters to influence ablation plume-water interaction. Based on the finding is the dissertation, the dependence of the nanoparticle structure and size distribution on the irradiation conditions, properties of target material and liquid environment will be systematically investigated in several series of simulations. The results of the simulations will be formulated in terms of theoretical description of the key processes responsible for the nanoparticle generation. Selected topics that can be the next steps of MD investigation of PLAL are presented as following:

Effect of liquid viscosity to ablation dynamics of PLAL in microscopic scale:

Liquid viscosity is one of the experimental parameters that have strong impact on cavitation bubble dynamics and nanoparticle output. Viscosity directly change the mass transport properties of liquids to influence the collision rate for nanoparticle and its agglomerate[253-254]. The change of liquid viscosity also influences the life time of cavitation bubble that can result in unique nanoparticle structure[32]. While the simulations in the dissertation are performed with water environment, the effect of viscosity of the liquid medium on surface nanostructuring and nanoparticle generation can be investigated through addition of short polymer chains simulated with the bead-and-spring model[189] into the coarse-grained representation of water described in Chapter 1.2.3. This approach will mimic mixing of water with aliphatic alcohols that can be used to modify the viscosity of aqueous solutions in experiments[255], and effect of liquid viscosity to microscopic pictures of PLAL can be studied systematically.

Uncover key intrinsic materials properties through Lennard Jones potential mapping

Most results of simulations reported in the dissertation is based on Ag, a noble metal, and the simulations performed with Cr, a transition metal, show a distinctively different picture of ablation plume-water interaction that is delineated below and prompted the further investigation of key intrinsic materials properties controlling the microscopic dynamics of PLAL.

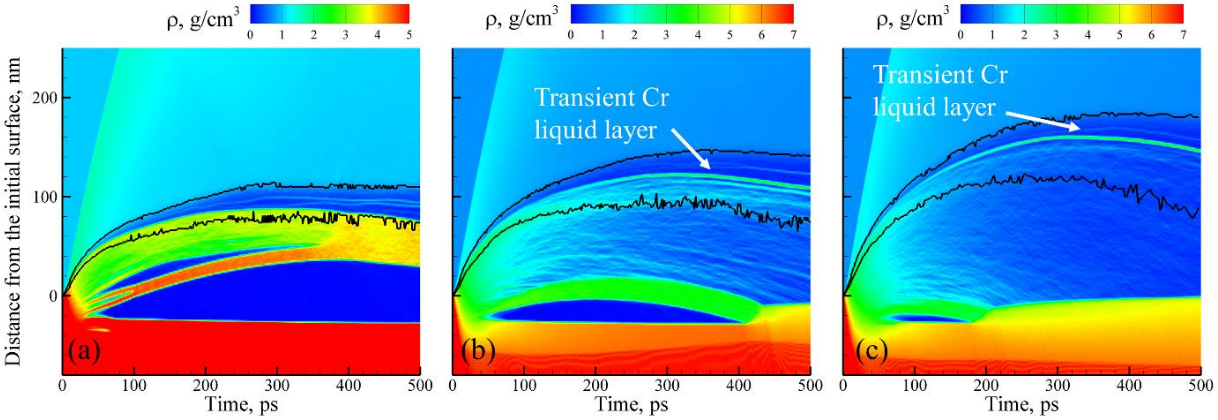

Figure 9.2. (a) Density contour plot predicted in atomistic simulation of laser ablation of a bulk Cr target irradiated in water by a 200 fs laser pulse at an absorbed fluence of 200 mJ/cm^2. (b) Density contour plot predicted in atomistic simulation of laser ablation of a bulk Cr target irradiated in water by a 200 fs laser pulse at an absorbed fluence of 250 mJ/cm^2. (c) Density contour plot predicted in atomistic simulation of laser ablation of a bulk Cr target irradiated in water by a 200 fs laser pulse at an absorbed fluence of 300 mJ/cm^2.

Three small scale simulations of Cr bulk target ablated in water with 200 fs laser pulse, density contour plots shown in Fig. 9.2, are performed at 2000, 2500, and 3000 J/m^2 to understand general effect of water environment toward formation and expansion of Cr ablation plume. At absorbed fluence of 2000 J/m^2, shown in Fig. 9.2a, the ejected Cr vapor and liquid droplets accumulate at the plume-water interface to form a dense molten layer, and liquid layer spalled from the deeper part of the target thickens the molten layer that is similar to simulations observed for short pulse laser ablation of Ag bulk target in water. At absorbed fluence of 2500 J/m^2, shown in Fig. 9.2b, distinctively different ablation plume-water dynamics appear between Ag and Cr. The plume front is constituted with mixture of Cr vapor and liquid droplets, and the expansion of the mixture pushed back the spalled layer from the deeper part of the target. The front of the plume condenses to form a thin transient liquid layer due to the interface cooling from water. At absorbed fluence of 3000 J/m^2, the overall dynamics between ablation plume and water are similar to that of 2500 J/m^2, the higher fluence results in stronger expansion of the Cr vapor and liquid mixture, as shown in Fig. 9.2c. The dynamics between ablation plume and water observed from femtosecond laser pulse simulations performed for Cr at absorbed fluence of 2500 and 3000 J/m^2 are different from previous MD simulation performed for Ag bulk target in water with femtosecond and short picosecond pulses (Fig. 7.1), but qualitatively similar to previous MD simulation performed for Ag bulk target in water with nanosecond pulse (Fig. 7.5).

The overall pictures of MD simulations performed for Ag bulk target in water can be categorized to two regimes based on pulse durations. The first regime, as presented in Chapter 5, is observed for short pulse when the stress confinement condition is strong; hence, the explosive release of vapor and liquid droplets are followed by spallation of large liquid layers. The large amounts of materials ejection are decelerated and accumulated at the front of plume to form a dense molten layer. The second regime, as presented in Chapter 7, is observed for long pulse when the stress confinement condition is weak; the gentle ablation occurs without spallation from deeper part of the target. While the surface of the target undergoes phase explosion, the ejected materials do not accumulate into dense molten layer, but remains as mixture of Ag vapor and liquid droplets

The comparison between simulations performed for Ag and Cr shows the importance of intrinsic materials properties to dynamics of ablation plume and liquid environment to nanoparticle generation mechanisms. The counter-intuitive results shown in Fig. 9.2b and c are related to the fundamental difference in material property between Ag and Cr. The effective laser energy deposition depths, summation of optical penetration depth and ballistic range of excited electron, are estimated as 68 and 9.6 nm for Ag[102] and Cr,[90] respectively. The long effective laser energy deposition depth for Ag resulting in much deeper ablation depth than that of Cr. While the simulations for Ag shows that the ablation depth can easily reach hundreds of nanometers for short pulse laser ablation, shown in Fig. 9.2d, the contour plots on Fig. 9.2b and c show only ablation depth ~ 25 nm. The shallow effective laser energy deposition depth for Cr cannot facilitate sufficient vapor and liquid droplets to densely accumulate at the plume front, so the overall picture is similar to simulations performed for Ag at long pulse when the stress confinement condition is not satisfied. The finding shows that the dynamics at ablation plume-water interface is not only dedicated by laser parameters (pulse duration and fluence), but also intrinsic materials properties.

The modern many body potentials while accurately reproduce wide range of properties of a specific material, its complexity render study of general materials parameters and their effect on phenomena of interests difficult. The simplicity and generality of Lennard Jones potential is ideal to map out the generic effect of key materials properties on PLAL, since the behavior of the potential is well-understood. Through systematically changing the LJ potential parameters, the materials properties of interests can be isolated and compared to study its effect on dynamics of ablation plume-liquids and nanoparticle generation mechanisms.

(Another well-received Ag EAM potential fitted by Williams et. Al,[256] is used to study the generality of simulation results of Ag ablation in water reported in the dissertation, presented in Appendix A5. The microscopic dynamics at the interface between Ag ablation plume and liquid environment is found to be general, and insensitive to details of Ag potentials.)

Control of nanoparticle size distribution through manipulation of Rayleigh-Taylor instability

The generation of large nanoparticles through the combination of Rayleigh-Taylor and Richtmyer-Meshkov instabilities emerging from the simulations performed in Chapter 5 and 6 shows a potential to engineer characteristic size of the large nanoparticles generated by PLAL through controlling the Rayleigh-Taylor instability of the plume-water interface. This hypothesis can be verified in a series of specially designed simulations and, if confirmed, will be used to suggest experimental setups aimed at improved control over the nanoparticle generation. In particular, the possibility of destabilizing the superheated metal layer by a shock wave generated in the liquid environment and timed to arrive at the specific moment to have the maximum effect on the layer disintegration process will be explored and suggested for experimental verification.

9.3. Surface morphology and microstructure produced by PLAL

Another area of application of PLAL can be explored with the hybrid atomistic model is the modification of surface morphology, microstructure, and composition by laser processing of metal surfaces in liquid environment. While lightly studied in Chapter 4.3.1, 4.3.2 and 8, the experimental evidence[167-171, 174] of the strong influence of the liquid environment on the morphology of laser-processed surfaces shows the potential to extend PLAL to surface structure processing. The choice of the target materials, liquid medium, and irradiation parameters will be aimed at revealing the key processes that control surface nanostructuring in PLAL. The investigation can be further extended to hyperdoping of surface regions of Si targets undergoing laser-induced melting and resolidification in liquid environment. The laser-assisted hyperdoping has been demonstrated in experiments performed in vacuum or air for targets supersaturated by ion implantation followed laser-induced melting and resolidification.[257-260] The mechanisms of dopant activation by laser processing are still not fully understood, and the proposed study will start from analysis of the hyperdoping in vacuum and proceed to the investigation of the effect of the liquid environment when the mechanisms and kinetic pathways leading to incorporation of dopants into the crystal lattice is established. A particular focus of this part of the study will be on finding the balance between maximizing the hyperdoping and avoiding generation of large densities of sub-surface defects that can quench photo-carriers and negatively affect the performance of photonic devices.

10. Summary of the dissertation

A hybrid computational model combining an atomistic description of laser interactions with metal targets, a coarse-grained representation of liquid (parameterized for water), and acoustic impedance matching boundary conditions designed to mimic non-reflecting propagation of the laser-induced pressure waves through the boundaries of the computational domain is developed and applied to study microscopic dynamics of laser-metal interactions in liquid leading to nanoparticle generation and surface structuring. To summarize the dissertation, the research objectives listed in Chapter 1.3 are used as the guideline, and the key results obtained while meeting these objectives are briefly outlined below.

1. ***Understand the fundamental microscopic dynamics at the interface between ablation plume and liquid environment leading to nanoparticle generation***

The presence of liquid environment prevents direct expansion of ejected ablation plume. The ejected ablation plume is rapidly decelerated by the interaction with the liquid to form a molten metal layer if the condition of stress confinement is strong. Extensive nanoscale roughness can develop in the upper part of the molten metal layer due to the Rayleigh-Taylor instability of the interface between the higher density metal layer decelerated by the pressure from the lighter supercritical water. The nanoscale surface roughness can facilitate disintegration of the hot metal layer through thin liquid layer instability or Richtmyer-Meshkov instability to form large nanoparticles (10s of nanometers). The water in contact with the ablation plume is also heated to the supercritical state, and a low-density vapor region forms and expands during simulation time (precursor of cavitation bubble in experiments). Small nanoparticles (< 10 nanometers) are observed to form from the vapor of metal atoms through the nucleate and grow in the low-density vapor region.

2. ***Understand the effect of pulse duration on nanoparticle generation mechanisms and size distribution***

Short pulse laser ablation: Rapid nucleation and growth of small nanoparticles in the metal-water mixing region, and the breakup of the hot metal layer into larger droplets due to the cascade of hydrodynamic instabilities represent two distinct mechanisms of the nanoparticle formation that are found to yield nanoparticles of two different size ranges. This computational prediction provides a plausible explanation for experimental observations of bimodal nanoparticle size distributions in short pulse PLAL experiments. The direct injection of large nanoparticle into liquid environment is supported by the stroboscopic videography experiments performed by our collaborators from the University of Duisburg-Essen, Germany. The experimental images reveal the appearance of small satellite mircobubbles surrounding the main cavitation bubble after single pulse laser ablation. The properly time second laser pulse irradiation induces rapid expansion of the satellite microbubbles, thus supporting the hypothesis that the satellites mircobubbles contain large nanoparticles absorbing the laser irradiation.

Long pulse laser ablation: laser irradiation with longer laser pulses allow the irradiated target to gradually dissipate deposited laser energy resulting in a “gentler” ablation. In contrast to the formation of dense molten metal layer at the plume – liquid interface in short pulse PLAL, the ablation plume generated by longer pulses consists of a mixture of metal vapor and liquid droplets. The mixing of water with ablation plume can result in condensation of a transient thin molten metal layer that later disintegrates into nanoparticles (10s of nanometers), as well as in rapid nucleation of small nanoparticles (< 10 nanometers) in the ablation plume due to the cooling from the water.

3. *Explore the role of spatial energy confinement in thin film ablation in liquids and in vacuum*

For thin film ablation in vacuum, four distinct ablation regimes corresponding to different characteristic nanoparticle distributions are discovered and mapped based on the film thickness and laser fluence. The introduction of a liquid environment results in confinement and deceleration of the ablation plume. While a dense molten metal layer is formed at the plume – water interface, its thickness is much thinner compared to ablation of bulk targets in water, since the thickness of the film indirectly defines the energy deposition range and limits the ablation depth. Since the large nanoparticles are produced through disintegration of the molten metal layer, the thickness of the film can be used as an additional parameter to control the nanoparticle size distribution. Moreover, the molten metal layer can be utilized to fine tune alloy nanoparticle structure and composition, if the multi-layer metal ablation target is used.

4. Study fast quenching and rapid crystallization of nanoparticles

The thermodynamic conditions in the expanding metal-water mixing region not only facilitate rapid nucleation and growth of metal clusters and nanoparticles but also ensure highly efficient cooling and solidification of the nanoparticles that are found to crystallize within nanoseconds after the laser pulse. If the larger nanoparticles produced through the hot molten metal layer disintegration via a cascade of hydrodynamic instabilities are injected into the water environment, they can also be rapidly cooled and solidified, with cooling rates in excess of 10^{12} K/s observed in the simulations. The ultrahigh cooling and solidification rates suggest the possibility for generation of nanoparticles featuring metastable phases and highly nonequilibrium structures.

5. **Investigate the effect of water environment on laser-induced surface structure**

For irradiation condition corresponding to melting and resolidification regime in vacuum, the water environment suppresses the formation of sub-surface voids and provides an additional cooling channel through the heat conduction to the water. Formation of a nanocrystalline surface with high concentration of defects is observed in the simulation, suggesting that liquid environment can be utilized as a key parameter in the laser-induced engineering of surface nanostructure. For irradiation condition corresponding to photomechanical spallation regime in vacuum, the water environment prevents the ejection of spalled metal layer from the target, resulting in expansive surface swelling. The range of fluence for sub-surface void formation is significantly broadened with the presence of water.

6. **Explore the incubation effect introduced by the presence of sub-surface voids in pulsed laser ablation in liquids**

The generation of subsurface voids or extended porous surface morphology can significantly alter the response of the target to irradiation by subsequent laser pulses applied to the same laser spot. The spatially localized laser energy deposition to the top surface layer separated from the rest of the target by a low-conductivity porous region is found to induce a confined phase explosion resulting in dramatic reduction of the threshold fluence for ablation and more efficient generation of nanoparticles. The findings provide important insights into the incubation effect in multipulse laser ablation in liquids.

7. Investigation of the effect of water on generation of laser-induced periodic surface structures in single pulse irradiation regime

The spatial confinement by water environment coupled with modulated laser energy deposition results in a complex material flow in the ablation plume. The net results of the laser-induced material flow dynamics are 1) formation of qualitatively different laser-induced surface structure as compared to the one observed in a simulation performed in vacuum and 2) generation of a broad size distribution of nanoparticles in water. Moreover, the entrapment of water molecules observed below the irradiated surface suggests the potential role of liquid environment in hyperdoping of laser-processed surfaces.

11. Appendix

A1. Testing of water parameters

Although various physical properties directly affect laser ablation in liquid phenomena are considered, fitted and shown in ref [127] for Coarse-grained (CG) water, it is still pertinent to verify more physical properties relating to laser ablation to have full understanding the capability and limitation of CG model on application of laser ablation in liquid or any general simulation task in the future. The additional tested physical properties are viscosity, thermal conductivity, heat of vaporization, saturated vapor pressure and equilibrium vapor and liquid densities. The complete list of coarse grain water properties is shown in Table 1.1. For each physical property, the testing methodology, experimental comparison, and possible improvement of the model are discussed.

Dynamic and Kinematic Viscosity

Viscosity is a property of a fluid that measures its resistance to deformation or flow by stresses, and has similar concept as the frictional force in solids. Depending on the purpose of scientific study, there are two common physical definitions for viscosity: dynamic and kinematic. Dynamic viscosity is defined as the resistance of a fluid to shear stresses. Kinematic viscosity is a derivative property that is used in the Navier-Stokes equations, and it is equal to dynamic viscosity divided by the density.

The dynamic viscosity, η, can be related to self-diffusion coefficient through Stokes-Einstein equation:

$$\eta = \frac{k_B T}{6\pi D r} \qquad \text{Equation 11-1}$$

The D is the self-diffusion coefficient, and r is the radius of the CG sphere molecule. Through finding the self-diffusion coefficient, one can obtain the dynamic viscosity.

A computational system with 10 ×10 × 10 cells with 4000 molecules with PBC in all directions is created. The system is thermalized and equilibrated at 300 K and 0 GPa for 200 ps. After equilibrium, 100 molecules are randomly marked in the system to observe their random walk specifically. The equilibrated system undergoes free dynamics for 5 ns. The folding due to periodic boundary condition is taken into account to calculate the real water displacement. The diffusion coefficient is then determined from the time dependences of the mean square displacement of the

CG molecules. In order to obtain the statistically accurate mean squared displacement (MSD), the MSD has been averaged temporally every 200 ps, and spatially for the 100 molecules. Fig. 11.1 shows the evolution of MSD for water self-diffusion, and since MSD = 6Dt; the fitted slope is 6D. The fitted slope has value of 0.01814, corresponding to $3.02 \times 10^{-9}\ m^2 s^{-1}$. The experimental self-diffusion coefficient, D_{exp}, for water at 300 K is in the range of 2.296 ~ $2.299 \times 10^{-9}\ m^2 s^{-1}$ [261-262]. The corresponding η via Stokes-Einstein equations is 0.910 cP. There is only 2.2 % deviation from the experimental measurement of 0.894 cP [263], the η for CG model agrees well with the experimental measurement. Since the CG models reproduces correct water density, the kinematic viscosity, $\nu = \frac{\eta}{\rho}$, is reproduced with good agreement with experiments.

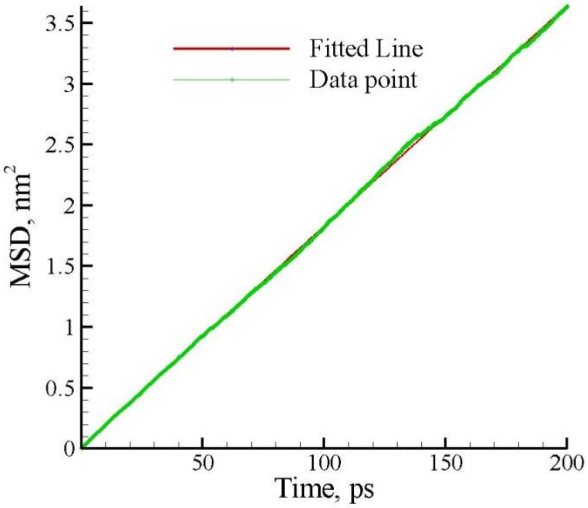

Figure 11.1. Evolution of mean square displacement of water self-diffusion after spatial and temporal averaging.

Thermal conductivity

Thermal conductivity is a material property defining the ability of a material to conduct heat, and it is measured as the thermal energy transferred from a hotter surface to a colder surface per unit surface area and per unit of time divided by the temperature gradient between two surfaces.

A computational system with size of 7nm × 7nm × 600 nm that consists of 346400 atoms is equilibrated at 300 K. Three sets of simulations are ran by velocity scaling and controlling the temperature in the center 8 Å to be constant at 350, 400 and 600 K, respectively. The total simulation time is 1.5 ns to obtain equilibrium profile. In order to reduce the statistical noise, the profile is averaged temporally for the last 50 ps. The obtained profile is fitted for the heat diffusion equation tailored for the system setup; heat source in the middle with length considered infinite for the time scale:

$$T = T_0 - (T - T_0) \times Erf\left(\frac{x}{\sqrt{4Dt}}\right) \qquad \text{Equation 11-2}$$

T_0 is the initial temperature profile, x is the distance from the center heat source, t is the simulation time, and D is the fitting constant that can be described as $D = \frac{K}{C_v}$. C_v is the heat capacity at constant volume, 4180 $\frac{kJ}{m^3 K}$, and K is the thermal conductivity. The fitted curves and experimental data are shown in Fig. 11.2.

The same fitting constant 13.7×10^{-9} is obtained for three different temperatures. The corresponding thermal conductivities are 0.13 $\frac{W}{m \cdot K}$. Experimental measurements show that water at 293 K is 0.6 $\frac{W}{m \cdot K}$. The CG water underestimates the thermal conductivity by 5 times of magnitude.

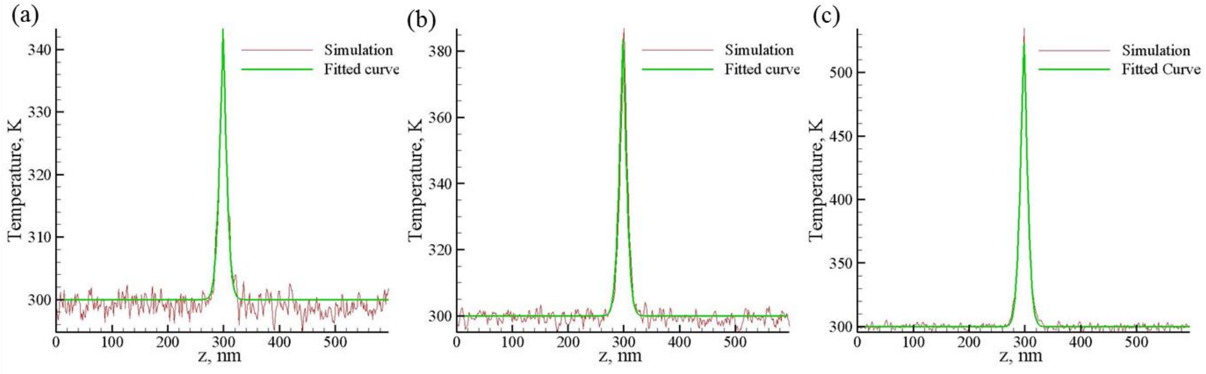

Figure 11.2. Fitted temperature-distance profile (green curve) based on simulation results (red curve) with the heat source temperature of (a) 350, (b) 450, and (c) 600 K.

For laser ablation in liquid, the thermal conductivity does not play significant role in the overall ablation phenomenon in the MD timescale. It has been experimentally and computational observed that a thin, low density vapor layer forms and expand in both directions to form cavitation bubble. The water in vapor phase has negligible thermal conductivity in the range of 0.016 ~0.0471 $\frac{W}{m \cdot K}$; hence, the plume is effectively insulated from the surrounding water by the vapor bubble.

Improvement of thermal conductivity

Even though the inaccuracy of thermal conductivity will not dramatically change the overall picture of laser ablation in liquid, it could result in unphysical results in other studies including study of nanoparticle heating in liquid surrounding or sonolunminescence.

To ensure that the thermal conductivity of CG water has the experimental value, a strategy of heat bath scaling has been implemented. The underestimation of thermal conductivity for CG water indicates that the energy transfer through phonon collision in the model is not effective. However, changing phonon mean free path requires change in interatomic potential, which could results in significant alteration of previous fitted physical properties. In order to correct the thermal conductivity without changing other physical properties, the modification of the model has been focused on heat bath related solution, since heat bath is an independent object that does not directly affect interatomic potentials.

The missing thermal conductivity is remedied by directly transferring the heat bath temperature between individual atom and its surrounding. The heat bath temperature of particle i is compared directly with every heat bath temperature of its neighboring particle. If the particle i has heat bath temperature higher than its neighboring particle j, a fraction of the heat bath temperature difference is adding into particle j and subtracted from particle i. The strategy can be represented in the form of Fick's first law:

$$J = D\frac{T_{HB}(i) - T_{HB}(j)}{dx} \qquad \text{Equation 11-3}$$

The energy transfer is inversely related to distance between two particles, and controlled by a constant K. However, the strategy is not the same as Fick's first law, since one cannot consider the J term in Eq. (11-3) as flux; there is no well-defined area for heat transfer. J in Eq. (11-3) is simply the energy exchange between two particles. The only parameter needs to be fitted is constant D. Two loops of particle neighbor list are required to complete the energy exchange routine. The first loop through particle neighbor list is to compare the temperature, and calculate the desirable energy transfer between particle i and surrounding neighbors. However, one cannot update the temperature during the first loop. The first loop only records the desirable energy transfer between atoms, since every neighboring atom must be compared with the same temperature of particle i.

The energy redistribution will be done during the second loop, so every atom receives or gives out temperature at the same time, and there is perfect energy conservation.

The same computational setup and procedure in previous section has been used, and the heat source temperature is set at 450 K. The simulations last for 2050 ps, and the last 50 ps is averaged temporally to obtain the distance-temperature profile. The optimal D constant is found to be 0.00012 , giving the K = 0.598 $\frac{W}{m \cdot K}$. The fitted curve and experimental date is shown in Fig. 11.3. With the heat bath temperature transfer implementation, there is only 0.3 % deviation from the experimental measurements.

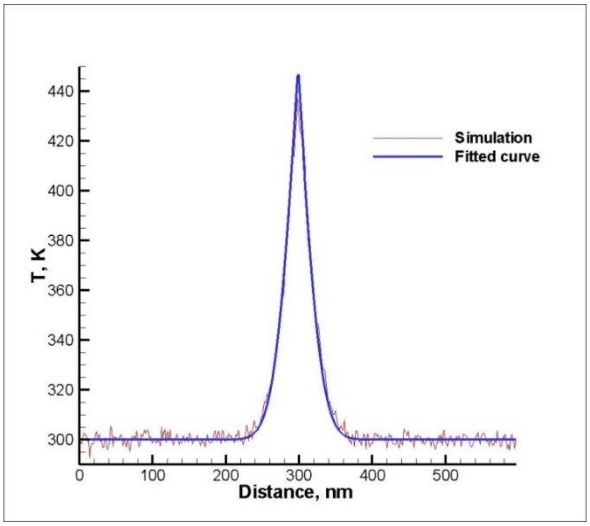

Figure 11.3. Fitted temperature and distance profile (blue curve) based on simulation results (red curve) after the implementation of heat bath scaling with the heat source temperature of 450 K.

Construction of liquid-vapor coexistence curve

Since there is a significant amount of water undergoes phase transformation at elevated temperature and pressure conditions during the laser ablation in liquid process, it is imperative to construct and scrutinize the phase diagram along liquid-vapor coexistence curve. Through the construction of liquid-vapor coexistence curve, various physical properties can be recovered including equilibrium vapor and liquid densities, saturated vapor pressure, and heat of vaporization.

Equilibrium vapor and liquid densities

The tested temperatures are ranged from 350 to 500 K. A sample of rectangular shape is created. Empty spaces are given in z direction of each side; the purpose of creating empty space on both sides of the sample is to let the atoms to vaporize, and balance the pressure between vapor and liquid to achieve equilibrium. The higher the temperature, longer the sample and empty space are needed to take into account the larger volume expansion of liquid and more vigorous vaporization. The details of simulation samples are shown in Table 11.1.

Temperature, K	Unit cells (x,y,z)	Empty length on each z side, nm
350	10×10×15	5
375	10×10×15	5
400	10×10×15	5
425	10×10×15	5
450	10×10×15	5
475	10×10×15	10
500	10×10×30	10

Table 11.1. Details of computaionl setup prepared for simulations of equilibirum vapor and liquid coexistence curve.

The sample has always been kept under PBC in all directions, and been thermalized with velocity distribution for the first 20 ps, and followed with constant temperature for 5 ns. The heating rate is reduced appropriately as the temperature becomes higher to ensure that the sample does not undergo spallation or explosive boiling due to rapid temperature and pressure fluctuation.

In order to check whether the vapor pressure is saturated, the number of vapor atoms is tracked throughout the simulation. The criteria for determining whether an atom is vapor or liquid is based on the number of its neighbors, if an atom has neighbor less than 5, it is considered as vapor. This criterion is just served as a way to determine whether the system reaches the equilibrium through a reasonable approximated threshold, hence, the numerical value of the criteria does not have specific physical meaning. It has found that the number of vapor atoms increase and plateau within 300 ps; a sign that the system reaches equilibrium.

The spatial profile of the equilibrated sample has been averaged from 1ns to 5 ns to obtain a smooth density curve in z direction. An example profile from simulation of 350 K is shown in Fig. 11.4; the middle flat line corresponds to liquid density distribution, and the flat lines on the end correspond to vapor density distribution. The liquid and vapor densities are averaged along z direction. This profile also shows the interfacial region between liquid and vapor, which is excluded from the averaging calculation. Through averaging the spatial profile, the averaged equilibrium liquid and vapor densities are shown in Fig. 11.5a, the two curves approach to each other rapidly as temperature raised closer to the critical temperature, and will collapse to one point at the critical temperature eventually. However, this simulation method cannot provide information for the liquid-coexistence curve beyond 500 K, since the sample approaches the limit of explosive boiling. Beyond 500 K, the sample becomes easily fragmented as any temperature and pressure fluctuated within the system, and system undergoes explosive phase separation into liquid and vapor mixtures. The interface between liquid and vapor is not sharp enough for proper judgment of liquid and vapor regions. An ideal gas density curve is constructed, based on the temperature and pressure of the equilibrium vapor, to compare with the obtained vapor density curve. One can observe that the vapor density deviates from the ideal gas density, and the deviation becomes more significant as temperature rises. Such observation indicates that the vapor atoms at high temperature show cluster like behavior, and it is confirmed by visualizing the simulation snapshots.

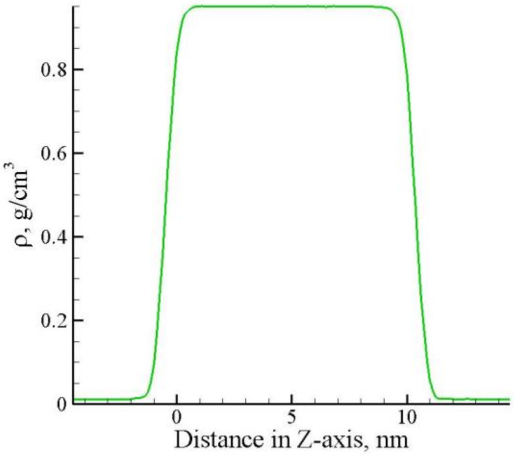

Figure 11.4. The eqilibirum denisty profile at 350 K shown as a visual example of eqilbirum vapor and liquid density calculation procedure.

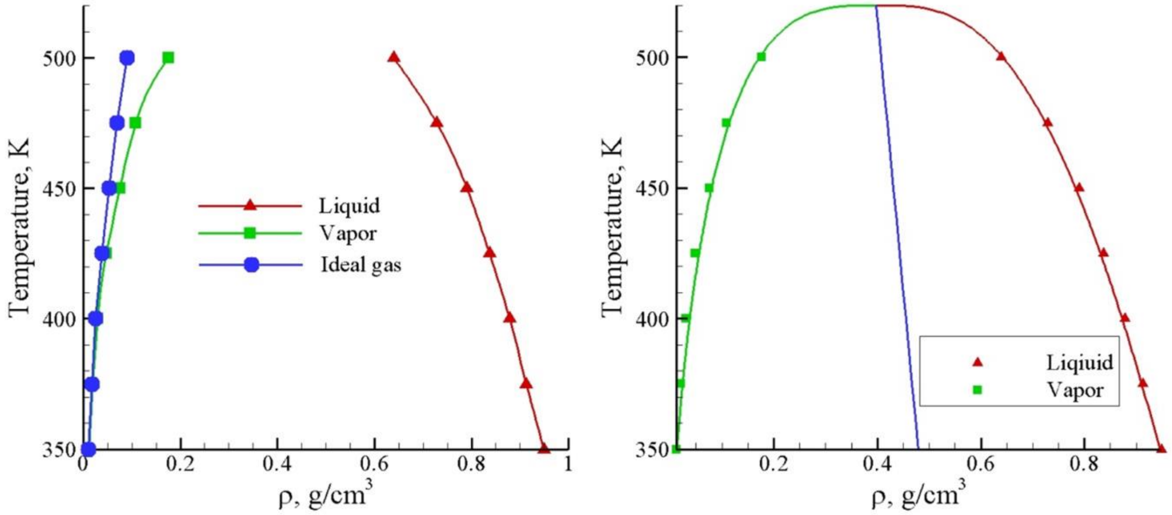

Figure 11.5. (a) Averaged eqilibrium liquid and vapor densities obstained from the simulations (b) Fitted liquid-vapor coexistence curve based on the results of the simulations.

Calculation of critical temperature and completion of liquid-vapor coexistence curve

Since the critical temperature and density of CG model have not been rigorously tested before, one cannot simply interpolate the liquid-vapor coexistence curve. In order to accurately predict the liquid-vapor coexistence curve beyond 500 K, the renormalization theory is applied with fitting based on the obtained liquid and vapor densities with the following equations[128]:

$$\rho_l = \rho_c + A_0(T_c - T)^{\beta} + A_1(T_c - T)^{\beta+\theta} + B(T_c - T) \qquad \text{Equation 11-4}$$

$$\rho_v = \rho_c - A_0(T_c - T)^{\beta} - A_1(T_c - T)^{\beta+\theta} + B(T_c - T) \qquad \text{Equation 11-5}$$

$$\rho_l + \rho_v = 2\rho_c + 2B(T_c - T) \qquad \text{Equation 11-6}$$

T_c and $\rho_c$are critical tempreature and critical denisty, respectively. A_0, A_1 and B are fitting parameters. There are total 5 variables needed to be fitted. β is the critical exponent of the density difference between ρ_l and ρ_v, and is estimated as 0.326.[264] θ is the exponent of the correction to the scaling , and is estimated as 0.54.[265]

The fitting is started with using Eq. (11-6), which is the summation of Eqs. (11-4) and (11-5). Eq. (11-6) can be represented as a linear function; fitting parameter, B, is the slope of the function, and found to be 4.8×10^{-4}. The two unknown T_c and ρ_c are fitted to Eq. (11-6). The Excel non-linear solver is used to predict the possible T_c and ρ_c, and is compared with simulation data thorugh mean square error (MSE). The solver solves the T_c and ρ_c that is subjected to minimize the MSE.

The fitted T_c and ρ_c are 520 K and 0.398 g/cm^3, with the MSE of 0.0001 %. The fitted Eq. (11-6) is shown in Fig. 11.5b as the blue line. The remaining two unknown A_0 and A_1 are fitted with Eqs. (11-4) and (11-5) simultaneously, and same procedure of MSE minimization is applied. The Excel non-linear solvers give 0.089 and -0.0001 for A_0 and A_1, respectively. The fitted Eqs. (11-4) and (11-5) have MSE of 0.001 and 0.0008 %, respectively. The fitted liquid and vapor coexsitnce curves are shown in red and green lines accordingly in Fig. 11.5b. The experimental measurement of critical temperature and density are 647 K and 0.322 g/cm^3, respectively. The CG models give 19.6 % deviation of critical tempeature and 23.6 % deivation of critical density.

Saturated vapor pressure and heat of vaporization

To obtain accurate heat of vaporization and saturated vapor pressure, the liquid and vapor samples are created separately in a fixed size computational box with PBC condition in all directions. Through this way, the uncertainty of vapor volume and surface energy effect are eliminated. The fixed size computational box with length of 6.9251 nm is filled with atoms with corresponding liquid and vapor densities for given temperature shown in Fig. 11.5a. The samples are thermalized with velocity distribution for the first 20 ps, and followed with constant temperature for 2 ns to achieve equilibrium states. The total energy and pressure of the systems are averaged from 500 ps to 2ns.

Fig. 11.6a shows the saturated vapor pressure as function of temperature, and the CG model has higher saturated vapor pressure than real water.[266-268] Fig. 11.6b shows the corresponding equilibrium energy of the individual vapor and liquid atom at given temperature. Noticeably, the energy of vapor increases slightly, but starts to decrease after 425 K, this is due to the aforementioned vapor density deviation from ideal gas. The extra potential energy interaction gets stronger as temperature increases. By subtracting the energy difference between liquid and vapor at given temperature, one obtains the heat of vaporization, as shown in Fig. 11.6c., the CG model underestimates the heat of vaporization by about 6 times. Such underestimation is intuitively clear, since each CG unit has only 4 degrees of freedom, and cannot be further disintegrate into smaller unit.

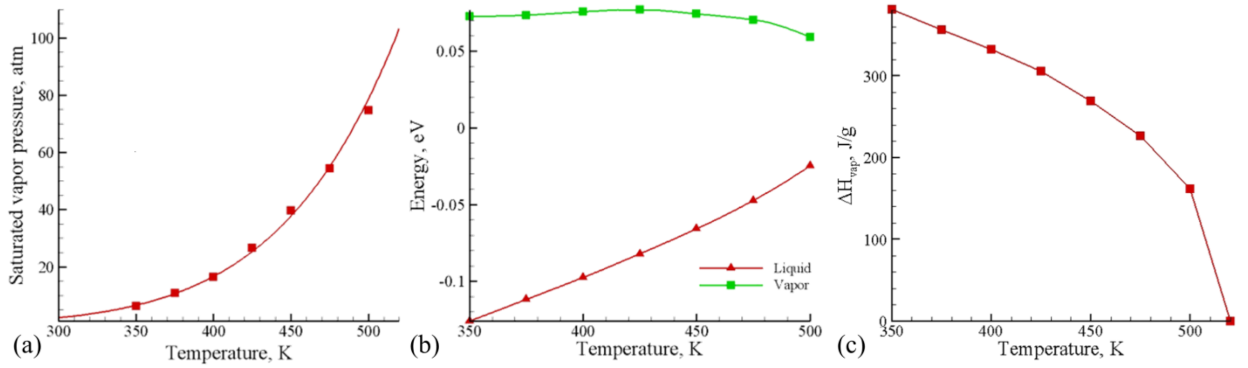

Figure 11.6. (a) Saturated vapor pressure, (b) equilbirium vapor and liqiud energies, (c) heat of vaproization of CG-water.

A2. Joint experimental and computational study of origins of bimodal nanoparticle size distribution for femtosecond laser ablation of ultrathin Pt films

(Dr. C. M. Rouleau performed the experiments and led the writing shown below.)

We recently study through thin film ablation (TTFA)[143] with a femtosecond laser source, and found that much like TTFA using a ns laser source, two populations of nanoparticles were produced in the deposit.[269] However, unlike ns-TTFA wherein elevated background gas pressures were observed to affect the nanoparticle populations by gas-phase condensation of atomic and molecular species within the plume, it was found that the same pressures had *no* effect on the populations produced by fs-TTFA. To understand this discrepancy and the mechanism of fs-TTFA, here we explore nanoparticle formation, transport dynamics, and size distributions as a function of metal film thickness for a laser fluence near the threshold for film removal.

Single 800 nm, 40 fs pulses from a Coherent Legend HE laser were attenuated and used to illuminate a rectangular aperture that was imaged through a 1.5 mm thick window onto the interface between 1 mm thick fused silica substrates and e-beam deposited Pt films. The laser spot size and incident fluence at the interface were 20 µm x 25 µm and 40-60 mJ/cm^2, respectively (see ref. 269 for additional details). Films less than 20 nm thick were chosen in accordance with the ~13 nm optical penetration depth of Pt, to provide both complete and partial absorption conditions. A gated, intensified CCD (ICCD) camera was used to capture time-resolved, side-view images of the ejecta and its transport between source and receiving substrates. The entire processing chamber was mounted on an XYZ stage to provide a fresh Pt film region for every laser shot.

Fig. 11.7c shows a typical sequence of ICCD images obtained during backside ablation of a 20 nm Pt film in vacuum. Most notable in the figure was the formation of an unusual and compact, highly forward-directed plume that, contrary to those observed from bulk targets, had a high minimum velocity (~100 m/s for the trailing edge). The elongation of the plume in the propagation direction is similar to that observed for heavy biomolecules in MALDI,[270] indicating that the observed ejecta were likely nanoparticles. Measurement of the FWHM of an actual deposit showed an angular spread of ~2.6 degrees,[269] which is in good agreement with the value of the included angle defined by the bright waist of the plume in the figure. Spectrally-resolved imaging of the plume through a series of 40 nm optical bandpass filters revealed blackbody-like spectra at time delays of 5 µs and 50 µs after ablation, which after radiometric calibration, permitted temperature estimates of ~1900 K and ~1700 K, respectively, consistent with incandescent Pt nanoparticles that were nearly molten.

To gain insight into the composition of the plume, a lacey carbon TEM grid was placed on the receiving substrate located 5-10 mm from the source substrate, and the captured material was analyzed by TEM. As shown in Fig. 11.7a, the deposit was composed of large and small (see inset) spherical nanoparticles, and as shown in Fig. 11.7b, there size distribution was bimodal with one mode centered near 10 nm and the other near 200 nm. Separate experiments to slow the ejecta with high background gas pressures indicated that the small mode could be eliminated in the deposit, but without any noticeable change to ICCD images of the plume as in Fig. 11.7c., thereby indicating that the present images follow the propagation of the primarily larger 80-320 nm nanoparticles in the large mode. Detailed comparison of the size-dependent particle slowing will be the subject of a separate publication. Thus, the physical origin and the time/place of the formation of the small nanoparticles is subject to interpretation. Three possible scenarios may be considered for the mechanisms of nanoparticles formation: (1) splashing or fragmentation of larger nanoparticles upon impact on the receiver, (2) condensation of ablated atomic species, or (3) generation at the early stage of the ablation of the film and simultaneous ejection with the large nanoparticles.

To evaluate the splashing contribution, the material transport from the source and its interaction with the receiver were analyzed by time-resolved imaging. The sequence of plume images in Fig. 11.7c not only revealed rebounding of the plume from the surface of the receiver, but from the source as well. A total of 3 rebound events were observed as shown in the distance versus time plot of Fig. 11.7d. This points out that particle size distributions measured using witness plate techniques may be skewed with respect to the *true* distribution in the incoming plume. Note that while some of the nanoparticles rebounded from the receiving substrate (Fig. 11.7c,d) and others were collected and contributed to the large-size mode of the particle size distribution (Fig. 11.7b), it is reasonable to consider a question on whether the fragmentation or splashing of the larger nanoparticles represent a possible alternative outcome of the nanoparticle interaction with the substrates.

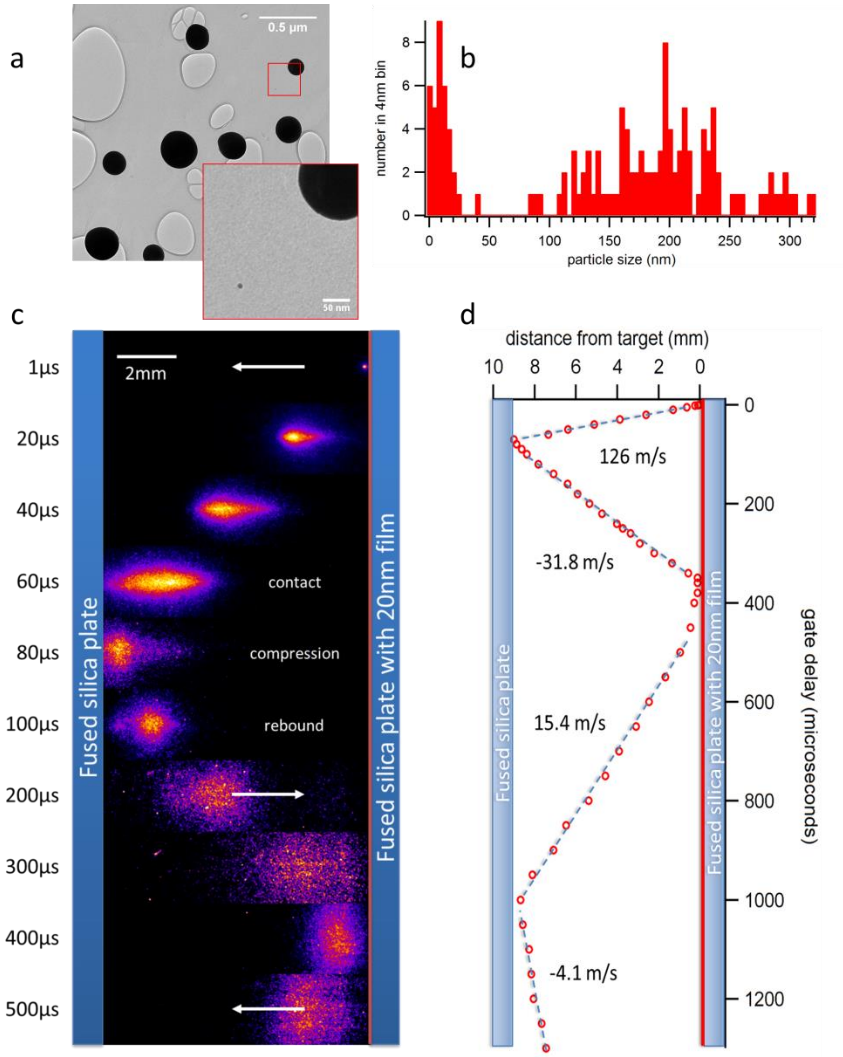

Figure 11.7. Particle morphology (a), particle size distribution (b), false color ICCD image sequence at fixed gain and f-stop (c), and position of maximum plume intensity vs. time plot derived from time-resolved ICCD imaging of a 20 nm Pt film irradiated in vacuum at an incident fluence of 40-60 mJ/cm^2 (d). The gate width used for imaging was 20% of the respective gate delay, and particle collection was performed at 5mm on a lacey carbon TEM grid. The size histogram was the result of 3600 ablation events from unique locations, and derived by measuring the diameter of ~200 particles in a series of TEM micrographs. The laser entered the source substrate at the right, and ejecta traveled to the left as a compact mm-scale packet having a collective velocity of 126 m/s as shown in the range vs. time plot. Three rebound events were observed thereafter, wherein the velocity was reduced with each bounce.

An examination of the Reynolds, Weber, and Ohnesorge numbers for an impinging particle does provide some guidance as to whether fragmentation in the present case was likely. The Reynolds number, *Re,* for Pt particles with diameters < 300 nm (Fig. 11.7b), mean velocity of 126 m/s (Fig. 11.7), and dynamic viscosity and density (at 1600 K) of 9.5 mPa·s and 20.6 g/cc, respectively,[271] is *less than* 95. Similarly, with the above parameters and the surface tension of Pt at 1600 K taken as 1.72 N/m,[271] the Weber number, *We*, would have been *less than* 75. Lastly, the Ohnesorge number, $Oh = We^{1/2}/Re$, that relates viscous forces to the inertia and surface tension of the particle, would therefore be *greater than* 0.1 under the present conditions.

To determine if splashing was likely one needs to estimate a critical Ohnesorge number, Oh_{cr}. Using the formalism of Mundo et al.,[272] and references therein, Oh_{cr} can be shown to be not only a function of the contact angle of the particle at maximum spread, but the ratio of the maximum spread of the particle on impact to its original diameter. For high viscosity liquids, *Re* and *We* as above, and using the formalism by Mao et al.,[273] it can be shown that the latter ratio is ~2 for a wide range of contact angles. This leaves one to estimate a contact angle, and a reasonable assumption here is that it was greater than 90°, due to the relatively high viscosity of Pt particles under the present conditions. Consequently, Oh_{cr} was always *less than* 0.1, and since it marks the boundary *below* which splashing is considered likely, it can be concluded that splashing-induced nanoparticle generation was *not* likely under the present conditions.

Turning to gas-phase condensation as a possible source of the small mode in Fig. 11.7b, this scenario was tested recently by comparing the size distribution of particles collected in vacuum to that of particles collected in 1 Torr Ar gas.[269] Note that the same 10 nm source film and 5 mm distance to the receiving substrate were used in both cases, and both distributions were found to be bimodal with one mode near 10 nm and the other near 120 nm. Most notable was that in contrast to ns-ablation of thin metal films,[143] *no* change in the magnitude of the smaller mode was observed upon performing the collection at 1 Torr. This observation is *inconsistent* with the hypothesis of condensation being the source of the small nanoparticles in the small mode.

We are left with the last possible interpretation - that the small nanoparticles directly form in the film ablation process. To understand the highly nonequilibrium process the initial stage of fs laser ablation of a 20 nm Pt film is investigated here using an atomistic simulation performed with a hybrid model[71-72, 88] that combines a classical molecular dynamics (MD) method with a continuum description of the laser excitation of conduction band electrons, electron-phonon coupling, and electron heat conduction based on a two-temperature model (TTM).[111] The dimensions of the computational system in the lateral (parallel to the surface of the film) directions were 100 nm × 100 nm and the total number of atoms in the system was 13.3 million. The interatomic interactions in the Pt film were described by the embedded atom method potential[99] and the parameters of the TTM equation for the electron temperature are from ref. 274. The transparent silica substrate was represented by a dynamic acoustic impedance matching boundary condition, which accounted for the elastic response of the substrate and reproduced the work of adhesion between Pt and fused silica.[275]

The conditions leading to the ejection and disintegration of the 20 nm Pt film irradiated by a 40 fs laser pulse at an absorbed fluence of 37 mJ/cm^2 (about 2.4 times the threshold fluence for complete melting of the film) are illustrated in Fig. 11.8. The excitation of electrons within the optical penetration depth followed by the rapid energy redistribution by the excited electrons results in the homogeneous heating of the film (Fig. 11.8a) on the timescale of the electron-phonon equilibration, $\tau_{\text{e-ph}} \approx 6$ ps, defined here as the time constant of the exponential decay of the energy of the excited electrons.

The fast heating occurring under conditions of stress confinement[88, 133, 157, 161] ($\tau_{e\text{-}ph} \leq L_f/C_s \approx$ 7 ps, where L_f = 20 nm is the thickness of the film and $C_s \approx$ 3000 m/s is the speed of sound in Pt) leads to the buildup of high compressive pressure (Fig. 11.8b). In agreement with predictions of earlier atomistic[72] and continuum-level simulations,[145] the relaxation of the compressive pressure causes rapid expansion of the film and generation of strong tensile stresses in the upper portion of the film 8 to 15 ps after the laser pulse. The tensile stresses induce cavitation and eventual disintegration/spallation of the film into a thicker layer adjacent to the substrate and a thinner layer moving away from the substrate with a velocity of ~300 m/s. As shown in the inset of Fig. 11.8d, the pressure from the vapor released in the process of the film disintegration and subsequent evaporation from the liquid fragments results in additional acceleration of the top layer, leading to a velocity of 480 m/s by the end of the simulation. The thicker layer also separates from the substrate and gradually accelerates to 110 m/s by 1.5 ns. The time dependences of the velocities of both layers show signs of saturation by 1.5 ns, and extrapolation to longer times suggests steady state values of ~500 m/s and ~150 m/s for the two parts of the film, respectively.

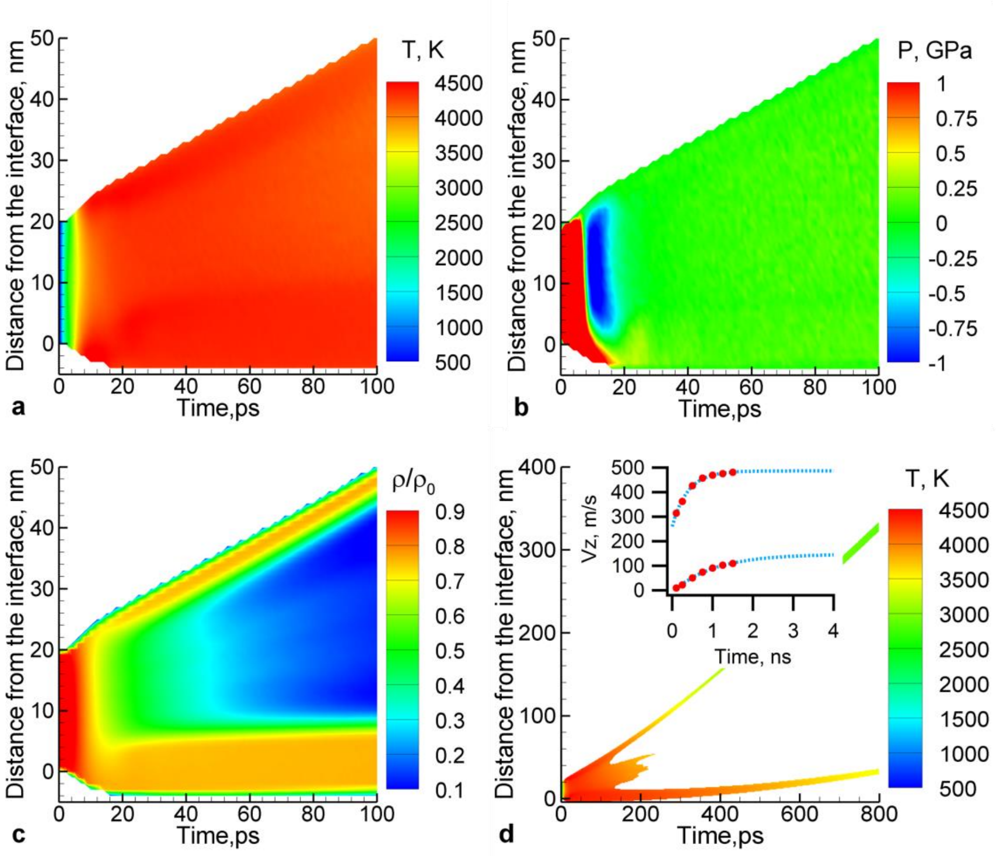

Figure 11.8. Contour plots showing the evolution of temperature (a,d), pressure (b), and density (c) in a TTM-MD simulation of a 20 nm Pt film deposited on a silica glass substrate and irradiated by a 40 fs laser pulse at an absorbed fluence of 37 mJ/cm^2. The density scale is normalized to the initial density before the irradiation, ρ_0. Areas where the density of the material is less than $0.05\rho_0$ are not shown in the plots. The laser pulse is directed through the silica substrate, i.e., along the Y-axis from the bottom of the contour plots. The inset in (d) shows the time dependence of the ejection velocity of the upper and lower portions of the film that is split during the ablation process.

A visual picture of the film disintegration and ejection is provided in Fig. 11.9, where snapshots from the simulation are shown. The initial spallation of the film into two layers is followed by a rapid decomposition of the upper molten layer into a 28 nm diameter droplet with two smaller clusters (see 1.5 ns snapshot). While the small (100 × 100 nm^2) lateral size of the computational system does not allow us to predict the particle size distribution emerging from the layer decomposition, we can conclude that the particle diameters are in the range of 10s of nm. Similarly, while the thicker lower spalled layer is stabilized by the periodic boundary conditions and retains its integrity during the simulation, the layer can be expected to decompose into individual droplets under conditions realized in the present experiments. Using a theoretical analysis of the stability of thin liquid films developed by Vrij[64] and applied to spalled layers in ref.

[88], droplets with diameters of ~160 nm are estimated from the dominating perturbation wavelength leading to spontaneous rupture of the film.[88]

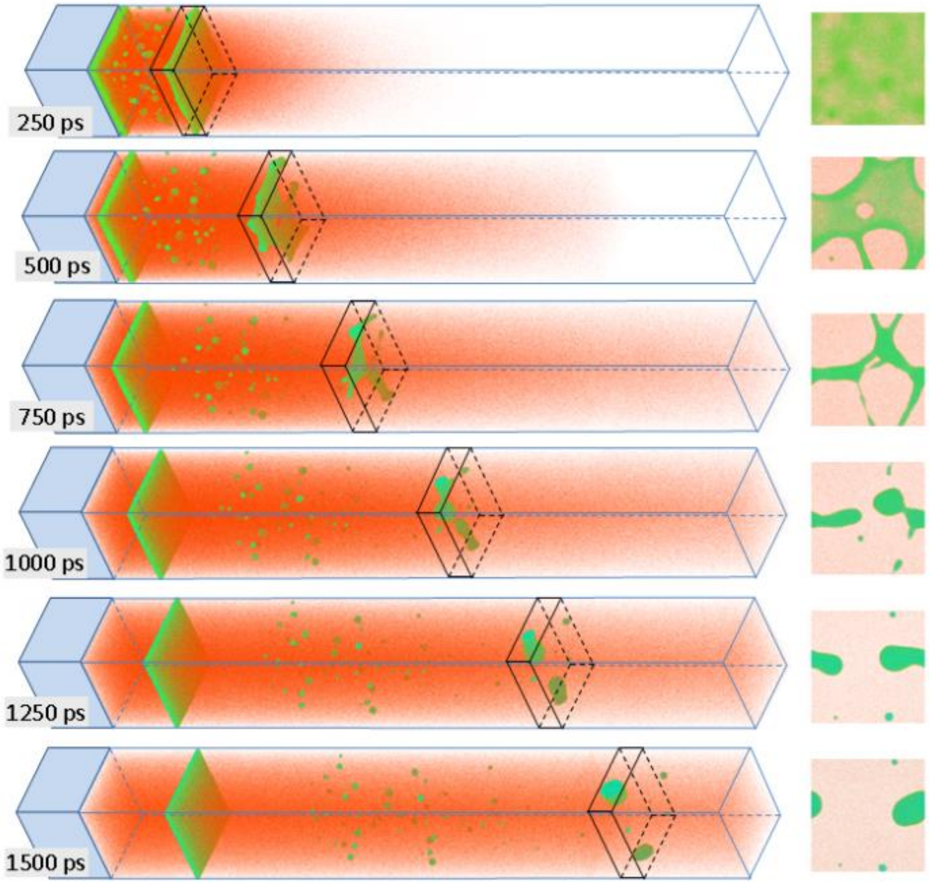

Figure 11.9. Snapshots of atomic configurations predicted in a TTM-MD simulation of laser ablation of a 20 nm Pt film irradiated by a 40 fs laser pulse at an absorbed fluence of 37 mJ/cm^2. The atoms are colored by their potential energies, from red, for the vapor-phase atoms, to green, for atoms in liquid droplets. The square frames shown on the right are plan views of 30 nm sections of the plume outlined in the snapshots. Note that the laser pulse enters the film from the left, through the transparent substrate shown by the blue rectangular parallelepipeds.

Making connections to the experimental observations, the small mode of the bimodal distribution in Fig. 11.7b can be attributed to droplets in the range of 10s of nm that originate from the fast moving portion of the film that spalls in the early stages of ablation, as well as the small clusters that form in the spallation process and are located between the fast and slower moving portions of the film (Fig. 11.9). On the other hand, the droplets contributing to the large mode of the size distribution in Fig. 1b are expected to result from the rupture of the slower moving portion of the film as both the sizes of the larger droplets, in 100s of nm, and the ejection velocity, ~150 m/s, are in a good agreement with the measured values. Moreover, the computational prediction that the large particles originate from decomposition of a liquid layer moving away from the irradiated target with a common collective velocity is consistent with the observation of the detached compact plumes in the ICCD images in Fig. 11.7c.

While the initial temperature of the droplets in the simulations is ~4000 K, by 1.5 ns fast evaporative cooling brings the temperature of the top and bottom layer down to 2570 K and 2850 K, respectively. Additional evaporative cooling combined with radiative energy loss can be expected to bring the temperature below the melting point and cause solidification on a timescale of µs.[276] This scenario is consistent with the temperature of ~1700 K evaluated from spectrally-resolved imaging of the plume at 5 and 50 µs.

Based on the insights into the origin of the bimodal size distribution provided by the simulations, the conditions for the transition from a bimodal to unimodal size distribution can be suggested. Since splitting of the film into two layers contributing to the two modes of the particle size distribution is defined by the conditions of stress confinement, a decrease in film thickness, L_f, would necessarily reduce the magnitude of the laser-induced compressive and tensile stresses, thereby preventing the film from splitting. To verify this prediction, 15, 10, 5, and 2 nm films were ablated and the particle size distributions were analyzed. The results are shown in Fig. 11.10, and most notable is the collapse of the two modes of the distribution into a *single* mode as the nominal film thickness approaches 2 nm, thereby confirming the computational prediction.

In summary, the generation and transport dynamics of Pt nanoparticles synthesized by backside fs-laser ablation of optically-thin Pt films on a transparent substrate is investigated experimentally and computationally. Multiple rebound events were observed in particle collection experiments, suggesting that the size distributions measured using witness plates may represent skewed versions of the nascent distributions generated in fs-ablation. In nearly all cases, the collected distributions were bimodal, with one mode in the 10s of nm range, and the other in the 100s of nm range. The results of a TTM-MD simulation suggest that the smaller mode largely originates from a thin, fast-moving layer that spalls in the early stage of ablation, leaving an underlying, slower-moving unstable liquid layer wholly responsible for the larger mode. Generation of smaller particles by gas phase condensation in the ablation plume or through splashing of the larger particles upon impact was ruled unlikely under the present conditions.

Finally, in agreement with modeling, the reduction in film thickness from 20 to 2 nm was found to result in a commensurate shift in the large mode of the particle size distribution toward smaller mean values until finally, at a nominal thickness of 2 nm, the distribution became unimodal. These results suggest a synthesis route for production of metastable nanoparticles with a narrow size distribution in the range of 10s of nm, delivered to a surface in a localized and well-controlled fashion.

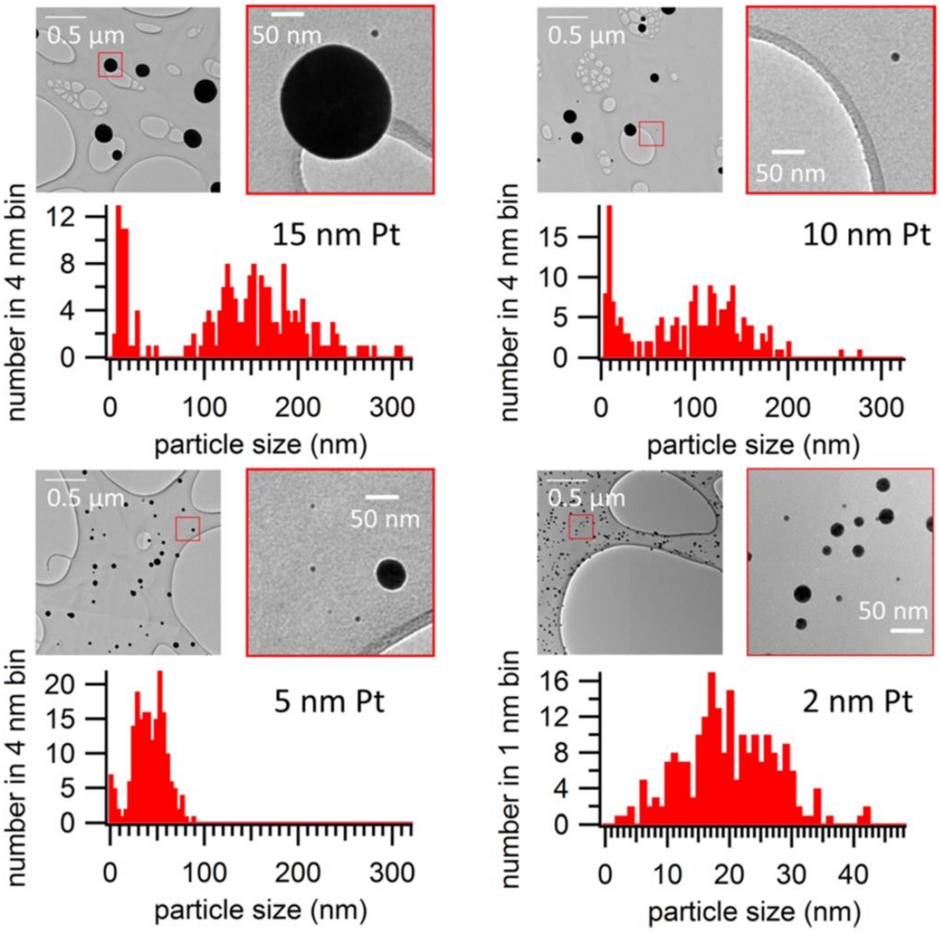

Figure 11.10. Particle size distribution and representative TEM images at high and low magnifications as a function of nominal film thickness (shown). In all cases, particle collection was performed in vacuum, at 5 mm, and using an incident fluence of 40-60 mJ/cm^2.

A3. Formation of large clusters: Molten Layer stability analysis

In MD simulations performed in Chapter 2, the thick spalled layers do not disintegrate into large clusters within simulation time. However, if the simulations are continued for longer time, in experiments these layers will eventually decompose into individual droplets. The size of the droplets can be roughly estimated according to the theoretical analysis of the stability of thin free molten films[64] that predicts the dominating perturbation wavelength that leads to spontaneous rupture of the film. This wavelength can be estimated by $\Lambda(h) = \left[\left(8\pi^3\gamma\right)/A_H\right]^{1/2}\mathrm{h}^2$, where h is the film thickness, γ is the surface energy of molten Ag, and A_H is the Hamaker constant. Assuming that a circular section of the film with the diameter Λ and thickness h contributes to one spherical droplet, the droplet diameter can be estimated as $d = \left[\left(12\pi^3\gamma\right)/A_H\right]^{1/3}\mathrm{h}^{5/3}$. Since the actual density of the bottom molten layers is only about 50% of the actual density of molten silver at the melting temperature, we use the effective thickness recalculated in respect to this density. After the conversion, the effective thicknesses of the layer are 10.8 nm for the case of 20nm film, and 4.6 nm for the the case of 10nm film. The temperature of the layer is 2753 K for the 20nm film, and 2682 K for the 10nm film

For a molten Ag freestanding layer, Λ and d can be evaluated by using the Hamaker constant equal to $A_H = 1.33 \times 10^{-19}$ J, [277] and a semi-empirical equation for the temperature dependence of the surface energy of molten metals,[278] $\gamma = \gamma_0\left(1 - T/T_c\right)^{1.2}$, which ensures that the energy of the molten-vapor interface vanish at the critical temperature T_c. The parameter $\gamma_0 = 1472$ mJ/m^2 is determined by using the values of the surface energy of molten Ag at the melting temperature T_m = 1139 K, $\gamma(T_m) = 910$ mJ/m^2,[278] and the critical temperature T_c = 3450 K determined in ref. [101]. By applying these parameters, the perturbation wavelength and the cluster size are estimated to be equal to $\Lambda = 0.45$ μm and d = 112 nm in the case of 10nm film and Λ = 2.34 μm and d = 446 nm in the case of 20 nm film.

With the estimates of Λ being of the order of a typical laser spot size used in laser material processing experiments, it is clear that the stability analysis done above can only provide an overestimated upper bound value of the maximum size of droplets emerging from the decomposition of the molten layers separated from the film in the spallation regime. The instabilities related to the process of separation of the layer from the foamy molten structures, as well as the spatial variation of the thickness of the layer are likely to induce decomposition at a scale smaller than Λ. Thus, it can be expected to have smaller, on the order of hundreds nanomiters, characteristic size of droplets ejected during the laser spallation that is in the agreement with experiments.[117]

A4. Estimation of the experimental absorbed laser fluence

(Mr. Maxim Shugaev performed the TTM calculation and wrote the summary shown below.)

To facilitate comparison of the experimental observations with computational predictions, the incident laser fluence applied in the experimental part of this study is converted to the absorbed laser fluence with the help of TTM simulation accounting for the electron temperature dependence of the reflectivity and optical absorption coefficient, as well as for the kinetics of surface melting as described in ref. 162.

In the experiment, Au target is irradiated by a 10 ps laser pulse at the wavelength of λ = 1064 nm and incident fluence of 3400 mJ/cm^2. The irradiation of the target by a laser pulse is represented through a source term added to the TTM equation for the electron temperature. The source term accounts for the excitation of the conduction band electrons by a laser pulse with a Gaussian temporal profile and reproduces attenuation of laser intensity with depth under the surface according to Beer–Lambert law.

The electron temperature dependences of the electron-phonon coupling factor and electron heat capacity are taken in the forms that account for the thermal excitation from the electron states below the Fermi level.[274] The electron thermal conductivity of Au is approximated as suggested in ref. 192. The lattice heat capacity of Au is taken to be 25.41 J mol^{-1} K^{-1}, density is 19300 kg/m^3, melting temperature is 1337 K, and the heat of fusion is 12.7 kJ/mol.[105]

The reflectivity and the absorption depth are calculated based on complex permittivity coefficient according to:

$$R = \left| \frac{\sqrt{\varepsilon_{Au}} - \sqrt{\varepsilon_w}}{\sqrt{\varepsilon_{Au}} + \sqrt{\varepsilon_w}} \right|^2, \ l_{abs} = \frac{\lambda}{4\pi \operatorname{Im}\left(\sqrt{\varepsilon_{Au}}\right)},$$

where ε_{Au} and ε_w are relative permittivities of Au and water, $\varepsilon_w = 1.78$.[105] The complex permittivity of Au is parametrized based on ref. 193:

$$\varepsilon_{Au} = \varepsilon_\infty - \frac{\omega_p^2}{\omega \cdot \left(\omega + i\nu_{ef}\right)} - \frac{f\Omega_L^2}{\left(\omega^2 - \Omega_L^2\right) + i\Gamma_L \omega},$$

where Γ_L = 0.659×10^{15} Hz and Ω_L = 4.085×10^{15} Hz are the oscillator strength and the spectral width of the Lorentz oscillators, respectively, f = 1.09 is the weighting factor, ω_p = 1.328×10^{16} Hz is the plasma frequency, ε_∞ = 5.9673 is a dc dielectric function, $\omega = 2\pi c/\lambda$ is the angular laser frequency, ν_{ef} is an effective electron collision frequency, $\nu_{ef} = \min(\nu_e, \nu_c)$. The electronic collision frequency is the sum of the electron-electron and electron-phonon collision frequencies $\nu_e = AT_e^2 + BT_l$, A = 1.2×10^7 $K^{-2}s^{-1}$ and B = 1.23×10^{11} $K^{-1}s^{-1}$.[279] The maximum critical electron collision frequency is estimated as $\nu_c = (4\pi n_0/3)^{1/3}\sqrt{v_f^2 + k_B T_e/m_e}$,[280] n_0 = 5.90×10^{28} m^{-3}, v_f = 1.40×10^6 m/s.

To account for the energy transport occurring before the thermalization of the excited electrons, the optical absorption depth, l_{abs}, is combined with the effective depth of the "ballistic" energy transport, l_b, yielding the effective range of the laser energy deposition and redistribution by the non-thermal electrons, $l_{eff} = l_{abs} + l_b$. The ballistic range is roughly estimated as a product of the Fermi velocity and the Drude relaxation time, $l_b = v_f/\nu_e$. In the TTM simulation, the instantaneous value of reflectivity is defined by the evolving electron and lattice temperatures on the surface, while the energy deposition fully accounts for the variation of l_{abs} and l_b with depth under the surface. As an example of the strong dependence of the reflectivity and the effective range of the laser energy deposition on the electron temperature, the magnitudes of R and l_{eff} are shown in Fig. 11.11a for a broad range of electron temperatures and the lattice temperature fixed at 300 K.

The evolution of the surface temperature obtained in a TTM simulation is shown in Fig. 11.11b. At an incident laser fluence 3400 mJ/cm^2, the absorbed fluence predicted in the simulation is 1940 mJ/cm^2. Since reflectivity of Au rapidly drops with increase of the electron temperature, the absorbed laser fluence and, therefore, the increase of the electron and lattice surface temperatures is much larger than that predicted in a simulation performed with constant optical properties of Au, shown as dashed lines in Fig. 11.11b. In the latter case, the reflectivity of water-gold interface is assumed to be 0.972, the optical absorption depth is 12 nm,[230] and the electron temperature dependent ballistic range, similar to the simulation discussed above, is used. Due to the constant high value of reflectivity, the absorbed laser fluence is found to be 93.8 mJ/cm^2. On the other hand, if the ballistic range is fixed at 100 nm,[281] and the variation of the optical properties are taken into account as discussed above, the predicted absorbed fluence becomes ~1030 mJ/cm^2.

The high sensitivity of the predicted value of the absorbed fluence to the temperature dependence of the ballistic range suggests that the value of 1940 mJ/cm^2 can be considered to be an upper bound estimate of the real value. Indeed, the assumption of the electron equilibration within the characteristic time of a single scattering event is likely to result in a substantial underestimation of the ballistic range. The longer ballistic range leads to a slower heating of the surface and, as a result, prolongs the time when the value of reflectivity remains at a high level. Given the uncertainty in the range of the ballistic energy redistribution, we conclude that the absorbed laser fluence under experimental conditions is within the range of 1000 to 2000 mJ/cm^2.

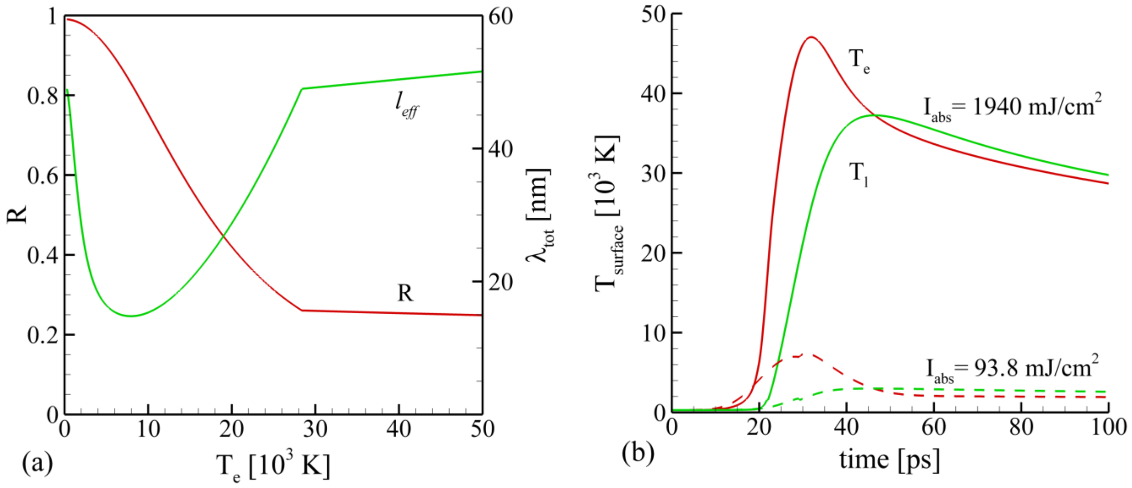

Figure 11.11. The dependence of the reflectivity and the total absorption depth on the electron temperature at the lattice temperature fixed at 300 K (a) and the evolution of the temperature at the surface of Au target irradiated by a 10 ps laser pulse at the incident fluence 3400 mJ/cm^2 (b). In (a), red and green lines illustrate to the reflectivity and the total effective range of the laser energy deposition, while in (b), red and green lines depict the electron and lattice temperatures, respectively. In the second plot, solid lines correspond to results obtained with accounting for the temperature dependence of optical properties of Au target, while dashed lines correspond to results of a simulation performed for constant optical properties.

A5. Comparison of microscopic dynamics at the interface between ablation plume and liquid environment for FBD and Mishin-Ag EAM potential

The results from Chapter 5 and 7 show the importance of pulse duration to the microscopic at the interface dynamics between ablation plume and water that can define the possible nanoparticle generation mechanisms. When the stress confinement condition is strong for short pulse as presented in Chapter 5, rapid accumulation of vapor and liquid droplets mixtures and large liquid layers facilitates a dense molten layer formation at plume-water interface. When pulse duration is extended away from condition of stress confinement, the characteristics of ablation plume becomes dominated by mixtures of vapor and liquid droplets, as presented in Chapter 7. Ag FBD EAM potential is the main interatomic potential applied in the dissertation, since various high-temperature thermodynamics properties relevant to laser ablation are well-represented. However, we also test another well-received Ag EAM potential in high fluence regime to evaluate the generality of our results obtained based on Ag FBD potential.

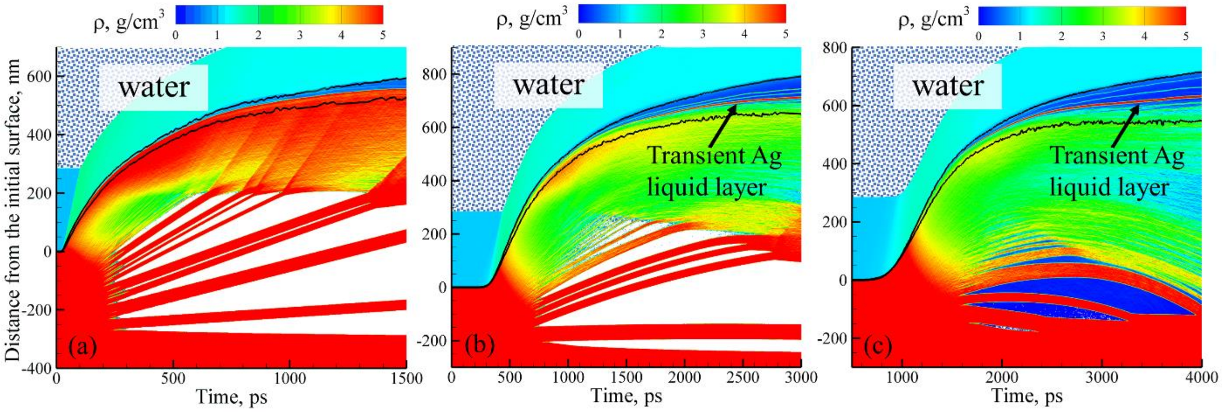

Figure 11.12. Density contour plots predicted in atomistic simulations of laser ablation of a bulk silver target (Mishin-Ag) irradiated in water by a 10 ps(a), 150 ps (b) and 400 ps (c) laser pulse at an absorbed fluence of 800 mJ/cm^2. The two black lines in each figure outline the water-Ag mixing region defined as a region where both water molecules and Ag atoms are present.

The alternative potential is constructed by Williams et al.,[256] abbreviated as Mishin-Ag potential. In addition to the well-fitted low-temperature thermodynamic properties, the testing of high temperature thermodynamic properties indicate that it is also a viable potential for simulations of laser ablation. The critical temperature and pressure are found to be 5368 K and 0.105 GPa, tested with NVT plus particle test method.[128] Three small scale simulations are performed with Mishin-Ag bulk target in water at 800 mJ/cm^2 with pulse duration of 10, 150 and 400 ps. The density contour plots for these three simulations, shown in Fig. 11.12, share great similarity of microscopic dynamics at interface between ablation plume and water with results obtained based on Ag-FBD potentials. A formation of dense metal molten layer is formed at plume-water interface for simulation performed at 10 ps, shown in Fig. 11. 12a. As pulse durations extend to 150 and 400 ps, the dense metal molten layer does not form at plume-water interface, and the components of Ag vapor and liquid droplets increase in the ablation plume, shown in Fig. 11. 12b and 11.12c; the trend confirms with observation from simulations performed with FBD-Ag (Chapter 7). Moreover, a thin transient metal layer condenses from Ag vapor and liquid droplets mixture at plume-water interface is observed for simulations performed at 150 and 400 ps laser pulses, as marked on Fig. 11.12b and 11.12c, that is also reported for simulations with FBD-Ag potential in longer laser pulse duration (Chapter 7.3.3). The effect of pulse duration on trend of microscopic dynamics at the interface between ablation plume and water prestend in the dissternation is a general phenomona that is not sensitive to change of well-constructed Ag potentials.

References

1. Asahi, T.; Mafune, F.; Rehbock, C.; Barcikowski, S., Strategies to Harvest the Unique Properties of Laser-Generated Nanomaterials in Biomedical and Energy Applications. *Appl. Surf. Sci.* **2015,** *348*, 1-3.

2. Rehbock, C.; Jakobi, J.; Gamrad, L.; van der Meer, S.; Tiedemann, D.; Taylor, U.; Kues, W.; Rath, D.; Barcikowski, S., Current State of Laser Synthesis of Metal and Alloy Nanoparticles as Ligand-Free Reference Materials for Nano-Toxicological Assays. *Beilstein J. Nanotechnol.* **2014,** *5*, 1523-1541.

3. Yang, G. W., Laser Ablation in Liquids: Applications in the Synthesis of Nanocrystals. *Prog. Mater. Sci.* **2007,** *52*, 648-698.

4. Tarasenko, N. V.; Butsen, A. V., Laser Synthesis and Modification of Composite Nanoparticles in Liquids. *Quant. Electron.* **2010,** *40*, 986-1003.

5. Mafune, F.; Kohno, J.; Takeda, Y.; Kondow, T.; Sawabe, H., Formation of Gold Nanoparticles by Laser Ablation in Aqueous Solution of Surfactant. *J. Phys. Chem. B* **2001,** *105*, 5114-5120.

6. Compagnini, G.; Scalisi, A. A.; Puglisi, O., Ablation of Noble Metals in Liquids: A Method to Obtain Nanoparticles in a Thin Polymeric Film. *Phys. Chem. Chem. Phys.* **2002,** *4*, 2787-2791.

7. Kabashin, A. V.; Meunier, M., Synthesis of Colloidal Nanoparticles During Femtosecond Laser Ablation of Gold in Water. *J. Appl. Phys.* **2003,** *94*, 7941-7943.

8. Sylvestre, J. P.; Kabashin, A. V.; Sacher, E.; Meunier, M., Femtosecond Laser Ablation of Gold in Water: Influence of the Laser-Produced Plasma on the Nanoparticle Size Distribution. *Appl. Phys. A* **2005,** *80*, 753-758.

9. Tsuji, T.; Thang, D. H.; Okazaki, Y.; Nakanishi, M.; Tsuboi, Y.; Tsuji, M., Preparation of Silver Nanoparticles by Laser Ablation in Polyvinylpyrrolidone Solutions. *Appl. Surf. Sci.* **2008,** *254*, 5224-5230.

10. Xiao, J.; Liu, P.; Wang, C. X.; Yang, G. W., External Field-Assisted Laser Ablation in Liquid: An Efficient Strategy for Nanocrystal Synthesis and Nanostructure Assembly. *Prog. Mater. Sci.* **2017,** *87*, 140-220.

11. Zhang, D.; Gökce, B.; Barcikowski, S., Laser Synthesis and Processing of Colloids: Fundamentals and Applications. *Chem. Rev.* **2017,** *117*, 3990-4103.

12. Hess, C.; Schwenke, A.; Wagener, P.; Franzka, S.; Sajti, C.; Pflaum, M.; Wiegmann, B.; Haverich, A.; Barcikowski, S., Dose-Dependent Surface Endothelialization and Biocompatibility of Polyurethane Noble Metal Nanocomposites. *J. Biomed. Mater. Res. A* **2014,** *102*, 1909-1920.

13. Petersen, S.; Barcikowski, S., In Situ Bioconjugation: Single Step Approach to Tailored Nanoparticle-Bioconjugates by Ultrashort Pulsed Laser Ablation. *Adv. Funct. Mater.* **2009,** *19*, 1167-1172.

14. Amendola, V.; Meneghetti, M., Controlled Size Manipulation of Free Gold Nanoparticles by Laser Irradiation and Their Facile Bioconjugation. *J. Mater. Chem.* **2007,** *17*, 4705-4710.

15. Kumar, V. L.; Siddhardha, R. S. S.; Kaniyoor, A.; Podila, R.; Molli, M.; Kumar, V. S. M.; Venkataramaniah, K.; Ramaprabhu, S.; Rao, A. M.; Ramamurthy, S. S., Gold Decorated Graphene by Laser Ablation for Efficient Electrocatalytic Oxidation of Methanol and Ethanol. *Electroanalysis* **2014,** *26*, 1850-1857.

16. Zhang, J.; Chen, G.; Guay, D.; Chaker, M.; Ma, D., Highly Active Ptau Alloy Nanoparticle Catalysts for the Reduction of 4-Nitrophenol. *Nanoscale* **2014,** *6*, 2125-2130.

17. Hunter, B. M.; Blakemore, J. D.; Deimund, M.; Gray, H. B.; Winkler, J. R.; Muller, A. M., Highly Active Mixed-Metal Nanosheet Water Oxidation Catalysts Made by Pulsed-Laser Ablation in Liquids. *J. Am. Chem. Soc.* **2014,** *136*, 13118-13121.

18. Liu, P.; Liang, Y.; Lin, X.; Wang, C.; Yang, G., A General Strategy to Fabricate Simple Polyoxometalate Nanostructures: Electrochemistry-Assisted Laser Ablation in Liquid. *ACS Nano* **2011,** *5*, 4748-4755.

19. Intartaglia, R.; Das, G.; Bagga, K.; Gopalakrishnan, A.; Genovese, A.; Povia, M.; Di Fabrizio, E.; Cingolani, R.; Diaspro, A.; Brandi, F., Laser Synthesis of Ligand-Free Bimetallic Nanoparticles for Plasmonic Applications. *Phys. Chem. Chem. Phys.* **2013,** *15*, 3075-3082.

20. Neumeister, A.; Jakobi, J.; Rehbock, C.; Moysig, J.; Barcikowski, S., Monophasic Ligand-Free Alloy Nanoparticle Synthesis Determinants During Pulsed Laser Ablation of Bulk Alloy and Consolidated Microparticles in Water. *Phys. Chem. Chem. Phys.* **2014,** *16*, 23671-23678.

21. Tilaki, R. M.; Zad, A. I.; Mahdavi, S. M., Stability, Size and Optical Properties of Silver Nanoparticles Prepared by Laser Ablation in Different Carrier Media. *Appl. Phys. A* **2006,** *84*, 215-219.

22. Bärsch, N.; Jakobi, J.; Weiler, S.; Barcikowski, S., Pure Colloidal Metal and Ceramic Nanoparticles from High-Power Picosecond Laser Ablation in Water and Acetone. *Nanotechnology* **2009,** *20*, 445603.

23. Gökce, B.; van't Zand, D. D.; Menéndez-Manjón, A.; Barcikowski, S., Ripening Kinetics of Laser-Generated Plasmonic Nanoparticles in Different Solvents. *Chem. Phys. Lett.* **2015,** *626*, 96-101.

24. Kanitz, A.; Hoppius, J. S.; del Mar Sanz, M.; Maicas, M.; Ostendorf, A.; Gurevich, E. L., Synthesis of Magnetic Nanoparticles by Ultrashort Pulsed Laser Ablation of Iron in Different Liquids. *ChemPhysChem* **2017**, 10.1002/cphc.201601252.

25. De Giacomo, A.; De Bonis, A.; Dell’Aglio, M.; De Pascale, O.; Gaudiuso, R.; Orlando, S.; Santagata, A.; Senesi, G. S.; Taccogna, F.; Teghil, R., Laser Ablation of Graphite in Water in a Range of Pressure from 1 to 146 Atm Using Single and Double Pulse Techniques for the Production of Carbon Nanostructures. *J. Phys. Chem. C* **2011,** *115*, 5123-5130.

26. Dell'Aglio, M.; Santagata, A.; Valenza, G.; De Stradis, A.; De Giacomo, A., Study of the Effect of Water Pressure on Plasma and Cavitation Bubble Induced by Pulsed Laser Ablation in Liquid of Silver and Missed Variations of Observable Nanoparticle Features. *ChemPhysChem* **2017**, 10.1002/cphc.201601231.

27. Menendez-Manjon, A.; Chichkov, B. N.; Barcikowski, S., Influence of Water Temperature on the Hydrodynamic Diameter of Gold Nanoparticles from Laser Ablation. *J. Phys. Chem. C* **2010,** *114*, 2499-2504.

28. Mafuné, F.; Kohno, J.-y.; Takeda, Y.; Kondow, T.; Sawabe, H., Formation of Gold Nanoparticles by Laser Ablation in Aqueous Solution of Surfactant. *J. Phys. Chem. B* **2001,** *105*, 5114-5120.

29. Compagnini, G.; Scalisi, A. A.; Puglisi, O.; Spinella, C., Synthesis of Gold Colloids by Laser Ablation in Thiol-Alkane Solutions. *J. Mater. Res.* **2004,** *19*, 2795-2798.

30. Sylvestre, J. P.; Kabashin, A. V.; Sacher, E.; Meunier, M.; Luong, J. H. T., Stabilization and Size Control of Gold Nanoparticles During Laser Ablation in Aqueous Cyclodextrins. *J. Am. Chem. Soc.* **2004,** *126*, 7176-7177.

31. Yan, Z.; Compagnini, G.; Chrisey, D. B., Generation of Agcl Cubes by Excimer Laser Ablation of Bulk Ag in Aqueous Nacl Solutions. *J. Phys. Chem. C* **2011,** *115*, 5058-5062.

32. Yan, Z. J.; Bao, R. G.; Huang, Y.; Chrisey, D. B., Hollow Particles Formed on Laser-Induced Bubbles by Excimer Laser Ablation of Al in Liquid. *J. Phys. Chem. C* **2010,** *114*, 11370-11374.

33. Yan, Z.; Bao, R.; Wright, R. N.; Chrisey, D. B., Hollow Nanoparticle Generation on Laser-Induced Cavitation Bubbles Via Bubble Interface Pinning. *Appl. Phys. Lett.* **2010,** *97*, 124106.

34. Rehbock, C.; Merk, V.; Gamrad, L.; Streubel, R.; Barcikowski, S., Size Control of Laser-Fabricated Surfactant-Free Gold Nanoparticles with Highly Diluted Electrolytes and Their Subsequent Bioconjugation. *Phys. Chem. Chem. Phys.* **2013,** *15*, 3057-3067.

35. Zhang, D.; Gökce, B.; Notthoff, C.; Barcikowski, S., Layered Seed-Growth of Agge Football-Like Microspheres Via Precursor-Free Picosecond Laser Synthesis in Water. *Sci. Rep.* **2015,** *5*, 13661.

36. Pearce, S. R. J.; Henley, S. J.; Claeyssens, F.; May, P. W.; Hallam, K. R.; Smith, J. A.; Rosser, K. N., Production of Nanocrystalline Diamond by Laser Ablation at the Solid/Liquid Interface. *Diamond Relat. Mater.* **2004,** *13*, 661-665.

37. Hashimoto, S.; Werner, D.; Uwada, T., Studies on the Interaction of Pulsed Lasers with Plasmonic Gold Nanoparticles toward Light Manipulation, Heat Management, and Nanofabrication. *J. Photochem. Photobiol. C* **2012,** *13*, 28-54.

38. Besner, S.; Kabashin, A. V.; Winnik, F. M.; Meunier, M., Synthesis of Size-Tunable Polymer-Protected Gold Nanoparticles by Femtosecond Laser-Based Ablation and Seed Growth. *J. Phys. Chem. C* **2009,** *113*, 9526-9531.

39. Wang, H. Q.; Pyatenko, A.; Kawaguchi, K.; Li, X.; Swiatkowska-Warkocka, Z.; Koshizaki, N., Selective Pulsed Heating for the Synthesis of Semiconductor and Metal Submicrometer Spheres. *Angew. Chem. Int. Ed.* **2010,** *49*, 6361-6364.

40. Streubel, R.; Barcikowski, S.; Gökce, B., Continuous Multigram Nanoparticle Synthesis by High-Power, High-Repetition-Rate Ultrafast Laser Ablation in Liquids. *Opt. Lett.* **2016,** *41*, 1486-1489.

41. Streubel, R.; Bendt, G.; Gökce, B., Pilot-Scale Synthesis of Metal Nanoparticles by High-Speed Pulsed Laser Ablation in Liquids. *Nanotechnology* **2016,** *27*, 205602.

42. Amendola, V.; Meneghetti, M., What Controls the Composition and the Structure of Nanomaterials Generated by Laser Ablation in Liquid Solution? *Phys. Chem. Chem. Phys.* **2013,** *15*, 3027-3046.

43. Tamura, A.; Sakka, T.; Fukami, K.; Ogata, Y. H., Dynamics of Cavitation Bubbles Generated by Multi-Pulse Laser Irradiation of a Solid Target in Water. *Appl. Phys. A* **2013,** *112*, 209-213.

44. Ibrahimkutty, S.; Wagener, P.; Menzel, A.; Plech, A.; Barcikowski, S., Nanoparticle Formation in a Cavitation Bubble after Pulsed Laser Ablation in Liquid Studied with High Time Resolution Small Angle X-Ray Scattering. *Appl. Phys. Lett.* **2012,** *101*, 103104.

45. Ibrahimkutty, S.; Wagener, P.; Rolo, T. D.; Karpov, D.; Menzel, A.; Baumbach, T.; Barcikowski, S.; Plech, A., A Hierarchical View on Material Formation During Pulsed-Laser Synthesis of Nanoparticles in Liquid. *Sci. Rep.* **2015,** *5*, 16313.

46. Letzel, A.; Gökce, B.; Wagener, P.; Ibrahimkutty, S.; Menzel, A.; Plech, A.; Barcikowski, S., Size Quenching During Laser Synthesis of Colloids Happens Already in the Vapor Phase of the Cavitation Bubble. *J. Phys. Chem. C* **2017,** *121*, 5356-5365.

47. Wagener, P.; Ibrahimkutty, S.; Menzel, A.; Plech, A.; Barcikowski, S., Dynamics of Silver Nanoparticle Formation and Agglomeration inside the Cavitation Bubble after Pulsed Laser Ablation in Liquid. *Phys. Chem. Chem. Phys.* **2013,** *15*, 3068-3074.

48. Lam, J.; Amans, D.; Dujardin, C.; Ledoux, G.; Allouche, A.-R., Atomistic Mechanisms for the Nucleation of Aluminum Oxide Nanoparticles. *J. Phys. Chem. A* **2015,** *119*, 8944-8949.

49. Lam, J.; Lombard, J.; Dujardin, C.; Ledoux, G.; Merabia, S.; Amans, D., Dynamical Study of Bubble Expansion Following Laser Ablation in Liquids. *Appl. Phys. Lett.* **2016,** *108*, 074104.

50. Lam, J.; Amans, D.; Chaput, F.; Diouf, M.; Ledoux, G.; Mary, N.; Masenelli-Varlot, K.; Motto-Ros, V.; Dujardin, C., Γ-Al2o3 Nanoparticles Synthesised by Pulsed Laser Ablation in Liquids: A Plasma Analysis. *Phys. Chem. Chem. Phys.* **2014,** *16*, 963-973.

51. Dell'Aglio, M.; Gaudiuso, R.; De Pascale, O.; De Giacomo, A., Mechanisms and Processes of Pulsed Laser Ablation in Liquids During Nanoparticle Production. *Appl. Surf. Sci.* **2015,** *348*, 4-9.

52. Tanabe, R.; Nguyen, T. T. P.; Sugiura, T.; Ito, Y., Bubble Dynamics in Metal Nanoparticle Formation by Laser Ablation in Liquid Studied through High-Speed Laser Stroboscopic Videography. *Appl. Surf. Sci.* **2015,** *351*, 327-331.

53. Sakka, T.; Takatani, K.; Ogata, Y. H.; Mabuchi, M., Laser Ablation at the Solid-Liquid Interface: Transient Absorption of Continuous Spectral Emission by Ablated Aluminium Atoms. *J. Phys. D* **2002,** *35*, 65.

54. Polman, A., Solar Steam Nanobubbles. *ACS Nano* **2013,** *7*, 15-18.

55. Putterman, S. J.; Weninger, K. R., Sonoluminescence: How Bubbles Turn Sound into Light. *Annu. Rev. Fluid Mech.* **2000,** *32*, 445-476.

56. Philipp, A.; Lauterborn, W., Cavitation Erosion by Single Laser-Produced Bubbles. *J. Fluid Mech.* **1998,** *361*, 75-116.

57. Putterman, S.; Evans, P. G.; Vazquez, G.; Weninger, K., Cavitation Science: Is There a Simple Theory of Sonoluminescence? *Nature* **2001,** *409*, 782-783.

58. De Giacomo, A.; Dell'Aglio, M.; Santagata, A.; Gaudiuso, R.; De Pascale, O.; Wagener, P.; Messina, G. C.; Compagnini, G.; Barcikowski, S., Cavitation Dynamics of Laser Ablation of Bulk and Wire-Shaped Metals in Water During Nanoparticles Production. *Phys. Chem. Chem. Phys.* **2013,** *15*, 3083-3092.

59. Giorgetti, E.; Marsili, P.; Muniz-Miranda, M.; Gellini, C.; Giammanco, F., Spectroscopic Evidence of Positive Clusters in Ag Colloids Obtained by Laser Ablation in Aqueous Solutions. *Appl. Phys. A* **2014,** *117*, 327-331.

60. Jendrzej, S.; Gökce, B.; Amendola, V.; Barcikowski, S., Barrierless Growth of Precursor-Free, Ultrafast Laser-Fragmented Noble Metal Nanoparticles by Colloidal Atom Clusters – a Kinetic in Situ Study. *J. Colloid Interface Sci.* **2016,** *463*, 299-307.

61. Itina, T. E., On Nanoparticle Formation by Laser Ablation in Liquids. *J. Phys. Chem. C* **2011,** *115*, 5044-5048.

62. Povarnitsyn, M. E.; Itina, T. E., Hydrodynamic Modeling of Femtosecond Laser Ablation of Metals in Vacuum and in Liquid. *Appl. Phys. A* **2014,** *117*, 175-178.

63. Povarnitsyn, M. E.; Itina, T. E.; Levashov, P. R.; Khishchenko, K. V., Mechanisms of Nanoparticle Formation by Ultra-Short Laser Ablation of Metals in Liquid Environment. *Phys. Chem. Chem. Phys.* **2013,** *15*, 3108-3114.

64. Vrij, A., Possible Mechanism for the Spontaneous Rupture of Thin, Free Liquid Films. *Discuss. Faraday Soc.* **1966,** *42*, 23-33.

65. Allen, M. P.; Tildesley, D. J., *Computer Simulation of Liquids*. Clarendon: Oxford, 1987.

66. Frenkel, D.; Smit, B., *Understanding Molecular Simulation: From Algorithms to Applications*. Academic: San Diego, 1996.

67. Wu, C.; Karim, E. T.; Volkov, A. N.; Zhigilei, L. V., Atomic Movies of Laser-Induced Structural and Phase Transformations from Molecular Dynamics Simulations. In *Lasers in Materials Science, Springer Series in Materials Science*, Castillejo, M.; Ossi, P. M.; Zhigilei, L. V., Eds. Springer International Publishing: Switzerland, 2014; Vol. 191, pp 67-100.

68. Zhigilei, L. V.; Lin, Z. b.; Ivanov, D. S.; Leveugle, E.; Duff, W. H.; Thomas, D.; Sevilla, C.; Guy, S. J., Atomic/Molecular-Level Simulations of Laser-Materials Interactions. In *Laser-Surface Interactions for New Materials Production: Tailoring Structure and Properties*, Miotello, A.; Ossi, P. M., Eds. Springer-Verlag Berlin Heidelberg: Berlin, Germany, 2010; Vol. 130, pp 43-79.

69. Karim, E. T.; WU, C.; Zhigilei, L. V., Molecular Dynamics Simulations of Laser-Materials Interactions: General and Material-Specific Mechanisms of Material Removal and Generation of Crystal Defects. In *Fundamentals of Laser-Assisted Micro- and Nanotechnologies*, Veiko, V. P.; Konov, V. I., Eds. Springer International Publishing: Switzerland, 2014; Vol. 195, pp 27-49.

70. Zhigilei, L. V.; Leveugle, E.; Garrison, B. J.; Yingling, Y. G.; Zeifman, M. I., Computer Simulations of Laser Ablation of Molecular Substrates. *Chem. Rev.* **2003,** *103*, 321-347.

71. Zhigilei, L. V.; Lin, Z.; Ivanov, D. S., Atomistic Modeling of Short Pulse Laser Ablation of Metals: Connections between Melting, Spallation, and Phase Explosion. *J. Phys. Chem. C* **2009,** *113*, 11892-11906.

72. Ivanov, D. S.; Zhigilei, L. V., Combined Atomistic-Continuum Modeling of Short-Pulse Laser Melting and Disintegration of Metal Films. *Phys. Rev. B* **2003,** *68*, 064114.

73. Herrmann, R. F. W.; Gerlach, J.; Campbell, E. E. B., Ultrashort Pulse Laser Ablation of Silicon: An Md Simulation Study. *Appl. Phys. A* **1998,** *66*, 35-42.

74. Xu, X.; Cheng, C.; Chowdhury, I. H., Molecular Dynamics Study of Phase Change Mechanisms During Femtosecond Laser Ablation. *J. Heat Transfer* **2004,** *126*, 727-734.

75. Cheng, C.; Xu, X., Mechanisms of Decomposition of Metal During Femtosecond Laser Ablation. *Phys. Rev. B* **2005,** *72*, 165415.

76. Wang, X.; Xu, X., Molecular Dynamics Simulation of Heat Transfer and Phase Change During Laser Material Interaction. *J. Heat Transfer* **2001,** *124*, 265-274.

77. Lorazo, P.; Lewis, L. J.; Meunier, M., Thermodynamic Pathways to Melting, Ablation, and Solidification in Absorbing Solids under Pulsed Laser Irradiation. *Phys. Rev. B* **2006,** *73*, 134108.

78. Nedialkov, N. N.; Atanasov, P. A., Molecular Dynamics Simulation Study of Deep Hole Drilling in Iron by Ultrashort Laser Pulses. *Appl. Surf. Sci.* **2006,** *252*, 4411-4415.

79. Colombier, J. P.; Combis, P.; Audouard, E.; Stoian, R., Guiding Heat in Laser Ablation of Metals on Ultrafast Timescales: An Adaptive Modeling Approach on Aluminum. *New J. Phys.* **2012,** *14*, 013039.

80. Richardson, C. F.; Clancy, P., Picosecond Laser Processing of Copper and Gold. *Mol. Simul.* **1991,** *7*, 335-355.

81. Hakkinen, H.; Landman, U., Superheating, Melting, and Annealing of Copper Surfaces. *Phys. Rev. Lett.* **1993,** *71*, 1023-1026.

82. Ivanov, D. S.; Zhigilei, L. V., Combined Atomistic-Continuum Modeling of Short-Pulse Laser Melting and Disintegration of Metal Films. *Phys. Rev. B* **2003,** *68*.

83. Ivanov, D. S.; Zhigilei, L. V., Combined Atomistic-Continuum Model for Simulation of Laser Interaction with Metals: Application in the Calculation of Melting Thresholds in Ni Targets of Varying Thickness. *Appl. Phys. A* **2004,** *79*, 977-981.

84. Zhigilei, L. V.; Ivanov, D. S., Channels of Energy Redistribution in Short-Pulse Laser Interactions with Metal Targets. *Appl. Surf. Sci.* **2005,** *248*, 433-439.

85. Duff, W. H.; Zhigilei, L. V., Computational Study of Cooling Rates and Recrystallization Kinetics in Short Pulse Laser Quenching of Metal Targets. *J. Phys. Conf. Ser* **2007,** *59*, 413.

86. Lin, Z.; Zhigilei, L. V., Time-Resolved Diffraction Profiles and Structural Dynamics of Ni Film under Short Laser Pulse Irradiation. *J. Phys. Conf. Ser* **2007,** *59*, 11.

87. Lin, Z.; Johnson, R. A.; Zhigilei, L. V., Computational Study of the Generation of Crystal Defects in a Bcc Metal Target Irradiated by Short Laser Pulses. *Phys. Rev. B* **2008,** *77*, 214108.

88. Wu, C.; Zhigilei, L. V., Microscopic Mechanisms of Laser Spallation and Ablation of Metal Targets from Large-Scale Molecular Dynamics Simulations. *Appl. Phys. A* **2014,** *114*, 11-32.

89. Wu, C.; Zhigilei, L. V., Nanocrystalline and Polyicosahedral Structure of a Nanospike Generated on Metal Surface Irradiated by a Single Femtosecond Laser Pulse. *J. Phys. Chem. C* **2016,** *120*, 4438-4447.

90. Karim, E. T.; Lin, Z.; Zhigilei, L. V., Molecular Dynamics Study of Femtosecond Laser Interactions with Cr Targets. *AIP Conf. Proc.* **2012,** *1464*, 280-293.

91. Leveugle, E.; Ivanov, D. S.; Zhigilei, L. V., Photomechanical Spallation of Molecular and Metal Targets: Molecular Dynamics Study. *Appl. Phys. A* **2004,** *79*, 1643-1655.

92. Schafer, C.; Urbassek, H. M.; Zhigilei, L. V.; Garrison, B. J., Pressure-Transmitting Boundary Conditions for Molecular-Dynamics Simulations. *Comput. Mater. Sci,* **2002,** *24*, 421-429.

93. Gill-Comeau, M.; Lewis, L. J., Ultrashort-Pulse Laser Ablation of Nanocrystalline Aluminum. *Phys. Rev. B* **2011,** *84*, 224110.

94. Li, X.; Jiang, L., Size Distribution Control of Metal Nanoparticles Using Femtosecond Laser Pulse Train: A Molecular Dynamics Simulation. *Appl. Phys. A* **2012,** *109*, 367-376.

95. Salomon-Ferrer, R.; Götz, A. W.; Poole, D.; Le Grand, S.; Walker, R. C., Routine Microsecond Molecular Dynamics Simulations with Amber on Gpus. 2. Explicit Solvent Particle Mesh Ewald. *J. Chem. Theory Comput.* **2013,** *9*, 3878-3888.

96. Anderson, J. A.; Lorenz, C. D.; Travesset, A., General Purpose Molecular Dynamics Simulations Fully Implemented on Graphics Processing Units. *J. Comp. Phys.* **2008,** *227*, 5342-5359.

97. Titan-Oak Ridge Leadership Computing Facility. https://www.olcf.ornl.gov/titan/.

98. Mira-Argonne Leadership Computing Facility. https://www.alcf.anl.gov/mira/.

99. Foiles, S. M.; Baskes, M. I.; Daw, M. S., Embedded-Atom-Method Functions for the Fcc Metals Cu, Ag, Au, Ni, Pd, Pt, and Their Alloys. *Phys. Rev. B* **1986,** *33*, 7983-7991.

100. Voter, A. F.; Chen, S. P., Accurate Interatomic Potentials for Ni, Al, and Ni_3Al. *Mat. Res. Soc. Symp. Proc.* **1986,** *82*, 175-180.

101. Karim, E. T.; Shugaev, M.; Wu, C. P.; Lin, Z. B.; Hainsey, R. F.; Zhigilei, L. V., Atomistic Simulation Study of Short Pulse Laser Interactions with a Metal Target under Conditions of Spatial Confinement by a Transparent Overlayer. *J. Appl. Phys.* **2014,** *115*, 183501.

102. Wu, C.; Christensen, M. S.; Savolainen, J. M.; Balling, P.; Zhigilei, L. V., Generation of Subsurface Voids and a Nanocrystalline Surface Layer in Femtosecond Laser Irradiation of a Single-Crystal Ag Target. *Phys. Rev. B* **2015,** *91*, 035413.

103. Wu, C.; Thomas, D. A.; Lin, Z. B.; Zhigilei, L. V., Runaway Lattice-Mismatched Interface in an Atomistic Simulation of Femtosecond Laser Irradiation of Ag Film-Cu Substrate System. *Appl. Phys. A* **2011,** *104*, 781-792.

104. Foiles, S. M.; Adams, J. B., Thermodynamic Properties of Fcc Transtition-Metals as Calculated with the Embedded-Atom Method. *Phys. Rev. B* **1989,** *40*, 5909-5915.

105. Haynes, W. M., Handbook of Chemistry and Physics. 97th ed.; CRC Press: Boca Raton, Florence, 2016.

106. Garrison, B. J.; Itina, T. E.; Zhigilei, L. V., Limit of Overheating and the Threshold Behavior in Laser Ablation. *Phys. Rev. E* **2003,** *68*, 041501.

107. Miotello, A.; Kelly, R., Laser-Induced Phase Explosion: New Physical Problems When a Condensed Phase Approaches the Thermodynamic Critical Temperature. *Appl. Phys. A* **1999,** *69*, S67-S73.

108. Bulgakova, N. M.; Bulgakov, A. V., Pulsed Laser Ablation of Solids: Transition from Normal Vaporization to Phase Explosion. *Appl. Phys. A* **2001,** *73*, 199-208.

109. Ohse, R. W.; Tippelskirch, H. v., The Critical Constants of the Elements and of Some Refractory Materials with High Critical Temperatures. *High Temp-High Press* **1977,** *9*, 367-385.

110. Kaganov, M. I.; Lifshitz, I. M.; Tanatarov, L. V., Relaxation between Electrons and the Crystalline Lattice. *Sov. Phys. JETP* **1957,** *4*, 173-178.

111. Anisimov, S. I.; Kapeliovich, B. L.; Perel'man, T. L., Electron Emission from Metal Surfaces Exposed to Ultrashort Laser Pulses. *Sov. Phys. JETP* **1974,** *39*, 375-377.

112. Thomas, D. A.; Lin, Z.; Zhigilei, L. V.; Gurevich, E. L.; Kittel, S.; Hergenröder, R., Atomistic Modeling of Femtosecond Laser-Induced Melting and Atomic Mixing in Au Film – Cu Substrate System. *Appl. Surf. Sci.* **2009,** *255*, 9605-9612.

113. Noël, S.; Hermann, J.; Itina, T., Investigation of Nanoparticle Generation During Femtosecond Laser Ablation of Metals. *Appl. Surf. Sci.* **2007,** *253*, 6310-6315.

114. Itina, T. E.; Gouriet, K.; Zhigilei, L. V.; Noël, S.; Hermann, J.; Sentis, M., Mechanisms of Small Clusters Production by Short and Ultra-Short Laser Ablation. *Appl. Surf. Sci.* **2007,** *253*, 7656-7661.

115. Zhigilei, L. V.; Garrison, B. J., Pressure Waves in Microscopic Simulations of Laser Ablation. *Mat. Res. Soc. Symp. Proc.* **1999,** *538*, 491-496.

116. Zhigilei, L. V.; Ivanov, D. S., Channels of Energy Redistribution in Short-Pulse Laser Interactions with Metal Targets. *Appl. Surf. Sci.* **2005,** *248*, 433-439.

117. Rouleau, C. M.; Shih, C.-Y.; Wu, C. P.; Zhigilei, L. V.; Puretzky, A. A.; Geohegan, D. B., Nanoparticle Generation and Transport Resulting from Femtosecond Laser Ablation of Ultrathin Metal Films: Time-Resolved Measurements and Molecular Dynamics Simulations. *Appl. Phys. Lett.* **2014,** *104*, 193106.

118. Lin, Z.; Zhigilei, L. V.; Celli, V., Electron-Phonon Coupling and Electron Heat Capacity of Metals under Conditions of Strong Electron-Phonon Nonequilibrium. *Phys. Rev. B* **2008,** *77*, 075133.

119. Lin, Z.; Zhigilei, L. V., Temperature Dependences of the Electron–Phonon Coupling, Electron Heat Capacity and Thermal Conductivity in Ni under Femtosecond Laser Irradiation. *Appl. Surf. Sci.* **2007,** *253*, 6295-6300.

120. Lin, Z.; Leveugle, E.; Bringa, E. M.; Zhigilei, L. V., Molecular Dynamics Simulation of Laser Melting of Nanocrystalline Au. *J. Phys. Chem. C* **2010,** *114*, 5686-5699.

121. Lin, Z.; Zhigilei, L. V. In *Thermal Excitation of D Band Electrons in Au: Implications for Laser-Induced Phase Transformations*, High-Power Laser Ablation VI, Phipps, C. R., Ed. Proc. SPIE: 2006; pp 62610U-14.

122. Groeneveld, R. H. M.; Sprik, R.; Lagendijk, A., Femtosecond Spectroscopy of Electron-Electron and Electron-Phonon Energy Relaxation in Ag and Au. *Phys. Rev. B* **1995,** *51*, 11433-11445.

123. Mills, K. C.; Monaghan, B. J.; Keene, B. J., Thermal Conductivities of Molten Metals: Part 1 Pure Metals. *Int. Mater. Rev.* **1996,** *41*, 209-242.

124. Zhigilei, L. V.; Kodali, P. B. S.; Garrison, B. J., Molecular Dynamics Model for Laser Ablation and Desorption of Organic Solids. *J. Phys. Chem. B* **1997,** *101*, 2028-2037.

125. Phares, D. J.; Srinivasa, A. R., Molecular Dynamics with Molecular Temperature. *J. Phys. Chem. A* **2004,** *108*, 6100-6108.

126. Jacobs, W. M.; Nicholson, D. A.; Zemer, H.; Volkov, A. N.; Zhigilei, L. V., Acoustic Energy Dissipation and Thermalization in Carbon Nanotubes: Atomistic Modeling and Mesoscopic Description. *Phys. Rev. B* **2012,** *86*, 165414.

127. Tabetah, M.; Matei, A.; Constantinescu, C.; Mortensen, N. P.; Dinescu, M.; Schou, J.; Zhigilei, L. V., The Minimum Amount of "Matrix" Needed for Matrix-Assisted Pulsed Laser Deposition of Biomolecules. *J. Phys. Chem. B* **2014,** *118*, 13290-13299.

128. Okumura, H.; Yonezawa, F., Reliable Determination of the Liquid-Vapor Critical Point by the Nvt Plus Test Particle Method. *J. Phys. Soc. Jpn* **2001,** *70*, 1990-1994.

129. Michaelides, A.; Ranea, V. A.; de Andres, P. L.; King, D. A., General Model for Water Monomer Adsorption on Close-Packed Transition and Noble Metal Surfaces. *Phys. Rev. Lett.* **2003,** *90*, 216102.

130. Ren, J.; Meng, S., First-Principles Study of Water on Copper and Noble Metal (110) Surfaces. *Phys. Rev. B* **2008,** *77*, 054110.

131. Hughes, Z. E.; Wright, L. B.; Walsh, T. R., Biomolecular Adsorption at Aqueous Silver Interfaces: First-Principles Calculations, Polarizable Force-Field Simulations, and Comparisons with Gold. *Langmuir* **2013,** *29*, 13217-13229.

132. Michaelides, A.; Alavi, A.; King, D. A., Insight into H2o-Ice Adsorption and Dissociation on Metal Surfaces from First-Principles Simulations. *Phys. Rev. B* **2004,** *69*, 113404.

133. Yingling, Y. G.; Zhigilei, L. V.; Garrison, B. J., The Role of the Photochemical Fragmentation in Laser Ablation: A Molecular Dynamics Study. *J. Photochem. Photobiol. A* **2001,** *145*, 173-181.

134. Yingling, Y. G.; Zhigilei, L. V.; Garrison, B. J., Photochemical Fragmentation Processes in Laser Ablation of Organic Solids. *Nucl. Instrum Meth. B* **2001,** *180*, 171-175.

135. Amoruso, S.; Nedyalkov, N. N.; Wang, X.; Ausanio, G.; Bruzzese, R.; Atanasov, P. A., Ultrafast Laser Ablation of Gold Thin Film Targets. *J. Appl. Phys.* **2011,** *110*, 124303.

136. Oguri, K.; Okano, Y.; Nishikawa, T.; Nakano, H., Dynamics of Femtosecond Laser Ablation Studied with Time-Resolved X-Ray Absorption Fine Structure Imaging. *Phys. Rev. B* **2009,** *79*, 144106.

137. Noël, S.; Hermann, J., Reducing Nanoparticles in Metal Ablation Plumes Produced by Two Delayed Short Laser Pulses. *Appl. Phys. Lett.* **2009,** *94*, 053120.

138. Murphy, R. D.; Torralva, B.; Yalisove, S. M., The Role of an Interface on Ni Film Removal and Surface Roughness after Irradiation by Femtosecond Laser Pulses. *Appl. Phys. Lett.* **2013,** *102*, 181602.

139. Haustrup, N.; O'Connor, G. M., Impact of Wavelength Dependent Thermo-Elastic Laser Ablation Mechanism on the Generation of Nanoparticles from Thin Gold Films. *Appl. Phys. Lett.* **2012,** *101*, 263107.

140. Amoruso, S.; Bruzzese, R.; Wang, X.; Nedialkov, N. N.; Atanasov, P. A., Femtosecond Laser Ablation of Nickel in Vacuum. *J. Phys. D* **2007,** *40*, 331.

141. Amoruso, S.; Nedyalkov, N. N.; Wang, X.; Ausanio, G.; Bruzzese, R.; Atanasov, P. A., Ultrashort-Pulse Laser Ablation of Gold Thin Film Targets: Theory and Experiment. *Thin Solid Films* **2014,** *550*, 190-198.

142. Rouleau, C. M.; Puretzky, A. A.; Geohegan, D. B., Slowing of Femtosecond Laser-Generated Nanoparticles in a Background Gas. *Appl. Phys. Lett.* **2014,** *105*, 213108.

143. Murray, P. T.; Shin, E., Formation of Silver Nanoparticles by through Thin Film Ablation. *Mater. Lett.* **2008,** *62*, 4336-4338.

144. Bäuerle, D., *Laser Processing and Chemistry*. Springer-Verlag Berlin Heidelberg: Berlin, Germany, 2000.

145. Shugaev, M. V.; Bulgakova, N. M., Thermodynamic and Stress Analysis of Laser-Induced Forward Transfer of Metals. *Appl. Phys. A* **2010,** *101*, 103-109.

146. Schrider, K. J.; Torralva, B.; Yalisove, S. M., The Dynamics of Femtosecond Pulsed Laser Removal of 20 Nm Ni Films from an Interface. *Appl. Phys. Lett.* **2015,** *107*, 124101.

147. Miotello, A.; Kelly, R., Critical Assessment of Thermal Models for Laser Sputtering at High Fluences. *Appl. Phys. Lett.* **1995,** *67*, 3535-3537.

148. Bubb, D. M.; O'Malley, S. M.; Schoeffling, J.; Jimenez, R.; Zinderman, B.; Yi, S., Size Control of Gold Nanoparticles Produced by Laser Ablation of Thin Films in an Aqueous Environment. *Chem. Phys. Lett.* **2013,** *565*, 65-68.

149. Scaramuzza, S.; Zerbetto, M.; Amendola, V., Synthesis of Gold Nanoparticles in Liquid Environment by Laser Ablation with Geometrically Confined Configurations: Insights to Improve Size Control and Productivity. *J. Phys. Chem. C* **2016,** *120*, 9453-9463.

150. Schäfer, C.; Urbassek, H. M.; Zhigilei, L. V.; Garrison, B. J., Pressure-Transmitting Boundary Conditions for Molecular-Dynamics Simulations. *Comput. Mater. Sci,* **2002,** *24*, 421-429.

151. Wellershoff, S. S.; Hohlfeld, J.; Gudde, J.; Matthias, E., The Role of Electron-Phonon Coupling in Femtosecond Laser Damage of Metals. *Appl. Phys. A* **1999,** *69,* S99-S107.

152. Amendola, V.; Meneghetti, M., Laser Ablation Synthesis in Solution and Size Manipulation of Noble Metal Nanoparticles. *Phys. Chem. Chem. Phys.* **2009,** *11*, 3805-3821.

153. Santillán, J. M. J.; Fernández van Raap, M. B.; Mendoza Zélis, P.; Coral, D.; Muraca, D.; Schinca, D. C.; Scaffardi, L. B., Ag Nanoparticles Formed by Femtosecond Pulse Laser Ablation in Water: Self-Assembled Fractal Structures. *J. Nanopart. Res.* **2015,** *17,* 86.

154. Kull, H. J., Theory of the Rayleigh-Taylor Instability. *Phys. Rep.* **1991,** *206*, 197-325.

155. Barber, J. L.; Kadau, K.; Germann, T. C.; Alder, B. J., Initial Growth of the Rayleigh-Taylor Instability Via Molecular Dynamics. *Eur. Phys. J. B* **2008,** *64*, 271-276.

156. Kadau, K.; Germann, T. C.; Hadjiconstantinou, N. G.; Lomdahl, P. S.; Dimonte, G.; Holian, B. L.; Alder, B. J., Nanohydrodynamics Simulations: An Atomistic View of the Rayleigh-Taylor Instability. *Proc. Natl. Acad. Sci. U.S.A.* **2004,** *101*, 5851-5855.

157. Zhigilei, L. V.; Garrison, B. J., Microscopic Mechanisms of Laser Ablation of Organic Solids in the Thermal and Stress Confinement Irradiation Regimes. *J. Appl. Phys.* **2000,** *88*, 1281-1298.

158. Kunze, H. J., Introduction to Plasma Spectroscopy. *Introduction to Plasma Spectroscopy* **2009,** *56*, 1-242.

159. Griem, H. R., High-Density Corrections in Plasma Spectroscopy. *Phys. Rev.* **1962,** *128*, 997-1003.

160. Taccogna, F., Nucleation and Growth of Nanoparticles in a Plasma by Laser Ablation in Liquid. *J. Plasma.Phys.* **2015,** *81*.

161. Paltauf, G.; Dyer, P. E., Photomechanical Processes and Effects in Ablation. *Chem. Rev.* **2003,** *103*, 487-518.

162. Sedao, X.; Shugaev, M. V.; Wu, C.; Douillard, T.; Esnouf, C.; Maurice, C.; Reynaud, S.; Pigeon, F.; Garrelie, F.; Zhigilei, L. V.; Colombier, J.-P., Growth Twinning and Generation of

High-Frequency Surface Nanostructures in Ultrafast Laser-Induced Transient Melting and Resolidification. *ACS Nano* **2016,** *10*, 6995-7007.

163. Savolainen, J. M.; Christensen, M. S.; Balling, P., Material Swelling as the First Step in the Ablation of Metals by Ultrashort Laser Pulses. *Phys. Rev. B* **2011,** *84*.

164. Ionin, A. A.; Kudryashov, S. I.; Ligachev, A. E.; Makarov, S. V.; Seleznev, L. V.; Sinitsyn, D. V., Nanoscale Cavitation Instability of the Surface Melt Along the Grooves of One-Dimensional Nanorelief Gratings on an Aluminum Surface. *Jetp Lett+* **2011,** *94*, 266-269.

165. Starikov, S. V.; Pisarev, V. V., Atomistic Simulation of Laser-Pulse Surface Modification: Predictions of Models with Various Length and Time Scales. *J. Appl. Phys.* **2015,** *117*.

166. Zhigilei, L. V., Dynamics of the Plume Formation and Parameters of the Ejected Clusters in Short-Pulse Laser Ablation. *Appl. Phys. A* **2003,** *76*, 339-350.

167. Zavedeev, E. V.; Petrovskaya, A. V.; Simakin, A. V.; Shafeev, G. A., Formation of Nanostructures Upon Laser Ablation of Silver in Liquids. *Quant. Electron.* **2006,** *36*, 978-980.

168. Truong, S. L.; Levi, G.; Bozon-Verduraz, F.; Petrovskaya, A. V.; Simakin, A. V.; Shafeev, G. A., Generation of Ag Nanospikes Via Laser Ablation in Liquid Environment and Their Activity in Sers of Organic Molecules. *Appl. Phys. A* **2007,** *89*, 373-376.

169. Stratakis, E.; Zorba, V.; Barberoglou, M.; Fotakis, C.; Shafeev, G. A., Laser Writing of Nanostructures on Bulk Al Via Its Ablation in Liquids. *Nanotechnology* **2009,** *20*.

170. Barmina, E. V.; Stratakis, E.; Fotakis, K.; Shafeev, G., Generation of Nanostructures on Metals by Laser Ablation in Liquids: New Results. *Quant. Electron.* **2010,** *40*, 1012-1020.

171. Podagatlapalli, G. K.; Hamad, S.; Sreedhar, S.; Tewari, S. P.; Rao, S. V., Fabrication and Characterization of Aluminum Nanostructures and Nanoparticles Obtained Using Femtosecond Ablation Technique. *Chem. Phys. Lett.* **2012,** *530*, 93-97.

172. Bashir, S.; Rafique, M. S.; Nathala, C. S.; Husinsky, W., Surface and Structural Modifications of Titanium Induced by Various Pulse Energies of a Femtosecond Laser in Liquid and Dry Environment. *Appl. Phys. A* **2014,** *114*, 243-251.

173. Bashir, S.; Rafique, M. S.; Nathala, C. S.; Husinsky, W., The Formation of Nanodimensional Structures on the Surface of Tin Exposed to Femtosecond Laser Pulses in the Ambient Environment of Ethanol. *Appl. Surf. Sci.* **2014,** *290*, 53-58.

174. Barmina, E. V.; Shafeev, G. A.; Kuzmin, P. G.; Serkov, A. A.; Simakin, A. V.; Melnik, N. N., Laser-Assisted Generation of Gold Nanoparticles and Nanostructures in Liquid and Their Plasmonic Luminescence. *Appl. Phys. A* **2014,** *115*, 747-752.

175. Razi, S.; Madanipour, K.; Mollabashi, M., Laser Surface Texturing of 316l Stainless Steel in Air and Water: A Method for Increasing Hydrophilicity Via Direct Creation of Microstructures. *Opt Laser Technol* **2016,** *80*, 237-246.

176. Zhang, D. S.; Gökce, B.; Sommer, S.; Streubel, R.; Barcikowski, S., Debris-Free Rear-Side Picosecond Laser Ablation of Thin Germanium Wafers in Water with Ethanol. *Appl. Surf. Sci.* **2016,** *367*, 222-230.

177. Starinskiy, S. V.; Shukhov, Y. G.; Bulgakov, A. V., Laser-Induced Damage Thresholds of Gold, Silver and Their Alloys in Air and Water. *Appl. Surf. Sci.* **2017,** *396*, 1765-1774.

178. *Factsage*, 2017.

179. Shih, C.-Y.; Wu, C. P.; Shugaev, M. V.; Zhigilei, L. V., Atomistic Modeling of Nanoparticle Generation in Short Pulse Laser Ablation of Thin Metal Films in Water. *J. Colloid Interface Sci.* **2017,** *489*, 3-17.

180. Chandrasekhar, S., *Hydrodynamic and Hydromagnetic Stability*. Clarendon Press: Oxford, 1961, p 652.

181. Gloor, G. J.; Jackson, G.; Blas, F. J.; de Miguel, E., Test-Area Simulation Method for the Direct Determination of the Interfacial Tension of Systems with Continuous or Discontinuous Potentials. *J. Chem. Phys.* **2005,** *123*.

182. Barcikowski, S.; Devesa, F.; Moldenhauer, K., Impact and Structure of Literature on Nanoparticle Generation by Laser Ablation in Liquids. *J. Nanopart. Res.* **2009,** *11*, 1883-1893.

183. Sylvestre, J.-P.; Kabashin, A. V.; Sacher, E.; Meunier, M., Femtosecond Laser Ablation of Gold in Water: Influence of the Laser-Produced Plasma on the Nanoparticle Size Distribution. *Appl. Phys. A* **2005,** *80*, 753-758.

184. Marzun, G.; Nakamura, J.; Zhang, X.; Barcikowski, S.; Wagener, P., Size Control and Supporting of Palladium Nanoparticles Made by Laser Ablation in Saline Solution as a Facile Route to Heterogeneous Catalysts. *Appl. Surf. Sci.* **2015,** *348*, 75-84.

185. Gamrad, L.; Rehbock, C.; Krawinkel, J.; Tumursukh, B.; Heisterkamp, A.; Barcikowski, S., Charge Balancing of Model Gold-Nanoparticle-Peptide Conjugates Controlled by the Peptide's Net Charge and the Ligand to Nanoparticle Ratio. *J. Phys. Chem. C* **2014,** *118*, 10302-10313.

186. Soliman, W.; Takada, N.; Sasaki, K., Growth Processes of Nanoparticles in Liquid-Phase Laser Ablation Studied by Laser-Light Scattering. *Appl. Phys. Express* **2010,** *3*, 035201.

187. Tsuji, T.; Tsuboi, Y.; Kitamura, N.; Tsuji, M., Microsecond-Resolved Imaging of Laser Ablation at Solid–Liquid Interface: Investigation of Formation Process of Nano-Size Metal Colloids. *Appl. Surf. Sci.* **2004,** *229*, 365-371.

188. Shugaev, M. V.; Wu, C. P.; Armbruster, O.; Naghilou, A.; Brouwer, N.; Ivanov, D. S.; Derrien, T. J. Y.; Bulgakova, N. M.; Kautek, W.; Rethfeld, B.; Zhigilei, L. V., Fundamentals of Ultrafast Laser-Material Interaction. *MRS Bull.* **2016,** *41*, 960-968.

189. Zou, J.; Wu, C. P.; Robertson, W. D.; Zhigilei, L. V.; Miller, R. J. D., Molecular Dynamics Investigation of Desorption and Ion Separation Following Picosecond Infrared Laser (Pirl) Ablation of an Ionic Aqueous Protein Solution. *J. Chem. Phys.* **2016,** *145,* 204202.

190. Shih, C.-Y.; Shugaev, M. V.; Wu, C.; Zhigilei, L. V., Generation of Subsurface Voids, Incubation Effect, and Formation of Nanoparticles in Short Pulse Laser Interactions with Bulk Metal Targets in Liquid: Molecular Dynamics Study. *J. Phys. Chem. C* **2017**, 10.1021/acs.jpcc.7b02301.

191. Liu, J. M., Simple Technique for Measurements of Pulsed Gaussian-Beam Spot Sizes. *Opt. Lett.* **1982,** *7,* 196-198.

192. Yu, V. P.; Inogamov, N. A.; Anisimov, S. I.; Migdal, K. P.; Khokhlov, V. A.; Khishchenko, K. V., Thermal Conductivity of Condensed Gold in States with the Strongly Excited Electron Subsystem. *J. Phys. Conf. Ser* **2015,** *653,* 012087.

193. Ren, Y.; Chen, J. K.; Zhang, Y.; Huang, J., Ultrashort Laser Pulse Energy Deposition in Metal Films with Phase Changes. *Appl. Phys. Lett.* **2011,** *98,* 191105.

194. Marzun, G.; Levish, A.; Mackert, V.; Kallio, T.; Barcikowski, S.; Wagener, P., Laser Synthesis, Structure and Chemical Properties of Colloidal Nickel-Molybdenum Nanoparticles for the Substitution of Noble Metals in Heterogeneous Catalysis. *J. Colloid Interface Sci.* **2017,** *489,* 57-67.

195. Brouillette, M., The Richtmyer-Meshkov Instability. *Annu. Rev. Fluid Mech.* **2002,** *34,* 445-468.

196. Buttler, W. T.; Oro, D. M.; Preston, D. L.; Mikaelian, K. O.; Cherne, F. J.; Hixson, R. S.; Mariam, F. G.; Morris, C.; Stone, J. B.; Terrones, G.; Tupa, D., Unstable Richtmyer-Meshkov Growth of Solid and Liquid Metals in Vacuum. *J. Fluid Mech.* **2012,** *703,* 60-84.

197. Zhang, D.; Liu, J.; Li, P.; Tian, z.; Liang, C., Recent Advances in Surfactant-Free, Surface Charged and Defect-Rich Catalysts Developed by Laser Ablation and Processing in Liquids. *ChemNanoMat* **2017**, 10.1002/cnma.201700079.

198. Tomko, J.; Naddeo, J. J.; Jimenez, R.; Tan, Y.; Steiner, M.; Fitz-Gerald, J. M.; Bubb, D. M.; O'Malley, S. M., Size and Polydispersity Trends Found in Gold Nanoparticles Synthesized by Laser Ablation in Liquids. *Phys. Chem. Chem. Phys.* **2015,** *17*, 16327-16333.

199. Strasser, M.; Setoura, K.; Langbein, U.; Hashimoto, S., Computational Modeling of Pulsed Laser-Induced Heating and Evaporation of Gold Nanoparticles. *J. Phys. Chem. C* **2014,** *118*, 25748-25755.

200. Lukianova-Hleb, E. Y.; Kim, Y.-S.; Belatsarkouski, I.; Gillenwater, A. M.; O'Neill, B. E.; Lapotko, D. O., Intraoperative Diagnostics and Elimination of Residual Microtumours with Plasmonic Nanobubbles. *Nat. Nanotechnol.* **2016,** *11*, 525-532.

201. Kirkwood, S. E.; van Popta, A. C.; Tsui, Y. Y.; Fedosejevs, R., Single and Multiple Shot near-Infrared Femtosecond Laser Pulse Ablation Thresholds of Copper. *Appl. Phys. A* **2005,** *81*, 729-735.

202. Krüger, J.; Dufft, D.; Koter, R.; Hertwig, A., Femtosecond Laser-Induced Damage of Gold Films. *Appl. Surf. Sci.* **2007,** *253*, 7815-7819.

203. Raciukaitis, G.; Brikas, M.; Gecys, P.; Gedvilas, M.; Phipps, C. R., Accumulation Effects in Laser Ablation of Metals with High-Repetition-Rate Lasers. *HPLA* **2008,** *7005*.

204. Armbruster, O.; Naghilou, A.; Kitzler, M.; Kautek, W., Spot Size and Pulse Number Dependence of Femtosecond Laser Ablation Thresholds of Silicon and Stainless Steel. *Appl. Surf. Sci.* **2017,** *396*, 1736-1740.

205. Mikaelian, K. O., Richtmyer-Meshkov Instability of Arbitrary Shapes. *Phys. Fluids* **2005,** *17*, 034101.

206. Durand, O.; Soulard, L., Power Law and Exponential Ejecta Size Distributions from the Dynamic Fragmentation of Shock-Loaded Cu and Sn Metals under Melt Conditions. *J. Appl. Phys.* **2013,** *114*, 194902.

207. Dimonte, G.; Terrones, G.; Cherne, F. J.; Ramaprabhu, P., Ejecta Source Model Based on the Nonlinear Richtmyer-Meshkov Instability. *J. Appl. Phys.* **2013,** *113*.

208. Dyachkov, S.; Parshikov, A.; Zhakhovsky, V., Ejecta from Shocked Metals: Comparative Simulations Using Molecular Dynamics and Smoothed Particle Hydrodynamics. *AIP Conf. Proc.* **2017,** *1793*, 100024.

209. Eggers, J.; Villermaux, E., Physics of Liquid Jets. *Rep. Prog. Phys.* **2008,** *71*.

210. Moseler, M.; Landman, U., Formation, Stability, and Breakup of Nanojets. *Science* **2000,** *289*, 1165-1169.

211. Merabia, S.; Keblinski, P.; Joly, L.; Lewis, L. J.; Barrat, J. L., Critical Heat Flux around Strongly Heated Nanoparticles. *Phys. Rev. E* **2009,** *79*, 021404.

212. Merabia, S.; Shenogin, S.; Joly, L.; Keblinski, P.; Barrat, J. L., Heat Transfer from Nanoparticles: A Corresponding State Analysis. *Proc. Natl. Acad. Sci. U.S.A.* **2009,** *106*, 15113-15118.

213. Hu, M.; Poulikakos, D.; Grigoropoulos, C. P.; Pan, H., Recrystallization of Picosecond Laser-Melted Zno Nanoparticles in a Liquid: A Molecular Dynamics Study. *J. Chem. Phys.* **2010,** *132*, 164504.

214. Deng, C.; Sansoz, F., Fundamental Differences in the Plasticity of Periodically Twinned Nanowires in Au, Ag, Al, Cu, Pb and Ni. *Acta Mater.* **2009,** *57*, 6090-6101.

215. Garrison, B. J.; Itina, T. E.; Zhigilei, L. V., Limit of Overheating and the Threshold Behavior in Laser Ablation. *Phys. Rev. E* **2003,** *68*.

216. Daria, R.; Mohamed, C.; Joëlle, M., Dependence of Gold Nanoparticle Production on Pulse Duration by Laser Ablation in Liquid Media. *Nanotechnology* **2012,** *23*, 135603.

217. Barcikowski, S.; Menendez-Manjon, A.; Chichkov, B.; Brikas, M.; Raciukaitis, G., Generation of Nanoparticle Colloids by Picosecond and Femtosecond Laser Ablations in Liquid Flow. *Appl. Phys. Lett.* **2007,** *91*, 083113.

218. Gamaly, E. G.; Rode, A. V.; Luther-Davies, B.; Tikhonchuk, V. T., Ablation of Solids by Femtosecond Lasers: Ablation Mechanism and Ablation Thresholds for Metals and Dielectrics. *Phys. Plasmas* **2002,** *9*, 949-957.

219. Baldacchini, T.; Carey, J. E.; Zhou, M.; Mazur, E., Superhydrophobic Surfaces Prepared by Microstructuring of Silicon Using a Femtosecond Laser. *Langmuir* **2006,** *22*, 4917-4919.

220. Eichstädt, J.; Römer, G. R. B. E.; Veld, A. J. H. i. t., Towards Friction Control Using Laser-Induced Periodic Surface Structures. *Phys. Procedia* **2011,** *12*, 7-15.

221. Vorobyev, A. Y.; Guo, C., Colorizing Metals with Femtosecond Laser Pulses. *Appl. Phys. Lett.* **2008,** *92*, 041914.

222. Li, X.-M.; Reinhoudt, D.; Crego-Calama, M., What Do We Need for a Superhydrophobic Surface? A Review on the Recent Progress in the Preparation of Superhydrophobic Surfaces. *Chem. Soc. Rev.* **2007,** *36*, 1350-1368.

223. Subhash Latthe, S.; Basavraj Gurav, A.; Shridhar Maruti, C.; Shrikant Vhatkar, R., Recent Progress in Preparation of Superhydrophobic Surfaces: A Review. *J Surf Eng Mater Adv Technol* **2012,** *2*, 76-94.

224. Shugaev, M. V.; Gnilitskyi, I.; Bulgakova, N. M.; Zhigilei, L. V., Mechanism of the Single-Pulse Ablative Generation of Laser Induced Periodic Surface Structures **2017**, Final stage of preparation

225. Shugaev, M. V.; Shih, C.-Y.; Karim, E. T.; Wu, C.; Zhigilei, L. V., Generation of Nanocrystalline Surface Layer in Short Pulse Laser Processing of Metal Targets under Conditions of Spatial Confinement by Solid or Liquid Overlayer. *Appl. Surf. Sci.* **2017,** *417*, 54-63.

226. Drelich, J.; Chibowski, E.; Meng, D. D.; Terpilowski, K., Hydrophilic and Superhydrophilic Surfaces and Materials. *Soft Matter* **2011,** *7*, 9804-9828.

227. Israelachvili., J., *Intermolecular and Surface Forces*. Academic Press: London, 1992, p 450.

228. Kittel, C., *Introduction to Solid State Physics*. 7th ed.; Wiley: New York, 1996.

229. Brorson, S. D.; Kazeroonian, A.; Moodera, J. S.; Face, D. W.; Cheng, T. K.; Ippen, E. P.; Dresselhaus, M. S.; Dresselhaus, G., Femtosecond Room-Temperature Measurement of the Electron-Phonon Coupling Constant \Ensuremath{\Gamma} in Metallic Superconductors. *Phys. Rev. Lett.* **1990,** *64*, 2172-2175.

230. Palik, E. D., *Handbook of Optical Constants of Solids*. Academic Press: 1998.

231. Wang, D.; Li, Y., Bimetallic Nanocrystals: Liquid-Phase Synthesis and Catalytic Applications. *Adv. Mater.* **2011,** *23*, 1044-1060.

232. Lee, Y.-W.; Ko, A. R.; Han, S.-B.; Kim, H.-S.; Park, K.-W., Synthesis of Octahedral Pt-Pd Alloy Nanoparticles for Improved Catalytic Activity and Stability in Methanol Electrooxidation. *Phys. Chem. Chem. Phys.* **2011,** *13*, 5569-5572.

233. Amendola, V.; Scaramuzza, S.; Litti, L.; Meneghetti, M.; Zuccolotto, G.; Rosato, A.; Nicolato, E.; Marzola, P.; Fracasso, G.; Anselmi, C.; Pinto, M.; Colombatti, M., Magneto-Plasmonic Au-Fe Alloy Nanoparticles Designed for Multimodal Sers-Mri-Ct Imaging. *Small* **2014,** *10*, 2476-2486.

234. Amendola, V.; Scaramuzza, S.; Agnoli, S.; Granozzi, G.; Meneghetti, M.; Campo, G.; Bonanni, V.; Pineider, F.; Sangregorio, C.; Ghigna, P.; Polizzi, S.; Riello, P.; Fiameni, S.; Nodari, L., Laser Generation of Iron-Doped Silver Nanotruffles with Magnetic and Plasmonic Properties. *Nano Res.* **2015,** *8*, 4007-4023.

235. Messina, G. C.; Sinatra, M. G.; Bonanni, V.; Brescia, R.; Alabastri, A.; Pineider, F.; Campo, G.; Sangregorio, C.; Li-Destri, G.; Sfuncia, G.; Marletta, G.; Condorelli, M.; Proietti Zaccaria, R.; De Angelis, F.; Compagnini, G., Tuning the Composition of Alloy Nanoparticles through Laser Mixing: The Role of Surface Plasmon Resonance. *J. Phys. Chem. C* **2016,** *120*, 12810-12818.

236. Wagener, P.; Jakobi, J.; Rehbock, C.; Chakravadhanula, V. S. K.; Thede, C.; Wiedwald, U.; Bartsch, M.; Kienle, L.; Barcikowski, S., Solvent-Surface Interactions Control the Phase Structure in Laser-Generated Iron-Gold Core-Shell Nanoparticles. *Sci. Rep.* **2016,** *6*, 23352.

237. Ferrando, R.; Jellinek, J.; Johnston, R. L., Nanoalloys: From Theory to Applications of Alloy Clusters and Nanoparticles. *Chem. Rev.* **2008,** *108*, 845-910.

238. Amendola, V.; Scaramuzza, S.; Agnoli, S.; Polizzi, S.; Meneghetti, M., Strong Dependence of Surface Plasmon Resonance and Surface Enhanced Raman Scattering on the Composition of Au-Fe Nanoalloys. *Nanoscale* **2014,** *6*, 1423-1433.

239. Amendola, V.; Meneghetti, M.; Bakr, O. M.; Riello, P.; Polizzi, S.; Anjum, D. H.; Fiameni, S.; Arosio, P.; Orlando, T.; de Julian Fernandez, C.; Pineider, F.; Sangregorio, C.; Lascialfari, A., Coexistence of Plasmonic and Magnetic Properties in Au89fe11 Nanoalloys. *Nanoscale* **2013,** *5*, 5611-5619.

240. Scaramuzza, S.; Agnoli, S.; Amendola, V., Metastable Alloy Nanoparticles, Metal-Oxide Nanocrescents and Nanoshells Generated by Laser Ablation in Liquid Solution: Influence of the Chemical Environment on Structure and Composition. *Phys. Chem. Chem. Phys.* **2015,** *17*, 28076-28087.

241. Swiatkowska-Warkocka, Z.; Pyatenko, A.; Krok, F.; Jany, B. R.; Marszalek, M., Synthesis of New Metastable Nanoalloys of Immiscible Metals with a Pulse Laser Technique. *Sci. Rep.* **2015,** *5*, 9849.

242. Swiatkowska-Warkocka, Z.; Koga, K.; Kawaguchi, K.; Wang, H.; Pyatenko, A.; Koshizaki, N., Pulsed Laser Irradiation of Colloidal Nanoparticles: A New Synthesis Route for the Production of Non-Equilibrium Bimetallic Alloy Submicrometer Spheres. *RSC Adv.* **2013,** *3*, 79-83.

243. Besner, S.; Meunier, M., Femtosecond Laser Synthesis of Auag Nanoalloys: Photoinduced Oxidation and Ions Release. *J. Phys. Chem. C* **2010,** *114*, 10403-10409.

244. Malviya, K. D.; Chattopadhyay, K., Synthesis and Mechanism of Composition and Size Dependent Morphology Selection in Nanoparticles of Ag–Cu Alloys Processed by Laser Ablation under Liquid Medium. *J. Phys. Chem. C* **2014,** *118*, 13228-13237.

245. Amendola, V.; Scaramuzza, S.; Carraro, F.; Cattaruzza, E., Formation of Alloy Nanoparticles by Laser Ablation of Au/Fe Multilayer Films in Liquid Environment. *J. Colloid Interface Sci.* **2017,** *489*, 18-27.

246. Kriegel, I.; Scotognella, F.; Manna, L., Plasmonic Doped Semiconductor Nanocrystals: Properties, Fabrication, Applications and Perspectives. *Phys. Rep.* **2017,** *674*, 1-52.

247. Erwin, S. C.; Zu, L.; Haftel, M. I.; Efros, A. L.; Kennedy, T. A.; Norris, D. J., Doping Semiconductor Nanocrystals. *Nature* **2005,** *436*, 91-94.

248. Buonsanti, R.; Milliron, D. J., Chemistry of Doped Colloidal Nanocrystals. *Chem. Mater.* **2013,** *25*, 1305-1317.

249. Dongare, A. M.; Neurock, M.; Zhigilei, L. V., Angular-Dependent Embedded Atom Method Potential for Atomistic Simulations of Metal-Covalent Systems. *Phys. Rev. B* **2009,** *80*, 184106.

250. Wang, L.; Clancy, P.; Thompson, M. O.; Murthy, C. S., Thermodynamic and Kinetic Studies of Laser Thermal Processing of Heavily Boron-Doped Amorphous Silicon Using Molecular Dynamics. *J. Appl. Phys.* **2002,** *92*, 2412-2419.

251. Liu, B.; Zhang, H.; Tao, J.; Liu, Z.; Chen, X.; Zhang, Y. a., Development of a Second-Nearest-Neighbor Modified Embedded Atom Method Potential for Silicon–Phosphorus Binary System. *Comput. Mater. Sci*, **2016,** *120,* 1-12.

252. Sellinger, A. T.; Aburada, T.; Fitz-Gerald, J. M. In *Synthesis of Multimetallic Nanoparticles Using a Solution-Based Pulsed Laser Deposition Approach*, 2008; pp 700516-700516-14.

253. Oseguera-Galindo, D. O.; Martínez-Benítez, A.; Chávez-Chávez, A.; Gómez-Rosas, G.; Pérez-Centeno, A.; Santana-Aranda, M. A., Effects of the Confining Solvent on the Size Distribution of Silver Nps by Laser Ablation. *J. Nanopart. Res.* **2012,** *14*, 1133.

254. Compagnini, G.; Scalisi, A. A.; Puglisi, O., Production of Gold Nanoparticles by Laser Ablation in Liquid Alkanes. *J. Appl. Phys.* **2003,** *94*, 7874-7877.

255. Franks, F.; Ives, D. J. G., The Structural Properties of Alcohol-Water Mixtures. *Q. Rev. Chem. Soc.* **1966,** *20*, 1-44.

256. Williams, P. L.; Mishin, Y.; Hamilton, J. C., An Embedded-Atom Potential for the Cu–Ag System. *Model. Simul. Mater. Sci. Eng.* **2006,** *14*, 817.

257. Umezu, I.; Warrender, J. M.; Charnvanichborikarn, S.; Kohno, A.; Williams, J. S.; Tabbal, M.; Papazoglou, D. G.; Zhang, X.-C.; Aziz, M. J., Emergence of Very Broad Infrared Absorption Band by Hyperdoping of Silicon with Chalcogens. *J. Appl. Phys.* **2013,** *113*, 213501.

258. Said, A. J.; Recht, D.; Sullivan, J. T.; Warrender, J. M.; Buonassisi, T.; Persans, P. D.; Aziz, M. J., Extended Infrared Photoresponse and Gain in Chalcogen-Supersaturated Silicon Photodiodes. *Appl. Phys. Lett.* **2011,** *99*, 073503.

259. Recht, D.; Smith, M. J.; Charnvanichborikarn, S.; Sullivan, J. T.; Winkler, M. T.; Mathews, J.; Warrender, J. M.; Buonassisi, T.; Williams, J. S.; Gradečak, S.; Aziz, M. J., Supersaturating Silicon with Transition Metals by Ion Implantation and Pulsed Laser Melting. *J. Appl. Phys.* **2013,** *114*, 124903.

260. Sher, M.-J.; Mazur, E., Intermediate Band Conduction in Femtosecond-Laser Hyperdoped Silicon. *Appl. Phys. Lett.* **2014,** *105*, 032103.

261. Mills, R., Self-Diffusion in Normal and Heavy Water in the Range 1-45.Deg. *J. Phys. Chem.* **1973,** *77*, 685-688.

262. Easteal, A. J.; Price, W. E.; Woolf, L. A., Diaphragm Cell for High-Temperature Diffusion Measurements. Tracer Diffusion Coefficients for Water to 363 K. *J. Chem. Soc. Faraday Trans.* **1989,** *85*, 1091-1097.

263. Serway, R. A., *Physics for Scientists & Engineers* 4th ed.; Saunders College Publishing: 1996.

264. Sengers, J. V.; Sengers, J. M. H. L., Thermodynamic Behavior of Fluids near Critical Point. *Ann. Rev. Phys. Chem.* **1986,** *37*, 189-222.

265. Chen, J.-H.; Fisher, M. E.; Nickel, B. G., Unbiased Estimation of Corrections to Scaling by Partial Differential Approximants. *Phys. Rev. Lett.* **1982,** *48*, 630-634.

266. Saul, A.; Wagner, W., International Equations for the Saturation Properties of Ordinary Water Substance. *J. Phys. Chem. Ref. Data* **1987,** *16*, 893-901.

267. Saul, A.; Wagner, W., A Fundamental Equation for Water Covering the Range from the Melting Line to 1273 K at Pressures up to 25 000 Mpa. *J. Phys. Chem. Ref. Data* **1989,** *18*, 1537-1564.

268. Hill, P. G., A Unified Fundamental Equation for the Thermodynamic Properties of H2o. *J. Phys. Chem. Ref. Data* **1990,** *19*, 1233-1274.

269. Rouleau, C. M.; Tian, M.; Puretzky, A. A.; Mahjouri-Samani, M.; Duscher, G.; Geohegan, D. B. In *Catalytic Nanoparticles for Carbon Nanotube Growth Synthesized by through Thin Film Femtosecond Laser Ablation*, 2014; pp 896907-896907-6.

270. Puretzky, A. A.; Geohegan, D. B.; Hurst, G. B.; Buchanan, M. V.; Luk'yanchuk, B. S., Imaging of Vapor Plumes Produced by Matrix Assisted Laser Desorption: A Plume Sharpening Effect. *Phys. Rev. Lett.* **1999,** *83*, 444-447.

271. Takehiko, I.; Paul-François, P.; Junpei, T. O.; Yuki, W., Viscosity Measurements of Molten Refractory Metals Using an Electrostatic Levitator. *Meas. Sci. Technol.* **2012,** *23*, 025305.

272. Mundo, C.; Sommerfeld, M.; Tropea, C., Droplet-Wall Collisions: Experimental Studies of the Deformation and Breakup Process. *Int. J. Multiphase Flow* **1995,** *21*, 151-173.

273. Mao, T.; Kuhn, D. C. S.; Tran, H., Spread and Rebound of Liquid Droplets Upon Impact on Flat Surfaces. *AIChE Journal* **1997,** *43*, 2169-2179.

274. Lin, Z.; Zhigilei, L. V.; Celli, V., Electron-Phonon Coupling and Electron Heat Capacity of Metals under Conditions of Strong Electron-Phonon Nonequilibrium. *Phys. Rev. B* **2008,** *77*.

275. Yu, R.; Song, H.; Zhang, X.-F.; Yang, P., Thermal Wetting of Platinum Nanocrystals on Silica Surface. *J. Phys. Chem. B* **2005,** *109*, 6940-6943.

276. Landström, L.; Heszler, P., Analysis of Blackbody-Like Radiation from Laser-Heated Gas-Phase Tungsten Nanoparticles. *J. Phys. Chem. B* **2004,** *108*, 6216-6221.

277. Krishna, H.; Sachan, R.; Strader, J.; Favazza, C.; Khenner, M.; Kalyanaraman, R., Thickness-Dependent Spontaneous Dewetting Morphology of Ultrathin Ag Films. *Nanotechnology* **2010,** *21*, 155601.

278. Howe, J. M., *Interfaces in Materials: Atomic Structure, Thermodynamics and Kinetics of Solid-Vapor, Solid-Liquid and Solid-Solid Interfaces*. John Wiley & Sons: New York, NY, 1997.

279. Wang, X. Y.; Riffe, D. M.; Lee, Y. S.; Downer, M. C., Time-Resolved Electron-Temperature Measurement in a Highly Excited Gold Target Using Femtosecond Thermionic Emission. *Phys. Rev. B* **1994,** *50*, 8016-8019.

280. Gurevich, E. L.; Levy, Y.; Gurevich, S. V.; Bulgakova, N. M., Role of the Temperature Dynamics in Formation of Nanopatterns Upon Single Femtosecond Laser Pulses on Gold. *Phys. Rev. B* **2017,** *95*, 054305.

281. Hohlfeld, J.; Wellershoff, S. S.; Güdde, J.; Conrad, U.; Jähnke, V.; Matthias, E., Electron and Lattice Dynamics Following Optical Excitation of Metals. *Chem. Phys.* **2000,** *251*, 237-258.

List of Publications

Published:

1. C.-Y. Shih, M. V. Shugaev, C. Wu, and L. V. Zhigilei, Generation of Subsurface Voids, Incubation Effect and Formation of Nanoparticles in Short Pulse Laser Interactions with Bulk Metal Targets in Liquid: Molecular Dynamics Study, J. Phys. Chem. C, DOI:10.1021/acs.jpcc.7b02301, 2017

2. C.-Y. Shih, C. Wu, H. Wu, M. V. Shugaev, and L. V. Zhigilei, Atomistic simulations of the generation of nanoparticles in short-pulse laser ablation of metals: The effect of background gas and liquid environments, in *Pulsed Laser Ablation: Advances and Applications in Nanoparticles and Nanostructuring Thin Films*, Edited by I. N. Mihailescu and A. P. Caricato (Pan Stanford, 2017), pp. 421-466.

3. M. V. Shugaev, C.-Y. Shih, E. T. Karim, C. Wu, and L. V. Zhigilei, Generation of nanocrystalline surface layer in short pulse laser processing of metal targets under conditions of spatial confinement by solid or liquid overlayer, *Appl. Surf. Sci.* 417, 54-63, 2017.

4. C.-Y. Shih, C. Wu, M.V. Shugaev, and L.V. Zhigilei, Atomistic modeling of nanoparticle generation in short pulse laser ablation of thin metal films in water, *J. Colloid Interface Sci.* 489, 3-17, 2017.

5. C. M. Rouleau, C.-Y. Shih, C. Wu, L. V. Zhigilei, A. A. Puretzky, and D. B. Geohegan, Nanoparticle generation and transport resulting from femtosecond laser ablation of ultrathin metal films: Time-resolved measurements and molecular dynamics simulations, *Appl. Phys. Lett.* 104, 193106, 2014.

Submitted:

1. C. -Y Shih, R. Streubel, J. Heberle, M. V. Shugaev, C. Wu, M. Schmidt, B. Gökce, S. Barcikowski, and L. V. Zhigilei , Two mechanisms of nanoparticle generation in pulsed laser ablation in liquids: The origin of the bimodal size distribution, ACS Nano

In Final stages of preparation:

1. C.-Y. Shih, M.V. Shugaev, C. Wu, and L.V. Zhigilei, The effect of pulse duration on nanoparticle generation mechanisms in pulsed laser ablation in liquids: Molecular dynamics study
2. C.-Y. Shih, M.V. Shugaev, and L.V. Zhigilei, Effect of liquid environment on single-pulsed ablative generation of laser induced periodic surface structures and nanoparticle generation
3. C.-Y Shih, C. Wu, M.V. Shugaev, L.V. Zhigilei, Atomistic simulations of nanoparticle generation by fs-pulsed laser ablation of thin Ag films
4. C.-Y Shih, M.V. Shugaev, L.V. Zhigilei, Atomistic simulations of alloy nanoparticle generation for short pulsed laser ablation of Ag-Cu multi-layers

List of Presentations

Presenter is underlined

Oral presentation:

1. L. V. Zhigilei, C. Wu, C.-Y. Shih, and M. V. Shugaev, Atomistic modeling of material modification and nanoparticle formation by short pulse laser irradiation in vacuum and in liquid environment, *Summer School on Ultra-short Pulse Lasers Applications in Material Processing (APPOLO)*, Vilnius, Lithuania, July 2017. *(Invited)*
2. L. V. Zhigilei, C. Wu, C.-Y. Shih, and M. V. Shugaev, Large-scale atomistic simulations of nanoparticle generation and material modification by short laser pulses, Seminar at the *Institute of Applied Physics, Johannes Kepler University*, Linz, Austria, May 2017. *(Invited)*
3. L. V. Zhigilei, C.-Y. Shih, C. Wu, and M. V. Shugaev, Two mechanisms of nanoparticle generation in pulsed laser ablation in liquids: The origin of the bimodal size distribution, *European Materials Research Society (E-MRS) 2017 Spring Meeting*, Strasbourg, France, May 2017. *(Invited)*
4. L. V. Zhigilei, C. Wu, C.-Y. Shih, and M. V. Shugaev, Large-scale atomistic simulations of nanoparticle generation and material modification by short laser pulses in vacuum and liquid environment, *European XFEL Theory seminar*, Hamburg, Germany, May 2017. *(Invited)*
5. L. V. Zhigilei, C.-Y. Shih, C. Wu, and M. V. Shugaev Computational study of generation of nanoparticles and surface nanocrystallization by short pulse laser irradiation of metal targets in liquid environment, 7th European Conference on Applications of Femtosecond Lasers in Materials Science (FemtoMat 2017), Mauterndorf, Austria, March 2017. *(Invited)*
6. C.-Y. Shih, M. V. Shugaev, C. Wu, and L. V. Zhigilei Atomistic modeling of pulsed laser interactions with metal targets in liquid environment, Materials Science Seminar at the Department of Physical Chemistry, University of Vienna, Austria, January 2017. *(Invited)*

7. C.-Y. Shih, C. Wu, M. V. Shugaev, L. V. Zhigilei Atomistic simulations of short pulse laser-metal interactions in liquid environment, *83rd Annual Meeting of the Southeastern Section of the American Physical Society*, Charlottesville, Virginia, November 2016.
8. L. V. Zhigilei, C. Wu, C.-Y. Shih, H. Wu, E. T. Karim, and M. V. Shugaev, Simulations of short pulse laser ablation and nanoparticle formation under spatial confinement: From background gas to liquid environment and to solid overlayer, *10th International Conference on Photo-Excited Processes and Applications (ICPEPA-10)*, Brasov, Romania, August 2016.
9. H. Wu, C. Wu, M. V. Shugaev, C.-Y. Shih, L. V. Zhigilei, Large scale molecular dynamics simulations of femtosecond laser ablation of Al in Ar gas environment, *Light Conference*, Changchun, China, July 2016.
10. C.-Y. Shih, C. Wu, M. V. Shugaev, L. V. Zhigilei Atomistic simulations of short pulse laser-metal interactions in liquid environment, Advanced Nanoparticle Generation and Excitation by Lasers in Liquids (ANGEL), Essen, Germany, May 2016.
11. C.-Y. Shih, C. Wu, M. V. Shugaev, L. V. Zhigilei, Atomistic simulations of nanoparticle generation in femtosecond laser ablation of thin metal films, European Materials Research Society (EMRS), Lillie, France, May 2016.
12. L. V. Zhigilei, C.-Y. Shih, C. Wu, and M. V. Shugaev, Atomistic simulations of short pulse laser-metal interactions in liquid environment, *11th International High Power Laser Ablation & Directed Energy Symposium*, Santa Fe, New Mexico, April 2016.
13. L. V. Zhigilei, C.-Y. Shih, C. Wu, and M. V. Shugaev, Molecular dynamics simulation study of femtosecond laser ablation of silver thin films and bulk targets in water environment, *13th Conference on Laser Ablation (COLA-2015)*, Cairns, Australia, August 2015.
14. M. V. Shugaev, E. T. Karim, C.-Y. Shih, C. Wu, and L. V. Zhigilei, Interaction of short pulse laser irradiation with metal targets under condition of spatial confinement, *APS March Meeting*, San Antonio, Texas, March 2015.
15. C. Wu, E. T. Karim, M. Shugaev, C.-Y. Shih, and L. V. Zhigilei, Large-scale atomistic simulations of laser ablation, generation of sub-surface voids, crystal defects and nanocrystalline surface layers in short pulse laser processing of metals, *9th International*

Conference on Photo-Excited Processes and Applications, Matsue, Japan, September 2014.

16. E. T. Karim, M. Shugaev, C. Wu, C.-Y. Shih, L. V. Zhigilei, Z. Lin, and R. Hainsey, Atomistic simulation study of short pulse laser interactions with metal targets under conditions of spatial confinement, *International Symposia on High-Power Laser Ablation and Beamed Energy Propulsion*, Santa Fe, New Mexico, April 2014.
17. C. M. Rouleau, A. A. Puretzky, D. B. Geohegan, M. Yoon, K. L. More, G. Duscher, C.-Y. Shih, C. Wu, and L. V. Zhigilei, Catalytic nanoparticles for carbon nanotube growth synthesized by through thin film femtosecond laser ablation, SPIE Photonics West 2014, San Francisco, California, February 2014.
18. M. Shugaev, E. T. Karim, C. Wu, C.-Y. Shih, L. V. Zhigilei, Z. Lin, and B. Hainsey, Computational and experimental study of short pulse laser ablation under conditions of spatial confinement, *12th International Conference on Laser Ablation (COLA 2013), Ischia,* Italy, October 2013.

Poster presentation:

1. M. V. Shugaev, C.-Y. Shih, and L. V. Zhigilei, Mechanisms of the generation of highly-regular laser induced periodic surface structures, *2017 Oak Ridge Leadership Computing Facility (OLCF) User Meeting*, ORNL, Oak Ridge, Tennessee, May 2017.
2. C.-Y. Shih, C. Wu, M. Shugaev, L. V. Zhigilei, C. M. Rouleau, A. A. Puretzky, and D. Geohegan, Atomistic simulations and experimental study of nanoparticle generation in femtosecond laser ablation of thin metal films, *International Symposia on High-Power Laser Ablation and Beamed Energy Propulsion*, Santa Fe, New Mexico, April 2014. (***First Place Award***)
3. Z. Lin, H. Matsumoto, M. Conneran, J. Kleinert, R. Hainsey, S. Concina, E. T. Karim, M. Shugaev, C. Wu, C.-Y. Shih, and L. V. Zhigilei, Experimental investigation and atomistic simulation of short pulse laser interactions with spatially confined metal targets, *International Symposia on High-Power Laser Ablation and Beamed Energy Propulsion*, Santa Fe, New Mexico, April 2014. (***Second Place Award***)

4. C.-Y. Shih, C. Wu, M. Shugaev, and L. V. Zhigilei, Atomistic simulations of nanoparticle generation in femtosecond laser ablation of thin metal films, Engineering Science Symposium at UVa, April 2014.
5. C.-Y. Shih, C. Wu, M. Shugaev, and L. V. Zhigilei, Atomistic simulations of nanoparticle generation in femtosecond laser ablation of thin metal films, University of Virginia Presidential Research Competition Symposium, April 2013.
6. C.-Y. Shih, C. Wu, and L. V. Zhigilei, Atomistic simulations of nanoparticle generation by pulsed laser ablation of thin metal films and multilayers, *3rd Venice International School on Lasers in Materials Science (SLIMS)*, Isola di San Servolo, Venice, Italy, July 2012.